MEMS Scanners with Diffractive Optical Elements for LiDAR Applications

Inês Sofia Garcia

UMinho | 2024

Universidade do Minho
Escola de Engenharia

Inês Sofia Moreira Garcia

MEMS Scanners with Diffractive Optical Elements for LiDAR Applications

fevereiro de 2024

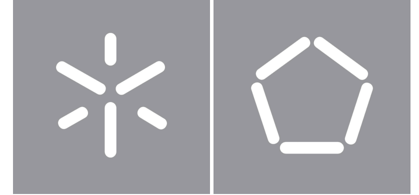

Universidade do Minho
Escola de Engenharia

Inês Sofia Moreira Garcia

MEMS Scanners with Diffractive Optical Elements for LiDAR Applications

Tese de Doutoramento
Programa Doutoral em Engenharia Eletrónica e de Computadores (PDEEC) na especialidade de Instrumentação e Microssistemas Eletrónicos

Trabalho efetuado sob a orientação de
Professor Doutor Jorge Miguel Nunes dos Santos Cabral
Doutora Rosana Maria Alves Dias

fevereiro 2024

Direitos de Autor e Condições de Utilização do Trabalho por Terceiros

Este é um trabalho académico que pode ser utilizado por terceiros desde que respeitadas as regras e boas práticas internacionalmente aceites, no que concerne aos direitos de autor e direitos conexos.

Assim, o presente trabalho pode ser utilizado nos termos previstos na licença abaixo indicada.

Caso o utilizador necessite de permissão para poder fazer um uso do trabalho em condições não previstas no licenciamento indicado, deverá contactar o autor, através do RepositóriUM da Universidade do Minho.

Licença concedida aos utilizadores deste trabalho:

CC BY-NC-ND

https://creativecommons.org/licenses/by-nc-nd/4.0/

Acknowledgements

This thesis is the culmination of 4 years of research, which was only made possible by the indispensable support and incentives of several people whom I cannot fail to thank.

First, I want to thank my family, especially my parents, Clara and João, and my sister, Carolina, a huge thank you for always being on my side, even when I disappeared for days to the cleanroom, and always believing in me. Thanks also to my grandmothers, Celeste and Isabel, for the warm Sunday lunches that made me pause and breathe for some precious moments. To my grandfather, Emídio, wherever you are, a huge thank you full of "*saudade*".

A big thank you to my supervisors, Professor PhD Jorge Cabral and PhD Rosana Dias, for all the availability, guidance, and support. To PhD João Gaspar, my supervisor in my first steps of this work, for bring up this opportunity, the challenge and confidence in my capabilities to solve it. To PhD Diogo Aguiam for his optics knowledge, patience, time and motivation. I also want to thank you, PhD Filipe Alves, who, although not an official supervisor, has been a mentor from the beginning of my MEMS journey when I was only a master's student and from whom I especially thank all the words of encouragement and shared joy over the past six years.

To my friends, Ana Miranda, Carlos Areias, Diana Soares, Filipe Leite, Francisca Fonseca, Marco Luís, Mariana Ferreira, Michael Oliveira, Rafael Pereira, Sofia Teixeira, and Vitor Fernandes, for not putting any more pressure in me, for the laughter and fellowship. To Fernando Ribeiro, Marisa Alcântara, Inês Ribeiro, António Ribeiro and Francisco Ribeiro, a warm thank you for the support and joyful times as well.

To my colleagues and, most of all, friends from INL, for the sharing, support, laughter and good times within lab walls, Dimitri Santos, Eurico Moreira, Hélder Fonseca, Inês Pires, Joana Santos, João Vieira, Jorge Pereira, José Fernandes, José Queiroz, Patricia Oliveira, André Araújo and Pedro Anacleto. To Carlos Ferreira and Carlos Silva, thank you for the teamwork and companionship during sensible times. And most of all, to Filipa Mota, the student who became my work bestie so fast, for giving me her hand and always saying that everything would be all right.

A special thank you to Tiago Ribeiro, for believing in me more than I do.

And finally, to my princess Leia.

This work was supported by the European Structural and Investment Funds in the FEDER Component through the Operational Competitiveness and Internationalization Programme (COMPETE 2020) under Project 037902 Sensible Car (POCI-01-0247-FEDER-037902).

STATEMENT OF INTEGRITY

I hereby declare having conducted this academic work with integrity. I confirm that I have not used plagiarism or any form of undue use of information or falsification of results along the process leading to its elaboration.

I further declare that I have fully acknowledged the Code of Ethical Conduct of the University of Minho.

Universidade do Minho, Braga, Fevereiro 2024

Inês Sofia Moreira Garcia

Title: MEMS scanners with diffractive optical elements for LiDAR applications

Abstract

MEMS (Micro-Electro-Mechanical Systems) applied to optical scanning systems have the ability to modulate light using a miniaturised system and have driven several developments in Light Detection and Ranging (LiDAR), motivated by the demand for autonomous vehicles. LiDAR MEMS scanning devices are able to replace current state-of-the-art bulky mechanical LiDAR systems, not only by reducing size and costs but also by facilitating their integration in vehicles. The integration of diffraction optical elements into scanning MEMS mirrors further enables a large field of view (FoV) to be obtained by diffracting the incident beam into a regular spot pattern and is being explored for LiDAR applications.

This work presents the development of an optical MEMS device to integrate the scanning module of a LiDAR system that is capable of achieving up to 86° per 13° field of view with five diffracted uniform beam spots. The device presents novel features related to its key performance aspects and the micromachining process. In this device, a surface relief DOE is integrated onto the MEMS mirror surface to split the laser beam into five uniform spots, with a diffraction angle of 2.6°. The device also exploits the use of asymmetric electrodes to enable the control of the mirror angle in two- axes. These electrostatic actuators were defined using a novel self-aligned micromachining process combining standard bulk techniques with grayscale lithography. With these novel beam splitting and steering features, the required mechanical deflection of the MEMS actuator is smaller, resulting in a more robust mechanical structure. In addition, a nanoimprint lithography process was developed to replicate the multilevel patterns and to further optimize the throughput to a batch production level, decreasing 40 times the necessary time and 82 times the overall lithography costs.

The device's mechanical and optical properties were experimentally obtained. The results show a resonant plus non-resonant configuration, useful for a better non-lissajous scanning coverage, with a large horizontal angle (above 60°) at the natural frequency of 1240 Hz, taking advantage of the Q-factor of 24 and five quasi-static vertical FoVs (10 Hz) of 2.6° each. The DOE uniformity and angular aperture were within the expected values, above 30% and within 2.6°±0.15°, respectively, for all incident laser angular conditions, given the MEMS torsional motion.

Keywords: Asymmetric electrodes, Diffractive optical element, Grayscale lithography, Multispot LiDAR, 2D MEMS mirror.

Título: Scanner MEMS com elementos óticos difrativos para aplicações LiDAR

Resumo

A tecnologia MEMS, devido à sua capacidade de modular luz através de um sistema miniaturizado, tem sido fundamenral em sistemas de varrimento que, aliados ao progresso de veículos autónomos, têm impulsionado vários desenvolvimentos em *Light Detection and Ranging* (LiDAR) baseados em MEMS. Estes são capazes de substituir os atuais sistemas LiDAR presentes na literatura, que dependem de mecanismos mecânicos volumosos, reduzindo não só o tamanho e custos associados, mas também facilitando a sua integração num veículo. A integração de elementos ópticos de difração em espelhos MEMS tem sido investigado para aplicações LiDAR mostrando se particularmente promissora. Esta abordagem, que utiliza a difração de um feixe laser para expandir o campo de visão (FoV), tem mostrado grande potencial.

Esta tese apresenta o desenvolvimento de um dispositivo MEMS óptico para aplicações LiDAR, capaz de atingir até 86° por 13° de FoV, difratando o feixe laser em cinco pontos uniformes. As inovações inerentes ao dispositivo incluem aspectos de funcionamento e técnicas de microfabricação. Neste dispositivo, o elemento difrativo, integrado na superfície refletiva do espelho, divide o feixe de laser em cinco pontos, com um ângulo de difração de 2,6°. Este apresenta eletrodos assimétricos para atuar e defletir o espelho em dois eixos, criados através de um processo de microfabricação inovador, combinando técnicas de fabricação *bulk* com litografia *grayscale*. Com a fusão de técnicas de varrimento e difração, reduz-se a deflexão mecânica máxima necessária do atuador MEMS, resultando numa estrutura mecânica mais robusta. Para otimizar ainda mais o processo para produção em massa, litografia de nano-impressão foi implementada para replicar as estruturas assimétricas, diminuindo 40 vezes o tempo necessário e 82 vezes os custos gerais da litografia quando comparada com o processo normalizado.

As propriedades mecânicas e ópticas do dispositivo foram obtidas experimentalmente. Estes mostram uma configuração ressonante mais não-ressonante, com um ângulo horizontal de mais de 60° à frequência natural de 1240 Hz, explorando o fator-Q de 24, e cinco FoVs verticais (a 10 Hz) de 2,6° cada. A uniformidade e a abertura angular do padrão difratado apresentaram resultados dentro dos esperados, acima de 30% e dentro de 2,6°±0,15°, respectivamente, para todas as condições angulares do laser incidente, dado o movimento torcional do espelho.

Palavras-Chave: Elementos óticos difrativos, Eletrodos assimétricos, Espelho MEMS 2D, LiDAR de múltiplos feixes, Litografia *grayscale*.

Table of Contents

Acknowledgements .... **ii**

Abstract .... **v**

Resumo .... **vi**

Table of Contents .... **vii**

List of figures .... **xiii**

List of Tables .... **xxii**

List of Acronyms .... **xxiv**

1. Introduction **1**

1.1 LiDAR scanning systems 2

1.2 Diffractive Optical Elements 5

1.2.1 Single-slit diffraction principle simplification 6

1.2.2 DOEs topologies 7

1.2.3 Reflective and transmissive DOES 8

1.3 MOEMS for scanning systems 9

1.3.1 Principle of operation 11

1.3.2 Actuation principles 12

1.3.3 MEMS mirror for LiDAR literature review 14

1.4 MEMS-based diffractive optical devices 16

1.4.1 Multibeam steering based on MEMS and DOE technology for LiDAR 18

1.4.2 Integration of DOEs in different optical elements 20

1.4.3 Grating-based optical element merged with MEMS 21

1.5 Motivation 22

1.6 Objectives 24

1.7 Document organisation 26

2. Process equipment & experimental techniques 28

2.1 Depositions Techniques 29

2.1.1 Physical Vapour Deposition - PVD 29

2.1.2 Chemical Vapour Deposition – CVD & PECVD 30

2.1.3 Electroplating Deposition 32

2.1.4 Atomic Layer Deposition – ALD 33

2.1.5 Spin coating 34

2.1.6 Summary 35

2.2 Lithography Techniques 35

2.2.1 Photolithography – Mask Aligner System 38

2.2.2 Direct-Write-laser Lithography 38

2.2.3 E-beam Lithography 40

2.2.4 Nano-imprint Lithography (NIL) 41

2.2.5 Summary 42

2.3 Etching Techniques 43

2.3.1 Wet-etching 43

2.3.2 Dry Etching 44

2.3.3 Summary 48

2.4 Cleaning 49

2.5 MEMS standard micromachining process 51

2.5.1 Silicon-on-Insulator (SOI) wafer 51

2.5.2 Process flow 51

2.6 SOI-based asymmetric electrodes processes 54

2.7 Conclusions 56

3. MEMS Mirror 58

3.1 Theoretical Foundations 60

3.1.1 Field of view static analysis 63

3.1.2 Analysis of the MEMS mirror dynamic behaviour 66

3.2 Device analytical evaluation 69

3.2.1 Electrostatic and elastic torque 72

3.2.2 Damping coefficient and quality factor 75

3.3 Device dynamic performance evaluation 77

3.3.1 MEMS mirror dynamic model 77

3.3.2 Perturbation response 78

3.3.3 Resonant mode Field of View (FoV) 79

3.4 Device FEM Evaluation 80

3.4.1 The Resonance Frequency – Modal Simulation 81

3.4.2 Elasticity coefficient – Static Structural Simulation 84

3.4.3 Electrostatic field of asymmetric electrodes – Electrostatic Simulation 85

3.4.4 Out-plane natural deflection – Structural Simulation 89

3.5 Designed MEMS Structures 90

3.5.1 Electrical routing 94

3.5.2 2D MEMS Mirror variation 95

3.6 Conclusions 96

4. Optical Elements 98

4.1 Theoretical Foundations 99

4.1.1 Light propagation foundations 99

4.1.2 Damman diffractive element 101

4.1.3 Aperture angle between the diffracted beams 104

4.1.4 Constraints from the merging of DOE on the MEMS surface 104

4.2 Analytic evaluation of diffractive optical element..... 107

4.2.1 Projection pattern 109

4.2.2 Grating depth 110

4.2.3 DOE Dynamic performance..... 112

4.2.4 Incident beam collimation effects 114

4.2.5 Field of View simulation 116

4.3 Reflective Dammann DOE micromachining techniques 117

4.3.1 Microfabrication Sof surface reliefs..... 117

4.3.2 Device reflective surface 118

4.3.3 Single Metal layer modelling..... 120

4.4 Dammann Integration with MEMS Mirror 121

4.5 Conclusions..... 123

5. Micromachining process 124

5.1 Preliminary micromachining studies 125

5.1.1 Reflective coating..... 125

5.1.2 DOE micromachining process optimization..... 127

5.1.3 Front-side (FS) multilevel process optimization 129

5.1.4 Back-side (BS) process optimization..... 133

5.2 MEMS Mirror micromachining process on SOI wafer..... 138

5.2.1 Wafer preparation 139

5.2.2 DOE pattern and reflective layer 139

5.2.3 Silicon oxide (SiO_2) Hard-masks..... 140

5.2.4 Structure Etching..... 143

5.2.5 Structure release 145

5.2.6 Fabricated 2D MEMS mirrors with DOEs 146

5.2.7 Process simplification for 1D MEMS mirror 148

5.3 Packaging 149

5.4 Nanoimprint Lithography (NIL) 151

5.4.1 Master 151

5.4.2 Intermediate working stamp 151

5.4.3 Replica 153

5.4.4 Replication with alignment 156

5.5 Conclusions 158

6. Experimental Characterization 160

6.1 Experimental setups development 160

6.1.1 Surface Metrology 161

6.1.2 Scanning laser-Doppler vibrometer setup 162

6.1.3 Large optical FoV setup (with $\theta i \approx 0°$) for visible laser wavelength 164

6.1.4 NIR optical FoV setup (with configurable θi) for 1550 nm laser wavelength 164

6.2 2D MEMS mirror experimental characterization 166

6.2.1 Topography 166

6.2.2 Inner natural resonance frequency 167

6.2.3 Pull-in voltage 169

6.2.4 Inner and outer axis mechanical deflection 171

6.2.5 Inner axis large FoV 174

6.3 Experimental characterization of the diffractive optical element 174

6.3.1 Topography 174

6.3.2 Diffraction pattern measurements 175

6.3.3 Diffraction angular aperture 177

6.3.4 Diffraction pattern uniformity 178

6.4 Multibeam field-of-view scans 179

6.5 Conclusions 180

7. Conclusions 182

7.1 Thesis main achievements 183

7.2 Scientific contributions 186

7.3 Future work 187

References 189

List of figures

Figure 1-1 – LiDAR measuring system schematic. 2

Figure 1-2 – LiDAR scanning architectures scheme, (a) flash LiDAR; (b) OPAs-based LiDAR; (c) motorized LiDAR; and (d) MEMS-based LiDAR system. 3

Figure 1-3 – Wave diffraction based on Huygens-Fresnel principle. 6

Figure 1-4 – Diffraction pattern from a single slit aperture 7

Figure 1-5 – Schematic of surface relief and refractive transmissive DOEs. 9

Figure 1-6 – Schematic of surface relief and refractive, reflective DOEs. 9

Figure 1-7 – Two-dimensional FOV by the (a) combination of two 1D scanners or (b) a 2D scanner. 10

Figure 1-8 – Scanning profile for the 2D MEMS micromirror. In a) the Quasi-static profile on both axes is shown. In b), the fast axis is scanning in resonant mode, and the slow axis is scanning in Quasi-static mode. In c), both axes are scanning in resonant mode [3] 12

Figure 1-9 – Top, front, and cross-sectional view schematics and SEM images of a (a) grating light valve from [73]. 17

Figure 1-10 – Top, front, and cross-sectional view schematics and SEM images of[69] a 1D MEMS OPA from [70]. 17

Figure 1-11 – Piston-like DMD mirror states schematic [74]. 17

Figure 1-12 – (a) SEM images of the 8 × 8 MEMS OPA HCG array [75]. (b) SEM images of the 32 x 32 MEMS 2D OPA [76]. 18

Figure 1-13 – Multi-spot LiDAR architectures presented in the literature, with 1D MEMS mirror [80] and 2D MEMS mirror [81] and multiple laser sources. 19

Figure 1-14 – All-MEMS multibeam LiDAR steering system from (a) [82] and (b) [83]. 20

Figure 1-15 – Schematic of the electromagnetic 1-DOF MEMS scanning mirror with the blazed grating from [66]. 21

Figure 1-16 – In-plane scanner schematic with grating embedded on the reflective surface for spectrometry application [93]. 22

Figure 1-17 – MEMS grating-based OPA based on surface micromachining, from [94]. 22

Figure 1-18 – Schematic of the proposed 2D MEMS with a DOE merged LiDAR projection. 23

Figure 1-19 – MEMS scanner merged with a DOE (grating) schematic. 24

Figure 1-20 – Thesis structure flow. 27

Figure 2-1 – Typical micromachining process sequence, a) deposition – lithography – etching – cleaning, and b) deposition of sacrificial layer – lithography – deposition of target material – lift-off. 28

Figure 2-2 – Deposition techniques schematic, (a) PVD, (b) CVD, and (c) electroplating. 29

Figure 2-3 – Photolithography process flow. 38

Figure 2-4 – DWL lithography process flow. 39

Figure 2-5 – DWL grayscale lithography process flow. 40

Figure 2-6 – E-beam lithography process flow. 41

Figure 2-7 – Nano-imprint lithography process flow. 42

Figure 2-8 – Isotropic (a) and anisotropic (b) cross-section profile. 44

Figure 2-9 – Silicon-on-isolator wafer cross-sectional schematic and correspondent nomenclature. 51

Figure 2-10 – SOI-based MEMS standard micromachining process flow. 53

Figure 2-11 – Device layer main micromachining steps implemented in [132] and [135] to create asymmetric vertical electrodes based on a double-layer mask with different materials. 55

Figure 2-12 – SEM images of the asymmetric vertical electrodes presented in [108], based on a double layer mask with different materials process. 55

Figure 2-13 – Device layer main micromachining steps implemented in [133] to create asymmetric vertical electrodes based on a double-layer mask with the same material. 55

Figure 2-14 – Proposed multilevel self-aligned process using grayscale lithography. 56

Figure 3-1 – Designer inputs in the modelling process [139]. 59

Figure 3-2 – 1-DOF micro actuator: in-plane motion, gap (a), or overlapped area changing (b) and out-plane motion (c). 60

Figure 3-3 – Step response of different quality factor 2nd order mechanical systems. 63

Figure 3-4 – Symmetric (a) and asymmetric (b) electrodes schematic of different overlapping areas for different mirror deflection angles, θ. 64

Figure 3-5 – Cross-sectional schematic of the fringe field in asymmetric electrodes, in the rest position and in equilibrium. 64

Figure 3-6 – Outer axis electrodes topology schematic – staggered vertical electrodes. 65

Figure 3-7 – Torsional spring beam referential and variables. 65

Figure 3-8 – 1D and 2D MEMS mirror gimbal schematic. 71

Figure 3-9 – Electrostatic torque dependence on the applied voltage in symmetric electrodes geometry with $drot$ with 500 µm, and d with 4 µm. 72

Figure 3-10 – Symmetric electrostatic torque dependence on the electrodes gap, with $drot$ with 500 μm, and V with 50 V. 73

Figure 3-11 – Maximum torque evolutions for different applied voltages and electrode gap values combos. 73

Figure 3-12 – Symmetric electrostatic torque dependence on $drot$, with the electrodes gap of 3 μm, and V with 100 V. 73

Figure 3-13 – Asymmetric electrostatic torque angular expected profile. 74

Figure 3-14 – Torsional elastic torque dependance on the spring's width. 74

Figure 3-15 – Torsional elastic torque dependance on the spring's length. 75

Figure 3-16 – Quality factor versus mirror side dimensions, from 1 to 10 mm. 75

Figure 3-17 – Quality factor versus pressure conditions, from 0.001 to 1 atm. 76

Figure 3-18 – Effect of the mirror side dimensions increase on the moment of inertia and natural frequency of the device. 76

Figure 3-19 – Symulink MEMS mirror model 78

Figure 3-20 – Dynamic theoretical behaviour for an initial perturbation. 78

Figure 3-21 – Dynamic theoretical behaviour for different actuation voltages. 79

Figure 3-22 – Maximum mirror deflection evolution for different applied voltages when different electrode gaps (top), distances to the torsional axis (middle) and damping conditions (bottom) are implemented. 80

Figure 3-23 – Simplified 3D model for the modal FEM analysis of the (a) inner axis, and (b) outer axis. 81

Figure 3-24 – MEMS Mirror's inner axis resonance modes. 82

Figure 3-25 – MEMS Mirror's outer axis resonance modes. 83

Figure 3-26 – Inner axis structural FEM simulation 3D results of the mechanical deflection [μm] (a) and resultant stress [N/m^2] (b). 85

Figure 3-27 – Outer axis structural FEM simulation 3D results of the mechanical deflection [μm] (a) and resultant stress [N/m^2] (b). 85

Figure 3-28 – Asymmetric electrodes' electrical potential [V] in the rest (a), middle (b) and in the aligned positions (c). 86

Figure 3-29 – Asymmetric electrodes x-electric field [V/m], in the rest (a), middle (b) and in the aligned positions (c). 86

Figure 3-30 – Asymmetric electrodes y-electric field [V/m], in the rest (a), middle (b) and in the aligned positions (c). 86
Figure 3-31 – Asymmetric electrostatic actuators FEM simplified model with a short distance to the rotation axis and (b) longer. 87
Figure 3-32 – FEM results of the symmetric electrode geometry for different $drot$ (left) and electrode's gaps (right) values. 88
Figure 3-33 – FEM results of the asymmetric electrodes geometry for different $drot$ (left) and electrode's gaps (right) values. 88
Figure 3-34 – Comparison between symmetric and asymmetric FEM results and the analytical model. 89
Figure 3-35 – Three-dimensional FEM results for an external gravitational acceleration in the zz direction (9.8 m/s^2). 89
Figure 3-36 – Three-dimensional FEM results for an external gravitational acceleration in the yy direction (9.8 m/s^2). 90
Figure 3-37 – Three-dimensional FEM results for an external gravitational acceleration in the xx direction (9.8 m/s^2). 90
Figure 3-38 – 3D model of the MEMS mirror designed. 91
Figure 3-39 – Schematic of the 2D MEMS mirror. 92
Figure 3-40 – Fast axis and slow axis movement design. 93
Figure 3-41 – 2D Mirror electrical routing. 94
Figure 4-1 – Sketch of three different imaging regions in a lens-less imaging system as a function of the Fresnel distance [17], [162]. 99
Figure 4-2 – Damman diffraction optical setup. 102
Figure 4-3 – One-dimensional, symmetrical, binary function having values +1 and -1 only from [19]. 103
Figure 4-4 – Grating pitch relation with target aperture angle and wavelength. 104
Figure 4-5 – Optical path schematic of two rays of a laser beam that comes from a coherent laser source. 105
Figure 4-6 – Mirror angle influence on the laser source incidence angle. 106
Figure 4-7 – Beams optical path schematic for an incident angle, θ (a) < 0° and (b) > 0°. 107
Figure 4-8 – Damman grating parameters used on optical analytical simulations – one segment perspective view. 108

Figure 4-9 – Damman grating parameters used on optical analytical simulations – full reflective area layout top view. 108

Figure 4-10 – Schematic of the influence of the mirror motion on the angle of incidence, with the inner, AoI_y and outer axes, AoI_x. 108

Figure 4-11 – Dammann grating diffraction simulation tool architecture. 109

Figure 4-12 – Laser source simulated beam, perspective, and top view. 110

Figure 4-13 – Simulated diffracted beam, perspective, and top view. 110

Figure 4-14 – Grating depth and angle of incidence assuming a phase shift of π. 111

Figure 4-15 – Diffracted projection, assuming an AoI_y of 45°, for different grating depths (100, 300, 500, and 700 nm). 111

Figure 4-16 – Diffracted projection, assuming an AoI_y of 30, 40, 50 and 60°, for a grating depth of 548 nm. 112

Figure 4-17 – Diffracted pattern central spots intensity average normalized, as function of the grating depth and laser angle of incidence AoI_y. Highlight the initial assumption of a system with a normal AoI_y of 45° and the optimal solution with an AoI_y of 18°. 113

Figure 4-18 – Diffracted projection, assuming an AoI_y of 3, 13, 23 and 33°, for a grating depth of 407 nm. 113

Figure 4-19 – Diffracted projection, assuming an AoI_x of 0, 0.5, 1 and 1.5°, for a grating depth of 407 nm. 114

Figure 4-20 – Diffracted pattern central spots intensity average normalized, as function of the grating depth and laser angle of incidence, AoI_x. 114

Figure 4-21 – Grating projection pattern, assuming AoI_x of 0°, AoI_y of 18° and depth of 407 nm, for different incident laser beam widths (from 0.9 mm to 4 mm). 115

Figure 4-22 – Large diffracted FoV simulated at 2 meters from the DOE for a full motion cycle, with only inner axis motion. 116

Figure 4-23 – Large diffracted FoV simulated at 2 meters from the DOE for a full motion cycle, with only outer axis motion. 116

Figure 4-24 – Large diffracted FoV simulated at 2 meters from the DOE for a full mirror cycle, with inner and outer motion. 116

Figure 4-25 – Binary DOE by substrate etching. 117

Figure 4-26 – Binary DOE by different material reliefs. 117

Figure 4-27 – Multilevel DOE by (a) different material reliefs or (b) substrate etching. 118

Figure 4-28 – Binary reflective DOE by (a) substrate with reflective coating followed by different material reliefs or (b) substrate etching followed by reflective coating. 118

Figure 4-29 – (a) Metallic coating and (b) multilayer stacks coating (higher reflectivity and higher heat immunity). 118

Figure 4-30 – Schematic of the standard reflective stack structure simulated on TFCalc. 120

Figure 4-31 – Comparison of theoretical reflectance of the silicon substrate and a silicon substrate with a thin layer (500 nm) of aluminium. Red stars represent the reflectance for a wavelength of 1550 nm. 120

Figure 4-32 – 3D model of the MEMS mirror with DOE designed, with a schematic of the projected diffraction. 121

Figure 4-33 – Schematic of the 2D MEMS mirror with diffractive optical element. 122

Figure 5-1 – Reflectance characterization setup 125

Figure 5-2 – Reflective DOE topography micromachining process. 127

Figure 5-3 – DOE exposure results analysis, where (a) and (b) microscopic optical images from the tests using DWL and MA systems, respectively. 128

Figure 5-4 – Optical microscopic images of the grayscale calibration exposure for 20% and 25% energy. 130

Figure 5-5 – Grayscale characterization curve, showing that at least 80 different GS levels are possible. 130

Figure 5-6 – Mechanical profilometer scan of the photoresist thickness after GS lithography on the asymmetric electrodes. 131

Figure 5-7 – Optical microscopic image and measurements of the alignment between the grayscale lithography with previous masks 131

Figure 5-8 – Multilevel asymmetric electrodes SEM images after the sequential DRIE process, with and without the organic residue cleaning process. 132

Figure 5-9 – Optical microscopic images of the BS mirror cavity process. 133

Figure 5-10 – Silicon grass SEM image of the MEMS mirror cavity (a) and on the sacrificial grid solution (b). 134

Figure 5-11 – (a) Representation of the mask used to define the trenches on the whole wafer area. (b) Acquired cross sections of an example set of etched trenches with features extracted from trench cross sections using automatic computer vision algorithm. 135

Figure 5-12 – Wafer scale analysis of sidewall angle for different etch gas flow rates (a) and etching chamber pressures (b). Etch rate trends for gas flow rate and etching chamber pressure variation (c). 136

Figure 5-13 – Back side DRIE etching tests with different recipes. 136

Figure 5-14 – Process flow of BS double lithography process to create multilevel mask without grayscale lithography. 137

Figure 5-15 – OM images of BS double lithography process to create multilevel mask without grayscale lithography. 137

Figure 5-16 – 2D MEMS mirror with DOE micromachining process steps. 138

Figure 5-17 – Cross-section schematic of the 2D MEMS mirror with DOE structure 139

Figure 5-18 – Optical microscope images of the DOE and metal steps of the 2D MEMS mirror process. 140

Figure 5-19 – Cross-section process flow of the BS hard-mask patterning of the 2D MEMS mirror. ... 141

Figure 5-20 – Optical microscope images of the BS hard-mask of the 2D MEMS mirror process. 141

Figure 5-21 – Cross-section process flow of the FS multilevel hard-mask patterning of the 2D MEMS mirror. 142

Figure 5-22 – Optical microscope images of the FS multilevel hard-mask of the 2D MEMS mirror process. 142

Figure 5-23 – Cross-section process flow of the FS multilevel transfer to the device layer of the 2D MEMS mirror. 144

Figure 5-24 – Optical microscope images of the FS multilevel transfer of the 2D MEMS mirror process. 144

Figure 5-25 – SEM images of the asymmetric electrodes. 144

Figure 5-26 – Cross-section process flow of the BS multilevel transfer to the handle layer of the 2D MEMS mirror. 145

Figure 5-27 – Optical microscope images of the BS multilevel transfer of the 2D MEMS mirror process. 145

Figure 5-28 – Released devices suspended on DOI wafers frame. 146

Figure 5-29 – SEM images of the fabricated 2D MEMS mirror device. 147

Figure 5-30 – SEM images of the Dammann grating entailed in the reflective surface of the 2D MEMS mirror. 148

Figure 5-31 – 1D MEMS mirror micromachining process steps. 149

Figure 5-32 – SEM images of the 1D MEMS mirror device fabricated. 150
Figure 5-33 – Packaged MEMS mirror in a customized packaged solution. 150
Figure 5-34 – Multilevel silicon master micromachining process main steps, where (a) SiO_2 CVD; (b) photoresist spin coating; (c) grayscale lithography; (d) pattern transpose by a sequential RIE/O_2 strip to the had-mask layer. 151
Figure 5-35 – Intermediate working stamp micromachining process main steps: (a) Master anti-sticking treatment; (b) OrmoStamp disposal onto the Si master; (c) placing the glass substrate with adhesion promotor OrmoPrime08 on top of OrmoStamp; (d) OrmoStamp moulding and curing; and (e) Demolding. 152
Figure 5-36 – SEM images of the intermediate working stamp (with 10 nm-Au coating). 152
Figure 5-37 – OM images and profilometer data of the master, upon the GS lithography and the multilevel pattern and of the working stamp. 153
Figure 5-38 – Multilevel replica micromachining process main steps, where (a) photoresist spin coating; (b) stacking of replica wafer and stamp; (c) Stamp filling and curing (d) Separation. 154
Figure 5-39 – Optical microscopic images of the NIL replicas microfabricated. 155
Figure 5-40 – Optical microscopic images of the MEMS mirror pattern during the removal of the residual Layer. 156
Figure 5-41 – NIL alignment stage, with dedicated 3D printed holder. 157
Figure 5-42 – OM of the replica with alignment with the metal layer. 157
Figure 5-43 – Match between master and replica pattern. 158
Figure 6-1 – Surface metrology setup, using Polytec MSA-500 topography measurement systems (TMS). 161
Figure 6-2 – Out-of-plane displacement setup, using Polytec MSA-500 topography measurement systems (TMS). 163
Figure 6-3 – Measurement points for the (a) fast and (b) slow axis characterization. 163
Figure 6-4 – Large Optical FoV experimental setup schematic and images. 164
Figure 6-5 – NIR optical FoV experimental setup schematic and image. 165
Figure 6-6 – Schematic of the calibration of the device plane and laser source AoI to guarantee a normal projection on the photodiode plan. 165
Figure 6-7 – Asymmetric electrodes topography measurement, (a) x and y view; and (b) z view. 166
Figure 6-8 – IAx frequency response experimental data for different actuation voltages. 169
Figure 6-9 – OAx frequency response experimental data for different actuation voltages. 169

Figure 6-10 – Pull-in experimental data, where (a) is the applied voltage, (b) the pull-in on device A, and (c) of device B. 170

Figure 6-11 – IAx mechanical deflection. 171

Figure 6-12 – OAx mechanical deflection and FOV. 171

Figure 6-13 – Experimental IAx deflection angle and resultant FoV. 172

Figure 6-14 – Experimental OAx deflection angle and resultant FoV. 172

Figure 6-15 – OAx FoV as a function of the applied voltage for devices A (a) and B (b) 172

Figure 6-16 – IAx large surface deformation experimental data. 173

Figure 6-17 – OAx large surface deformation experimental data. 173

Figure 6-18 – IAx large filed of field (86°) experimentally achieved. 174

Figure 6-19 – DOE patterned on the reflective surface of the MEMS mirror topography measurement for an AoI of 18°. 175

Figure 6-20 – NIR optical FoV experimental setup schematic for static diffraction projection. 176

Figure 6-21 – Diffracted pattern scanned data lateral and top views. 176

Figure 6-22 – Diffracted pattern scanned data, perspective view. 177

Figure 6-23 – DOE pattern scan for z=0mm and z=40mm. 177

Figure 6-24 – Diffraction aperture angle, for a rest position incident angle of (a) 45° and (b) 18°. 178

Figure 6-25 – Diffraction pattern uniformity, for a rest position incident angle of (a) 45° and (b) 18°. 178

Figure 6-26 – Perspective view of the scanned FoV measured under the large scan photodiode setup, with (a) only IAx actuation, (b) IAx and low OAx actuation, and (c) IAx and high OAx actuation. 179

Figure 6-27 – Top view of the scanned FoV measured under the large scan photodiode setup, with (a) only IAx actuation, (b) IAx and low OAx actuation, and (c) IAx and high OAx actuation. 180

Figure 7-1 – Resonant plus non-resonant figure of merit comparison, based on [5]. 183

Figure 7-2 – Multibeam steering system schematic of the works compared in Table 7-2. 184

List of Tables

Table 1-1 – LiDAR categories comparison. 4

Table 1-2 – MEMS mirrors architectures, divided by the number of anchor points. 11

Table 1-3 – Performance of the electrostatic, electromagnetic, and piezoelectric MEMS mirror actuation, from the lowest performance rated as * to the highest as *** 13

Table 1-4 – MEMS mirrors for LiDAR applications with the highest FoM, based on [5]. 15

Table 1-5 – MEMS and DOE requirements. 25

Table 2-1 – Summary of the different deposition techniques and respective characteristics. 35

Table 2-2 – Summary of the different lithography techniques and respective characteristics. 42

Table 2-3 – Summary of the different etching techniques and respective characteristics. 48

Table 2-4 – Micromachining cleaning techniques summary. 50

Table 3-1 – Initial parameters application-driven 70

Table 3-2 – Initial parameters microfabrication limits-driven 70

Table 3-3 – Inner axis resonance modes for different spring' widths extracted from the modal FEM analysis. 82

Table 3-4 – Gimbal structure resonance modes for different outer axis spring' width extracted from the modal FEM analysis. 83

Table 3-5 – FEM analysis of the torsional elasticity of different spring and mirror masses geometries. 84

Table 3-6 – Parameters of the layouts developed. 96

Table 4-1 – Damman solutions for N = 2. 107

Table 4-2 – Power damage threshold of different materials per unit of area [W/cm^2], ... 119

Table 5-1 – Reference Mirrors Used 126

Table 5-2 – Reflectance percentages of the reference Thorlabs mirrors. 126

Table 5-3 – Experimental Reflectance measurements for a wavelength of 1550 nm 127

Table 5-4 – Specifications of the different DOE experimental runs. 128

Table 5-5 – Fabricated DOE grove measurements and comparison using DWL or MA exposure systems. 128

Table 5-6 – Silicon etch rate (ER) using different etching techniques. 129

Table 5-7 – Working stamp NIL recipe. 152

Table 5-8 – Photoresist initial thickness of the replicas 154

Table 5-9 – NIL replication parameters of the different replicas. 154

Table 5-10 – Comparison of the electrode gap size of the master, stamp and final replica. 158

Table 6-1 – Frequency response of the inner (IAx) and outer (OAx) axes of devices A and B. 167

Table 6-2 – Experimental natural frequency and Q-factor of devices A and B (two samples of each). 168

Table 6-3 – Experimental FoV and correspondent actuation values of devices A and B. 173

Table 6-4 – DOE depth measurements with Polytec MSA-500 tool. 175

Table 7-1 – Initial parameters application-driven and achieved values. 183

Table 7-2 – Multibeam steering for LiDAR applications comparison with this work. 184

List of Acronyms

1D One-dimensional

2D Two-dimensional

3D Three-dimensional

AC Alternate-current

AGV Automatic Guided Vehicles

ALD Atomic Layer Deposition

AM Alignment marks

AoI Angle of Incidence

AVC Angular Vertical Combs

BOX Buried Oxide layer

BS Back Side

CMOS Complementary metal–oxide–semiconductor

CVD Chemical Vapour Deposition

DC Direct-current

DMD Digital Mirror Device

DOE Diffractive Optical Element

DOF Degree of freedom

DRIE Deep Reactive Ion Etching

DSP Double Side Polished

DUT Device Under Test

DWL Direct-write laser

EDP Ethylenediamine pyrocatechol

EKC Electronic Grade Kleaner

EM Electromagnetic

ES Electrostatic

FEM Finite Element Method

FFT	Fast Fourier Transform
FoM	Figure of Merit
FoV	Field of View
FS	Front Side
FTM	Four-Target-Module
GLV	Grating Light Valves
GS	Grayscale
HCG	High-index-contrast subwavelength grating
HF	Hydron Fluoride
IAx	Inner axis
IBE	Ion beam etching
ICP	Inductively Coupled Plasma
INL	International Iberian Nanotechnology Laboratory
IPA	Isopropyl alcohol
LDD	Linear Dynamic Deposition
LiDAR	Light Detection and Ranging
LPCVD	Low-pressure Chemical Vapour Deposition
MA	Mask aligner
MEMS	Micro-electro-mechanical Systems
MOEMS	Micro Optical-Electro-Mechanical Systems
NIL	Nanoimprint lithography
NIR	Near-infrared
OAx	Outer axis
OM	Optical Microscopic
OPA	Optical Phase Array
OPD	Optical Path Difference
PECVD	Plasma Enhanced Chemical Vapour Deposition

PR	Photoresist
PVD	Physical Vapour Deposition
RF	Radio Frequency
RIE	Reactive Ion Etching
SEM	Scanning Electron Microscope
SGM	Scanning Grating Mirrors
SMT	Surface Mount Technology
SOI	Silicon-on-insulator
SSP	Single Side Polished
SVC	Staggered Vertical Combs
TMAH	Tetramethylammonium hydroxide
ToF	Time-of-flight
TSV	Through Silicon Vias
TX	Transmission optics
UHV	Ultra-high vacuum
UV	Ultraviolet light

1. Introduction

Since the beginning of Micro-Electro-Mechanical Systems (MEMS) in 1975, numerous scientific works have been published in the literature that highlight their applications in optical scanning systems. This technological evolution has led to the emergence of a new field known as Micro-Optical-Electro-Mechanical Systems (MOEMS). The capacity to modulate light through miniaturized systems has yielded many applications [1], including imaging displays, projectors, 2D scanners, optical spectrometers, print, and light detection and ranging (LiDAR) systems for automotive applications. Remarkable progress in perception and sensing has revolutionized industries spanning from autonomous vehicles and robotics to environmental monitoring and urban planning. LiDAR systems are based on dynamic distance measurement techniques and have been applied since the early 1960s in various fields, including meteorology, agriculture, archaeology, aeroplanes, and satellites. These advancements have assumed increasing importance in contemporary autonomous vehicles, such as self-driving cars and Automatic Guided Vehicles (AGVs), for obstacle detection and avoidance, object recognition, and mapping.

LiDAR systems use a modulated laser as the carrier to measure distance. The ability to scan a field of view (FoV) using a laser beam through MOEMS scanners offers several advantages when compared to their macro-scale counterparts, including miniaturization, cost-effectiveness, and low-power consumption. Notably, the scope of MOEMS technology's potential applications extends beyond these domains, and as MEMS and micro-optics continue to advance, the range of possible applications is expanding. The pivotal

role of MOEMS technology in modern research and industry remains paramount as it continues to pave the way for future technological innovations in the optical scanning field. The design of optical MEMS requires not only a thorough understanding of the physical phenomena in the electric and mechanical domains of MEMS but also an understanding of optics and optical propagation [2].

This introductory section presents an overview of the current state-of-the-art MOEMS scanning systems, Diffractive Optical Elements (DOEs), and MEMS technology combined with DOEs. Furthermore, this thesis's motivation, objectives, and organization are detailed. This thesis research will provide insights on optical scanning systems by examining the potential applications of MOEMS technology and the different categories of optical modulation.

1.1 LiDAR scanning systems

The development of LiDAR systems, driven by the pursuit of safer and more efficient navigation in complex environments, has been catalysed by the principles of laser-based remote sensing to capture and interpret the surrounding world. At its core, LiDAR operates by emitting rapid and precisely timed laser pulses towards the surrounding environment (Figure 1-1).

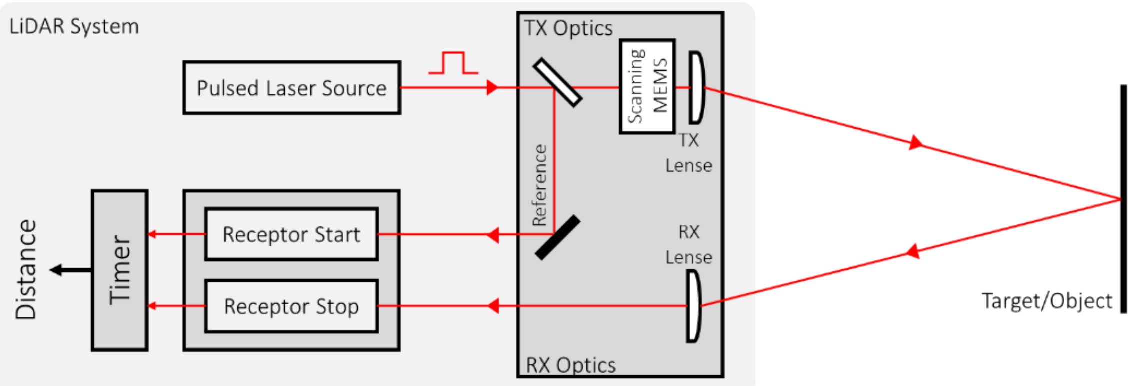

Figure 1-1 – LiDAR measuring system schematic.

Before exiting the LiDAR system, the laser passes through a set of transmission (TX) optics for focusing collimation and power detection, and through a scanning module. Then, it travels without obstructions until it encounters various objects in its path, such as buildings, trees, and terrain features. When a laser pulse strikes an object, a portion of the light is reflected towards the LiDAR system, which is then collected by the receiver optics and directed towards the photodetector (detector array) that converts the incoming light into electrical signals. By precisely measuring the time it takes for the emitted pulse to travel to the object and return, the LiDAR system can calculate the round-trip time, also known as the time-of-flight (ToF). Since the beam velocity may be assumed as a constant, the ToF information directly correlates to

the distance between the LiDAR system and the reflecting object. By iteratively executing this process with multiple laser pulses and in various scanning directions, the LiDAR system constructs a three-dimensional map of the environment, known as a point cloud, which accurately captures objects' spatial distribution and positions. False readings of nearby objects, known as ghost images [3], can occur due to laser beam reflections or pulse lasers emanating from nearby LiDAR systems, which can be solved using different pulse detection architectures [4]. The chosen laser properties must follow several specifications, such as the wavelength of the laser pulse, pulse energy or laser energy required for detection, which directly impacts the range (distance) of detection and eye safety requirements.

LiDAR can be categorized into two groups based on their laser beam scanning methodology: non-scanning LiDAR and scanning LiDAR [5]. Non-scanning LiDAR, also known as solid-state scanners, do not require moving parts. One example is the Flash LiDAR [6], [7], characterized by the complete illumination of the 2D field of view via a single laser source, Figure 1-2.a. Flash LiDAR emits a single light pulse and records the transit time of the emitted laser flash to each pixel on the detector array, which corresponds to the range from the object. While Flash LiDAR offers high reliability, cost-effectiveness, and compact dimensions, it may encounter limitations in detecting objects at distances exceeding a few tens of meters, rendering it suitable primarily for short-range applications [6], [8]. Another topology within the non-scanning category is the Optical Phased Arrays (OPAs), which can steer the incident laser beam [9], Figure 1-2.b. OPAs provide a way to modulate the individual phases of several optical antennas or emitters organized in an array. This technology promises high reliability, low cost, and compact size for increased appeal in high-volume production. However, there are disadvantages to the OPA design, from light loss in various components, which restricts its usable range to medium to long distances, to limited beam steering angles, that is constrained by the number of phase shifters. Besides, there are critical challenges to fabricate and actuate several individual optical phase modulators in a compact system at the energy levels required or LiDAR [10].

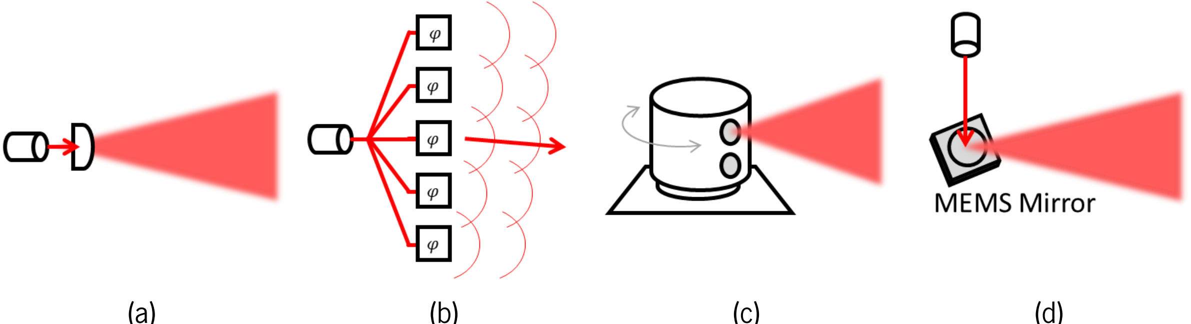

Figure 1-2 – LiDAR scanning architectures scheme, (a) flash LiDAR; (b) OPAs-based LiDAR; (c) motorized LiDAR; and (d) MEMS-based LiDAR system.

Motorized optomechanical scanners [11], [12], [13] and MEMS scanners belong to the scanning LiDAR category, being the last one considered as a quasi-solid-state LiDAR since the only moving part is the MEMS devices that steer the beam in free space. Macro mechanical scanning LiDAR uses one rotating scanning system to provide 360° FoV, Figure 1-2.c. This design offers the capability of 360° laser scanning sweeps with only one unit. However, its rotating functionality makes it less reliable, and its bulky size and steep costs restrict its appeal for high-volume production. On the other hand, MEMS scanners use oscillating mirrors to mechanically steer a beam or beams in one or more axes, Figure 1-2.d. This technology offers good reliability with minimal moving parts, low cost, and compact size for increased appeal in high-volume production. However, MEMS scanners are limited in terms of distance range to medium to long distances, field of view, and vulnerability to vibrations. The advantages and disadvantages of each scanning methodology are summarized in Table 1-1.

Current state-of-the-art LiDAR solutions predominantly employ mechanical scanning systems, which are typically implemented using large mechanical parts and classified as either macro or micro-scanners, depending on the size of the scanning element. While there are diverse implementations of macro-scanners, micro-scanners tend to scan in both horizontal and vertical directions. The ideal alternative would be to scan or steer the laser beam without the need for mechanical moving components. Nevertheless, optical phased arrays and other alternatives, while promising, remain at an incipient stage of development, lacking mass production implementations and cost-efficiency matching mass market product requirements [5].

Table 1-1 – LiDAR categories comparison.

	Flash	OPAs	Mechanical Scanning	MEMS
Mechanism	Static	Static	Rotating mechanism	Minimal / Quasi-static
Range	Short range	Medium to long-range	Long – to 200m	Medium to long-range
FoV		Limited by the number of phase shifters	360° Scans	Limited by MEMS mechanical deflection
Size	Compact	Compact	Bulky	Compact
Cost	Low	Low	High	Low
+	Beyond a few tens of meters, returning light is insufficient for reliable detection.	OPA component light loss limits usable range.		Vulnerability to vibrations.

MEMS-based micro-scanner systems present a viable solution for both single-source (employing a single laser source) and multi-beam (integrating multiple laser sources) LiDARs, leveraging current technological capabilities. MEMS devices propose a significant advantage in the automotive industry due to their size

and cost reduction, well-defined manufacturing process, and simplified integration of sensors for autonomous driving without substantial impact on the vehicle's aesthetics.

MEMS scanners combined with diffractive optical elements (DOE) have also shown promising performance for multibeam LiDAR applications. The combination of a MEMS scanner with a DOE has proven to be an innovative solution, as a large FoV can be obtained by diffracting the incident beam into a regular spot pattern, such as an array/matrix of spots or even a scan line [14], [15], [16]. Multibeam LiDAR solution can be achieved with traditional reflective MEMS mirrors and an array of laser sources, critically aligned, to achieve wide FoV. In contrast, when coupled with a DOE, MEMS scanners can deliver wide FoV without needing multiple laser sources. Here, the DOE effectively diffracts the incident laser beam, sculpting it into a pattern of discrete spots, which the MEMS scanner adeptly scans across a broad FoV, thereby changing the efficacy and versatility of LiDAR systems.

1.2 Diffractive Optical Elements

The field of optics is vast and complex, requiring the use of different models to study light propagation at both macroscopic and microscopic scales. At the macro-scale, light can be modelled as simple rays with a particular wavelength period, direction, and intensity that originate from a source point. These ray models can adequately approximate optical elements such as lenses and mirrors that refract and reflect light. However, the diffraction and interference phenomena of light waves require a more in-depth understanding of light with the medium at the microscopic scale, where the optical element feature sizes are of the same order of magnitude as the wavelength. In the wave modulation field, consider a plane electromagnetic (EM) wave with an electric field described in terms of its amplitude E_0 and phase φ as

$$E(x, y, t) = E_0 \, exp(\varphi_0 + \omega t) \tag{1-1}$$

A DOE inserted into the optical path at the coordinates (x, y) can be described as a thin optical filter that locally modulates the wave amplitude E_0 or the phase φ. Phase DOEs introduce local phase variations of the wavefront through surface reliefs and materials, which can be exploited to generate interference patterns. Contrary to optical apertures, phase DOEs have the advantage of not blocking any of the incoming light, enabling higher device transmission efficiencies.

Diffraction occurs whenever light waves interact with obstacles. At the microscopic scale, light behaves more similarly to a wave, and any obstacle or medium causes a local change in the wave's phase and/or amplitude, which affects the way light propagates and interferes with other waves. According to the

Huygens-Fresnel principle, a wave is composed of infinitesimally small point sources which radiate isotropically, each producing a spherical wavelet. In the near-field of an aperture, these wavelets significantly interfere locally with each other constructively and destructively, while in the far-field, the interference pattern remains mostly constant with the propagation distance. For a wide aperture, the uniform distribution of wavelets produces a mostly flat wavefront of constant phase at the center of the aperture and a rounded wavefront along its corners, as in Figure 1-3, which results from the diffraction effect. As aperture sizes decrease to the order of the wavelength, these diffractive effects become much more pronounced. Diffractive Optical Elements, also known as gratings, belong to the wave optics light modulation class and are structures that can block, transmit, reflect or impose a static phase shift on the incident waves.

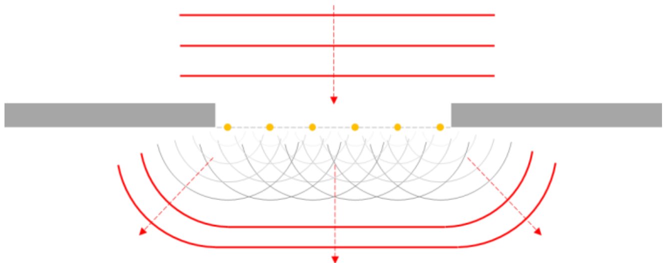

Figure 1-3 – Wave diffraction based on Huygens-Fresnel principle.

1.2.1 Single-slit diffraction principle simplification

Consider a planar wave incident on an aperture gap, as presented in Figure 1-3. The sum of these spherical wavelets, created at several points along with the aperture, forms the wavefront. The electric fields emanating from each source interfere with all the others at each point in space, leading to constructive or destructive interference, depending on their phase difference. As a result, a far-field interference pattern is formed. Consider a flat wave with wavelength λ propagating through a small slit aperture and a distant detector screen, Figure 1-4. The intensity, I, of the pattern for a single slit aperture with width, d, depends on the angle formed between the point on the projection plane and the source and the distance between the aperture and the detector screen (L) and can be given by the equation (1-2) [17].

$$I(\theta) = I_0 sinc^2\left(\frac{d\pi}{\lambda}\sin(\theta)\right) \tag{1-2}$$

Diffraction gratings are optical components with regular patterns on their surface, usually with a pattern density specified in lines per mm (lines/mm). These gratings generate an interference pattern on a screen whose intensity has multiple maxima at the angles θ_m, described by the grating equation (1-3).

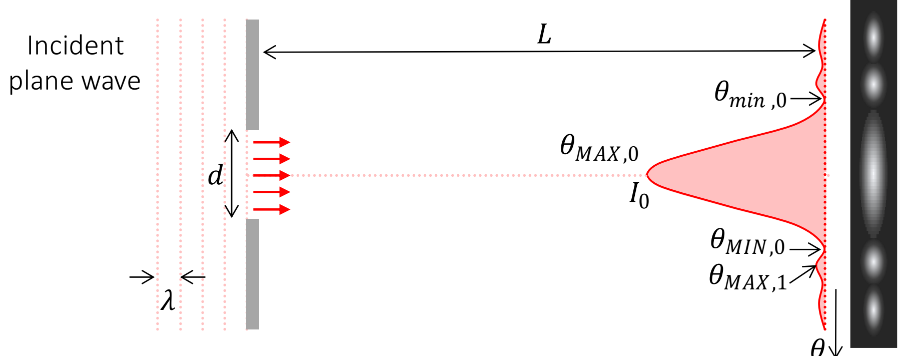

Figure 1-4 – Diffraction pattern from a single slit aperture.

$$d(sin\theta_m + sin\theta_i) = m\lambda, \quad (1\text{-}3)$$

where θ_i is the incident angle on the grating, d is the spacing between the grating elements, and m is the diffraction order, which can be a positive or negative integer.

In conclusion, understanding the behaviour of light waves at the microscopic scale is crucial in the study of optics, and different models have been developed to achieve this. DOEs and diffraction gratings are essential components that allow the modulation and manipulation of light waves, respectively, and their properties can be described using equations such as the ones presented above.

1.2.2 DOEs topologies

Diffractive Optical Elements are specialized devices that manipulate light through micro or nanostructured patterns, which can be opaque, transparent, or reflective, affecting the wave's phase and amplitude based on its wavelength and incidence angle. These patterns are designed with feature sizes on the order of the light wave's wavelength, allowing for precise interaction with light based on its wavelength and the angle at which it strikes the DOE. DOEs can be categorized by their physical thickness in relation to the phase shift they impart on the traversing light wave: thin DOEs induce a phase shift up to 2π, while thick DOEs exceed this value, resulting in significant phase alterations.

The utility of DOEs is evident in their ability to tailor the phase and amplitude of incident light, thereby controlling the spatial distribution of the diffracted light. This capability renders them invaluable in applications such as laser beam shaping, structured illumination, and the generation of intricate optical fields. The emergence of coherent light sources, notably lasers, has facilitated the creation of synthetic holograms, which are fabricated by encoding interference patterns onto a medium. The flexibility of DOEs extends to their ability to transform an input light beam into a desired output form, ranging from duplicating the input beam to generating specific shapes such as square spots. Commercially available

gratings demonstrate this versatility, achieving large angular outputs and providing uniform illumination; however, these can still present some limitations, such as specific material constraints and efficiency issues in certain spectral bands. Moreover, typically, they present large dimensions, which can also be complex to integrate into a miniaturized system. DOEs can be classified into different categories, distinguishing between regular and arbitrary types, as well as static and dynamic variants. Regular gratings, a subset of DOEs, consist of equidistant lines or slits that diffract light into discrete orders, finding use in a multitude of applications, including spectroscopy, beam splitting, and optical communication. Échelette-type gratings and metagratings, designed through dispersion engineering, are notable for their role in beam splitting across broad spectral ranges [18], [19]. Grating light valves exemplify the application of actuated gratings in display technologies, modulating light to produce images and serving in optical filtering and signal processing [20], [21].

Arbitrary DOEs, in contrast, offer a high degree of customization due to their non-periodic structures, enabling specific light manipulation for applications such as holography, 3D displays, and security features. These DOEs are instrumental in producing advanced visual effects like the vertical 3D/3D switch effect, a novel security feature [22], [23], [24], [25], [26], [27].

Static DOEs, characterized by their unchanging structure post-fabrication, are commonly employed in consistent optical functions and are made from materials like etched glass or polymers [28], [29]. Dynamic DOEs, however, are reconfigurable in real-time, responding to external stimuli for applications necessitating immediate light manipulation. Technologies enabling dynamic DOEs include Structured Light Modulators [30], [31], POLICRYPS structures [32], [33], [34], and MEMS-based devices [35], [36], each with specific uses ranging from holography to adaptive optics.

1.2.3 Reflective and transmissive DOES

By definition, the optical path refers to the distance travelled by light through an optical medium, adjusted for the refractive index of the medium. The optical path length is governed by:

$$OP = \int_{S} \frac{c}{n} ds, \tag{1-4}$$

where n is the reflection index, c the light velocity and s the path. Consider a coherent light source generating a beam with a specific spot size and intensity distribution incident on a DOE. Transmissive DOEs introduce a phase shift (φ) to the incident wavefront through the different optical paths that propagate through the medium (n_1) or free space (n_0) [17], as defined in equation (1-5). This can be

achieved through surface reliefs or changes in the refractive index of the medium material, as depicted in the schematics of Figure 1-5.

$$\varphi(x,y) = \frac{d(x,y)}{\lambda} 2\pi(n_1 - n_0) \tag{1-5}$$

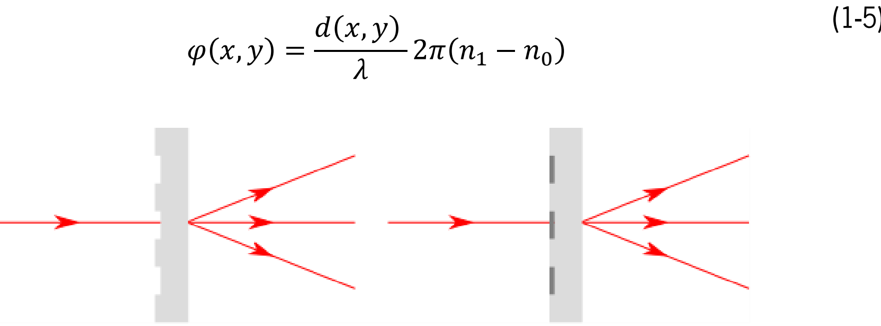

Figure 1-5 – Schematic of surface relief and refractive transmissive DOEs.

For reflective DOEs (Figure 1-6) with surface relief, the phase shift is introduced by the optical path difference between the first reflected surface at the top and the secondary reflected surfaces as the beam propagates through the free space medium (n_0), (1-6).

$$\varphi(x,y) = \frac{d(x,y)}{\lambda} 4\pi n_0 \tag{1-6}$$

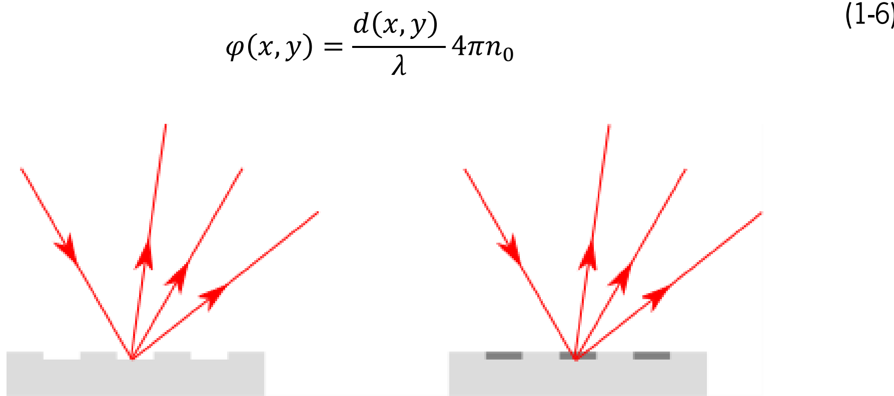

Figure 1-6 – Schematic of surface relief and refractive, reflective DOEs.

1.3 MOEMS for scanning systems

Reflection is the most common principle as a scanning engine among the full range of optical modulation. The MEMS scanning systems can mainly be categorized into one-dimensional (1D) and two-dimensional (2D). In a 1D scanner, light is scanned only in one dimension, comparatively, with the 2D ones that scan light in two perpendicular directions, resulting in a two-dimensional scan space, also known as the field of view. Several systems using MEMS mirrors have been presented with only one axis [37],[38], [39], even in LiDAR applications [40],[41]. Others combine two mirrors of one axis in a module, post-assembled, [39], [41] to be able to perform two axes scanning, as represented in the schematic of Figure 1-7. One of the significant advantages of a single-axis mirror scanner is that the mirror size can be larger, supporting more powerful laser sources.

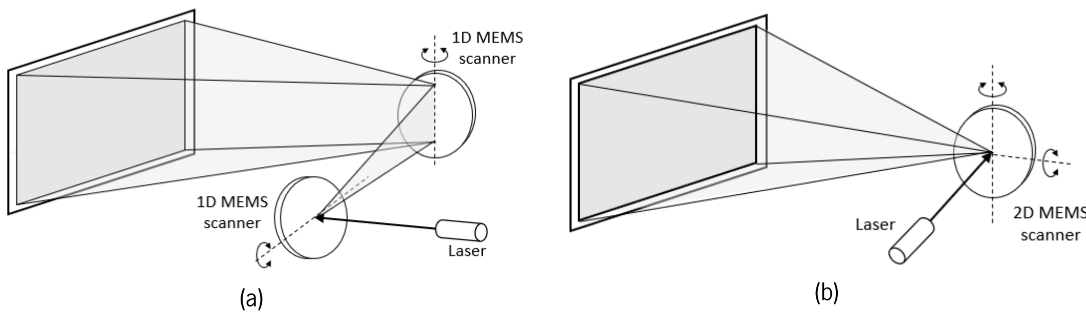

Figure 1-7 – Two-dimensional FOV by the (a) combination of two 1D scanners or (b) a 2D scanner.

Over the last three decades, diverse MEMS-based miniaturized laser scanners designed for 2D scanning applications have made their mark in the literature, presenting extensive technical reviews [1], [5]. These innovations encompass a spectrum of technologies, spanning from the utilization of digital mirror arrays, notably the Digital Micro mirror Device (DMD) [42], to the integration of 1D resonant MEMS scanners alongside Galvano scanners and even the deployment of paired resonant or non-resonant 1D scanners or 2D MEMS scanners.

DMD scanning employs a compact array of micro mirrors, each representing a pixel. These MEMS micro mirrors possess the capability to switch fast between positions, alternating from reflecting to not reflecting light. This dynamic manipulation enables the projection and scanning of intricate light patterns onto diverse surfaces. The utility of DMD technology extends to fields such as projectors and spatial light modulation, conferring precise control over light dispersion.

On the other hand, the 1D Resonant MEMS Scanner combined with the Galvano Scanner combines two types of scanners for enhanced scanning speed and accuracy and has been used in various applications like laser engraving and biomedical imaging. Here, a 1D resonant MEMS scanner oscillates at a resonant frequency, enabling high-speed scanning in one dimension, and the Galvano scanner moves a mirror for slower scanning, using electromagnetic fields, in the other dimension [43], [44].

The final architecture, either resonant or non-resonant 1D scanners or 2D MEMS scanners, employs a dual-scanner setup. Resonant scanners oscillate at their natural frequency, enabling rapid scanning. Non-resonant scanners move at controlled rates, offering precise positioning. The pairing of these scanners allows for intricate 2D space scanning [45], [46].

MEMS-based scanner systems have significant advantages due to their size and cost reduction, well-defined manufacturing process, and easier installation of the new sensors. Several properties of MEMS scanners differ from each other, as will be detailed in the following sections. These include principles of operations and architecture to the deflection actuation principle, which implies a dedicated micromachining process.

1.3.1 Principle of operation

There are various movement concepts for MEMS mirrors, classified by their mirror architectures. These range from architectures with a single pivot point suspending the reflective surface to architectures with multiple springs, such as bipod, tripod, and quadripod structures. Table 1-2 presents a summary of these architectures and their corresponding schematics.

Table 1-2 – MEMS mirrors architectures, divided by the number of anchor points.

Unipod	Bipod	Tripod	Quadripod	Gimbal
Cantilever [47];	Half gimbal [4];	Dual use spring [29];	Folded spring [30],[12];	Bipod structure inside a Bipod frame [29];
Pivot[48];	Dual use spring [28];		Dual use spring [31];	

The cantilever geometry is one example where the mirror support works as the spring that holds and drives the mirror to move. Conversely, the pivot mirror uses a single point, typically in the mirror's center, to hold and deform the mirror to change its position. In the bipod category, the half gimbal employs two torsion beams to deform and move the mirror, while the dual-use spring uses the spring holding the mirror to generate a force for steering, typically not a torsional force. Being a bipod, it steers in only one rotating axis plus the z-axis (out-of-plane) for beam focus.

The tripod geometry employs three springs spaced 120° apart to hold and move the mirror while generating a force that steers it, typically not a torsional force. In the quadripod mirror category, the folded spring geometry allows for mirror movement in the XYZ directions and creates rotational movements in two axes. Similarly, the dual-use spring generates a force to steer the mirror while holding it. Both tripod and quadripod architectures steer in two rotating axes plus the z-axis for beam focus.

The MEMS mirror's scanning profile depends on the actuation mode of each axis. There are two primary modes: the quasi-static mode, where the mirror position responds directly to the driver's command, and the resonance mode, where the MEMS mirror can operate dynamically. By combining these two modes, the mirror can perform scanning in three ways: (a) quasi-static mode on both axes, (b) fast axis in

resonance and slow axis in quasi-static mode, and (c) resonance mode on both axes, as depicted in Figure 1-8.

Figure 1-8.a shows the first operation mode, where the micromirror scans point-to-point. In this mode, both axes of the 2D mirror operate in vector-like mode, allowing MEMS operation from DC to a specific frequency, positioning the MEMS precisely, moving at a uniform velocity, and performing vectorial scanning. In contrast, Figure 1-8.b demonstrates the second operation mode, where both modes (quasi-static and resonance) are combined. One axis operates in a high-frequency mode, allowing for fast axis movement (on the order of kHz) that creates horizontal lines, while the other axis works in vector-like mode or at a low motion frequency and moves with a triangular-like waveform to create a raster pattern covering a rectangular area. The third and final operation mode on both axes operates at high frequencies for scanning, Figure 1-8.c. The mirror motion is confined to narrowband, sinusoidal trajectories with a phase lag to the applied voltage, resulting in circles, ellipses, and other Lissajous patterns that can be modulated at some rate.

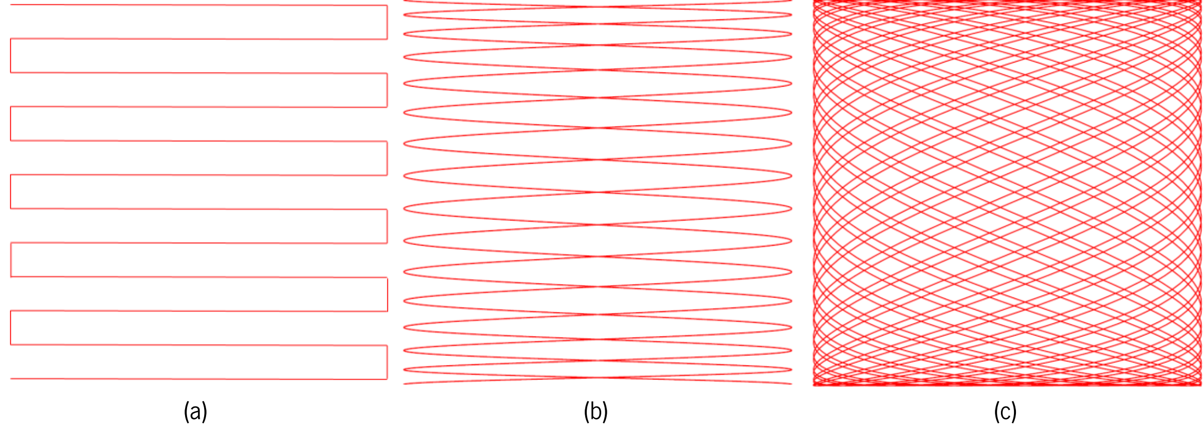

Figure 1-8 – Scanning profile for the 2D MEMS micromirror. In a) the Quasi-static profile on both axes is shown. In b), the fast axis is scanning in resonant mode, and the slow axis is scanning in Quasi-static mode. In c), both axes are scanning in resonant mode [3].

When operating these devices at resonance mode, with a frequency near their natural resonance frequency, it is possible to achieve large deflection angles at relatively low voltages and high speeds. The devices can be operated in modes b and c to achieve larger FoV. However, this can create some limitations regarding scanning speed and spot localization.

1.3.2 Actuation principles

The actuation principle of MOEMS (micro-opto-electromechanical systems) is a critical factor in achieving the performance of laser scanners, as it requires large out-of-plane displacements to steer the beam over

a wide scan field. Typical actuation mechanisms implemented in MEMS scanners include electrostatic (ES), electromagnetic (EM), thermal, and piezoelectric mechanisms [49].

Electrostatic (ES) actuators use the electrostatic force to attract micromechanical structures, generating mechanical motion by a change of stationary electric field in the material. This type of actuation is commonly used in MEMS mirrors, as it can be produced using conventional microfabrication processes and materials [50]. On the other hand, magneto-mechanical micro-actuation primarily exploits two effects: the action of electromagnetic forces (magneto-static) and magnetostriction (the strain magnetically inducible in ferromagnetic materials) [51]. Magnetic microactuators can be categorized according to the types of magnetic sources and microstructures involved. While this type of actuation is not as widely used as electrostatic actuators, it has its unique set of advantages for specific applications.

Piezoelectric actuation is based on the piezoelectric effect, which induces a mechanical strain in a stack of materials containing a piezoelectric component or thin film. When a voltage is applied across a piezo element, it deforms due to a reverse piezoelectric effect (voltage to stress/strain). Piezoelectric actuators are widely used in various applications, including MOEMS scanners [52]. Thermomechanical micro-actuation, on the other hand, exploits the thermal expansion of materials. Changes in the temperature profile result in mechanical displacements or force output through thermal expansion, contraction, or phase change. This type of actuation is less commonly used than the other three, but it has unique advantages for specific applications [53].

In terms of MEMS mirror actuation, electrostatic transduction is the dominant technology in the MEMS field. This is mainly due to the ease with which most electrical micro-actuators can be produced using conventional microfabrication processes and materials. A detailed analysis of the advantages and disadvantages of electrostatic, electromagnetic, and piezoelectric MEMS mirror actuation can be found in Table 1-3.

Table 1-3 – Performance of the electrostatic, electromagnetic, and piezoelectric MEMS mirror actuation, from the lowest performance rated as * to the highest as ***.

Category	Electrostatic	Electromagnetic	Thermal	Piezoelectric
Deflection	*	*	***	**
Natural frequency	***	**	*	**
Low power	**	*	*	***
Low voltage	*	***	*	**
Compactness	***	*	*	***
Linearity	*	***	**	**

Overall, the choice of actuation mechanism depends on the specific application and the desired level of performance. Each actuation mechanism has strengths and weaknesses, and careful consideration must be taken when selecting the most appropriate mechanism for a given application. In addition to the actuation method, the performance of MEMS mirrors for LiDAR applications also depends on the mirror size, shape, and material, as well as the design of the support structure and the driving circuitry.

1.3.3 MEMS mirror for LiDAR literature review

In the literature, several working topologies have been presented for LiDAR applications, from 2D scanning systems that can be implemented in self-driving cars to blind-spot detection systems, gesture recognition, and robotics, among others. MEMS mirrors offer advantages in terms of size, speed, and cost, making them ideal for LiDAR applications across a wide range of sectors [5]. Their use has led to a substantial reduction in the weight, size, and power consumption of LiDAR modules, enabling applications such as precise navigation in small UAVs [54].

Several LiDAR topologies have been presented, ranging from 2D scanning systems to more complex configurations. A recent comprehensive review by Wang et al. [5] categorizes MEMS mirrors into three scanning profiles with an alternative nomenclature: double resonant (Figure 1-8.c), double quasi-static (Figure 1-8.a), and non-resonant plus quasi-static (Figure 1-8.b). To better compare different MEMS mirror designs, the author defined as a figure of merit (FoM), the combination of effective optical scanning angular FoV in radian, θ_e, and the effective resonant frequency of the MEMS mirror in kHz, f_e, of a MEMS scanning mirror, to evaluate the performance of the device as:

$$FoM = \theta_e \cdot d_e \cdot f_e \tag{1-7}$$

where d_e is the effective dimension of the mirror plate in mm, defined as follows,

$$d_e = \sqrt{\frac{4A}{\pi}} \tag{1-8}$$

where A is the area of the mirror plate in mm^2. In order to uniformize the FoM values for non-resonant and resonant 1D and 2D devices, different θ_e calculations are used and extensively explained in [5], taking into consideration the device's Q-factor. For MEMS mirrors with Q lower than 10, Wang et al. defined Q as 10 for simplicity. In general, MEMS mirrors with larger FoM are more suitable for LiDAR applications, and 2D MEMS mirrors are desired in most cases. However, 1D MEMS mirrors usually have simpler structures and can be more easily designed with a wide scan angle, large aperture, and high

frequency. Table 1-4 summarizes the mirrors with the highest FoM presented in [5] for each scanning profile and actuation method.

Table 1-4 – MEMS mirrors for LiDAR applications with the highest FoM, based on [5].

Actuation Method	FoM	Mirror Area	Horizontal FoV	Vertical FoV	f_h (kHz)	f_v (kHz)	Horizontal Scan	Vertical Scan	
EM	0.97	D=1.5mm	65°	53°	0.4	21.3	Resonant	Resonant	[55]
EM	0.82	D=1.4mm	43.2°	24.3°	18	0.44	Resonant	Quasi-Static	[56]
EM	0.61	D=6.5mm	18°	30°	0.674	1.87	Resonant	Resonant	[57]
EM	0.42	D=2.5mm	60°	46°	0.16	0.21	Quasi-Static	Quasi-Static	[58]
EM	0.42	4x4 mm²	32°	32°	0.16	0.17	Quasi-Static	Quasi-Static	[59]
ES	1.29	D=0.8mm	24°	24°	3.8	3.9	Quasi-Static	Quasi-Static	[60]
ES	1.08	D=1.6mm	24°	24°	0.67	1.6	Quasi-Static	Quasi-Static	[60]
ES	0.62	D=7mm	26°	26°	1.57	1.57	Resonant	Resonant	[61]
ES	0.48	D=1mm	44°	24°	26	1.4	Resonant	Resonant	[62]
ET	0.98	D=1mm	16°	53°	2.7	2.7	Resonant	Quasi-Static	[63]
ET	0.45	D=0.5mm	4°	4°	12.8	12.8	Quasi-Static	Quasi-Static	[64]
PE	0.51	D=1mm	21°	31°	23.9	1.5	Resonant	Resonant	[65]

The best-performing mirrors in each category, according to the resultant FoM, are:

- A double resonant MEMS mirror, a biaxial mirror with an electromagnetic actuation method. This mirror achieves a horizontal resonant deflection angle of up to 65° at 400 Hz and a vertical resonant deflection angle of 56° at 21.3kHz., which is suitable for high-speed scanning (FoM of 0.97) [55];
- Double non-resonant MEMS mirror, a biaxial mirror with an electrostatic actuation method. This mirror achieves a deflection angle of up to 24° and a maximum scan rate of 3.8 kHz (FoM of 1.29) [60];
- A non-resonant plus resonant MEMS mirror, a biaxial mirror with an electromagnetic actuation method. This mirror achieves a resonant deflection angle of up to 43.2° at 18 kHz and a non-resonant deflection angle of 24.3° at 440 kHz., which is suitable for high-speed scanning (FoM of 0.82) [56].

Double resonant mirrors offer high scanning speed and large deflection angles, while double non-resonant mirrors have a simple design and are easy to fabricate. Non-resonant plus resonant mirrors combine the advantages of both resonant and non-resonant mirrors. The choice of MEMS mirror depends on the specific requirements of the LiDAR system, and further research and development are needed to improve the performance and reliability of these devices. The reliability and durability of MEMS mirrors have been proven through extensive testing. For instance, MEMS micromirrors have been characterized for space environments, showing that their performance remains unaffected after rigorous testing [66]. An

electrothermal Cu/W bimorph MEMS mirror survived 220 billion scanning cycles, further attesting to its stability and reliability [63].

1.4 MEMS-based diffractive optical devices

The convergence of MEMS technology with light modulation systems holds a well-established presence in the literature. Diffractive optical elements have also been combined with MEMS devices. MEMS-based DOEs are capable of real-time manipulation of the wavefront through the physical movement of microstructures and have a wide range of applications in optics and photonics. These systems offer dynamic, real-time control of the output beam's intensity, direction, and phase, enabling new functionalities such as beam steering, beam shaping, and optical switching. In optical communication, MEMS-based DOEs can be used to steer and shape laser beams for free-space communication, which has potential applications in satellite and deep-space communication [67].

One of the most promising MEMS-based DOEs is the optical phase array (OPA), which enables high-speed, high-resolution beam steering. OPAs are based on the same principle as DOEs but are not static elements, offering a dynamic, controllable output. In the literature, several types of phase modulators have been reported, from liquid crystals commonly used for large-scale OPAs [68], however, with slow rate, to silicon photonic waveguides with phase modulators and grating couplers, with high insertion loss and limited to infrared wavelengths transparent to silicon [69].

By using MEMS technology as the building blocks of an OPA-based scanner, it is possible to combine the possibility of customizable electronic steering of OPAs with the fast response of MEMS technology [70]. In a typical MEMS phased array, all the elements reflect coherently along a desired direction. This type of device has significant advantages over other phase modulators (liquid crystal, lithium niobate, and current silicon photonics devices) and has been designed in both 1D and 2D configurations [2].

One type of 1D MEMS-based OPA is the grating light valves (GLVs), which uses a diffraction grating built with parallel rows of suspended reflective micro-ribbons, as represented in Figure 1-9, that can be dynamically adjusted by applying a voltage to each micro-ribbon, producing a diffractive grating that switches between “on” and “off” states, redirecting light, as presented in [71]. By changing the voltage applied to each micro-ribbon, it is possible to produce different diffractive gratings, which can be used for beam shaping and steering. In a different alternative, the 1D array comprises several GLVs, all with the same pitch between micro-ribbons. In this alternative, the scanning is achieved by dynamically changing the period of the grating and, thus, the angle of the diffracted beam [72], [73]. One of the significant

drawbacks of this alternative is that there is only a limited number of available grating periods that are proportional to the pitch of the micro-ribbons. In [70], a different structure is presented to achieve a 1D MEMS phase shifter based on piston mirrors, which are displaced to provide the desired phase shift. This 256-element array MEMS OPA (Figure 1-10), designed to beam forming 905 nm wavelength with a fine pitch of 2.4 μm, obtained a 22° FOV and a response time of 2 μs.

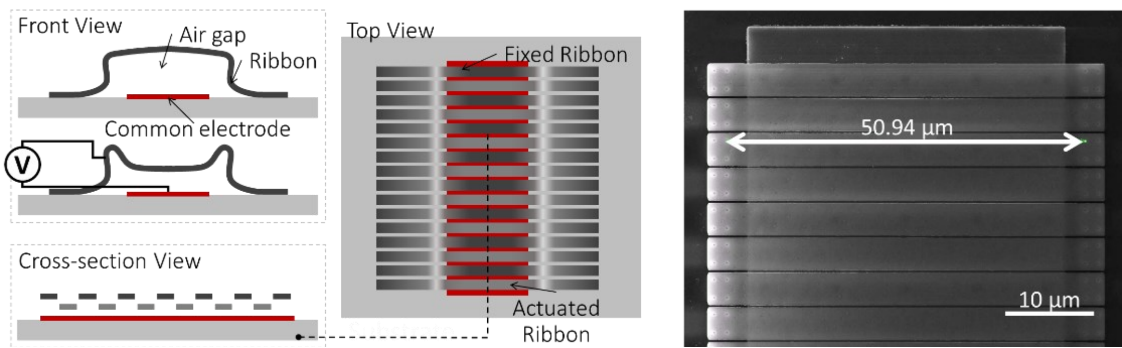

Figure 1-9 – Top, front, and cross-sectional view schematics and SEM images of a (a) grating light valve from [73].

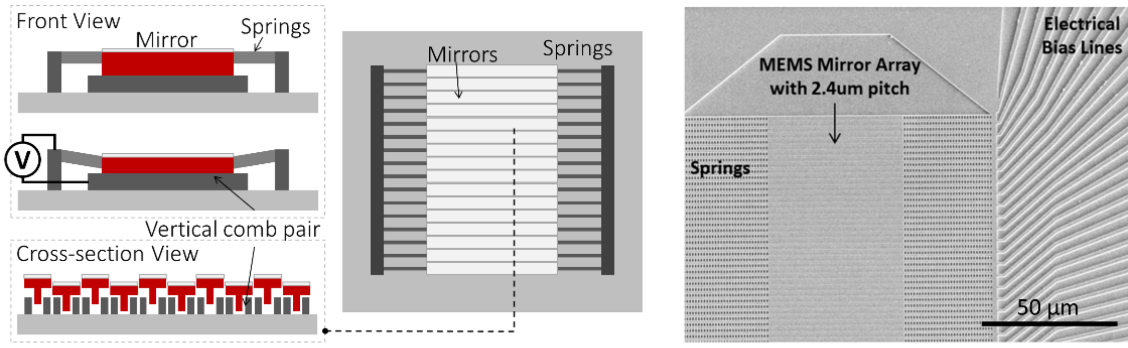

Figure 1-10 – Top, front, and cross-sectional view schematics and SEM images of[69] a 1D MEMS OPA from [70].

Another approach to build a MEMS-based OPAs is to produce a 2D array of micromirrors whose height can be dynamically adjusted via a piston-like movement, as represented in Figure 1-11. In this type of OPA, the height of each micromirror can be controlled, which in turn is converted into a phase shift on the incident wavefront. This offers high-resolution, high-speed beam steering capabilities and has been used in various applications, such as optical communication, laser machining, and holography [74].

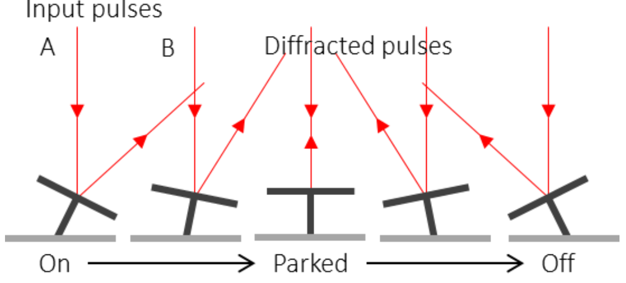

Figure 1-11 – Piston-like DMD mirror states schematic [74].

Regarding MEMS 2D OPA, a MEMS-based optical phased array incorporating a high-index-contrast subwavelength grating (HCG) for beamforming and beam steering was found in the literature. Each HCG reflector is suspended by four mechanical springs, one at each corner and electrostatically actuated. Figure 1-12.a presents an 8 × 8 optical phased array incorporating MEMS HCG mirrors on an SOI wafer with a schematic of the principle for beam steering [75].

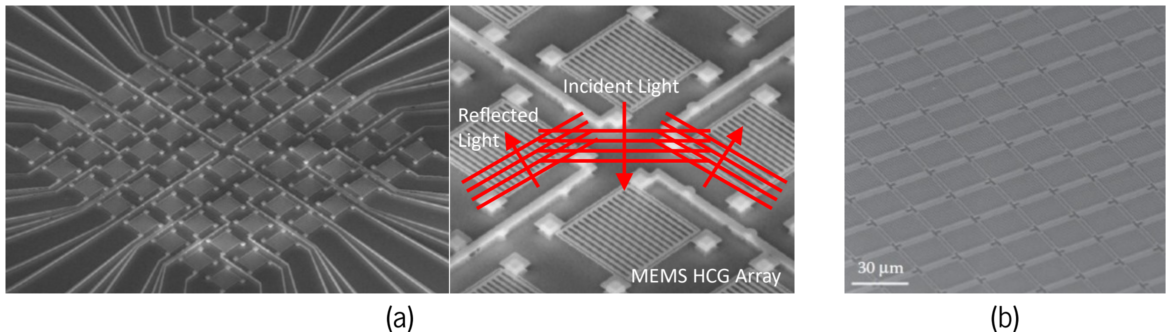

Figure 1-12 – (a) SEM images of the 8 × 8 MEMS OPA HCG array [75]. (b) SEM images of the 32 x 32 MEMS 2D OPA [76].

This optical MEMS reported a ±1.26° beam steering in two dimensions, with a 99.9% reflectivity at a wavelength of 1550 nm. Furthermore, Figure 1-12.b demonstrates other MEMS 2D OPA that comprises a 32 × 32 array of HCG elements [76]. This device reported a measured maximum beam steering angle of ±2.0° and a natural frequency of 0.46 MHz.

However, these are still very experimental techniques for LiDAR applications, either because of low angular resolution, less than perfect optical quality, due to beam deformation, limited angular amplitude and slow operation. OPAs for LiDAR applications are currently being developed [77], but there is no estimate for market availability, price or technical characteristics.

A recent extension of the combination of MEMS and DOEs has appeared in the domain of LiDAR, where preliminary signs of progress have been taken to leverage this approach for broadening the scanning FoV with a low-cost and small-volume solution. Within this sub-section, distinct approaches, wherein MEMS technology intersects with diffractive elements, are detailed.

1.4.1 Multibeam steering based on MEMS and DOE technology for LiDAR

The integration of MEMS scanners with Diffractive Optical Elements represents a significant advancement in the development of compact LiDAR systems. These MEMS-based LiDAR systems are increasingly recognized as a cost-effective and compact solution for commercial applications, particularly in autonomous vehicles [78]. Miniaturized LiDAR systems, essential for such applications, often require large mirror surfaces to achieve extended laser measurement ranges [5]. Different methodologies have

been explored to provide a broad field of view and high angular resolution. The combination of a MEMS scanner with a DOE has proven to be an innovative solution, as a large FoV can be obtained by diffracting the incident beam into a regular spot pattern, such as arrays or matrices of spots, or scan lines [14], [15], [16].

Several solutions for 3D LiDAR have been presented in recent years. One such method involves a 1D MEMS mirror combined with a diffuse laser beam produced by a diffuse lens to facilitate scanning in both vertical and horizontal directions [79]. However, in this topology, the maximum detection distance is short due to the laser power distribution in a line, resulting in a low optical power density. Another architecture uses an array of laser sources to create the vertical scanning lines, which are then redirected onto the MEMS mirror surface via a lens [80], [81], as illustrated in Figure 1-13. This design allows for the effective combination of low laser power, though it necessitates precise alignment and assembly.

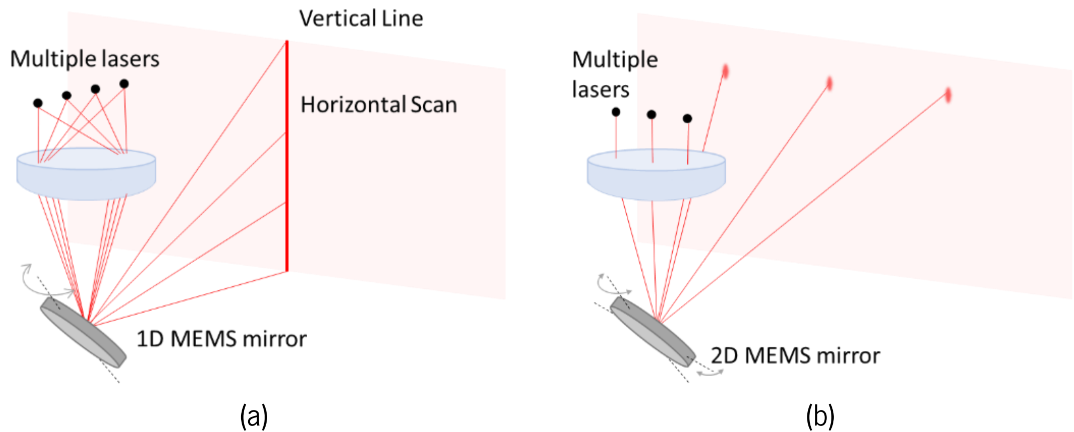

Figure 1-13 – Multi-spot LiDAR architectures presented in the literature, with 1D MEMS mirror [80] and 2D MEMS mirror [81] and multiple laser sources.

In [82], a different all-MEMS architecture has been presented where a 2-dimensional MEMS mirror and diffractive optical element, which is achieved by a DMD as a programmable blazed grating, to scan 5 points over a 48° FOV with a sampling rate of 3.4 kHz. The unexplored transition between the on- and off- states of the DMD is probed by the illumination of a nanosecond short-pulsed laser. With the short pulse illumination, the DMD is used as a highly-efficient programmable blazed grating. In [83], further advancements explore architectures incorporating multiple laser sources to enhance the angular resolution of LiDAR projections, as depicted in Figure 1-14.

An alternative approach involves MEMS scanners paired with beam-splitting DOEs, offering a wide FoV without the need for multiple laser sources. In this setup, the DOE diffracts the incident beam into a spot pattern, which is then scanned across a wide FoV by the MEMS scanner. One example is a 2D MEMS scanner combined with a DOE, yielding both a wide FoV and high resolution. This system is based on the

creation of a 2D spot pattern with a DOE, which is then scanned by a 2D MEMS scanner. The combination of MEMS scanning mirrors and DOE provides a compact, low-cost, and high-performance LiDAR solution.

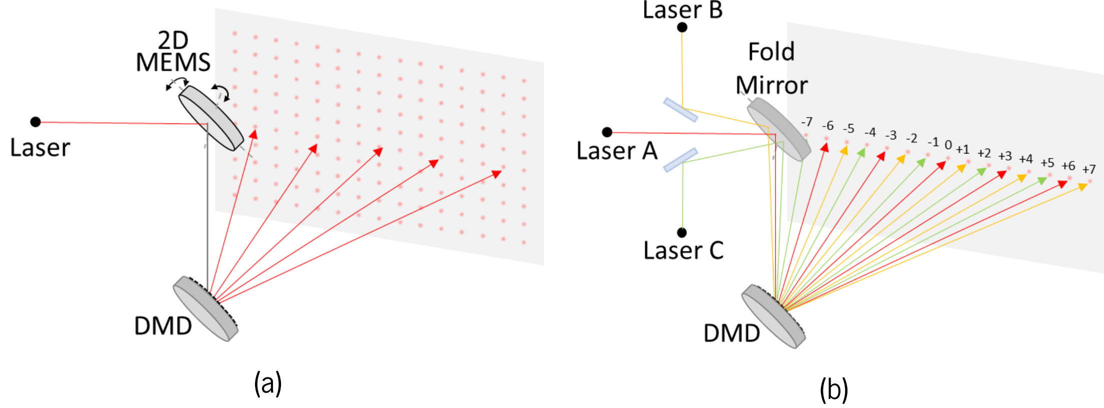

Figure 1-14 – All-MEMS multibeam LiDAR steering system from (a) [82] and (b) [83].

While this combination offers a promising avenue for achieving wide FoV and high resolution in LiDAR systems, these architectures typically rely on multiple components, such as single or multiple laser sources, MEMS scanners, and diffractive elements (lenses, transmissive gratings, DMDs), which imply a fine alignment and complex packaging between them. However, integrating diffractive structures directly onto MEMS scanner mirrors could herald a new compact, cost-effective, and high-performance LiDAR systems, reliant only on a single laser source and an integrated MEMS-DOE device.

1.4.2 Integration of DOEs in different optical elements

Diffractive Optical Elements have been integrated into various other elements, such as refractive lenses, lasers, optical fibres, cameras, gratings on curved surfaces, and MEMS, which has led its importance to a wide range of applications and functionalities. These integrations have enabled advancements in various fields, including imaging, communication, display technology, security, and more.

DOEs have been integrated with refractive lenses to create novel optical devices. For instance, the fabrication of antireflection structures on the surface of optical lenses using a liquid transfer imprint technique has been demonstrated, suitable for high-performance applications on curved surfaces like convex lenses [84]. Moreover, multibeam multi-wavelength semiconductor lasers have been designed, where DOE microlenses have been combined with lasers and optical filters, which can be integrated with various active or passive optical components for applications such as interferometry and demultiplexing [85]. Additionally, the integration of diffractive metalenses in designing different types of optical systems, including digital cameras, has been explored, leading to broad applications in microfluidic devices, virtual reality devices, telescopes, and eyeglasses [86]. The simplicity of the design and fabrication process of

ultrathin metasurfaces makes them good candidates for building flat optical elements that can be easily integrated into CMOS electronics and MEMS devices [87].

1.4.3 Grating-based optical element merged with MEMS

The integration of diffractive structures on the plate of a scanner mirror has been a topic of research for more than 20 years. In literature, these diffractive scanning systems are often used in micro spectrometers [88], [89], [90], [91], [92], as they allow for the detection of a spectrum with a single detector rather than requiring expensive diode arrays. These systems are also referred to as scanning grating mirrors (SGM) in the literature. MEMS SGMs split the incident beam into different spectral wavelengths and scan them sequentially.

In [88], an electromagnetic scanning mirror integrated with blazed grating and angle sensor for a near-infrared micro spectrometer is presented. Here, the merging of the MEMS mirror and the granting into one device allows the near-infrared micro spectrometer to span a spectral range of 800 nm–1800 nm accurately, with an architecture extremely simple and only one single Indium Gallium Arsenide (InGaAs) photodetector is achieved, instead of a detector array. As depicted in the cross-section of the device in Figure 1-15, the blazed grating is patterned directly into the silicon substrate and coated with a reflective aluminium layer, which was micromachined prior to the bulk micromachining MEMS structure process, without any constraint, as presented in [88].

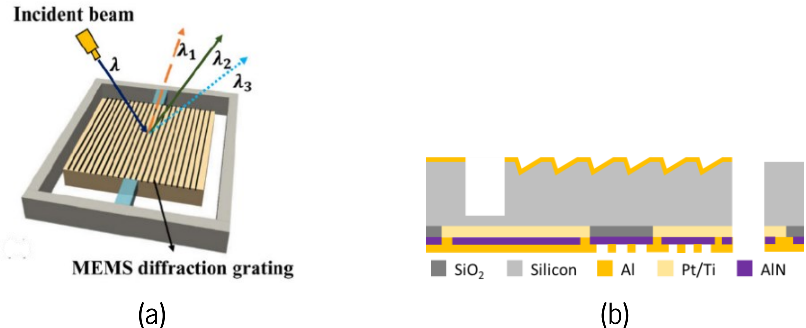

Figure 1-15 – Schematic of the electromagnetic 1-DOF MEMS scanning mirror with the blazed grating from [66].

Besides the spectrometer's application, some devices with grating merged into MEMS structures have been presented for beam steering applications. One example is a MEMS-based in-plane rotation vibratory diffraction grating scanner [93], Figure 1-16. The diffraction grating scanner was first implemented at the microscale, combining continuously rotating electrostatic micromotors to rotate the grating, which can be considered the MEMS version of the rotating holographic scanners. Following the same bulk micromachining approach as the previous device, the grating was patterned directly into the silicon substrate before the typical MEMS process.

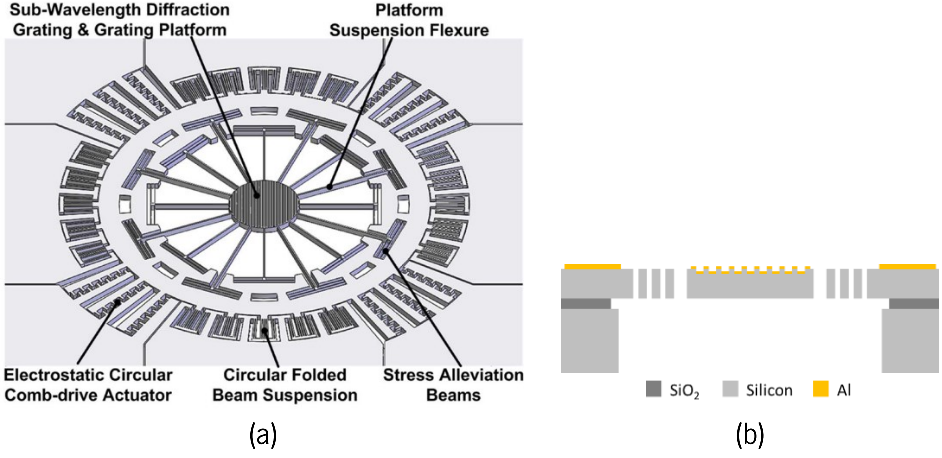

Figure 1-16 – In-plane scanner schematic with grating embedded on the reflective surface for spectrometry application [93].

Recently, a new concept for beam steering using a MEMS grating-based OPA has been proposed in [94] that uses the lateral displacement of a diffraction grating to produce a phase-shift proportional to the lateral displacement on the incident waves (Figure 1-17). The OPA has 160 × 160 independent phase shifters across an aperture of 3.1 mm × 3.2 mm. It has a measured beam divergence of 0.042° × 0.031°, a field of view of 6.6° × 4.4°, and a response time of 5.7 µs. This approach offers a new degree of freedom for beam steering, enabling the development of compact and efficient optical systems with high-speed and high-resolution capabilities. This device is based on a complex surface micromachining process, where the patterning of the grating was performed in the last few process steps, as shown in Figure 1-17.

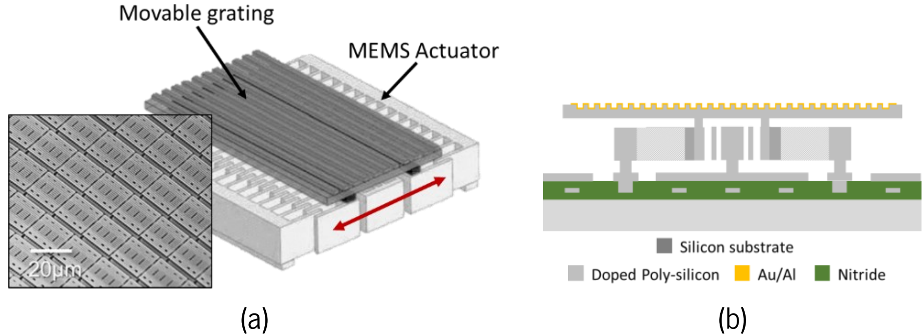

Figure 1-17 – MEMS grating-based OPA based on surface micromachining, from [94].

1.5 Motivation

As detailed in the previous sections, LiDAR systems can simultaneously measure the distance and intensity of every point in the scene. This application requires a device that deflects the beam into multiple positions to cover a specified FoV. State-of-the-art LiDAR systems use bulky mechanical systems, are hard to integrate into a vehicle and are susceptible to the vehicle's external forces. MEMS devices, in general,

have had a massive impact on the automotive industry, mainly due to their size, cost reduction, and manufacturing process.

Typical MEMS scanning systems are composed of a smooth and flat reflective surface attached to a set of MEMS actuators, capable of positioning it to the desired angle, limited by the actuator's maximum angle amplitude and speed. However, there are other approaches of scanning systems that take advantage of diffraction modulators.

In the past years, several architectures using reflection and diffractive optical elements, have been presented for Light Detection and Ranging applications. This combination as a way of achieving or increasing the scanning field of view with a more mechanically relaxed MEMS actuator presents several advantages.

The proposed research aimed to develop an optical MEMS device to split and steer a laser beam, a device where the capabilities of a typical MEMS mirror and a diffractive element are merged for LiDAR applications. The DOE will be added during the development process of the mirror itself, making the MEMS mirror and DOE a single component. In this way, this single component diffracts the incident beam into multiple ones instead of one, as can be achieved by the typical MEMS mirror approach, as represented in the schematic of Figure 1-18. This optical combination not only enables a multibeam LiDAR scanning system without the need of multiple laser sources, removing their alignment issues, but also to relax the target FoV and scanning speed and, consequently, increases the mechanical robustness of the MEMS structure.

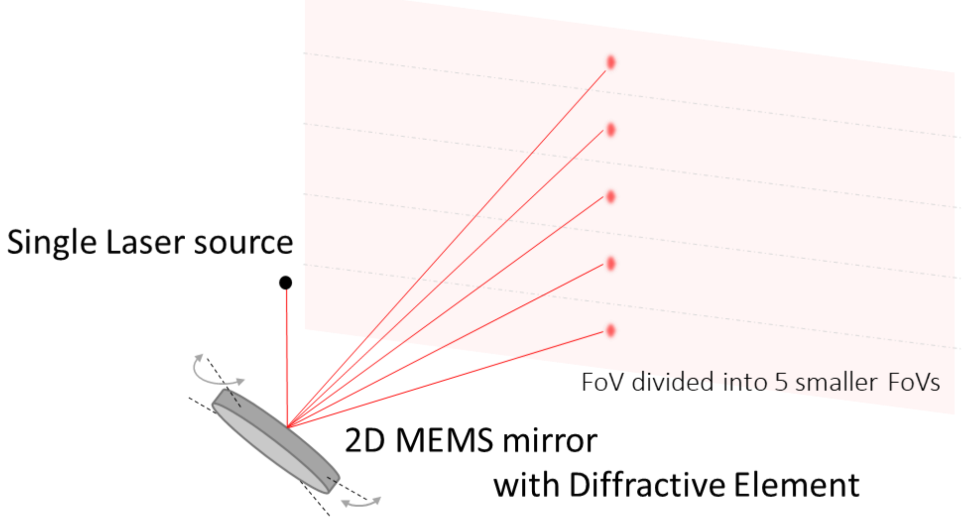

Figure 1-18 – Schematic of the proposed 2D MEMS with a DOE merged LiDAR projection.

The challenges that must be faced to accomplish a Diffractive Optical Element in a MEMS scanner thus become apparent since reaching such a level of scan resolution and uniformity pattern imposes an extensive analysis of both systems. Moreover, a critical analysis of the micromachining technologies is imperative to design a process capable of fabricating the desired device.

1.6 Objectives

The main objective of this research work is to develop a 2D MEMS scanner merged with a Diffractive Optical Element for LiDAR applications. The goal is to create a device capable of diffracting and redirecting a NIR (Near-infrared) beam into five beam spots within an established Field of View, Figure 1-19.

Mainly, this doctoral project was developed at International Iberian Nanotechnology Laboratory (INL), which has all the tools: software (MEMS design, model, and FEM) and systems (micromachining and characterization) needed to carry out this work. Given the study mentioned above, the MEMS scanner will be based on asymmetric electrostatic actuation, has it is possible to design a compact and low-power structure for higher natural frequencies, and is the most compatible actuator with INL micromachining technology.

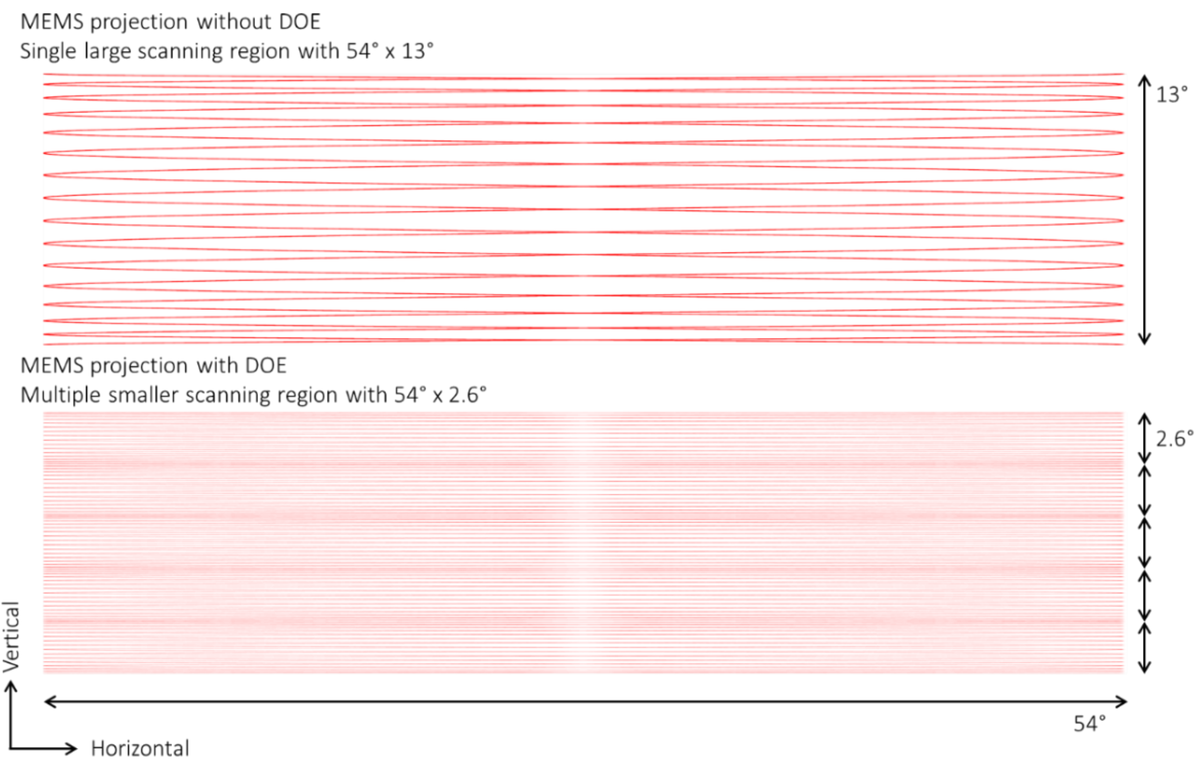

Figure 1-19 – MEMS scanner merged with a DOE (grating) schematic.

To achieve the envisioned microsystem, the following research milestones were defined:

- Analytical study of the mechanical aspects of the 2D MEMS mirror and the optical features of the DOEs.
- Structural and optical simulation of the MOEMS device. Implementation of finite-element method analysis (FEM) to study and validate the analytical models, the structural and modal performance of the MEMS actuator.
- Design and fabrication of the devices, considering the previous results. Novel micromachining techniques, such as direct-write laser (DWL) grayscale lithography and nanoimprint lithography (NIL), were analysed and used for the fabrication of the devices.
- Testing and characterization of the fabricated MOEMS with a DOE.

Table 1-5 presents a summary of the device requirements, taking into consideration the target application. This specification, such as field of view, scan resolution and rate, were defined by the project's industrial partner, namely Bosch, within the developments of the Sensible Car: Automated Driving (POCI-01-0247-FEDER-037902) project, assuming automotive application.

Table 1-5 – MEMS and DOE requirements.

MEMS Mirror Requirements		
	Vertical/Slow Axis	Horizontal/Fast Axis
Field of View	13°	54°
Deflection	± 1.3°	± 13.5°
Frequency	> 87 Hz	10 Hz
Reflective surface area	≈1 mm x 1 mm	
Scan Resolution	0.15°	
Scan Rate	10 Hz	
Diffractive Optical Element Requirements		
Diffraction Pattern	5 spots	
Angular spot separation	2.6° ± 0.15°	
Diffraction Uniformity	30 %	
Reflectivity	> 90%	

Here, the main innovation of the proposed work is the device itself, i.e., the implementation of the DOE on the mirror surface to meet LiDAR specifications. However, to achieve this, several new approaches will be implemented, such as:

- The use of grayscale lithography to create multilevel asymmetric electrodes for MEMS scanner actuation;
- The implementation of NIL to reduce costs and time of the multilevel process for mass production.

1.7 Document organisation

This document is divided into seven main chapters to better understand the proposed research work and activities that were essential during this doctoral thesis. Figure 1-20 describes the overall organization and flow of the present thesis, highlighting the main steps of each chapter, the correspondent milestone and scientific contributions, such as scientific presentations, journal papers and patents.

The introduction is the first one, where the literature review, motivation and context of the work are described. In the second chapter, it is detailed the process and experimental techniques review. Here, the theoretical foundations for the micromachining of the proposed device are presented. In the third section, MEMS mirror, all the theoretical foundations and analytical and FEM simulations of the MEMS scanner are detailed, including the final design of the MEMS structure of this thesis.

In the fourth section, Diffractive Optical Elements, the theoretical studies related to this device are also detailed with the analytical simulations of its performance and the final design. In section five, the micromachining process is detailed. Here, several preliminary studies and tests of the different processes are detailed, as well as the 1D and 2D MEMS scanners with the grating fabrication steps and results. This section is followed by the Experimental Characterization section, where the overall performance of the proposed and fabricated device is tested and characterized. Finally, the conclusions section includes a brief description of the results and main deductions of the presented thesis.

- Contextualization & Literature review
- Motivation
- Thesis goals

Scientific outcome: Patent application WO2023111667A1, "Scanning system for range detection sensor"

- Micromachining techniques: deposition, lithography, etching and cleaning
- INL SOI-based MEMS standard micromachining process
- Asymmetric electrodes fabrication review

- Theoretical bases of an electrostatic-based gimbal 2D MEMS mirror
- Analytical and FEM evaluations
- Designed Layouts

Milestone: Mechanical design of a 2D MEMS mirror, capable to steer within a FoV of 54° per 2.6

- Theoretical foundations of diffractive optical elements
- Analytical evaluations
- Designed Layouts

Milestone: Design of a Damman reflective DOE, to generate fice uniform spots within the AoI range from 3° to 33°.

- Preliminary studies and optimization of the fabrication process
- MEMS mirror merged with DOE fabrication
- Replication of multilevel pattern using NIL

Milestone: Fabrication of a 2D MEMS mirror with a Dammann grating integrated in its reflective surface.

Scientific outcome: I.S. Garcia et al., "Fabrication of a MEMS Micromirror Based on Bulk Silicon Micromachining Combined With Grayscale Lithography", JMEMS, 2020

I.S. Garcia et al., "Nanoimprint lithography for grayscale pattern replication of MEMS mirrors in a 200 mm wafer ", JMP, 2024

- Detail on the different experimental setups used
- Characterization of the MEMS structure and DOE separately
- Multi-beam steering characterization

Scientific outcome: I.S. Garcia et al., tentative tile "All-silicon, Multispot 2D MEMS Mirror for LiDAR Applications", to be published 2024

Figure 1-20 – Thesis structure flow.

2. Process equipment & experimental techniques

Microfabrication, as used in the microelectronics and MEMS field, relies on bulk and surface technologies, i.e., constructing the electronic devices and MEMS components on initially flat wafer substrates [95], [96]. Given the significant investment made by the microelectronics industry in developing wafer-based processes, MEMS designers stand to benefit significantly by exploring these processes or variations thereof. In line with the stated objectives of this thesis, one of the key objectives is the micromachining of MEMS 2D mirror and diffractive optical elements. This chapter describes the micromachining process techniques, from deposition, lithography, etching and cleaning, used for standard procedures in the MEMS process (Figure 2-1).

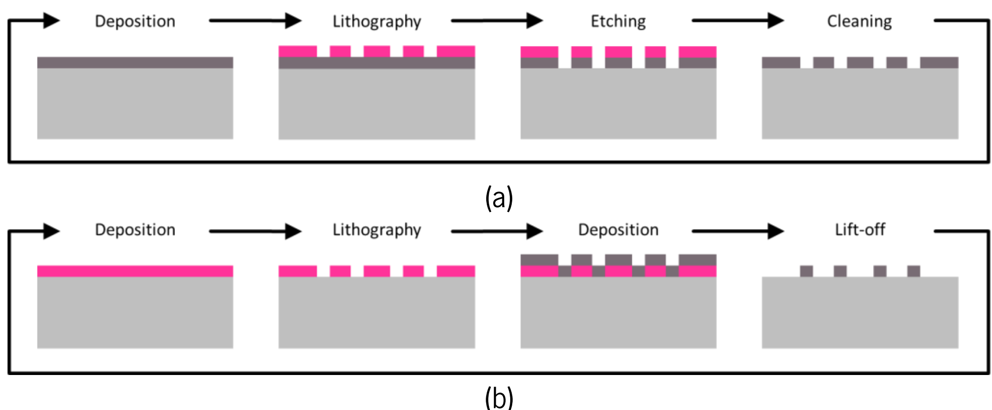

Figure 2-1 – Typical micromachining process sequence, a) deposition – lithography – etching – cleaning, and b) deposition of sacrificial layer – lithography – deposition of target material – lift-off.

2.1 Depositions Techniques

Within the micro and nanofabrication world, deposition plays a crucial role, enabling precise and controlled deposition of thin films onto substrates to create either functional layers, coatings, or sacrificial layers in various microfabrication applications, such as semiconductor devices, MEMS among others, with precise control over thickness, composition, and mechanical, optical, electrical properties. There are different deposition techniques in use in microfabrication, from Physical Vapour Depositions (PVD), Chemical Vapour depositions (CVD), and Atomic Layer deposition (ALD) to electroplating [95].

2.1.1 Physical Vapour Deposition - PVD

Physical vapour deposition techniques, such as sputtering, involve the physical transfer of material from a source (solid or vapour) to the substrate, up to a few micrometres [97], [98]. The sputtering process requires a target material as the source of the film material and typically ionized argon (Ar) as the bombarding agent under vacuum conditions (Figure 2-2.a). To create the bombarding agent, an electric field is applied to the inert gas, creating a plasma discharge. The high-voltage electric field ionizes the argon gas, creating a plasma of positively charged ions that are accelerated towards the target material due to the electric field. When these ions strike the target surface, they transfer momentum and energy to the atoms or molecules of the target material, causing them to be ejected or sputtered from the target surface. The sputtered atoms or molecules travel through the vacuum chamber and deposit onto the substrate, growing a thin film. Here, the film properties, such as thickness and composition, can be controlled by adjusting various parameters during sputtering. These parameters include the sputtering power, working gas pressure, deposition time, and target-substrate distance.

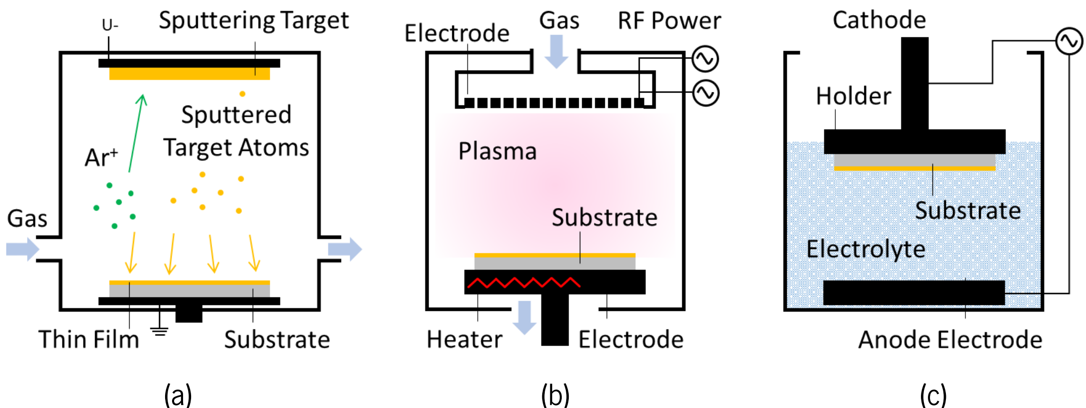

Figure 2-2 – Deposition techniques schematic, (a) PVD, (b) CVD, and (c) electroplating.

Sputtering offers several advantages as a thin-film deposition technique. It allows for high deposition rates, uniform film thickness distribution, and good adhesion between the film and substrate. Sputtered films

also exhibit excellent material purity, making them suitable for applications requiring high-quality films with high purity and good adhesion. This technique is highly versatile and compatible with various materials, including metals, alloys, oxides, nitrides, and semiconductors [98].

Within the cleanroom facilities of the International Nanotechnology Laboratory (INL), a variety of PVD systems are available for the deposition of diverse materials. These systems include:

- The Singulus multi-target sputtering tool (Timaris MTM) is designed for ultra-thin, magnetic, and high-quality film depositions, maintaining ultra-high vacuum conditions [99]. This UHV single wafer cluster tool includes a transport module, a multi-target PVD module with 10 DC/RF cathodes, and a soft etch/oxidation module. It deposits magnetic and non-magnetic layers on wafers up to 200mm diameter using DC/RF Magnetron Sputtering. The Linear Dynamic Deposition (LDD) technology in this tool allows for the creation of wedge films and alloy films with adjustable concentration gradients, enhancing film stack development and device advancement;
- The Kenosistec KS1000 multi-target confocal sputtering [100] tool, a multi-target UHV sputtering system, comprises a deposition chamber with 11 2" diameter magnetrons arranged in a confocal geometry. This arrangement is optimized for the co-deposition of materials on wafers up to 200mm in diameter;
- The Metallization Singulus sputtering tool (Timaris FTM) for Al, TiW(N), and Al_2O_3 is a Four-Target-Module (FTM) designed for high-quality metallic, conductive, and insulating films [99]. This UHV tool includes a transport module, a multi-target PVD module with up to four DC/RF cathodes, and a soft etch/oxidation module. It supports the deposition of various layers on wafers up to 200 mm diameter, ensuring film uniformity. The FTM incorporates LDD technology with up to four sputter targets in one vacuum chamber.

2.1.2 Chemical Vapour Deposition – CVD & PECVD

Chemical vapour deposition (CVD) techniques involve the deposition of thin films (in theory, up to a few micrometres) by chemical reactions between precursor gases and the substrate surface [95], [101]. These reactions result in the formation of solid films with controlled composition and desired properties. CVD techniques, including plasma-enhanced CVD (PECVD) and low-pressure CVD (LPCVD), are widely used for the deposition of a wide range of materials, including silicon dioxide (SiO_2), silicon nitride (Si_3N_4), and amorphous silicon (a-Si), widely employed to create dielectric films, passivation layers, and barrier coatings.

As depicted in Figure 2-2.b, the substrate, typically silicon or glass, is placed inside a sealed chamber and set to a vacuum pressure level to remove residual gases or contaminants. After achieving the desired vacuum level, precursor gases are introduced into the chamber. These precursor gases consist of reactive and non-reactive gases, chosen based on the film material to be deposited. The reactive gases often contain silicon, oxygen, nitrogen, or carbon. Regarding PECVD, in order to create the chemical reactions required, a plasma of the reacting gases is generated. A radio frequency (RF) power source is applied to create plasma within the chamber and to initiate the film deposition. The high-frequency electrical field applied to the precursor gases generates the plasma, causing the molecules to become ionized and dissociated. The energetic ions and radicals from the non-reactive gases in the plasma react with the precursor gases, leading to chemical reactions that result in the formation of the desired film. The film thickness is controlled by adjusting parameters such as gas flow rates, pressure, and deposition time. Monitoring and controlling these parameters are crucial to achieving the desired film properties, such as thickness, composition, and uniformity.

At the INL, a range of CVD-based systems are employed for various material depositions:

- The EasyTube 3000, a FirstNano hot wall quartz tube furnace, is used for graphene deposition [102]. This system, capable of operating under atmospheric or low-pressure/vacuum conditions, features a 3-zone furnace with precise temperature control through a feedback loop. It operates in either Furnace or Cascade modes, which ensures temperature stability (less than 0.2 °C variation) around the set point (up to 1100 °C) for prolonged depositions. The system, controlled by programmable proprietary software, handles substrates up to 10 cm x 15 cm, automating all steps of the CVD process except loading and unloading;
- The SPTS MPX CVD [103] system is dedicated to the deposition of oxides, oxynitrides, and amorphous silicon (a-SiH) using Plasma Enhanced Chemical Vapor Deposition (PECVD). It features a single wafer processing chamber and dual high/low-frequency RF options, employing plasma to accelerate chemical reactions, enabling thin film deposition at temperatures typically below 300°C;
- The MicroSys 400 from Roth & Rau Microsystems, a PECVD system designed for Carbon Nanotube (CNT) and carbon layer deposition, is tailored for nanoscale growth. It supports the growth of carbon nanotubes with varying aspect ratios for applications in field emission sources, biosensors, and microfluidics. This system offers high-performance growth with in-situ catalyst activation and rigorous process control, accommodating flexible temperatures up to 700°C;

- Additionally, INL houses a thin film silicon CVD system, which is hotwire and radio-frequency assisted, for the deposition of doped and intrinsic silicon layers. This system is integral for the development of advanced silicon-based thin films.

2.1.3 Electroplating Deposition

Electroplating is a deposition technique used to create metallic coatings on substrates through an electrochemical process. It involves the use of an electrolytic bath and the application of an electric current to drive the deposition of metal ions from the solution onto a conductive surface, resulting in the formation of a uniform and adherent metal layer up to several micrometres [104], [105].

The electroplating process begins with the preparation of the substrate, which is typically made of a conductive material such as metal or semiconductor. The substrate is thoroughly cleaned and pre-treated to ensure good adhesion and promote uniform deposition. Then, it is immersed in an electrolyte solution containing metal ions of the desired plating material, Figure 2-2.c. The electrolyte solution consists of a specific metal salt dissolved in a suitable solvent and various additives that help control the plating process, such as Ph adjusters. The process starts with the deposition of a seed layer, which is a thin, conductive coating applied to a non-conductive substrate to initiate and facilitate the uniform growth of the electroplated material. To initiate the electroplating, the substrate is connected to the cathode of an electrical circuit, and a metal electrode of the same material is connected to the anode. When an electric current is applied, metal cations from the electrolyte solution are reduced at the cathode (substrate) surface, resulting in the deposition of metal atoms or ions onto the substrate. During the electroplating process, various factors affect the quality and characteristics of the deposited film. These include the current density, seed layer thickness and uniformity, bath composition, temperature, and plating time. Careful control of these parameters is fundamental to achieve the plated metal layer's desired thickness, composition, and uniformity. Electroplating offers several advantages as a deposition technique. It enables the deposition of a wide range of metals and alloys, providing versatility in material selection. The process also allows for precise control over the thickness of the deposited film. Furthermore, electroplating produces highly adherent films with excellent coverage and surface finish. The electrochemical nature of the process ensures good adhesion between the plated layer and the substrate, leading to enhanced mechanical properties and durability of the coating. However, electroplating also has some limitations. It is primarily limited to conductive substrates due to the requirement of an electric current for the deposition process. Complex-shaped substrates may pose challenges in achieving uniform deposition, as uneven current distribution can lead to variations in film thickness. Additionally, the process may involve using

toxic or hazardous chemicals, requiring proper handling and disposal procedures. Furthermore, while several sputtering targets can be installed in the sputtering tool, each bath is specific for a given target metal species.

At the International Nanotechnology Laboratory (INL), the AMMT GmbH system is used for copper (Cu) electroplating [106]. The µGalv process tool, designed for Cu electrodeposition, accommodates wafers up to 200mm. This system features a media flow subsystem that ensures exceptional homogeneity across even large wafers. Additionally, the rotating wafer holders in the system are optimized to provide optimal uniformity in every plating cell design.

2.1.4 Atomic Layer Deposition – ALD

Atomic Layer Deposition (ALD) is a thin-film deposition technique that allows for precise control over film thickness and uniformity at the atomic level (a few tens of nanometers) [107], [108]. This technique is known for its ability to create high-quality thin films with excellent conformality and uniformity, making it particularly suitable for applications where precise control and uniformity are critical.

The ALD process involves sequential and self-limiting surface reactions to deposit thin films layer by layer. It typically begins with the introduction of a reactive precursor gas into a vacuum chamber containing the substrate to be coated. The precursor gas interacts with the substrate surface, forming a monolayer of chemisorbed molecules. After the adsorption step, an inert purge gas is introduced to remove unreacted or excess precursor molecules from the chamber. This ensures that only a single layer of molecules is deposited on the substrate surface. Then, a second precursor gas is introduced, which reacts with the first layer of adsorbed molecules on the substrate. The reaction between the two precursors forms a new layer on top of the initial layer. Again, a purge step follows to remove any remaining precursor gases. The alternating precursor exposure and purging process is repeated until the desired film thickness is achieved. The self-limiting nature of the reactions ensures precise control over film growth, as each deposition cycle adds a uniform layer of material.

ALD offers several advantages. One of its key strengths is the ability to deposit conformal films on complex and high-aspect-ratio structures, such as trenches, pores, or 3D structures. This conformality is achieved because self-limiting reactions can penetrate small gaps and uniformly coat all exposed surfaces. Moreover, it can deposit films of a wide range of materials, including oxides, nitrides, metals, and more, with excellent uniformity and control over film thickness down to the atomic level [108].

However, ALD has some limitations and considerations. The process is typically slower than other deposition techniques due to the sequential nature of deposition cycles. It may require multiple deposition cycles to achieve the desired film thickness, resulting in longer deposition times. Furthermore, it also requires highly volatile and reactive precursor gases, which can be expensive and challenging to handle. The process may also be sensitive to impurities or moisture, requiring careful control of the deposition environment.

At the INL, the Beneq TFS 200 [109] tool is used. This tool is engineered to facilitate the deposition of high-quality coatings on various substrates, including wafers, planar objects, porous bulk materials, and complex 3D objects, particularly those with high aspect ratio (HAR) features. The design of the Beneq TFS 200 is specifically tailored to minimize cross-contamination, a crucial consideration in a multi-user research environment.

2.1.5 Spin coating

The spin-coating deposition technique is a widely used method for applying thin films to substrates. It involves depositing a small puddle of fluid material onto the centre of a substrate and then spinning the substrate at high speed. The centrifugal force generated by the spinning motion causes the fluid to spread outwards and thin into a uniform film. The thickness of the film can be controlled by the viscosity of the solution, the speed of rotation, and the duration of the spin [110], [111].

Spin-coating is particularly advantageous for its simplicity, repeatability, and ability to produce uniform films over a relatively large area. It is a standard technique in the fabrication of microelectronics and for the deposition of materials in photovoltaics, sensor technology, and the creation of various nanostructured materials. The process parameters can be finely tuned to achieve the desired film thickness and uniformity, which is critical for the performance of the final device. The technique is also beneficial for its compatibility with a wide range of materials, including polymers, sol-gels, and small-molecule solutions. This versatility makes it an essential tool in research and development settings where new materials and layer structures are being explored.

At INL, both manual (SCS/EMS) and automatic (Karl Suss Gamma Cluster) spin coating tools are used. The Gamma Cluster’s automated tracks are designed for spin coating and developing processes on wafers up to 200 mm, catering to multi-layer and thick-resist coatings. The setup includes two distinct tracks: one for optical resist and another for electron beam resists.

2.1.6 Summary

The deposition techniques differ in several characteristics. The selection of a deposition technique depends on material requirements, substrate compatibility, film quality, process scalability, and other considerations in microfabrication design and manufacturing. Table 2-1 summarizes each technique's overall characteristics, comparing each other's, where:

- Film quality refers to the deposited films' overall quality, uniformity, and purity;
- Materials means the range of materials that can be deposited using the technique;
- Adhesion refers to the strength and durability of the film-substrate adhesion;
- Deposition Rate is the speed at which the film is deposited onto the substrate;
- Conformality is the ability of the technique to coat complex surface topographies uniformly;
- Temperature refers to the temperature requirements during the deposition process.

It is necessary to highlight that the ratings for each characteristic presented are relative and may vary depending on specific process parameters and equipment. INL cleanroom facility has available the presented deposition techniques, each with a specific set of target materials, namely, PECVD for non-conductive materials, such as silicon dioxide, silicon nitride, and amorphous silicon; sputtering for metals and alloys, such as gold, nickel, aluminium (AlSiCu), Tungsten, among others; electroplating, copper; ALD, alumina (Al_2O_3).

Table 2-1 – Summary of the different deposition techniques and respective characteristics.

Technique	Film Quality	Materials	Adhesion	Deposition Rate	Conformality	Temperature
CVD	High	Wide range	Good	Moderate	Moderate	High
PECVD	High	Wide range	Good	Moderate	High	Low
PVD	High	Metals, alloys	Good	High	Moderate	Moderate
Sputtering	High	Wide range	Good	High	High	Low
Electroplating	Moderate	Metals, alloys	Excellent	High	Low	Low
ALD	High	Wide range	Excellent	Low	High	Low

2.2 Lithography Techniques

Besides deposition, lithography techniques play a pivotal role in microfabrication, enabling the precise patterning and production of intricate structures at the microscopic scale. In microfabrication, lithography serves as the fundamental process for transferring patterns onto substrates, such as silicon wafers, using

light or radiation. Lithography is the means by which a given design is patterned using light in a photosensitive resin called optical resist. By employing the principles of optics and photochemistry, lithography techniques offer control over the creation of nano-sized features, allowing the fabrication of advanced electronic devices, integrated circuits, microelectromechanical systems (MEMS), and various other microscale structures. Over the years, lithography has undergone significant advancements, enabling higher resolution, increased throughput, and improved manufacturing capabilities, thereby revolutionizing the fields of electronics, photonics, biotechnology, and nanotechnology. The lithography process requires a series of steps, starting with the preparation of the desired substrate to be patterned, followed by the precise application of a photosensitive material coating. Then, the substrate undergoes pattern exposure, followed by a subsequent development stage. These critical steps collectively enable the formation of highly defined patterns and structures.

Substrate preparation

The preparation of the wafer is a critical step prior to the patterning process to increase its success. The cleaning from chemical impurities and particles, the heating for the desorption of water, and treatment with an adhesion promoter are all part of the substrate's preparation for the resist coating. SiO_2, in the form of quartz, glass or silicon with (native) oxide, as well as most base metals, form polar OH bonds on their surface after sufficiently long exposure to atmospheric humidity, becoming hydrophilic and therefore exhibiting a poor affinity for the non-polar or low polar resin molecules of the photoresist. To make such a substrate surface hydrophobic (water-repellent and thus photoresist-attractive), non-polar molecules of adhesion promoters, such as HMDS (Hexamethyldisilazane) primer, can be chemically bound on it. HMDS is an adhesion promoter commonly used on semiconductor surfaces. Its simplified reaction mechanism bonds on oxygen-free surfaces with its Si atom to the O atoms of oxidized substrate surfaces, releasing ammonia. The non-polar methyl groups directed away from the substrate form a hydrophobic surface with correspondingly good resist wetting and adhesion. This process requires an oven chamber system that can vapour prime the wafer with HMDS, dehydrating the surface to make it hydrophobic to improve photoresist adhesion.

Resist spin-coating and adhesion

In the spin-coating technique, a few millimetres of resist are typically dispensed on the substrate, typically brought to a rotational speed of several hundred rotations per minute. Due to the centrifugal force, the dispensed resist spreads into a uniform resist film with the desired thickness defined by the rotation speed and resist viscosity; excess resist is spun off the edge of the substrate. This process typically takes

only 10-20 seconds and permits the short cycle times of less than one minute required for industrial production, including dispensing and wafer handling. The resist films attained by spin-coating are very smooth, can be adjusted in their thickness very accurately and reproducibly, and show excellent thickness homogeneity, at least for circular substrates as wafers). These can be negative or positive photoresists, where positive photoresist becomes soluble when exposed to light, allowing for the selective removal of exposed regions, whereas negative photoresist becomes insoluble upon exposure, enabling the retention of exposed patterns during the development process.

Exposure

The exposure process is a fundamental stage within the lithography technique, serving as a critical step in microfabrication. It involves the precise projection of light or radiation onto a photosensitive material-coated substrate, forming intricate patterns and structures. The exposure process uses masks or reticles containing the desired pattern to be transferred onto the substrate surface.

These masks act as a pattern, selectively allowing or blocking the passage of light or radiation. When exposed to the light source, the photosensitive material undergoes a chemical or physical transformation, enabling the formation of distinct regions of exposed and unexposed material. Factors such as the wavelength of light, exposure dose, and the characteristics of the photosensitive material all contribute to the success of this process. Furthermore, different exposure techniques, such as mask-aligner, direct-write-laser, and electron beam lithography, offer versatile options for different layout feature sizes and throughput. In this section, these techniques will be detailed, summarizing the advantages and disadvantages of each.

Development

After the exposure of the photosensitive material, the substrate undergoes a meticulous development process using an aqueous solution. This solution acts as a selective solvent, dissolving the unexposed regions of the photosensitive material while leaving behind the exposed areas intact (in the case of a positive resist). The lithography defined pattern is, therefore, transferred to the resin on the wafer. The selection of the appropriate development solution and parameters, such as temperature and development time, is critical to achieving high-resolution patterns and ensuring the desired level of precision in microfabrication. Precise aqueous solution compositions and development times for a given resist thickness must be calibrated to avoid under and overdevelopment.

2.2.1 Photolithography – Mask Aligner System

One of the most common exposure techniques is photolithography, also known as mask aligner system (MA). In this technique, a photomask, or hard mask, previously micromachined, is required. This mask usually consists of a glass or quartz plate as the substrate on which a thin lithographically patterned chromium layer works as the non-transparent pattern. In order to expose the chromium pattern to the desired substrate, parallel light passes through the transparent areas of a photo mask onto the resist film. The dimensions of the structures on the photo mask correspond to 1:1 the dimensions of the exposed areas of the resist film.

Here, the photo mask and the surface of the resist film can be in direct contact to optimize the attained resolution, whereas, for example, textured substrates may require a gap between the mask and the resist film. At INL's cleanroom facilities, two mask aligner systems from Suss Microtec are available: the MA6BA6, designed for 6-inch exposure areas, and the MA/BA8, suitable for 8-inch exposure areas [112]. Both tools are equipped to perform front-side (FS) to FS alignment, as well as FS to back-side (BS) alignment, utilizing distinct alignment systems for each process. The standard process flow of lithography in the MA system is presented in Figure 2-3.

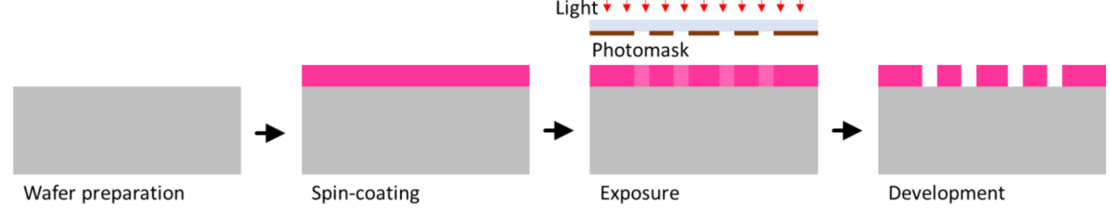

Figure 2-3 – Photolithography process flow.

2.2.2 Direct-Write-laser Lithography

Direct-Write-laser (DWL) lithography is a high-precision technique employed in micromachining that entails the creation of a pattern on the photoresist, which subsequently functions as a sacrificial layer during the etching or deposition processes of surface and bulk micromachining. Unlike traditional photolithography methods that rely on masks and indirect exposure, direct-write lithography employs a focused light source to directly write patterns onto a substrate, enabling intricate designs at the microscale level [113].

In this technique, precise control of the laser head and alignment allows the production of, in theory, down to half of the laser wavelength ($\lambda/2$) resolution lithography. Moreover, the substrate stage is controlled by an interferometer and moves continuously in the y-direction while the laser beam is scanning in the x-direction by fast acoustic-optical deflection. At INL facilities, the Heidelberg DWL 2000 system

[114] is available, which is a high-resolution, laser-based maskless optical lithography system. It has the capability of exposing at two different wavelengths: 405 nm, with digital design information on a 25 nm writeable address grid. It writes directly on photoresist-coated quartz or soda lime mask blanks as well as on wafers as large as 200 mm. The maximum speed is 105 mm^2 per minute, with a 700 nm minimum structure size.

DWL lithography offers several key benefits, such as high precision, relatively rapid prototyping, material flexibility and customization. Moreover, the ability to perform automatic dose modulation during exposure enables grayscale lithography, enabling new applications in optical devices. However, direct-write lithography also comes with challenges. The process can be relatively slow compared to other lithographic methods, and achieving high throughput for large-scale production can be a hurdle. Additionally, ensuring precise control over the energy source and maintaining stable operation is essential for achieving consistent results.

The standard process flow of lithography in the DWL system is presented in Figure 2-4.

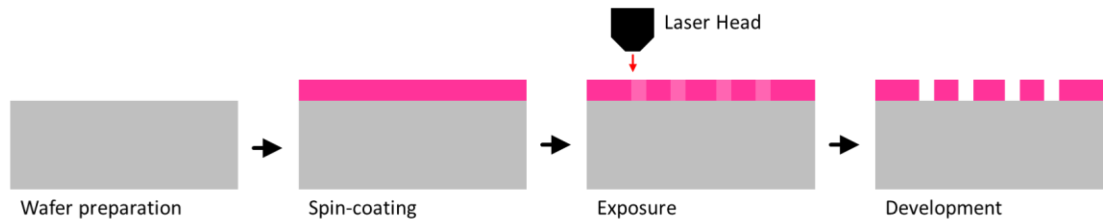

Figure 2-4 – DWL lithography process flow.

Grayscale Lithography (GS)

Grayscale lithography permits the microfabrication of masks with varying levels of photoresist thickness. This technique harnesses the power of focused laser beams to create intricate 2.5-dimensional structures [115], [116]. By incorporating varying levels of exposure across a substrate, grayscale direct-write lithography enables the fabrication of structures with smooth gradients, height variations, and fine details.

In GS lithography, the photoresist layer is exposed with a lateral exposure dose variation using an intensity-controlled laser beam. The local development rate of the exposed photoresist changes according to the exposure dose, as depicted in Figure 2-5, and the desired resist topography is generated during the development process, resulting in a multilevel mask with different thickness levels on the photoresist. This advanced lithographic technique is frequently used to pattern micro-lenses, diffractive optical elements, and computer-generated holograms. However, it is also capable of generating discrete photoresist levels. While grayscale direct-write lithography presents exciting opportunities, it also presents challenges. Accurately controlling exposure levels and material responses requires careful calibration and

optimization. Furthermore, the technique may involve complex multi-step processes to achieve the desired final structure [117]. In typical mask photolithography, GS exposures are not possible to be produced, given that the concept in this process is that the chromium areas on the hard mask block the exposure light. It is only possible to expose binary masks.

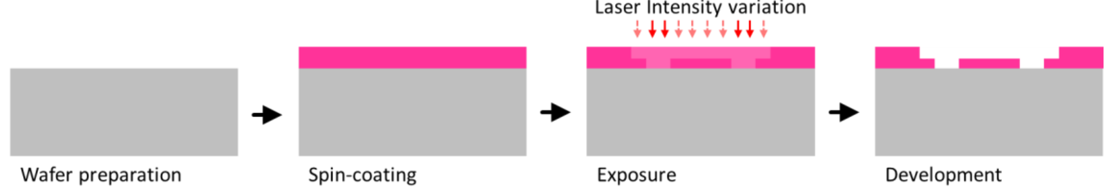

Figure 2-5 – DWL grayscale lithography process flow.

2.2.3 E-beam Lithography

E-beam (electron beam) lithography stands as a keystone in the realm of advanced nanofabrication techniques [118], [119]. Unlike traditional photolithography, which relies on light waves to create patterns, e-beam lithography employs a highly focused electron beam to write patterns directly onto a resist-coated substrate. This electron beam is generated by a precise electron gun, allowing precise control over the beam's position and intensity. The intricate patterns at a nanoscale level are generated by raster scanning the beam across the substrate's surface, as depicted in Figure 2-6. The resist material undergoes chemical or physical changes when exposed to the electron beam, facilitating the transfer of the pattern to the underlying substrate through subsequent development and etching steps. At INL, the Vistec 5200 ES 100 kV e-beam system is available and designed for high-resolution fabrication of patterns directly written on substrates up to 200 mm. This system enables the exposure of structures with minimum dimensions below 10 nm on various substrates, including silicon, glass, and SiO_2.

One of the standout features of e-beam lithography is its exceptional resolution. With electron beams being much smaller than UV light used in standard lithography, this technique can produce features on the order of a few nanometers, surpassing the limits of optical lithography (except EUV). This high-resolution capability allows the creation of nanoscale devices, such as transistor gates, sensors, and photonic components, which exhibit enhanced performance and novel functionalities.

However, despite its many advantages, e-beam lithography has specific challenges. The process can be relatively slow compared to other lithographic methods, which can limit its throughput for large-scale manufacturing. Additionally, the equipment and infrastructure required for e-beam lithography can be complex and expensive, making it more accessible to research environments and specialized fabrication facilities.

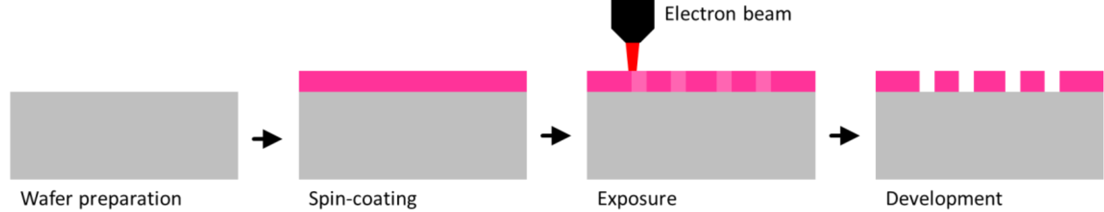

Figure 2-6 – E-beam lithography process flow.

2.2.4 Nano-imprint Lithography (NIL)

Nano-imprint lithography (NIL) has emerged as a powerful and versatile nanofabrication technique, offering the potential to create intricate patterns and structures at the nanoscale with high precision and efficiency [120], [121]. Inspired by the concept of a stamp, nano-imprint lithography employs a mould to transfer patterns onto a substrate through a combination of mechanical deformation and selective material deposition. The process typically involves several key steps, such as stamp/master fabrication, imprint process, curing and solidification, and de-moulding, as depicted in Figure 2-7. Initially, a master mould, with the desired pattern in relief, is created using conventional lithography techniques or more advanced methods, such as electron beam lithography, as previously detailed. Then, during the imprint process, the master is brought into contact with a thin layer of a resist material coated onto a substrate. By applying pressure and heat, the resist material is deformed, conforming to the shape of the master. After the imprint, the resist is cured or solidified through UV exposure or thermal treatment. This step stabilizes the pattern and enhances its durability. The master is separated from the resist-coated substrate, leaving behind the imprinted pattern on the substrate's surface. In some cases, an additional etching step may be employed to transfer the pattern from the resist to the underlying substrate material, resulting in a permanent nanoscale structure.

Nano-imprint lithography offers several advantages, from high resolution, throughput, and scalability (NIL can be relatively fast, especially for large-area patterning, which makes it suitable for both research and industrial-scale production) to its versatility since NIL can be applied to a variety of materials, including polymers, metals, semiconductors, and even biological materials. Moreover, nano-imprint lithography can offer cost savings compared to other nanofabrication methods due to its simplified process flow and potentially reduced infrastructure requirements. While nano-imprint lithography boasts numerous benefits, it also faces particular challenges and considerations. Template fabrication demands high precision and careful design to achieve the desired pattern fidelity. The imprinting process can also be sensitive to factors such as uniform pressure application and temperature control.

At INL, the Obducat Eitre8 is used for nano-imprint techniques. This system provides a semi-automated and cost-effective lithography solution, enabling the replication of patterns in the micro- and nanometer range for processing 200 mm wafers.

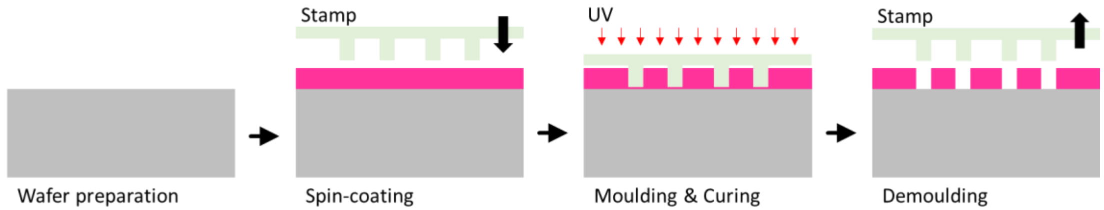

Figure 2-7 – Nano-imprint lithography process flow.

2.2.5 Summary

The lithography techniques differ between each other's in several characteristics. The selection of a technique depends on factors such as resolution, complexity, costs, processing time, throughput, mask requirements, and material compatibility, which are critical considerations in microfabrication design and manufacturing. Table 2-2 summarizes each method's overall characteristics, comparing each other's, where:

- Resolution refers to the ability to create fine features and achieve high resolution;
- Cost concerns the cost of equipment, materials, and process complexity varies among lithography techniques;
- Throughput is the throughput or the speed at which patterns can be produced;
- Mask Requirements refer to particular needs of some lithography techniques, such as photolithography and proximity lithography, which require the use of masks or templates to transfer the desired pattern. This adds an additional step and costs to the process.

It is necessary to highlight that the ratings for each characteristic presented are relative and may vary depending on specific process parameters and equipment.

Table 2-2 – Summary of the different lithography techniques and respective characteristics.

Technique	Resolution	Pattern Flexibility	Costs	Time	Complexity	Throughput	Mask Requirements
Photolithography	High	High	Moderate	Moderate	Moderate	High	Yes
Direct-Write Lithography	Variable	High	Moderate	Low	High	Low	No
Nano-imprint Lithography	High	High	Low	Low	Moderate	High	Yes
Electron Beam Lithography (EBL)	Ultra-high	High	High	Moderate	High	Low	No

2.3 Etching Techniques

Etching serves as the sculptor's tool, shaping patterns and structures with precision. By selectively removing material from a substrate, etching plays a pivotal role in creating complex nanostructures and can be broadly categorized into two main types: dry etching and wet etching [95], [96], [122]. Before starting the etching process, the surface that will be etched needs to be readied. This involves covering it with a protective layer, usually made of photoresist or a similar material that can withstand the etching chemicals in the plasma. To ensure precise etching, a mask or protective layer is typically applied to the substrate, guiding the etching process and confining it to specific regions.

2.3.1 Wet-etching

Wet etching involves immersing a substrate in a liquid chemical solution to dissolve and remove material. The process is guided by the choice of etchant and the design of a protective mask to ensure selective material removal. Wet etching offers simplicity, low cost, and ease of implementation, particularly for isotropic etching. Several types of wet etching techniques are commonly used:

Anisotropic Wet Etching

Anisotropic wet etching is a specialized chemical etching technique wherein the rate of material removal varies based on the crystallographic orientation of the substrate. This process is particularly prominent in the microfabrication of silicon wafers, where it exploits the differential etch rates of silicon in specific crystallographic directions to create well-defined geometric structures. When the substrate is immersed in a specific etchant solution, the etchant reacts preferentially with certain crystal planes, allowing for the creation of sharp, angular features such as V-grooves, channels, and pyramidal pits. The most used etchant for silicon is potassium hydroxide (KOH), although other solutions like tetramethylammonium hydroxide (TMAH) and ethylenediamine pyrocatechol (EDP) are also employed. Anisotropic wet etching is critical in the fabrication of microelectromechanical systems (MEMS) due to its ability to produce deep structures with precision. However, careful control of parameters such as etchant concentration, temperature, and etching time is required to achieve the desired geometric outcomes. At INL, TMAH and KOH silicon etch tanks from AMMT GmbH are available.

Isotropic Wet Chemical Etching

Isotropic wet etching is a chemical etching process in which material is removed uniformly in all directions. Unlike anisotropic etching, which etches preferentially along specific crystal planes, isotropic

etching results in rounded profiles. When a substrate is immersed in an etchant solution, the chemical reaction occurs at the same rate on all exposed surfaces, leading to a uniform lateral and vertical etch rate. Common etchants used for isotropic etching include hydrofluoric acid (HF) for silicon dioxide and a mixture of nitric acid, hydrofluoric acid, and acetic acid (often referred to as the "HNA" mixture) for silicon. Isotropic wet etching is often employed when the specific orientation of the substrate is not critical or when a rounded profile is desired. However, it is essential to monitor the process closely, as the uniform etching can lead to significant undercuts beneath masking layers, which might be detrimental in specific microfabrication applications. Figure 2-8.a illustrates the use of isotropic wet etching through the openings in a masking layer to pattern a thin film on a substrate.

Figure 2-8 – Isotropic (a) and anisotropic (b) cross-section profile.

Electrochemical etching

Electrochemical etching, often referred to as electro-etching, is a process used to selectively remove material from a metal or metallic alloy surface by employing an electric current [122]. In this technique, the metal workpiece is submerged in an electrolytic solution and acts as the anode, while a cathode, typically made of an inert material, is also immersed in the same solution. When a voltage is applied across the anode and cathode, an electrochemical reaction occurs, leading to the dissolution of the metal at the anode. The material removal rate and the etched surface quality can be controlled by adjusting parameters such as voltage, electrolyte composition, temperature, and etching time. Electrochemical etching offers several advantages over traditional etching methods, including minimized mechanical and thermal stresses, reduced surface roughness, and the capability to transfer complex and well-defined patterns.

2.3.2 Dry Etching

Dry etching, also known as plasma etching, involves the use of ionized gases or plasmas to chemically react with the material on a substrate's surface [95], [96]. The controlled bombardment of ions and reactive species removes material through physical sputtering or chemical reactions. Dry etching techniques are prized for their high selectivity, anisotropy (directional etching), and ability to etch fine features. There are several common types of dry etching techniques:

Reactive Ion Etching (RIE)

Reactive Ion Etching (RIE) harnesses the power of plasma to selectively remove material from a substrate's surface, providing high selectivity, anisotropy, and fine control over etching rates, which makes it an indispensable tool in the creation of cutting-edge semiconductor devices, MEMS, photonic components, and more [123].

The fundamental principle of the RIE technique lies in the controlled chemical reactions between reactive ions and the material to be etched. A low-pressure gas (often a mixture of chemically reactive gases) is introduced into the reaction chamber. The RF electromagnetic field generated by the coil induces ionization of the gas, creating a dense and highly reactive plasma. The energetic ions in the plasma are accelerated towards the substrate's surface due to the applied electric fields. These ions collide with the substrate material, physically sputtering away atoms or molecules. Reactive gas species within the plasma chemically react with the exposed material, forming volatile byproducts that can be removed from the substrate surface. The etching process can be controlled by adjusting parameters such as gas composition, pressure, power, and bias voltage. Anisotropic etching can be achieved by exploiting the directionality of the ion bombardment. Reactive Ion Etching is often chosen for nanofabrication due to its many benefits. These include its ability to anisotropically etch a substrate, with a high level of materials selectivity, good feature resolution, controllable process and effective pattern transfer. However, RIE does come with some challenges, such as the possibility of sidewall damage, issues with the mask's selectivity, and the risk of contamination. To address these issues, it is essential to carefully optimize and monitor the RIE process. At the International Nanotechnology Laboratory (INL), several reactive ion etching systems are used for material etching:

- Fluorine-based Reactive Ion Etch System (SPTS APS): This system is designed for anisotropic etching of silicon oxide, silicon nitride, polysilicon, and other materials using fluorine chemistry. It features a heated metallic process chamber with optimized geometry for improved plasma confinement and reduced chamber deposition;
- Oxide Vapor Etch Release System (SPTS/PRIMAXX uEtch): Comprising an uEtch module within a ventilated cabinet, this system includes an anhydrous hydrogen fluoride gas cabinet and a gas leak detection system for safety;
- XeF2 Isotropic Si Etch System (Xactic X4): This system utilizes XeF2 vapour phase etching, offering high selectivity of silicon over other materials, with etch rates dependent on the exposed silicon area.

Inductively Coupled Plasma Etching

Inductively Coupled Plasma Etching (ICP etching) etching uses ionized gases and electromagnetic fields to selectively remove material from a substrate [124]. Reactive Ion Etching (RIE) and Inductively Coupled Plasma (ICP) Etching are both plasma-based etching techniques used in semiconductor manufacturing, but they differ significantly in their mechanisms and capabilities. RIE generates plasma by applying RF power directly to the gas mixture, which ionizes the gas. This technique, however, offers limited control over ion density and energy, leading to less precise etching profiles. ICP, on the other hand, uses a coil to induce a magnetic field that ionizes the gas, creating a higher plasma density. Additionally, ICP systems often employ a separate RF power source for the wafer bias, allowing for independent control of plasma density and ion energy. This dual control system in ICP results in more anisotropic etching profiles, making it ideal for applications requiring high aspect ratio features and fine patterns. In contrast, RIE is more straightforward and cost-effective, suitable for applications with acceptable moderate etch rates and profiles.

The advantages of ICP etching over other etching techniques are numerous and significant: anisotropy [125], high aspect ratio structures, high selectivity, precision and fine details, and minimal damage. While ICP etching offers exceptional benefits, it also presents challenges. Process optimization, mask design, and precise control of parameters such as gas flow rates and RF power are required to achieve the desired results. Additionally, the equipment required for ICP etching can be complex and specialized, making it more suitable for research and advanced manufacturing facilities.

At INL, chlorine-based reactive ion etch systems are available for metal etching, specifically the SPTS ICP and SPTS C2L ICP systems. The SPTS ICP is primarily dedicated to etching aluminium (Al) but is also capable of etching titanium tungsten (TiW), titanium nitride (TiN), and aluminium oxide (Al_2O_3) layers. This system excels in etching deep sub-micron features with near-vertical sidewalls while maintaining good selectivity over the stopping layers and masks used.

Deep Reactive Ion Etching (DRIE)

Deep Reactive Ion Etching (DRIE), also known as the Bosch process, stands as a remarkable and highly specialized microfabrication technique designed to create deep, high-aspect-ratio features and structures with unprecedented precision and control [126].

In the DRIE process, also known as standard Bosch process, a combination of gases (SF_6, O_2 and C_4F_8) are injected into the DRIE chamber in short alternating etching and deposition cycles. DRIE distinguishes

itself from conventional etching methods by its ability to etch deep, narrow channels and cavities into a substrate, achieving aspect ratios (depth-to-width ratios) that can exceed 20:1 or more. This unique capability is for producing 2.5D structures that push the boundaries of microfabrication [126].

This process typically involves a cyclic sequence of etching and passivation steps, which allows for controlled and anisotropic material removal. Initially, a high-density plasma (containing ions and radicals) is generated by introducing reactive gases, such as SF_6 (sulfur hexafluoride) and O_2 (oxygen), into a vacuum chamber. After a certain etching period, the reactive gases are replaced with a passivation gas, often C_4F_8 (octafluorocyclobutane). This passivation layer forms a protective coating on the sidewalls of the etched features, preventing lateral etching and maintaining vertical profiles. The directionality of the plasma ions towards the substrate erodes preferably the horizontal passivation layer, exposing the silicon floor again to the etching gases, enabling the formation of highly vertical walls.

The etching and passivation steps are cycled to incrementally deepen the etched features. The number of cycles, layouts, features and gas compositions determines the final depth of the structures. While DRIE offers remarkable capabilities, it also presents challenges, like the other etching techniques, including precise process control, uniformity, and etch profile consistency. Additionally, it requires specialized equipment and expertise to achieve optimal results.

At the International Nanotechnology Laboratory (INL), the SPTS Pegasus, a Silicon Deep Reactive Ion Etching system, is available. This system is dedicated explicitly to deep reactive ion etching of silicon, utilizing the Bosch Process.

Ion beam etching

Ion beam etching (IBE), or ion milling, stands at the forefront of advanced nanofabrication techniques, offering a powerful method to shape and modify surfaces on the micro- and nanoscale [127]. By employing a focused beam of ions, ion beam etching enables researchers and engineers to pattern high-aspect-ratio structures and surface modifications with high resolution. At its essence, ion beam etching involves the controlled bombardment of a substrate's surface with energetic ions, which erode or sputter away material through physical and chemical processes. The ions accelerate with high energies, impact the substrate, and dislodge atoms from the surface, leading to material removal. The precision and selectivity of ion beam etching are determined by several factors, including the ion species, energy, angle of incidence, and process conditions. Key features and applications of ion beam etching include precision and control, anisotropic etching (depending on the ion incidence angle), selective etching (by choosing specific ion species and process conditions), surface modification (it can induce controlled

surface modifications, such as roughening, smoothing, or introducing new chemical functionalities). Ion beam etching can be achieved using different ion sources, such as reactive ion sources (reactive gas ionization) or inert ion sources (inert gas ionization). The ions can be directed to the substrate using electrostatic or magnetic fields, enabling precise control over ion trajectories.

At INL, the Nordiko 7500, a Broad Beam Ion Milling system with SIMS (Secondary Ion Mass Spectrometry) endpoint detection [128], is available. This system is built around a new 50 cm plasma source and features a high-reliability rotary substrate table. The ion source in this system is the largest among the series of RF (Radio Frequency) excited ion beam generators offered by the manufacturer. Interfaced to an industry-standard SEMI MESC-compliant wafer handling platform, the system is configured for processing various wafer sizes up to 200 mm diameter.

2.3.3 Summary

While wet etching offers simplicity, it may lack the precise control and anisotropy achievable with dry etching. Moreover, it can be limited by the availability of suitable etchants and the risk of contamination. The etching techniques differ in several characteristics. Table 2-3 summarizes the overall characteristics of each method, where:

- Process Type indicates whether the etching is performed using wet chemical solutions or dry plasma/ion beams;
- Selectivity refers to the ability to preferentially etch one material over another;
- Anisotropy is the degree of directional etching leading to well-defined vertical sidewalls;
- Resolution refers to the smallest feature size that can be achieved;
- Material Compatibility is the range of materials that can be etched using the technique;
- The process complexity level is involved with the implementation of the etching process.

Table 2-3 – Summary of the different etching techniques and respective characteristics.

Etch Technique	Process Type	Selectivity	Anisotropy	Resolution	Material Compatibility	Process Complexity
Wet Isotropic Etching	Wet Chemical	Low	Low	Moderate	Wide Range	Low
Wet Anisotropic Etching	Wet Chemical	Moderate	High	Moderate	Limited	Low
Electrochemical Etching	Wet Chemical	Variable	Variable	Moderate	Variable	Moderate
RIE	Dry Plasma	High	High	High	Wide Range	Moderate
ICP	Dry Plasma	High	High	High	Wide Range	Moderate
DRIE	Dry Plasma	High	High	High	Wide Range	High
Ion Beam Etching	Dry Ion Beam	High	High	High	Wide Range	Moderate

It is necessary to highlight that the ratings for each characteristic presented are relative and may vary depending on specific process parameters and equipment.

2.4 Cleaning

The role of cleaning processes is removing contaminants, and enhancing the yield of the microfabricated devices is indispensable. These processes are critical in enhancing device performance, ensuring reliability, and enabling the realization of cutting-edge technologies.

Solvent Cleaning

Solvent cleaning involves immersing the substrate in a suitable liquid solvent to dissolve and remove contaminants, oils, greases, and other organic or inorganic substances. Typical solvents include acetone, isopropyl alcohol (IPA), and deionized water. Solvent cleaning is often used as a preliminary step to remove surface debris before more aggressive cleaning methods.

Megasonic and Ultrasonic Cleaning

Megasonic and Ultrasonic cleaning employs high-frequency sound waves (megasonic and ultrasonic waves, respectively) in a liquid medium to create cavitation bubbles that release energy upon collapse. These energy releases help dislodge and remove particles and contaminants from the substrate surface.

Oxygen Plasma Ashing etching

Oxygen plasma ashing involves exposing the substrate to oxygen plasma, which chemically reacts with and removes organic residues and photoresists. This process is crucial for post-etch residue removal, such as passivation layers and photoresist masks, and is commonly used in microfabrication.

Piranha Cleaning

Piranha cleaning is a potent mixture of concentrated sulfuric acid and hydrogen peroxide. It removes organic materials, resists, residues and other contaminants. Piranha cleaning is particularly effective for cleaning glass and silicon surfaces.

Hot Acids/Base Cleaning

Immersing substrates in heated acidic or basic solutions, such as hydrochloric acid (HCl) or potassium hydroxide (KOH), can effectively remove residues, oxides, and other surface contaminants.

RCA Cleaning

RCA cleaning involves a sequence of chemical cleaning steps using deionized water, hydrogen peroxide, and ammonium hydroxide mixtures. It is commonly used to clean silicon wafers before further processing.

EKC Cleaning

Electronic Grade Kleaner (EKC) solutions are formulated chemicals designed to remove thin films, residues, and particles from semiconductor surfaces. They offer high selectivity and are widely used in semiconductor manufacturing.

Hydrogen Peroxide/Ozone Cleaning

A combination of hydrogen peroxide and ozone exposure can effectively remove organic and inorganic contaminants from substrate surfaces.

Supercritical CO_2 Cleaning

This technique can effectively remove organic and particulate contaminants from substrates without leaving residue by utilizing supercritical carbon dioxide in a solvent-like state.

Each cleaning process serves a unique purpose and addresses specific challenges in micromachining:

- Contamination Removal: Micromachining involves numerous fabrication steps, often leaving behind residues and contaminants that can degrade device performance. Cleaning processes ensure these unwanted substances are eradicated, safeguarding the integrity of the final product;
- Surface Preparation: Clean surfaces are crucial for proper adhesion and deposition of materials in subsequent fabrication steps. Properly cleaned surfaces enhance bonding, reduce defects, and contribute to uniform layer growth;
- Residue Elimination: Etching processes, such as plasma and wet etching, leave behind residues that can affect subsequent processes or alter device characteristics. Effective cleaning ensures these residues are eliminated, preventing undesirable effects.

It is necessary to highlight that the ratings for each characteristic presented are relative and may vary depending on specific process parameters and equipment. Table 2-4 summarizes the overall characteristics of each method.

Table 2-4 – Micromachining cleaning techniques summary.

Cleaning Technique	Process Type	Contaminant Removal	Selectivity	Surface Preparation	Effectiveness	Complexity
Solvent Cleaning	Wet	Moderate	Low	Good	Moderate	Low
Megasonic Cleaning	Wet	Good	Low	Good	Moderate	Low
Ultrasonic Cleaning	Wet	Good	Low	Good	Moderate	Low
Oxygen Plasma Ashing	Dry Plasma	Good	Moderate	Excellent	High	Moderate
Piranha Cleaning	Wet	Excellent	Moderate	Good	High	Moderate
Hot Acids/Base Cleaning	Wet	Good	Low	Good	Moderate	Moderate
RCA Cleaning	Wet	Good	Low	Good	Moderate	Moderate
EKC Cleaning	Wet/Dry	Excellent	High	Excellent	High	Moderate
Hydrogen Peroxide/Ozone	Wet/Dry	Good	High	Good	Moderate	Low
Supercritical CO_2 Cleaning	Wet/Dry	Good	High	Good	Moderate	Moderate

2.5 MEMS standard micromachining process

The micromachining process available in INL is an in-house process, which means it is not a commercial process. So, it is possible to make some variations in the method typically used within its limits. However, an SOI-based MEMS standard process, already implemented and tested, has been used to fabricate several MEMS devices, such as accelerometers and magnetometers, among others. This section details this standard process.

2.5.1 Silicon-on-Insulator (SOI) wafer

SOI wafers are most common in the fabrication of microelectromechanical systems. They are also used to fabricate complementary metal–oxide–semiconductor (CMOS) integrated circuits with particular applications. In the CMOS technology, these wafers provide a manufacturing solution which helps reduce power and heat while increasing the speed performance of a device [53]. SOI wafers are unique products for specific end-user applications.

The SOI process begins with a 200 mm SOI wafer consisting of a stack of a silicon handle layer (substrate layer), a buried oxide layer (SiO_2 - BOX) and a silicon device layer. Typically, the handle layer presents 625 µm-thickness, the oxide layer 2 µm-thick, and the device layer can be from only 5 µm-thick to some 100 µm. The device layer is also called the active layer since it is where the electromechanical structures are defined. To facilitate the wafer handling during manufacturing, the device layer is also called as the front side (FS) of the wafer, and the handle layer as the back side (BS) (Figure 2-9).

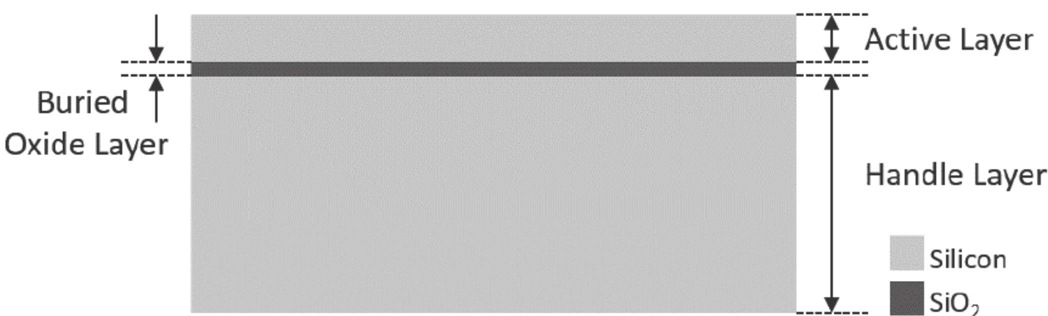

Figure 2-9 – Silicon-on-isolator wafer cross-sectional schematic and correspondent nomenclature.

2.5.2 Process flow

The INL's cleanroom has several systems capable of performing the different deposition, lithography and etching techniques previously detailed. In the MEMS process, not all of them are used, and the choice is

made considering the final goal of the process, the different characteristics of each, and the costs and time to produce. The main steps cross sections of the standard process [129], shown in Figure 2-10, where:

a. Wafer preparation;
b. Deposition of a thin metal layer film: A thin film typically of aluminium (or an alloy of AlSiCu) or a stack of TiW and AlSiCu are sputtered on the wafer's FS on the FTM Timaris system. Before the deposition, a pre-etch preparation process is performed to increase the adhesion of the metal layer to the silicon wafer;
c. Patterning of the metal: The sputtered metal layer is then patterned by DWL lithography, followed by etching. Here, a thin positive photoresist (AZP4110) layer is spin-coated with a few microns thickness on top of the metal layer. This photosensitive material is exposed using the Heidelberg DWL 2000 system, and the exposed material is then removed by the AZ4110 developer. Both coating and developing steps are automatically performed in the Karl Suss track. A wet etching process follows to remove the exposed metal areas, with Aluminium etchant 16:1:1:2, and the etch process is stopped by the submersion of the wafer into water. The electrical contacts and the alignment marks for the following processes are patterned in this process. After this process, the photosensitive layer is removed by Oxygen Plasma Ashing;
d. FS and BS SiO_2 layer deposition: Given the different selectivity of photoresist and silicon in the final wafer patterning, a sacrificial layer of a compatible material with a slower selectivity to work as a mask is desired. For that, a thick layer of silicon oxide (typically from 2 to 5 μm is deposited by chemical vapour deposition in the SPTS CVD tool on the wafer's FS and BS. The thickness of these layers is critical, not only for the final silicon layer depth desired to be etched but also to control the bow of the wafer since the films present residual stress that can result in a large wafer bow, making it impossible to process it;
e. BS Hard-mask patterning: To process the wafer's BS, alignment marks must be patterned on this side. The mask aligner from Suss Microtec, a high-resolution contact mask aligner with sub-micron feature capability, is used to transfer these marks to the bottom-side using a second alignment microscope. With these marks, it is possible to expose and develop the desired layout on the DWL system and track, respectively. Then, the exposed SiO_2 is anisotropically etched by RIE in the SPTS APS tool, using the silicon layer as an etch stopper. After this process, the photosensitive layer is removed by Oxygen Plasma Ashing;

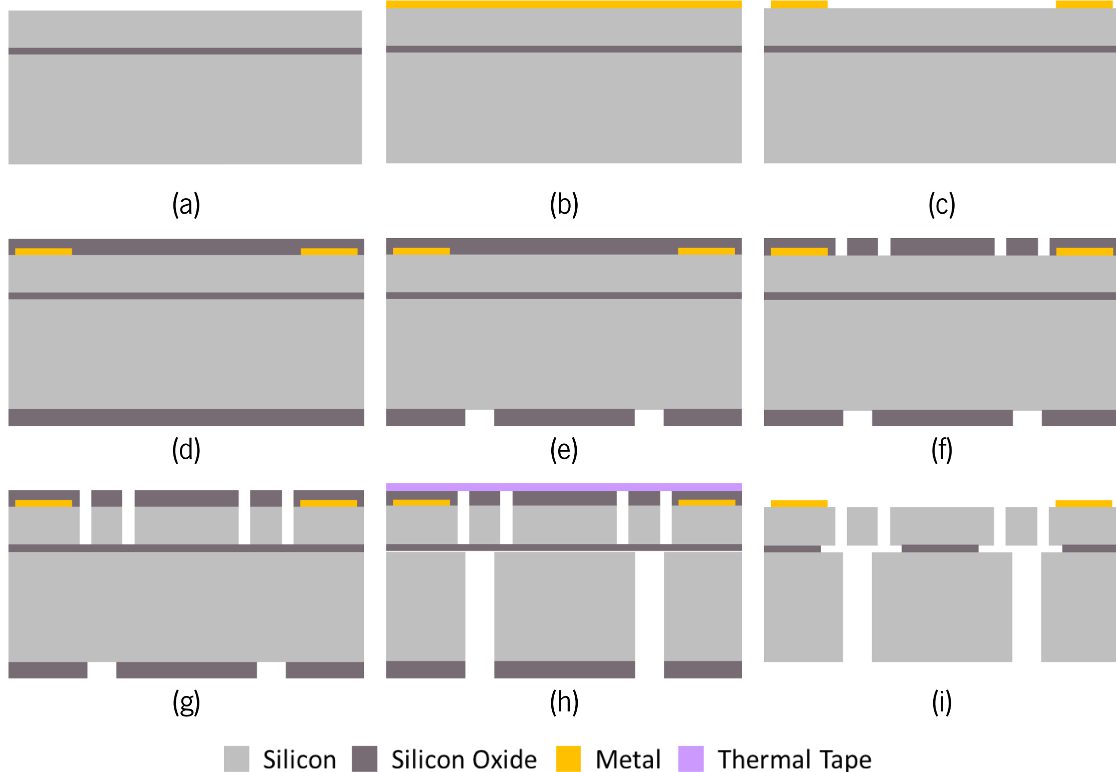

Figure 2-10 – SOI-based MEMS standard micromachining process flow.

f. FS Hard-mask patterning: Following the same logic of the previous layer patterning, the FS sacrificial layer is also patterned by DWL lithography, aligned with the pre-existing metal marks. Followed again by RIE and ashing;

g. FS Structure etching: With the hard-mask set on the BS and the FS, it is possible to transfer the pattern from the mask into the silicon layer. In this case, as it is necessary to etch the FS and the BS of the SOI wafer, it is fundamental to take a few particular cares in this process. One of which is the use of thermal tape. This film prevents damage to the hard-mask or the structures already etched on the opposite side of the wafer. Another care is the sequence of the process. It is essential to etch the structures on the FS first and only after those, the ones on the BS. This process sequence is essential to protect the most sensitive and small features implemented in the FS and the BOX layer (the etch stopper layer). So, initially, the FS structures are etched using the SPTS Pegasus system through a slow Silicon DRIE etch. Afterwards, the thermal tape is applied in the FS to protect the structures already patterned on this side;

h. BS Structure etching: The BS structures are then etched, also using the SPTS Pegasus systems, through a fast Silicon DRIE, and finally, the FS thermal tape is removed, and the residues left on the wafer from the etching process and from the thermal tape are removed through an O_2 cleaning;

i. Structures release: The structure release phase consists on the removal of the BOX that is exposed. This step uses the SPTS Primaxx – HF Vapour Etcher and is designed to etch isotropically sacrificial silicon oxide layers. The exposed silicon oxide is removed from the structure by an anhydrous hydrogen fluoride (HF) vapour. Due to its dry nature, this process avoids the stiction of released moving parts and damage to delicate structures.

2.6 SOI-based asymmetric electrodes processes

MEMS mirrors using out-of-plane electrostatic actuators have been presented in literature, which can be divided into two main categories, vertical comb actuators and parallel-plate actuators. In general, comb actuation allows for larger mirror angles (θ) and, consequently, a larger field of view when compared to parallel-plate actuation [122], since the relative positions of the electrodes in comb actuation do not limit the maximum displacement, as well as the fact that the pull-in phenomenon intrinsic to parallel-plate electrostatic actuation can be avoided. Several ways of combining vertical comb-drive actuators with micromirrors have also been presented in the literature, mainly as staggered vertical combs, SVC (same electrode dimensions with z-axis offset) [130], [131], angular vertical combs, AVC (same electrode dimensions with an angular offset) or vertically asymmetric combs-drives (different heights with z-axis offset) [132], [133], [134], [135]. Typical vertically asymmetric comb electrodes fabrication relies on the use of several lithography steps to define the masks to fabricate electrodes with thickness asymmetry on a single silicon layer. Different micromachining processes have been presented in the literature, some that use different materials to create a two-level mask, as presented in [132], [134] and others that use two layers of the same material defined in different lithographic steps, as in [133].

For instance, the work presented by H. Hamaguchi in [132] demonstrates the fabrication steps for micromachining asymmetry between the sensing capacitive electrodes of a three-axis SOI accelerometer. Figure 2-11 presents the main fabrication steps implemented in this work. Here, a double lithography is required, where (a) an initial SiO_2 layer is deposited and (b) patterned with the thicker structures layout; then, (c) a second mask layer of photoresist is deposited and patterned with the combination of the thinned and thicker mask layouts; in (d) the exposed SiO_2 is removed to ensure the self-align of the sensing electrodes. A sequential process composed by a step of silicon DRIE and mask thinning (removal of the remaining photoresist layer) is implement (e) - (g), followed by the release of the structures by HF vapour etching (h). Figure 2-12 displays SEM images of the asymmetric electrodes fabricated in [132].

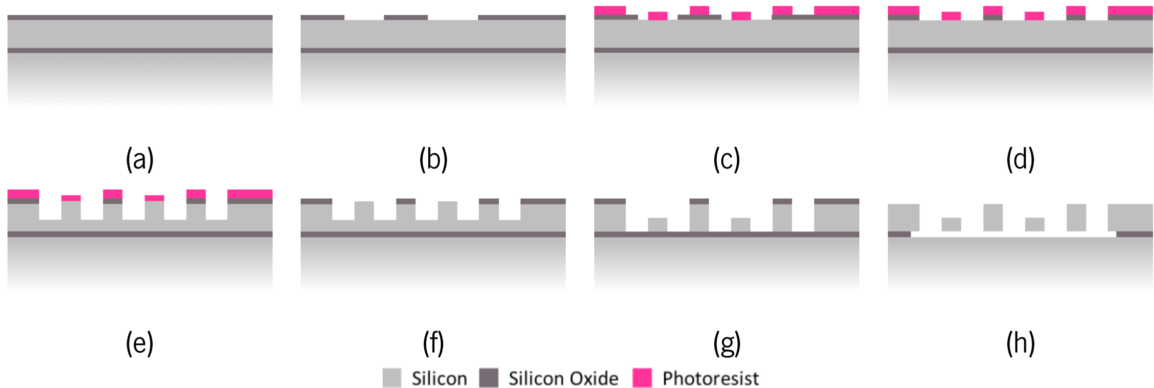

Figure 2-11 – Device layer main micromachining steps implemented in [132] and [135] to create asymmetric vertical electrodes based on a double-layer mask with different materials.

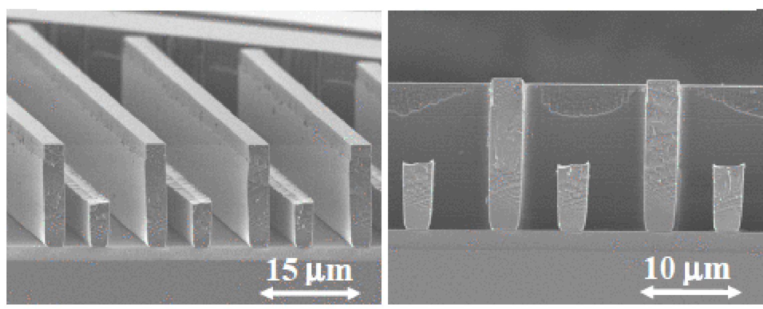

Figure 2-12 – SEM images of the asymmetric vertical electrodes presented in [108], based on a double layer mask with different materials process.

Other studies, such as [134], change the materials used as mask layers, step (b) to (e), employing aluminium (Al) and SiO_2, as presented in Figure 2-13, while [133] using a dual SiO_2 layer approach for the multilevel mask.

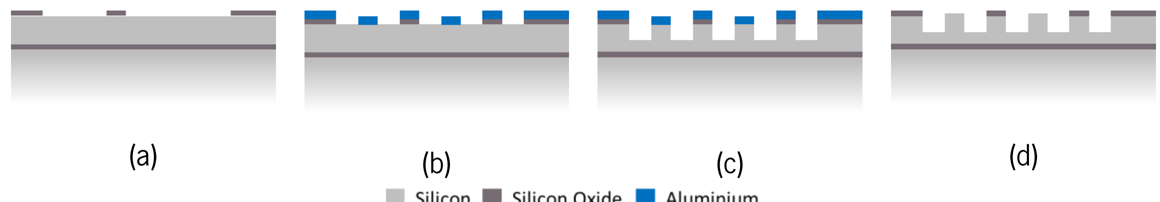

Figure 2-13 – Device layer main micromachining steps implemented in [133] to create asymmetric vertical electrodes based on a double-layer mask with the same material.

These are often prone to misalignments between actuators, and when designing a device with a minimal electrode gap (smaller than 3 µm given a 50 µm SOI layer), this misalignment can compromise the final device performance or process yield. More recently, new attempts to develop self-aligned comb electrodes have been presented. In [136], higher alignment tolerance is achieved by using dummy electrodes and SOI-SOI wafer bonding. Other approaches use electrodes with the same thickness, and an offset is

induced by out-of-plane actuation [130], [131] or by using suspended actuators and mechanically deflecting those at the expense of complex assembly procedures [137].

This thesis proposes a 2D MEMS mirror employing vertical asymmetric comb-drive electrostatic actuation, micromachined using a novel self-aligned, dicing-free [129] and low-cost fabrication process. This novel fabrication process combines typical SOI-based bulk micromachining and grayscale lithography to create a single mask with multilevel topography, followed by a sequence of etching and mask thinning steps, creating vertically asymmetric structures enabling a small and self-aligned electrode gap of approximately 2.8 μm, as presented in Figure 2-14. This process, when compared to previous references [130], [131], [132], [133], [134], [135], presents a more straightforward and cost-effective process to achieve non-resonant torsional motion using a single-layer device.

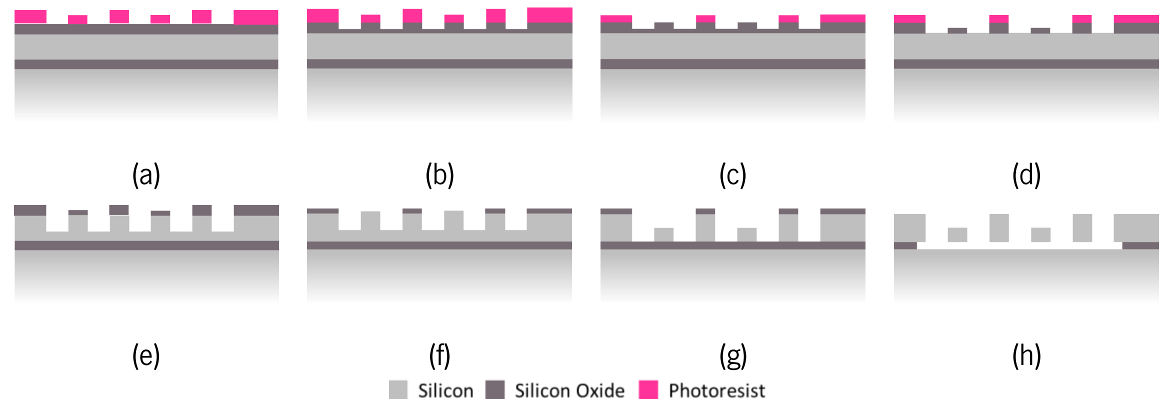

Figure 2-14 – Proposed multilevel self-aligned process using grayscale lithography.

Grayscale lithography is often used to pattern micro-lenses, diffractive optical elements, computer-generated holograms, among others [138]. However, this can also be used to create discrete photoresist levels that, when combined with a sequential bulk micromachining process, transpose this discrete mask to the substrate. This technique enables the patterning of perfectly aligned (no alignment between separate lithography steps is required) asymmetric structures that, in this application, enables the creation of self-aligned electrostatic combs where each GS level corresponds to a different thickness to be patterned on the silicon substrate. The fact that no alignment between separate lithography steps is required bypasses most misalignment sources from the lithography process, which may arise due to the resolution of the system camera or from the alignment marks' quality, among others.

2.7 Conclusions

Microfabrication, as used in the microelectronics and MEMS field, relies on bulk and surface technologies [96], [122]. This chapter has provided an in-depth exploration of various processes employed in

deposition, lithography, etching, and cleaning techniques. Furthermore, it has offered a comprehensive examination of the standard Silicon-On-Insulator (SOI)-based MEMS process implemented at the INL facility.

A primary challenge addressed in this thesis is the optimization and adaptation of the standard SOI-based MEMS micromachining process at INL. The objective was to fabricate structures with differing thicknesses yet perfectly aligned within the same silicon layer. To this end, the thesis reviews state-of-the-art processes documented in the literature. These processes range from the use of sacrificial layers composed of different materials, which exhibit varied etching rates, to methods involving sequential lithography and mask patterning. A significant issue with both approaches is the inherent challenge of aligning the different masks, which is critical to achieving the desired structural precision in MEMS devices.

This thesis proposes a novel self-aligned, dicing-free [7] and low-cost fabrication process to micromachine asymmetric electrodes. This novel fabrication process combines typical SOI-based bulk micromachining and grayscale (GS) lithography to create a single mask with multilevel topography, followed by a sequence of etching and mask thinning steps, creating vertically asymmetric structures enabling a small and self-aligned electrode gap.

This multilevel process, the techniques available at INL and the device's target application, imply various restrictions to the developments of desired device, raging from the MEMS structure and its minimal features and combination of DOEs and MEMS, to the selection of reflective materials suitable for mirror coatings, among others. The following chapters will detail into the analysis of the MEMS mirror, based on asymmetric electrodes, as an individual, as well as the Dammann DOE. Additionally, the subsequent sections will elucidate the integration and micromachining processes of the target device, considering the processing capabilities and materials available at INL.

3. MEMS Mirror

As previously detailed, this thesis aimed to develop an optical MEMS device to split and steer a laser beam, a device where the capabilities of a typical MEMS mirror and a diffractive element are merged for LiDAR applications. Even though the final device will be an integration of these two components, these need to be deeply studied initial as an individual and then set the restrictions that each implies to the other when combine. The MEMS mirror by itself presents several challenges. The process of modelling and designing a device or system is a complex and heuristic topic that depends on several inputs. In a designer's perspective, modelling a structure is a process that relies on the continuous analysis and verification of the device behaviour. These inputs can be highly simplified and classified into four categories: application, denoting the objective and the environment where the device will be implemented as well as the constraints/impositions that they imply: behaviour, concerns the physical theoretical foundations; the geometry, has its core in the MEMS design features; and finally, the fabrication process, which implies critical constraints to the device (Figure 3-1).

Given the process limitations, the MEMS mirror developed in this thesis employs asymmetric electrostatic actuation to induce a torque in the reflective movable structure to steer a laser beam. The angular deflection of the mirror is intrinsically dependent on the geometry and mechanical properties of the anchored springs, as well as the damping conditions, which must be designed to ensure the optimal performance.

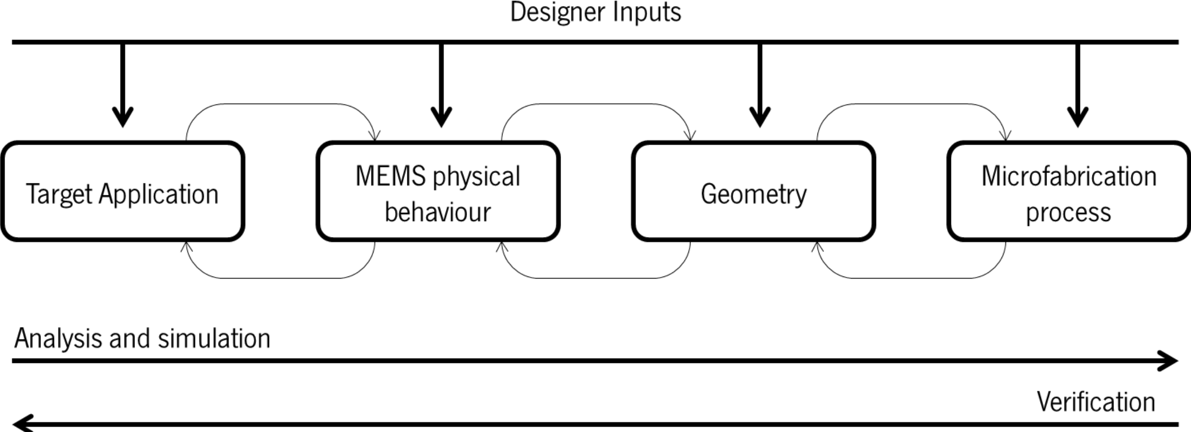

Figure 3-1 – Designer inputs in the modelling process [139].

This thesis aims to develop a two-dimensional MEMS mirror based on a gimbal architecture, featuring the inner axis responsible for achieving a 54° field of view and the outer axis for a 2.6° range, at resonance and quasi-static, respectively. Acknowledging the challenging demands associated with the inner axis, a simplified one-dimensional MEMS mirror was first designed. This 1D mirror presents the structure of the inner axis, facilitating a comprehensive performance analysis devoid of influence from the outer structure.

This chapter of the thesis provides the analysis of the theoretical principles behind the mirror's performance. For which, it is essential to analyse it through two distinct steps, the numerical analysis and FEM modelling, and the evaluation of the same. In this chapter, the different models that describe the mirror performance will be presented. Initially, the parameters, that are essential to the numerical evaluation (dynamic performance evaluation), and that can be computed analytically, will be studied considering the restrictions imposed. The dynamic performance of the device was evaluated using a block diagram model on the Simulink™ tool considering an established set of initial parameters. This analysis provides a better understanding of the system, especially the insights into the effects of changing either device dimensions or material properties.

With the results of the analytic analysis and the numerical model, a finite element method (FEM) simulation model of the MEMS mirror is also detailed in this chapter, where the electrostatic, elastic and damping torques acting in the MEMS device are analysed. And the design considerations of both the 1D and 2D devices are detailed.

3.1 Theoretical Foundations

The MEMS mirror to be developed in this thesis has a one degree-of-freedom (DOF) electrostatic out-of-plane micro-actuator as the base of operation. The parallel-plate electrostatic electrode is schematically represented in Figure 3-2. This actuator consists in a complex mechanical system constituted by an asymmetric parallel-plate capacitor, composed of a movable and a fixed plate. The movable plate, attached to the mirror surface, is suspended by a spring, allowing an out-plane torsional movement. As indicated by its nomenclature, this electrode is characterized by two conductive plates oriented in parallel. Although frequently employed in in-plane actuators, this can also be used to induce out-plane motions, as depicted in Figure 3-2.

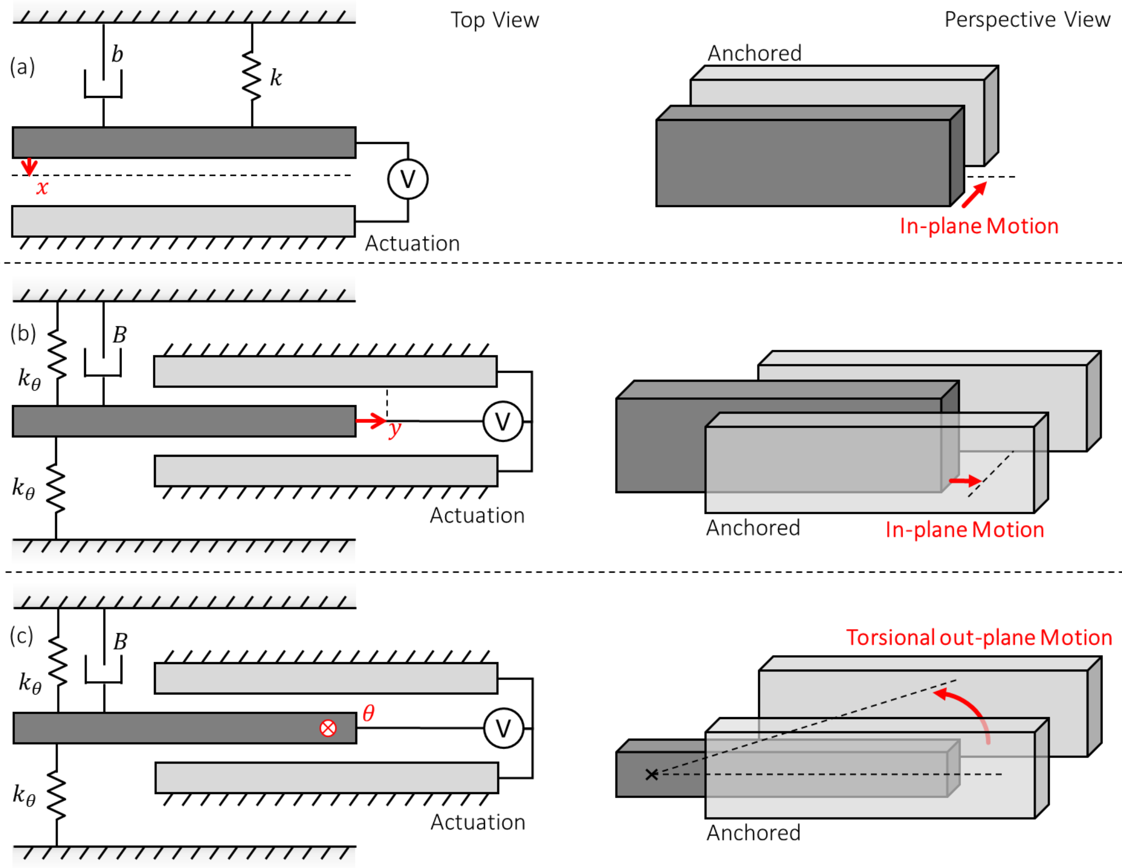

Figure 3-2 – 1-DOF micro actuator: in-plane motion, gap (a), or overlapped area changing (b) and out-plane motion (c).

In the in-plane actuator, an electrostatic force is generated when a voltage is applied, attracting the plates towards each other and reducing the inter-plate gap or pushing the movable plate, reducing the overalled area. While for out-plane configurations, an inherent disequilibrium is required, typically achieved by an asymmetry between both electrodes. Here, when a voltage is applied, the out-of-plane electrostatic force seeks to align the electrodes with each other. These systems are governed by a combination of

mechanical and electrical forces. However, in the case of asymmetric actuators which exhibit torsional out-of-plane motion, these forces manifest as torques, and the total force applied depends on the distance to the rotation axis (N.m). So, the electrical force is the electrostatic torque (T_{elect}), and the mechanical ones are the elastic torque ($T_{elastic}$), inertia (T_i), and damping (T_b).

$$T_i + T_b + T_{elastic} = T_{elect} \tag{3-1}$$

Since the electrostatic actuator is equivalent to a capacitor, the corresponding capacitance between two parallel-plates is defined by:

$$C_0 = \varepsilon \frac{A}{d} = \varepsilon_0 \varepsilon_r \frac{A}{d} \tag{3-2}$$

where ε is the dielectric constant of the material between the plates (usually air), computed by the multiplication of the electrostatic permittivity of vacuum, ε_0, and the relative permittivity of the insulator used, ε_r, ($\varepsilon = \varepsilon_0 * \varepsilon_r$), A is the overlapping area of the plates, and d is the distance between the plates. Once the system is actuated by the electrostatic torque, the movable plate shows a deflection angle (θ) that changes the capacitance value according to equation (3.3), where N is the number of electrodes.

$$C_\theta = \frac{N\, \varepsilon\, A(\theta)}{d}, \text{ for small angles} \tag{3-3}$$

The electrostatic torque produced between them can be expressed as (3-4) when a voltage V is applied across the plates of the capacitor.

$$T_{elect}(\theta) = \frac{1}{2}\frac{\partial C(\theta)}{\partial \theta} V^2 = \frac{1}{2} V^2 \frac{N\varepsilon}{d} \frac{\partial A(\theta)}{\partial \theta} \tag{3-4}$$

Structurally, the spring and the damper create a reaction torque on the movable structure opposite to the direction of the mirror movement. The elastic force appears because the movable plate is anchored to a spring with a torsional stiffness k. This torque increases linearly as the angle between the plates increases, θ [140].

$$T_{elastic} = k_\theta \theta(t) \tag{3-5}$$

The inertia (T_i) arises due to the mirror torsional moment of inertia J.

$$T_i = J * \frac{\partial^2 \theta(t)}{\partial t^2} \tag{3-6}$$

When dealing with a movable part structure, the flow of the fluid around it creates a damping force [141], [142], [143]. However, when the gap dimension between the parallel plates lies in the micrometres scale

and is extremely small when compared to the length and thickness of the plates and the large mirror surface, the damping force generated is dominated by the slide and drag damping coefficient, B [141], [144].

$$T_b = B * \frac{\partial \theta}{\partial t} \tag{3-7}$$

So, the equation (3-1) can be rewritten as:

$$J\frac{\partial^2 \theta(t)}{\partial t^2} + B\frac{\partial \theta(t)}{\partial t} + k_\theta \theta(t) = T_{elect}(\theta, V) \tag{3-8}$$

When there is no electrostatic force, that is, when no voltage is applied, the previous equation can be simplified to [145], [146]:

$$J\frac{\partial^2 \theta(t)}{\partial t^2} + B\frac{\partial \theta(t)}{\partial t} + k_\theta \theta(t) = 0 \tag{3-9}$$

Mechanically, the system can be represented as a second-order system [143], [147] (if the damping coefficient is considered linear). The respective Laplace transform function is the equation (3-10).

$$\frac{x(s)}{a(s)} = \frac{1}{s^2 + \frac{\omega 0}{Q} s + \omega 0^2} \tag{3-10}$$

where ω_0 is the natural resonance frequency of the system, defined as $\omega_0 = \sqrt{k_\theta / J}$ ($f_0 = 1/\, 2\pi * \sqrt{k_\theta / J}$), and Q is the quality factor, defined as $Q = \sqrt{k_\theta * J}/B$. The equation (3-9) can be rewritten as:

$$\frac{\partial^2 \theta(t)}{\partial t^2} + \frac{\omega_0}{Q}\frac{\partial \theta(t)}{\partial t} + \omega_0^2 \theta(t) = 0 \tag{3-11}$$

The parameters Q and ω_0 dictate the dynamic behaviour of the system. From a designer's perspective, defining the device parameters according to its application is critical to achieve the desired time and frequency-response. The dynamic response of a second-order mechanical system can be divided into three categories: underdamped when $Q > 0.5$, critically damped when $Q = 0.5$, and overdamped when $Q < 0.5$. Considering that the MEMS mirror can be operated both statically or dynamically, the system can be analysed in a different way. When operated in quasi-static mode, the inertia and damping can be neglected, and consequently, a static analysis can be used to find the balance between electrostatic and elastic torque that acts in opposite directions. When operated in resonant mode, the MEMS mirror can take advantage of the mechanical quality factor, Q, to increase the amplitude of the out-of-plane deflection, A ($A = T/k * Q$), with a low atmospheric pressure to reduce the air damping, Figure 3-3.

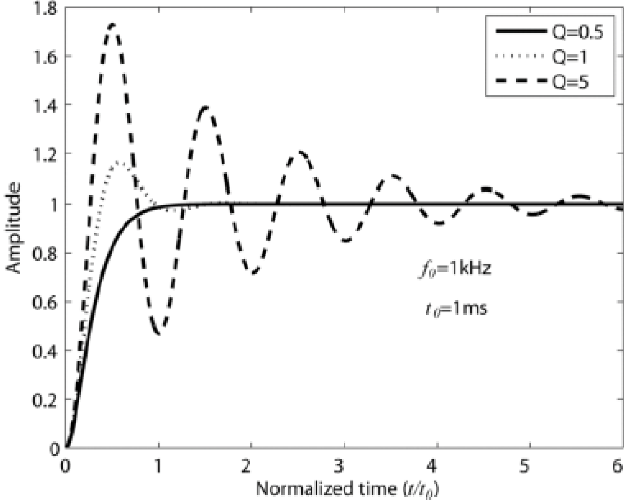

Figure 3-3 – Step response of different quality factor 2nd order mechanical systems.

3.1.1 Field of view static analysis

For the static analysis, the sum of the existing forces in the system can be rewritten as [146], [147]:

$$T_{total} = T_{elastic} + T_{elect} = \frac{1}{2}\frac{\partial C(\theta)}{\partial \theta}V^2 - k_\theta \theta \tag{3-12}$$

At a particular applied voltage, the magnitude of the electrostatic torque equals the mechanical one. At this point, the electrostatic and the mechanical restoring torque balance each other. The equilibrium points existing in this particular state can be found by solving the equation system:

$$\begin{cases} |T_{elastic}| = |T_{elect}| \\ \dfrac{d|T_{elastic}|}{d\theta} = \dfrac{d|T_{elect}|}{d\theta} \end{cases} \tag{3-13}$$

where the derivative of T_{elect} and $T_{elastic}$ are, as function of θ:

$$\frac{dT_{elect}}{d\theta} = \frac{1}{2}V^2 \frac{d}{d\theta}\left(\frac{\partial C(\theta)}{\partial \theta}\right), \quad \frac{dT_{elastic}}{d\theta} = k_\theta \tag{3-14}$$

Asymmetric vertical electrostatic structures

In the MEMS mirror, the fixed parallel plates find themselves interlaced with the movable plates, forming two structures like a comb. This organisation of the capacitors simplifies the fabrication process since it is possible to achieve higher capacitance areas in a smaller device total area (die area) [143]. In the inner axis, different heights in the fixed and movable combs present the inherent geometry imbalance in the actuators' rest position ($\theta = 0$), compared to symmetric geometries, which are perfectly aligned in this position as presented in the schematics of Figure 3-4.

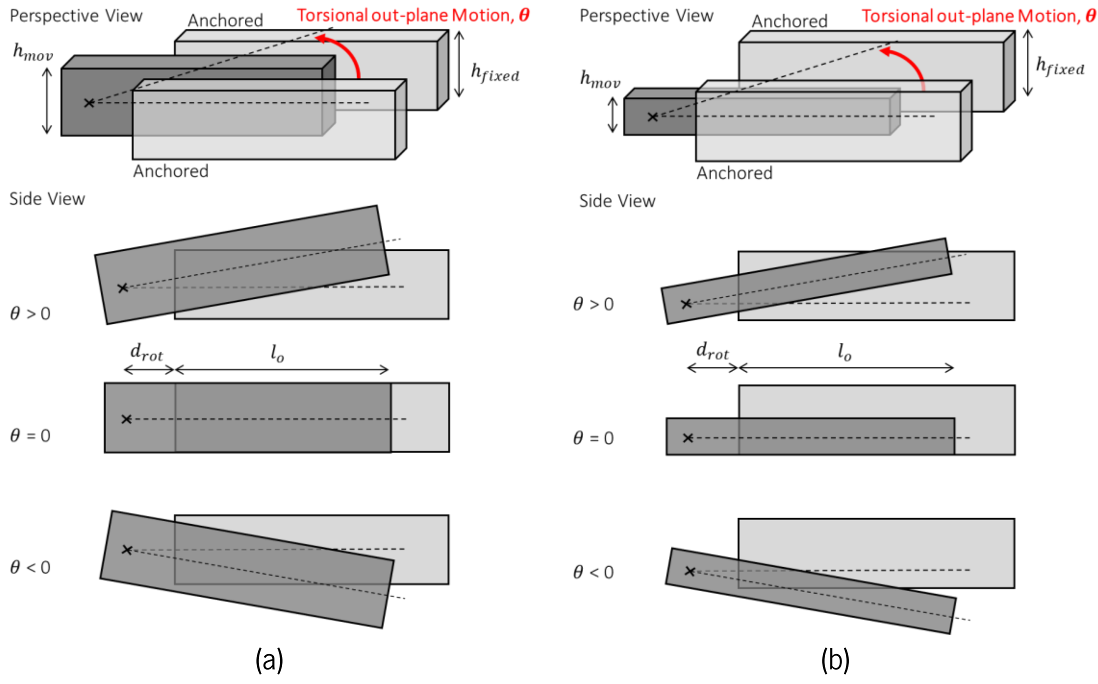

Figure 3-4 – Symmetric (a) and asymmetric (b) electrodes schematic of different overlapping areas for different mirror deflection angles, θ.

The electrostatic torque, as presented in equations (3-3) and (3-4), depends on several geometrical and actuation parameters, such as applied voltage, electrodes gap, and the number, and the overlapped area, which, on the other hand, depends on the mirror angle and the electrodes height and overlapped length, and the distance of the electrodes to the torsional/rotation axis. In the asymmetric geometry, the torque at rest position is given only by stray fields resulting from the geometrical imbalance, as depicted in Figure 3-5. When actuated in the quasi-static mode, the mirror will present a slight angle corresponding to the position where the different electrodes are aligned, and the electrostatic torque is equal to the spring torque. When actuated in the resonant mode, this imbalance reflects as the initial torque that produces an initial oscillational mirror motion.

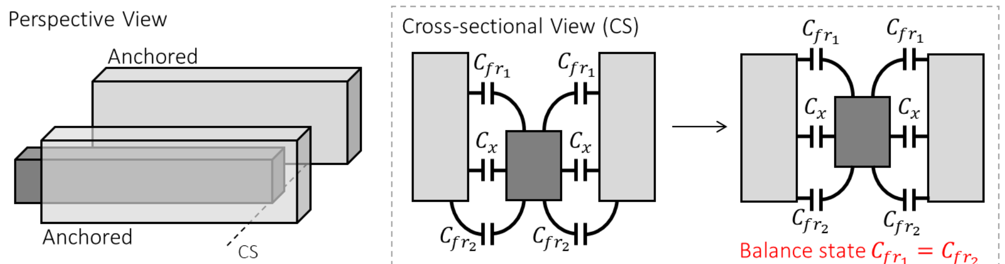

Figure 3-5 – Cross-sectional schematic of the fringe field in asymmetric electrodes, in the rest position and in equilibrium.

To achieve the high torque required to statically tilt the mirror in the outer axis, the fixed and movable electrodes were created in different silicon layers, known as staggered vertical electrodes (SVC) [130], [131], as displayed in Figure 3-6. At its rest position, the overlapped area is zero, and when a voltage across each other is applied, the movable plate will start to move, increasing the overlapped area.

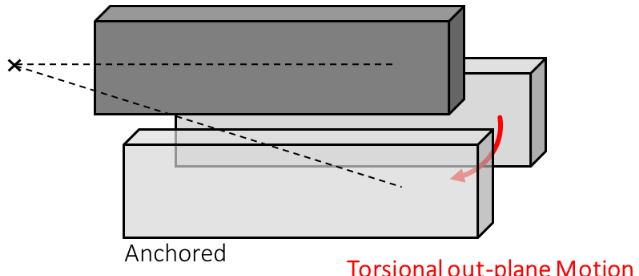

Figure 3-6 – Outer axis electrodes topology schematic – staggered vertical electrodes.

Torsional elastic springs

The stiffness of the springs, k, is defined to have a natural resonance frequency f_0, given by equation (3-15). This value corresponds to the total elastic coefficient of the mirror [148]. The maximum mirror deflection angle achievable resulting from the torsional springs can be computed by the equation (3-16).

$$k_\theta = (2\pi f_0)^2 * J, \quad (3\text{-}15)$$

$$\theta = \frac{T.l}{G.J}\ [rad], \quad (3\text{-}16)$$

where T is the applied torque, l is the spring length, G is the silicon shear modulus, and J is the torsional constant, which depends on the spring geometry[145]; i.e., thickness, h_s, and width, w_s, as illustrated in Figure 3-7. It can be derived by using the equation (3-17) [140].

$$J = h_s * w_s^3\left(\frac{1}{3} - \frac{0.21w_s}{h_s}\left(1 - \frac{w_s^4}{12h_s^4}\right)\right), h_s > w_s \quad (3\text{-}17)$$

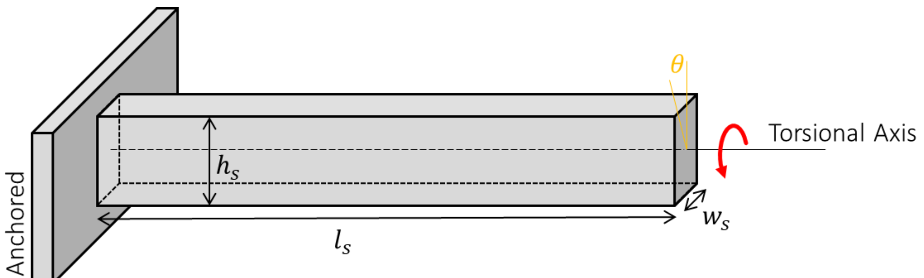

Figure 3-7 – Torsional spring beam referential and variables.

The spring torsional rigidity is the product between the shear modulus and the torsional constant [145]:

$$G.J = \frac{T.l_s}{\theta}\ [N\,m^2/rad] \quad (3\text{-}18)$$

And the torsional stiffness coefficient, k_θ, is the rigidity divided by the spring total length, equation (3-19) and (3-20), considering that the width of the spring is smaller than the spring thickness [145].

$$k_{\theta} = \frac{G.J}{l_s} = \frac{T}{\theta} \ [N\,m/rad] \tag{3-19}$$

$$k_{\theta} = \frac{G * h_s w_s^3 \left(\frac{1}{3} - \frac{0.21 w_s}{16 h_s}\left(1 - \frac{w_s^4}{12 h_s^4}\right)\right)}{l_s}, h_s \geqslant w_s \tag{3-20}$$

3.1.2 Analysis of the MEMS mirror dynamic behaviour

The MEMS mirror dynamic analysis, unlike the static one, considers all the forces acting on the system. In particular, the inertial and damping effects can significantly change the actuator's performance. This analysis illustrates the actual behaviour of the device during operation since the damping force is neglected in the static analysis but plays an essential role in the mirror operation. The focus of this section is to address the mirror's resonant mode dynamic characteristics.

Drag damping arises due to the motion of the mirror through the surrounding fluid, which can be air or another gas. As the mirror moves, it displaces the fluid around it, and this displacement leads to the generation of drag forces opposing the mirror's motion. The magnitude of these drag forces depends on several factors, including the mirror's geometry, the fluid's viscosity, and the relative velocity between the mirror and the fluid.

To mathematically describe the drag damping phenomenon, it is possible to use the concept of the damping coefficient, B, which relates the damping force to the angular velocity of the mirror, $\partial\theta/\partial t$, expressed in (3-7) [141]. The rotational damping coefficient, B, encapsulates the complex interactions between the mirror's geometry and the fluid, as well as the fluid's properties.

In [141], an extensive analysis of fluid flow interactions with high-frequency scanning micro-mirrors driven by angular vertical comb (AVC) actuators is presented to evaluate the effect of air damping on the maximum scan angle amplitude of micro-mirrors. In air damping theory, the pressure p and the velocity field u, of the fluid flow past an oscillating micro-mirror can be described by the Navier–Stokes model and continuity equations for unsteady, incompressible flow, where ρ is the fluid density and μ is the fluid viscosity:

$$\rho\left(\frac{\partial\vec{u}}{\partial t}\right) + \rho(\vec{u}\cdot\nabla)\vec{u} = -\nabla p + \mu\nabla^2\vec{u} \tag{3-21}$$

$$\nabla\cdot\vec{u} = 0 \tag{3-22}$$

Resonating MEMS structures are typically separated from the fixed substrate by a thin air gap and are driven to relatively small oscillation amplitudes. Gas damping is predominantly viscous, allowing for the

inertial terms on the left-hand side of (3-21) to be neglected. The ratio of inertial to viscous forces is defined by the Reynolds number, Re. Therefore, in the limit $Re \ll 1$, the thin gas films form either a Couette or squeeze-film viscous damper. Energy dissipation due to air damping in resonant micro-mirrors is derived from two main sources described below.

Vertical electrostatic combs structure

In the vertical electrostatic actuators, the viscous resistance due to the relative out-of-plane motion of adjacent fingers separated by a small air gap of width, d, can be estimated by the Couette flow model, and the maximum Reynolds number, Re_c of the flow in the electrodes is given by (3-23), and for $Re_c \ll 1$, the damping moment, M_d, of N number of comb fingers is given by (3-24):

$$Re_c = \frac{2\pi\rho f_s \theta_{max}(l_o + l_c)g}{\mu} \tag{3-23}$$

$$M_d = -\frac{4N\mu_{eff} t_m \pi f_s \theta}{3d}\left[(lo + lc)^3 - l_o^3\right] \tag{3-24}$$

where l_o is the distance between the electrodes and the rotation axis, l_c the electrode length, t_m the electrode thickness, f_s the mirror operating frequency, $\theta = \theta(t)$ and $\theta(t) = \theta_{max} sin(2\pi f_s t)$ [149]. For small values of d, the assumption of zero flow velocity at the rotating comb structure boundary may not be valid. To account for slip flow in the damping moment, a modification to the gas viscosity, μ_{eff} is applied, which is a function of the Knudsen number, Kn [141].

Rarefaction and compressibility effects

At an absolute limit, the typical intermolecular distances are comparable to the device dimensions, and the use of continuous fluid equations cannot describe the correct flow behaviour. For gases, the Knudsen number Kn computed from:

$$Kn = \frac{\lambda}{d}, \tag{3-25}$$

relates the gas-specific mean free path, λ, and the gas thickness d. When dealing with structures where the gas thickness changes over time, the Q_{pr} describes the relative flow rate for transitional flow regime (0.1<Kn<10), as:

$$Q_{pr} = 1 + 9.658Kn^{1.159} \tag{3-26}$$

The use of the relative flow rate coefficient is a reliable method to incorporate the boundary effects of the rarefied gas [141], [142]. Since Q_{pr} is computed in function to the Knudsen number, it depends on the film thickness and the static pressure value, P_a , because the mean free path is specified by $\lambda = P_0/P_a * \lambda_0$, where the λ_0 is the mean free path at a pressure P_0. In gas film theory, the slip-flow condition is usually included in the viscosity coefficient. The resulting coefficient is an effective viscosity, given by:

$$\mu_{eff} = \frac{\mu}{Q_{pr}} = \frac{\mu}{1 + 9.658Kn^{1.159}} \tag{3-27}$$

where μ is the viscosity of the gas. As a result, the damping moment of the electrodes can be computed by equation (3-28).

$$M_{elect} = -\frac{2N\mu_{eff}t_m\dot{\theta}}{3d}\left[(lo + lc)^3 - l_o^3\right] \tag{3-28}$$

Reflective plate of the MEMS mirror

As detailed in [141], the damping arising from the rotational oscillations of the micro-mirror plate confined within the cavity has been approximated utilizing the squeeze-film damping model. This model's validity is contingent on satisfying the condition $h/R \ll 1$, where h represents the depth of the cavity and R the mirror ray. The damping moment of a circular micro-mirror at $\theta = 0°$ has been deduced from the nonlinear Reynolds equation [150]:

$$M_d(\theta = 0°) = \frac{\mu\pi^2 f_s R^6 \theta_{max}}{4h^3} \tag{3-29}$$

Under conditions of sufficiently low values of f_s and θ_{max}, the surrounding air enveloping the mirror plate is governed by steady Stokes flow. In this scenario, the damping torque for an unbounded thin disk rotating at a fixed angular velocity can be expressed as [151]:

$$M_d = \frac{32\mu R^3\dot{\theta}}{3} \tag{3-30}$$

However, by preserving the temporal acceleration term in (3-21), the aerodynamic resistance of a circular disk undergoing small amplitude oscillations can be derived from the unsteady Stokes equation [152]:

$$\rho\left(\frac{\partial u}{\partial t}\right) = -\nabla p + \mu\nabla^2\vec{u} \tag{3-31}$$

By reducing the previous equation to dual integral equations, the high-frequency dependence of the damping moment of an oscillating disc in out-of-plane rotation is given by [153]:

$$M_d = \frac{32\mu R^3 \dot{\theta}}{3}(0.43\lambda\, cos(0.27\pi)) \tag{3-32}$$

where, $\lambda^2 = 2\pi\rho f_s R^2/\mu$ represents a dimensionless frequency parameter and characterizes the timescale for vorticity diffusion (the time it takes for the swirling or rotating motion of the fluid to spread out) into the surrounding fluid relative to the oscillation timescale (the time it takes for the MEMS mirror to complete one cycle of its back-and-forth movement) [141]. Additionally, the aerodynamic resistance of the oscillating disc consists of an added-mass term, which is $\pi/2$ out-of-phase with the angular velocity and does not contribute to energy dissipation.

While Stokes drag varies linearly with velocity, in the laminar flow regime, M_d is expected to be a quadratic function of the angular velocity. The overall aerodynamic moment, M_{plate} about the rotational axis can be deduced from Morison's equation intended for the hydrodynamic analysis of offshore floating structures. The damping and inertial components of M_{plate} are a function of the average damping coefficient, C_d, assumed as 2.42 for a Reynolds number of a plate oscillating in an out-of-plane rotation, $Re_m = 2\pi\rho f_s \theta_{max} R^2/\mu$, higher than 350 as demonstrated in [141].

$$M_{plate} = M_d = -\frac{4}{15} C_d \rho R^5 \dot{\theta}|\dot{\theta}| \tag{3-33}$$

The overall mirror damping coefficient is the sum of the damping from the plate and the vertical electrostatic electrodes, given by [141]:

$$T_b = B_{plate} + B_{elect} = \frac{M_{Plate}}{\dot{\theta}} + \frac{M_{elect}}{\dot{\theta}} \tag{3-34}$$

3.2 Device analytical evaluation

Selecting the optimal features for a MEMS device is a heuristic process, requiring consideration of multiple factors. All the parameters, except the non-linear damping coefficient, can be easily determined through analytical calculation, considering the established objectives and the existing restrictions. Initial parameters were defined considering the thickness of the wafer, the necessary reflective area to accommodate the incident beam, the operating frequency, and the limits of the fabrication process, among others.

1. At INL, the bulk micromachining MEMS process uses SOI wafers. The selected SOI wafer is composed by a stack of three layers: a thick handle silicon layer, a thin buried oxide layer, and a silicon active layer. A 50 µm-thickness SOI wafer was defined in order to increase the asymmetric parallel-plate electrode's overlapped area and the robustness of the device while minimizing changes to the INL standard process;
2. It was established that the reflective area of the device was within 1.1 mm x 1.1 mm in order to accommodate the full incident beam diameter (defined to 1 mm). Moreover, the application-driven requirements also define critical parameters, such as scanning frequency, defined as 10 Hz (i.e., the vertical operating frequency). The spatial resolution of the scanning is determined by the ratio between the resonant scanning frequency and the non-resonant scanning frequency. Given the scanning resolution of 0.15° and the frame rate, a horizontal axis minimum scanning frequency of 87 Hz is implied;
3. The fabrication process from the in-house INL process limits the minimum gap size. The initial parallel-plates gap was defined as 3 µm.

With these initial parameters established, it was possible to evaluate a wide range of additional parameters that impact the performance of the mirror. This includes the spring parameters, electrostatic actuator parameters, such as the number of electrodes, the gap between electrodes, their length, and overlapped area, as well as other factors such as the damping coefficient and the quality factor. The resulting parameters are detailed in Table 3-1 and Table 3-2.

Table 3-1 – Initial parameters application-driven.

Parameter	Value		Unit
Reflective area	1.1 x 1.1		mm^2
Horizontal Natural resonance frequency, f_0	Without DOE	>434	Hz
	With DOE	>87	
Horizontal FoV	54		°
Vertical scan frequency, f_0	10		Hz
Vertical FoV	2.6		°

Table 3-2 – Initial parameters microfabrication limits-driven

Parameter	Value	Unit
Parallel-plates gap ($d0$)	3	µm
Active layer thickness	50	µm
Buried Oxide layer thickness	2	µm
Handle layer thickness	625 ± 50	µm

To better understand the MEMS mirror's mechanical behaviour when operated in the quasi-static mode, an analytical model was developed and implemented in MATLAB. This model allows for a more

comprehensive evaluation of the mirror's performance and ensures that the device is optimized to meet the established objectives. By using analytical models, it is possible to evaluate, in a fast way, the influence of different parameters in the mirror operation.

In order to optimize the performance of the most challenging axis, a 1D scanning system presenting the inner axis structure was investigated. Here, to take advantage of resonant mechanical amplification and ensure minimal energy consumption, a half-gimbal movement concept was selected. This approach allows for the first resonant mode to be in the desired direction, specifically torsional, which effectively achieves the required field of view with maximum efficiency. By using this resonant mode, the 1D scanning system is able to achieve an optimal balance between deflection angle and frequency, as it requires less energy to reach the desired FoV.

The 2D MEMS mirror presents a gimbal architecture, Figure 3-8.b, which is a mechanical system consisting of two or more rotating rings mounted on a common axis. The outer ring is typically anchored to a stationary frame, while the inner one is free to rotate about their own axes perpendicular to each other and the common axis. The gimbal architecture is a versatile and widely used mechanism that allows for stable pointing and orientation control in a variety of applications. The inner axis consists of the 1D MEMS mirror suspended by two other torsional springs positioned in the outer orthogonal axis, and the outer axis moves the inner structures across this axis.

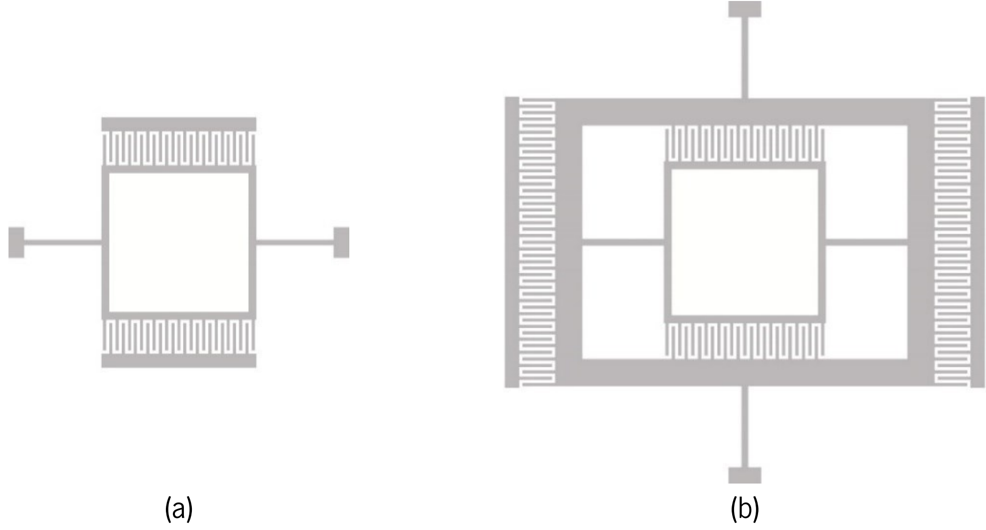

Figure 3-8 – 1D and 2D MEMS mirror gimbal schematic.

The inner axis is targeted to a resonant operation mode since it takes advantage of the device's high-quality factor and enables the device to reach a large FoV on the fast axis. This design follows the equation of forces given by (3-35).

$$J\ddot{\theta}_{IA} + B\dot{\theta}_{IA} + k\theta_{IA} = T_{Electrostatic\ IA} \tag{3-35}$$

A simplified approach was adopted for the gimbal movement concept to facilitate a more comprehensible and straightforward movement equation. It was determined that when the outer axis actuators are subjected to a constant DC voltage, resulting in a fixed electrostatic torque, the position of this axis for any applied voltage can be described by equation (3-36). This simplification does not consider the travelling between positions and the time to settle at that position, but allows for a simple analytical model.

$$k\theta_{OA} = T_{Electrostatic\ OA} \tag{3-36}$$

3.2.1 Electrostatic and elastic torque

In the proposed MEMS architecture, the pivotal role of electrostatic torque in achieving the targeted scanning FoV is highlighted. Diverse designs of electrostatic combs exist, primarily categorized as symmetric and asymmetric. Given the complexity of the fringe field effects inherent in asymmetric geometries, a simplified analytical model to attain the electrostatic torque in symmetric geometries was implemented since the expected peak electrostatic torque of symmetric electrodes is similar to the one achieved with asymmetric ones. This model computes the torque for mirror angles within the range of ±5°. This angular interval was established since it is the range in which the electrostatic actuators are overlapped.

Different geometry configurations and actuation conditions were assessed using analytical simulations. In Figure 3-9, the voltage applied across to the electrodes is increased from 25 V to 200 V (considering the maximum experimentally feasible voltage for the MEMS device) for a geometry with a gap of 3 μm and an electrode-to-rotation-axis distance of 500 μm. This variation demonstrates the expected quadratic increase in electrostatic torque with voltage.

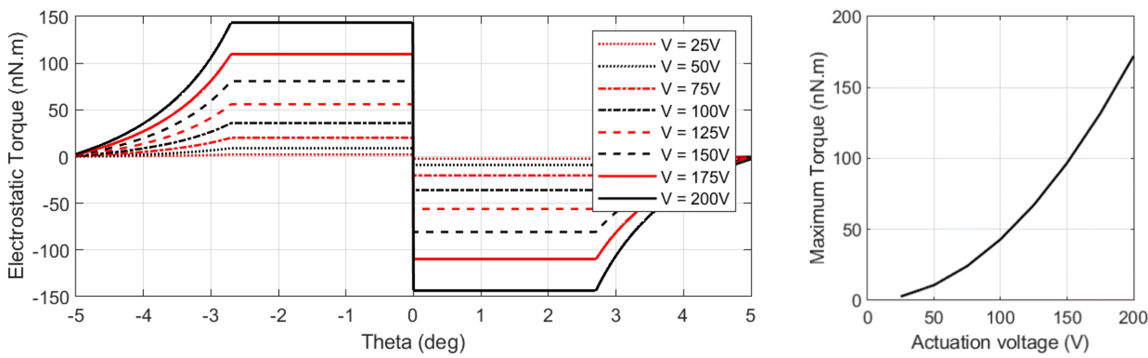

Figure 3-9 – Electrostatic torque dependence on the applied voltage in symmetric electrodes geometry with d_{rot} with 500 μm, and d with 4 μm.

In Figure 3-10, different gap sizes are compared at an applied voltage of 50 V and an electrode-to-rotation-axis distance of 500 μm. The results confirm the proportional decrease in

electrostatic torque with increasing gap size. In Figure 3-11, the maximum electrostatic torque is presented, considering different gap sizes and actuation voltages.

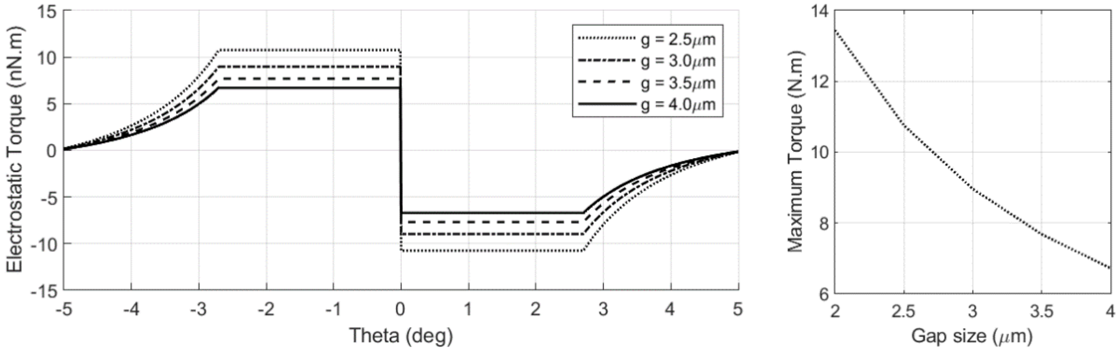

Figure 3-10 – Symmetric electrostatic torque dependence on the electrodes gap, with d_{rot} with 500 μm, and V with 50 V.

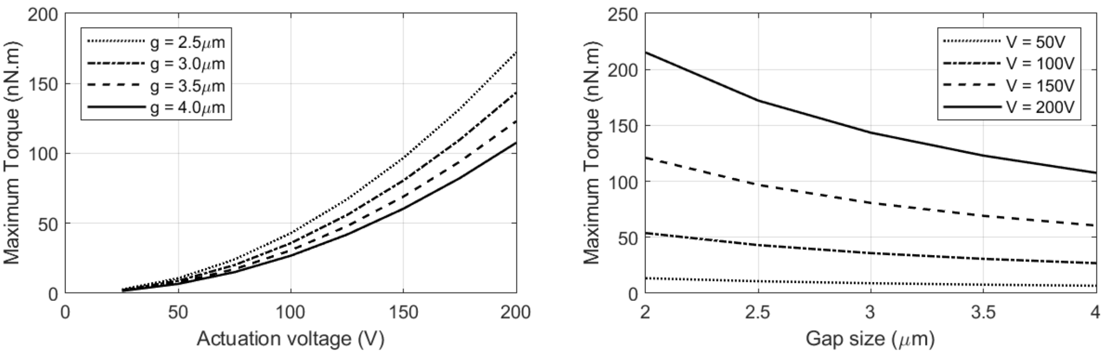

Figure 3-11 – Maximum torque evolutions for different applied voltages and electrode gap values combos.

Beyond these two variables, the distance to the rotation axis emerges as a critical parameter in these actuators. Figure 3-12 depicts the torque resulting from four distinct geometries, with distances from 250 μm to 1000 μm. This variable not only influences the maximum electrostatic torque but also delineates the angular range over which the electrodes can exert torque.

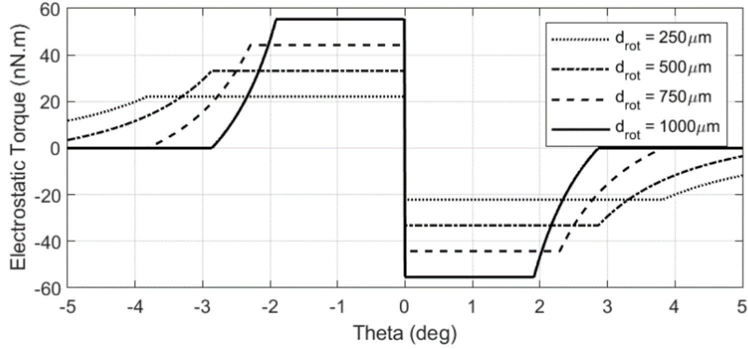

Figure 3-12 – Symmetric electrostatic torque dependence on d_{rot}, with the electrodes gap of 3 μm, and V with 100 V.

Larger distances from the rotation axis correlate with higher electrostatic torques but yield a narrower angular range. Therefore, the location of electrodes within the MEMS structure requires carefull consideration. This is essential whether the goal is to maximize the deflection angle in static operation or

to fine-tune the actuation torque for resonant operation. In the context of resonant operation, it is particularly important to supply energy to the system precisely when the structure is at its rest position. This strategy aims to avoid the generation of attraction forces in the opposite direction, which could potentially halt the resonant motion.

It is crucial to note that, in the case of symmetric electrode geometries, electrostatic torque is null at the rest position. Voltages applied to the mirror in this state will not induce mechanical deflection; i.e. the mirror will remain in its rest position. In this situation, the asymmetric geometry offers a significant advantage, as it permits the application of non-zero initial torque when the mirror is at rest, as illustrated in Figure 3-13. Nevertheless, it is essential to acknowledge that this analytical model simplifies the description of asymmetric electrostatic behaviour and does not faithfully represent the final angular torque profile due to the omission of fringe field effects.

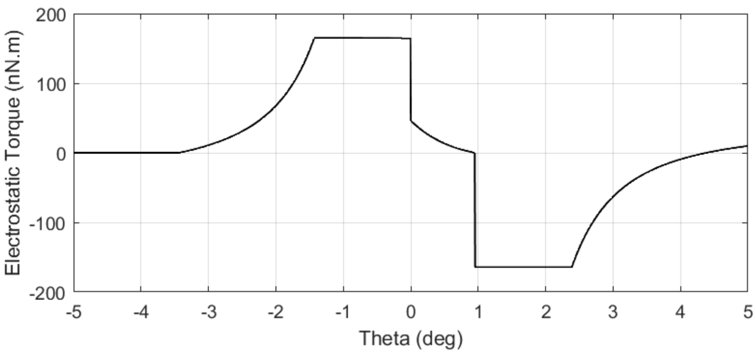

Figure 3-13 – Asymmetric electrostatic torque angular expected profile.

The torsional elastic torque presents a linear behaviour, resulting in higher torque for larger mirror angles. This characteristic significantly influences the maximum mirror amplitude during both quasi-static and resonant modes of operation. An increase in spring stiffness leads to elevated elastic torque, whereas an increase in spring length results in reduced torque, as depicted in Figure 3-14 and Figure 3-15.

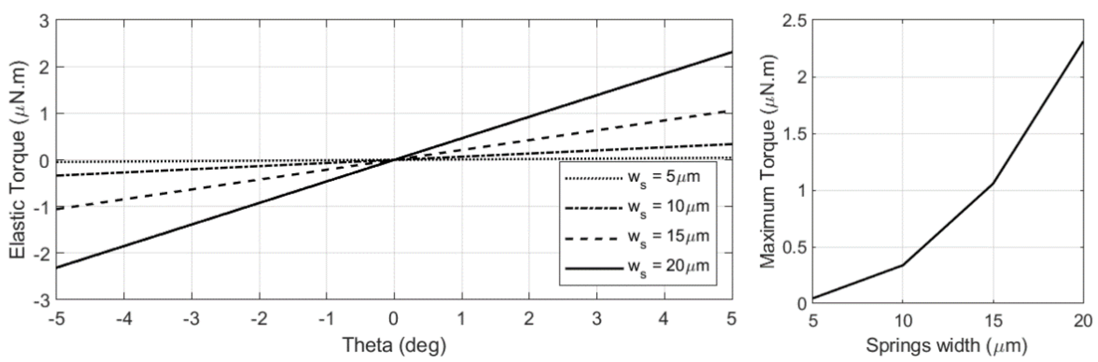

Figure 3-14 – Torsional elastic torque dependance on the spring's width.

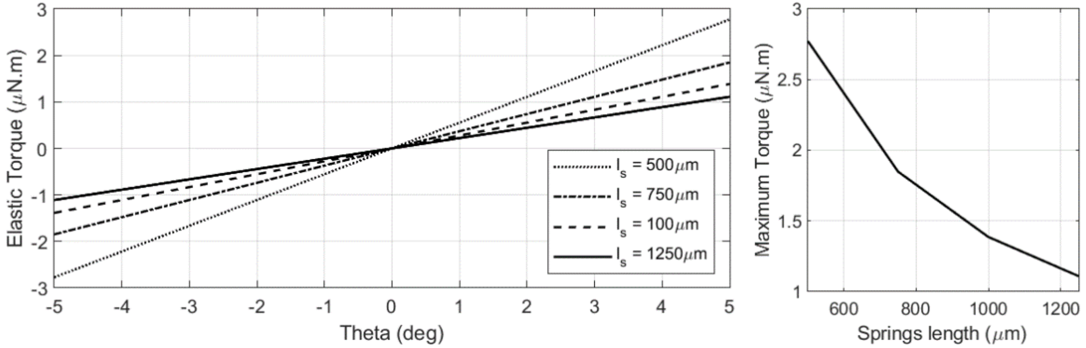

Figure 3-15 – Torsional elastic torque dependance on the spring's length.

3.2.2 Damping coefficient and quality factor

For the proposed device's inner axis, which is designed for resonant operation, achieving high Q-values (quality factors) is essential. The quality factor can be deduced by [2], [147]:

$$Q_{IA} = \frac{\sqrt{k_{IA} * J_{IA}}}{B_{IA}} \tag{3-37}$$

where k_{IA} is the inner axis elastic coefficient, J_{IA} the torsional moment of inertia of the reflective mirror component, and B_{IA} is the damping coefficient when the mirror is operated at high frequencies. The quality factor is influenced by various structural parameters, including spring geometry, the mirror's reflective surface area, and the number and placement of actuation electrodes, in addition to the damping coefficient.

Considering the dynamic behaviour of the damping coefficient, a simplified analytical model was employed to compute the Q-factor of the mirror for a known geometry and pressure conditions. Figure 3-16 and Figure 3-17 illustrate the impact of mirror size and pressure conditions on the quality factor. In the first scenario, mirror sizes ranging from 1 to 10 mm were simulated under three different pressure conditions. The second scenario analyses mirror sizes from 1 to 4 mm across a pressure range from 0.01 to 1 atm.

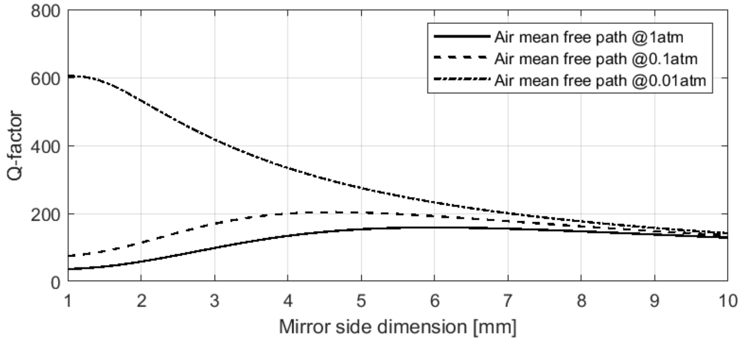

Figure 3-16 – Quality factor versus mirror side dimensions, from 1 to 10 mm.

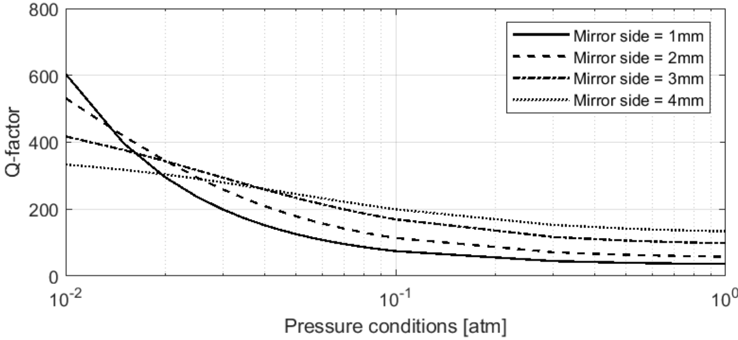

Figure 3-17 – Quality factor versus pressure conditions, from 0.001 to 1 atm.

Initial observations indicate that at atmospheric pressure, the Q-factor marginally increases up to a mirror size of 6 mm. When the mirror is at a pressure one decade lower, the Q-factor continues to increase up to 4 mm, and at a pressure two decades lower, the Q-factor decreases with increasing mirror size. Additionally, reducing the pressure enhances the quality factor for a given mirror size.

When using the analytical model, by comparing mirrors sizes of 1 mm and 4 mm with the same spring constant, it can be observed that for the smaller mirror, reducing the pressure drastically increases the Q-factor from 35 to 604 (a 17.2 times increase), whereas for the larger mirror (4 mm), the increase is from 133 to 333 (2.50 times). Although a smaller Q-value increase is noted for larger mirrors under reduced pressure, they can start with an initial Q-factor approximately four times higher than smaller mirrors, which translates into changes in the natural resonance frequency and the moment of inertia of the MEMS mirror, as shown in Figure 3-18. The smaller mirror (1 mm) exhibits a natural frequency close to 1.5 kHz, while the larger one has a frequency of 270 Hz.

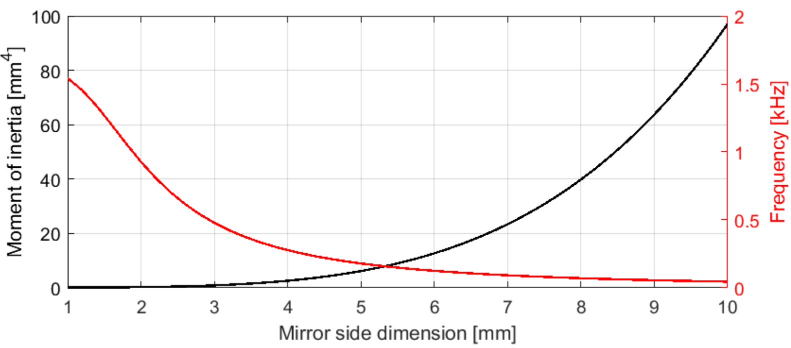

Figure 3-18 – Effect of the mirror side dimensions increase on the moment of inertia and natural frequency of the device.

Thus, while increasing the mirror size can lead to a higher moment of inertia for the same spring constant and higher quality factors, it also results in a significant decrease in the natural frequency. This decrease can potentially fail to meet the system requirements, highlighting the need for careful consideration of mirror area in relation to the desired operational parameters.

3.3 Device dynamic performance evaluation

In this section, the non-linear dynamic performance of the MEMS mirror will be simulated considering the analytical results and restrictions. These experimental simulations aim to achieve the design that presents the best theoretical behaviour for the MEMS actuator.

3.3.1 MEMS mirror dynamic model

When dealing with a dynamic MEMS mirror behaviour, the equation of motion can be rewritten assuming the notation $\dot{\theta} = f(\theta, V)$ [2]:

$$\begin{cases} \dot{\theta} = \omega \\ \dot{\omega} = \frac{1}{J} * (T_{elect} - B\omega - k\theta) \end{cases} \quad (3\text{-}38)$$

where θ is the mirror angular deflection, $\dot{\theta}$ and ω are the angular velocity, and $\dot{\omega}$ is the angular acceleration. Since it is very complex to solve this equation analytically, it can be represented by the block diagram model of Figure 3-19 via the Simulink™ tool. The Simulink model-based design is used to analyse multi-domain dynamic systems. The model of Figure 3-19 has as the actuation voltage input an initial angular perturbation, the reflective plate, and the asymmetric electrodes parameters, such as distance to the rotation axis, overlapping area, number of electrodes, and gap between the electrodes. As for the outputs, the subsystem returns the angular velocity of the movable mirror and its angular displacement, θ.

The damping coefficient model is a MATLAB function invoked by the block diagram, as well as the Electrostatic Torque. The damping function is the analytical calculation that computes the squeeze film and drag-damping effect generated by the electrodes and mirror plate when the movable plate has a certain velocity. The electrostatic torque function computes the actuation force generated on the mirror. These analytical functions are recalculated continuously during the Simulink simulation process since both the damping torque as well as the electrostatic torque vary with the motion of the device, i.e., they depend on the mirror angle, as studied in the previous analytic evaluations.

With this analytical model, it was possible to analyse the natural oscillatory behaviour for an initial perturbation and the time required to return to the rest position. Moreover, it was possible to compute the dynamic performance when an actuation voltage is applied in the electrodes for ambient pressure or vacuum conditions and the corresponding maximum deflection angle.

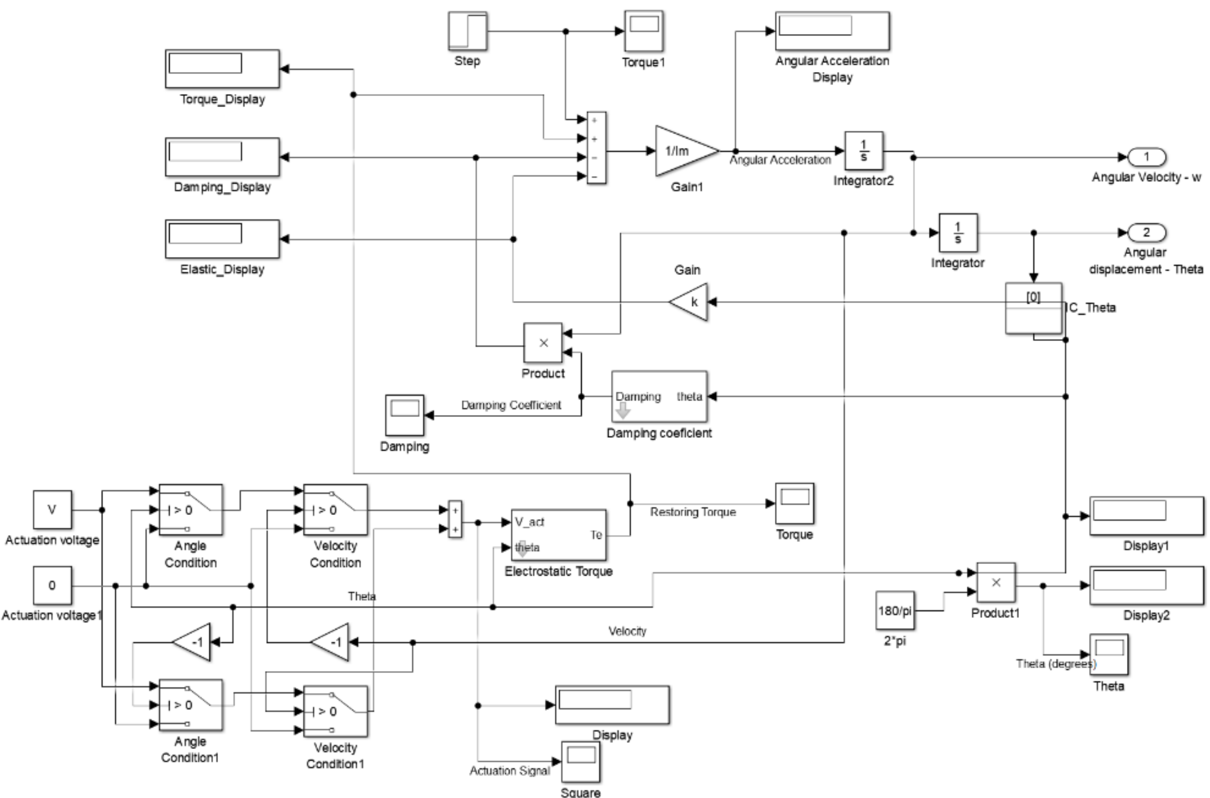

Figure 3-19 – Symulink MEMS mirror model.

3.3.2 Perturbation response

Figure 3-20 presents the natural response of the mirror for an initial angular perturbation during 1 ms, with 0.5 μN.m and 1.0 μN.m. Here, the voltage applied to the movable structure was set to 0 V to analyse the response when no external forces were applied. Two different values of perturbations were simulated, and as expected, with larger initial perturbations, the mirror deflection peak increased. Besides, it is possible to see that the mirror, independently of the perturbation, started moving with the same frequency, which corresponds to the structure's natural resonant frequency, f_0.

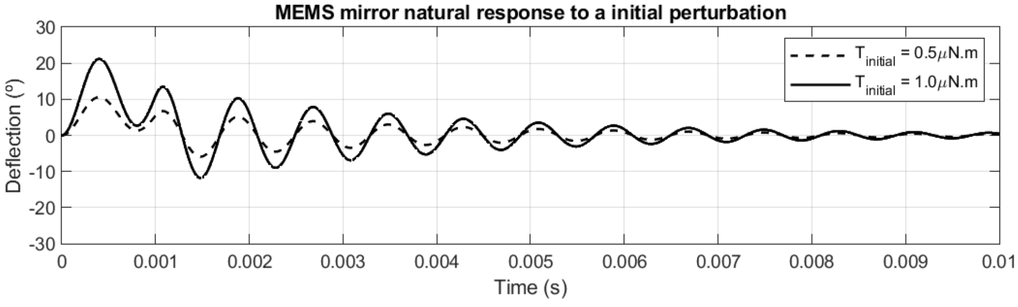

Figure 3-20 – Dynamic theoretical behaviour for an initial perturbation.

3.3.3 Resonant mode Field of View (FoV)

To calculate the maximum deflection angle of the MEMS mirror dynamically, the dynamic model of the MEMS mirror was modified to include a non-zero actuation voltage signal. This voltage generates an electrostatic torque on the movable structure each time it returns to its rest position, thereby simulating future experimental conditions, i.e., the square-wave actuation voltage. Following the same analysis performed in 3.2.1, different geometric configurations and actuation conditions were subjected to dynamic simulations. Figure 3-21 presents the mirror resonant response for different actuation voltages, respectively 30 V and 150 V, for the same geometry parameters. As can be seen, the maximum deflection angle of the mirror increases with the applied voltage, as expected.

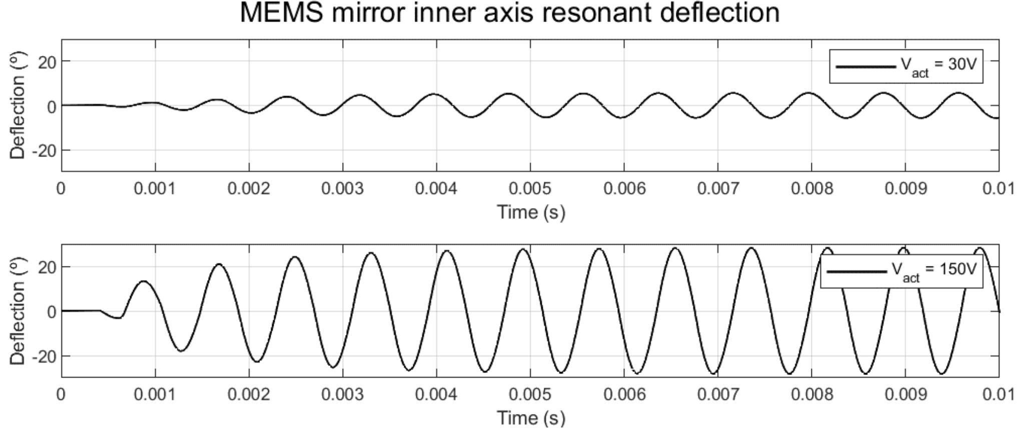

Figure 3-21 – Dynamic theoretical behaviour for different actuation voltages.

The first plot of Figure 3-22 presents the maximum deflection angle absolute value from a range of 10 V to 200 V applied to the device for different electrodes gaps at 500 μm from the torsional axis. The second one depicts the same relation however, here, the differing parameter is the distance to the torsional axis, computed for a range from 250 μm to 1000 μm, for an electrode gap of 3 μm. And the last one for a geometry with an electrodes gap of 3 μm at a distance of 500 μm for different damping conditions. As can be depicted from the different plots, **the electrodes gap does not significantly influence the maximum angle when operated at resonant mode**. Given that the inner axis is desired to be operated at resonance, this proves that the inner axis' asymmetric electrodes gap has some tolerance (regarding variations in the micromachining process, such as over-etch) while ensuring a minimal impact in the FoV range. Moreover, it is possible to conclude that for resonant mode, enlarging the distance of the electrodes from the torsional axis results in larger mechanical deflection angles and, consequently, larger FoV. And as expected, the decrease of the damping coefficient results in a substantial increase in the deflection angle, for example, a decrease of 50% of the damping coefficient regarding the one in atmospheric pressure conditions, b_0, resulting in an increase of 37% of the angular deflection.

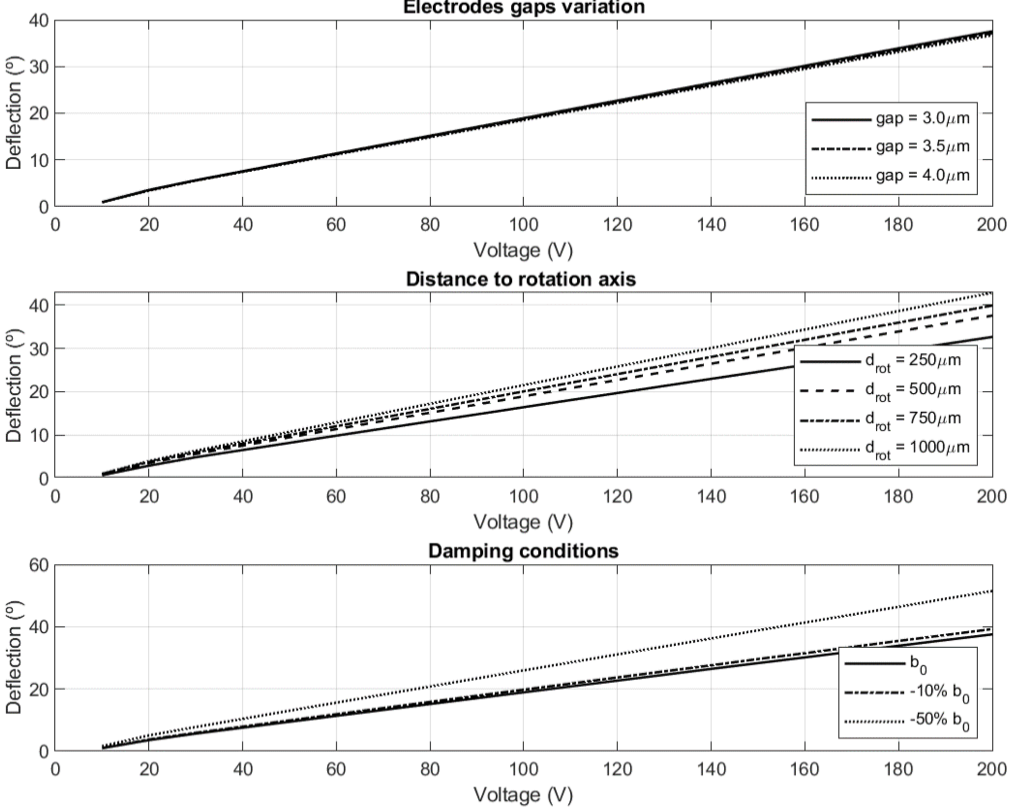

Figure 3-22 – Maximum mirror deflection evolution for different applied voltages when different electrode gaps (top), distances to the torsional axis (middle) and damping conditions (bottom) are implemented.

3.4 Device FEM Evaluation

To evaluate the MEMS mirror behaviour and validate the analytical results, various FEM (Finite Element Method) simulations of the device model were carried out using the COMSOL 5.6 tool. A FEM model and its simulation aim to represent complex physical phenomena through theoretical mathematical models, describing them by equations and solving them to get real phenomena approximations. These simulations were essential to analyse if the designed structure achieved the expected results as well as to understand the limitations of the design and the materials: stress and deformations, among others. So, the modelling and simulation process involves:

- The creation of a representation (model) of the system;
- The definition of the model constraints and simulation;
- The analyses of the behaviour of the system.

The FEM simulation can be computationally heavy due to mesh sizes and the physics considered, and take a long time to reach the solution, which can turn out to be detrimental regarding time optimisation.

Thus, to overcome this problem, the FEM models used in the various simulations are simplified models of the real device (reduced complexity of the structure compared to the actual structure).

3.4.1 The Resonance Frequency – Modal Simulation

The resonance frequency indicates the frequency at which a structure will naturally oscillate. During a modal FEM simulation, the main objective is to determine the natural modes and corresponding frequencies, as well as the associated modal shapes. This information helps to understand how the mirror structure will respond to external forces or excitations. To simplify the simulations, simplified models of the inner and outer axes were created, as shown in Figure 3-23 (a) and (b). The outer model includes the inner structure, allowing the analysis of the final gimbal architecture. Additionally, parametric variables such as spring width and electrode gaps were implemented to optimize the MEMS mirror performance.

The modal analysis was conducted to compare FEM results with analytical ones and to identify any undesirable resonance modes. These modes should be minimized and designed to appear at frequencies that are not used for device actuation to avoid being driven during operation, which could distort the laser beam.

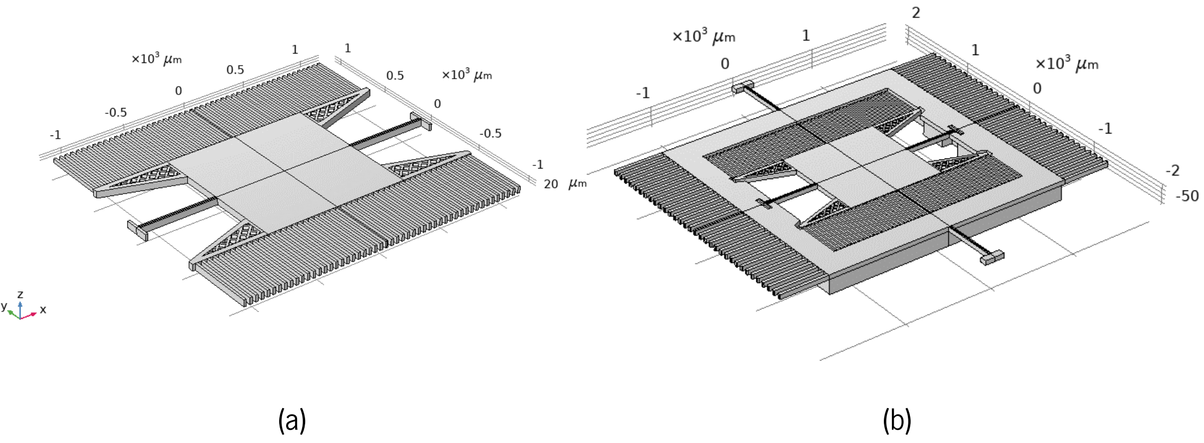

(a) (b)

Figure 3-23 – Simplified 3D model for the modal FEM analysis of the (a) inner axis, and (b) outer axis.

In Figure 3-24, the results of the resonance FEM simulations of the inner axis structure are presented. The first fundamental mode, depicted in Figure 3-24.a, is the target operation, i.e., the desirable resonance motion where the reflective surface moves around the torsional springs' axis. The following ones, Figure 3-24.b-f, are the other resonance motions, which appear at a higher frequency, far away from the operating one. Table 3-3 details the frequency values of the first six modes for the inner structure for different spring widths, as well as the expected analytical torsional resonance frequency previously computed.

(a) (b)

(c) (d)

(e) (f)

Figure 3-24 – MEMS Mirror's inner axis resonance modes.

Table 3-3 – Inner axis resonance modes for different spring' widths extracted from the modal FEM analysis.

	Springs Width	8 µm	9 µm	10 µm	11 µm	12 µm	Units
Analytical 1st mode		1083.3	1283.5	1492.6	1709.5	1933.6	Hz
FEM	1st mode	1055	1244	1444	1650	1870	Hz
	2nd mode	2729	3245	3789	4356	4947	
	3rd mode	3871	4505	5173	5871	6598	
	4th mode	12087	12489	12874	13210	13536	
	5th mode	20823	21600	22330	22984	23607	
	6th mode	49132	49153	49168	49188	49212	
Torsional moment				8.70E-14			N.m

The previous FEM analysis was also performed for the two-dimensional mirror, with the simplified model of Figure 3-23.b, and the six first resonant modes are depicted in Figure 3-25. Here, the first one, at a lower frequency, is the desired outer torsional motion, as expected, and the second one is the inner desired torsional motion. The third and fourth modes are in-plane motions related to the outer springs

since this has a lower elastic coefficient than the inner ones and the last two to the inner axis. Table 3-4 details the frequency values of the first six modes for the gimbal structure considering different spring widths, as well as the expected analytical torsional resonance frequency previously computed.

(a) (b)

(c) (d)

(e) (f)

Figure 3-25 – MEMS Mirror's outer axis resonance modes.

Table 3-4 – Gimbal structure resonance modes for different outer axis spring' width extracted from the modal FEM analysis.

Springs Width		9 µm	10 µm	11 µm	14 µm	15 µm	Units
Analytical 1st mode		271.8	316.2	362.0	508.3	559.4	Hz
FEM	1st mode	262.51	305.21	349.24	489.97	538.09	Hz
	2nd mode	1274.42	1443.62	1443.67	1443.78	1443.81	
	3rd mode	1443.55	1490.95	1718.05	2458.21	2722.86	
	4th mode	1618.37	1879.44	2151.98	3026.78	3330.96	
	5th mode	3785.25	3785.31	3785.35	3785.45	3785.48	
	6th mode	5310.00	5315.27	5322.19	5359.59	5381.95	
Torsional moment				1.96e-12			N.m

As expected, and according to the analytical models, larger the springs' width correlates with higher natural frequencies; however, the angular deflection will present a decrease. The slight difference between the first mode, calculated analytically and simulated by FEM, can be derived from the stiffness equation error of up to 4% error as detailed in [140], the mesh defined in the simulation and the torsional moment of the MEMS structure (simplified in the FEM analysis). Neither of the models presents a high percentage error, so this can be neglected.

3.4.2 Elasticity coefficient – Static Structural Simulation

A set of static structural simulations was carried to evaluate the torsional elasticity coefficient of the dimensioned springs. In this model, the conditions implemented specified input torques applied to the mirror surface and the fixed supports on the anchors of the springs. So, with a known torque, T, and moment of inertia, J, it was possible to simulate the induced body angle, θ. Thus, through equation (3-19), it is also possible to obtain the torsional elasticity constant of each spring. This analysis was also performed with the one-dimensional and the two-dimensional simplified 3D models. Table 3-5 displays the analytical and FEM torsional elasticity constant of the inner and outer axis springs.

Table 3-5 – FEM analysis of the torsional elasticity of different spring and mirror masses geometries.

FEM Model	Inner axis structure		Outer axis structure	
	Spring A	Spring B	Spring A	Spring B
Spring width	9 µm	10 µm	10 µm	15um
$k_{Analytical}$ [µN.m/rad]	5.3363	7.1146	7.7301	24.212
k_{FEM} [µN.m/rad]	5.3594	7.2404	7.020	21.890
$\%\ Error$	0.4329%	1.7682%	9.1862%	9.5903%

From the extracted data, it was possible to conclude that all the springs present an elasticity coefficient close to the theoretical value. Furthermore, besides the maximum deflection angle for a given torque, it is possible to simulate in this analysis if the mechanical stress of the structure suffers due to the induced deformation. When a force is applied to an object, the object will either compress or stretch as a response to that force. In this case, when a torque is applied, the object will twist around the torsional axis. The torque applied to a unit is called stress. The deformation of an object typically presents three distinct stages: the elastic deformation, plastic deformation, and rupture. The elastic deformation is the deflection that disappears upon removal of the external forces. Plastic deformation is a permanent deformation or change in the shape of a solid body without fracture under the action of a sustained force (irreversible).

Typically, the point of non-return of silicon deformation exists when the induced stress is higher than 1 GPa [154]. For this application, it is important to design a mirror working only in the elastic region.

Figure 3-26 and Figure 3-27 present images obtained through structural FEM simulation of the mechanical deflection and resultant stress intensity of the inner and outer structure. In structural terms, the points where the stress intensity is higher are the anchor points of the springs, which, in turn, are the most critical points of the structure.

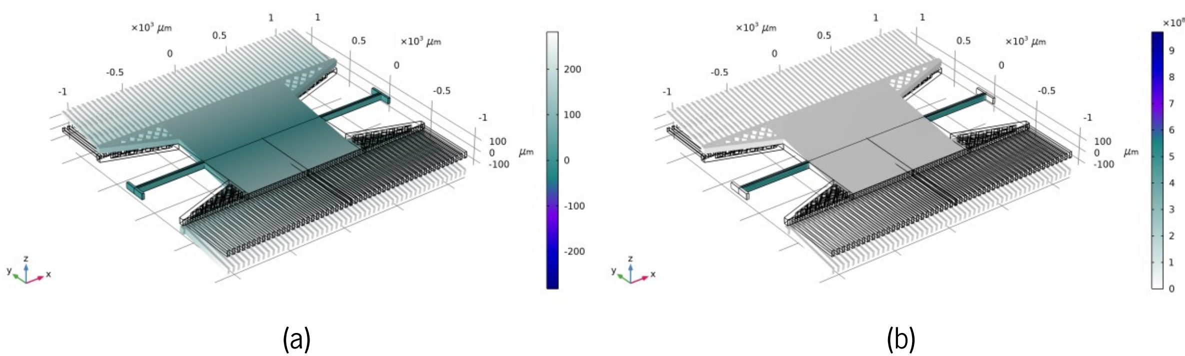

(a) (b)

Figure 3-26 – Inner axis structural FEM simulation 3D results of the mechanical deflection [μm] (a) and resultant stress [N/m²] (b).

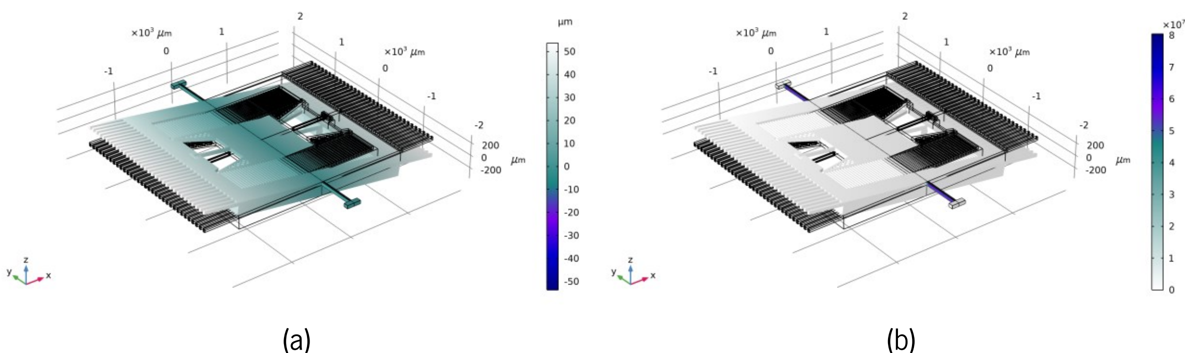

(a) (b)

Figure 3-27 – Outer axis structural FEM simulation 3D results of the mechanical deflection [μm] (a) and resultant stress [N/m²] (b).

As can be observed, in the maximum target angular deflection for the inner and outer axes, the stress induced in the torsional springs is within the safe range of elastic deformation, ensuring the robustness and longevity of the device when continuously operated.

3.4.3 Electrostatic field of asymmetric electrodes – Electrostatic Simulation

An analysis of the distribution of the electric field of the actuation electrodes, as well as the electrostatic torque generated, was also performed. This analysis aimed to gain a deeper understanding of the impact of the fringe field capacitances inherent to this type of actuator. The significance of the fringe fields cannot be overstated, as they are integral to the functioning of these asymmetrical electrostatic actuators and serve as the driving force behind the initial mirror motion. In theory, if a voltage V is applied across the

capacitor plates, a charge of $+Q$ and another of $-Q$ are accumulated between the electrodes. The surface charge density on the plates is $\pm\sigma$ where $\sigma = Q/A$. A two-dimensional simplified model was developed to analyse the electrostatic performance of the actuation electrodes. The model consisted of a cross-section of three sets of fingers, with four thicker fixed electrodes, 50 µm-thick, and three thinner movable ones, 20 µm-thick, separated by a 3 µm-wide gap. The movable electrodes were subject to an angular displacement. Figure 3-28 illustrates the electrical potential surface, with an actuation voltage of 25 V, for three different angular positions of the asymmetric electrodes: (a) at rest, (b) at a midpoint, and (c) in an equilibrium or balanced state, in which the movable and fixed electrodes are aligned at the middle.

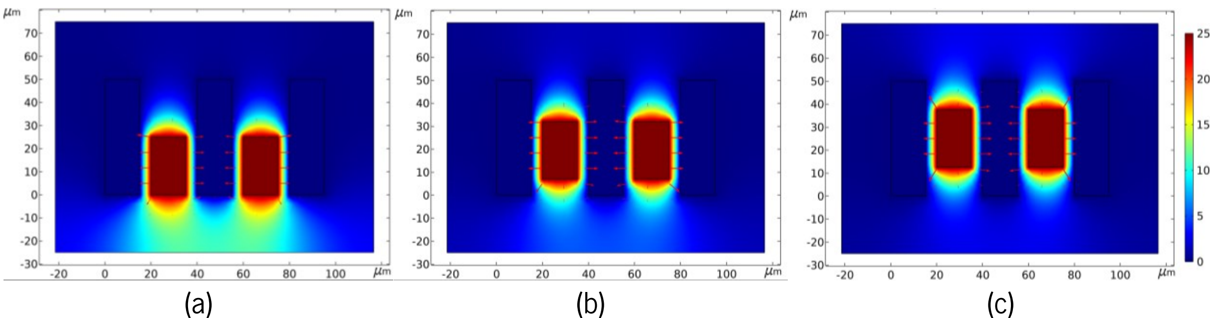

Figure 3-28 – Asymmetric electrodes' electrical potential [V] in the rest (a), middle (b) and in the aligned positions (c).

Figure 3-29 and Figure 3-30 depict the resultant electric field (x and y components, respectively) for the aforementioned angular positions. The x-component of the electric fields is responsible for generating in-plane forces within the actuators.

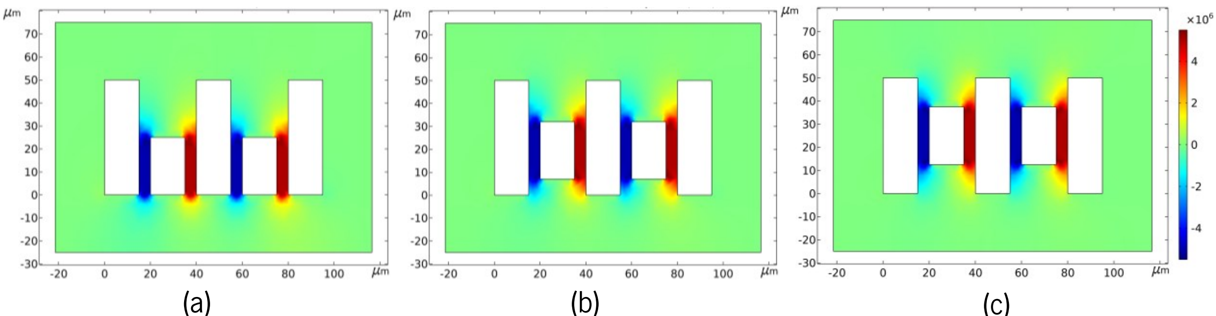

Figure 3-29 – Asymmetric electrodes x-electric field [V/m], in the rest (a), middle (b) and in the aligned positions (c).

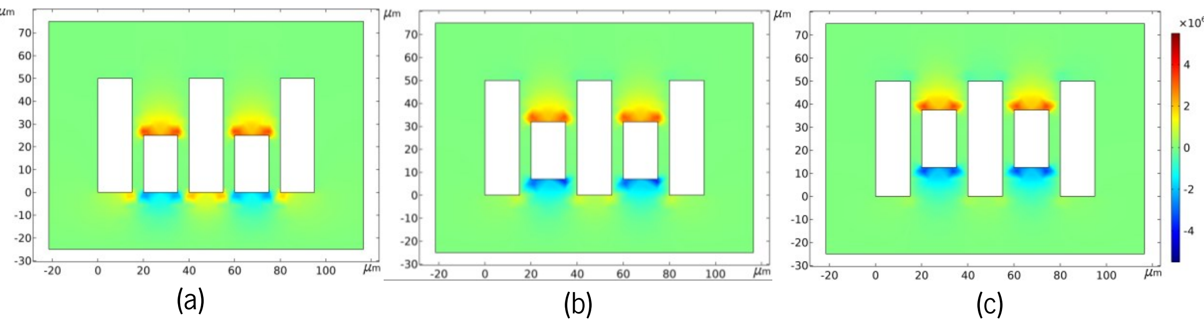

Figure 3-30 – Asymmetric electrodes y-electric field [V/m], in the rest (a), middle (b) and in the aligned positions (c).

As can be observed, the field is symmetrical in each movable electrode in this component, which is desirable since in-plane forces must be null. The symmetry is a result of the equal initial gap, d_0, which would not be the case if the device exhibited a slight variation in the left and right gap. On the other hand, the out-of-plane forces and resulting motion are generated from the y-component field. The surface plots show that for the rest positions, where the bottom edge of the electrodes is aligned, the electrical fields are misaligned, and an electrostatic torque is generated, pushing the thinner electrodes upwards.

In addition to the 2D model, a 3D model of the actuation electrodes was also developed so to evaluate to account for the fact that the overlapped area is dependent on the mirror angle, the distance between the electrodes and the rotation axis, and the length of the electrodes, as seen in the geometries presented in Figure 3-31. Furthermore, electrodes with both symmetric and asymmetric geometries were analysed to assess the difference in electrostatic torque generated by each.

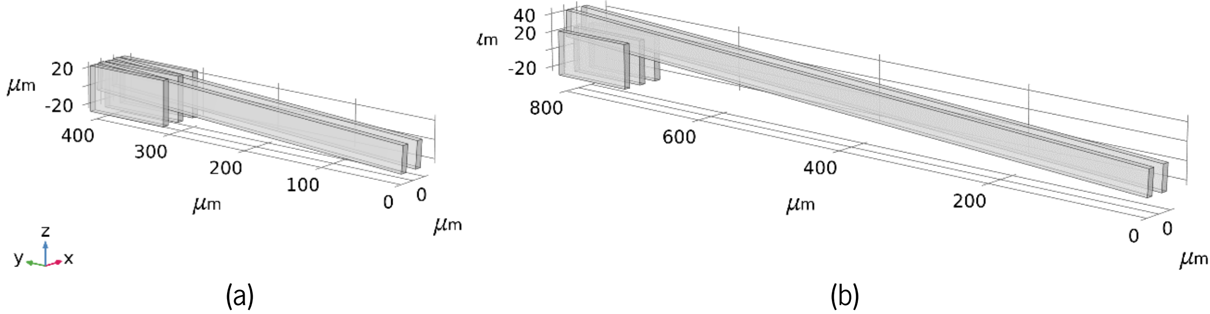

Figure 3-31 – Asymmetric electrostatic actuators FEM simplified model with a short distance to the rotation axis and (b) longer.

Different geometry configurations and actuation conditions were implemented, as performed in the analytical and dynamic analysis, varying the distance to the torsional axis and the electrode gaps. The torque generated between the two sets of electrodes was computed by geometrically inducing an angle on the movable one, ranging from -5° to 5°. Figure 3-32.a displays the computed torque, using the symmetric geometry, for different electrode-to-torsional-axis distances from 100 µm to 1000 µm, with an electrode gap of 4 µm and 100 V applied. Following the same behaviour of the analytical results, the electrostatic torque is null at the rest position, as the electrodes are perfectly aligned. Moreover, larger distances from the rotation axis correlate with higher electrostatic torques but yield a narrower angular range. Furthermore, it was also simulated with different electrode gaps with a fixed electrode-to-torsional-axis distance, as presented in Figure 3-32.b, and again, the results are aligned with the analytical ones, depicting a slight decrease in the maximum torque generated with the increase of the gap size.

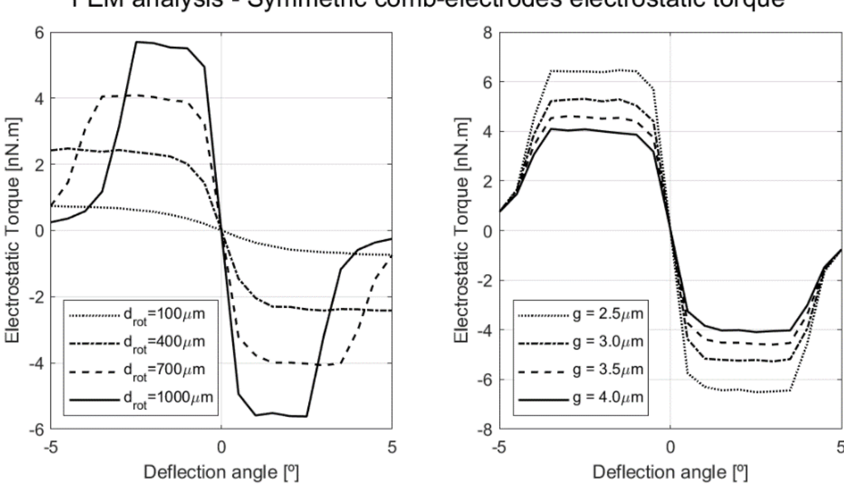

Figure 3-32 – FEM results of the symmetric electrode geometry for different d_{rot} (left) and electrode's gaps (right) values.

The same FEM simulations were implemented using now an asymmetric geometry. In contrast, the asymmetric geometry exhibits a non-null torque at the rest position, as expected, demonstrating that asymmetry is necessary to induce the initial torque. Figure 3-33.a shows the asymmetric model result for different electrode-to-torsional-axis distances from 100 μm to 1000 μm, with an electrodes' gap of 4 μm and 100 V applied, and Figure 3-33.b for a gap size of 4 μm with at a fixed distance. From these results, it is possible to see that in terms of maximum torque and angular range, the asymmetric geometric presents the same assumptions: the larger the distance, the larger the torque and narrow the angular range and the larger the gap size, the lower the maximum torque but with a constant angular range.

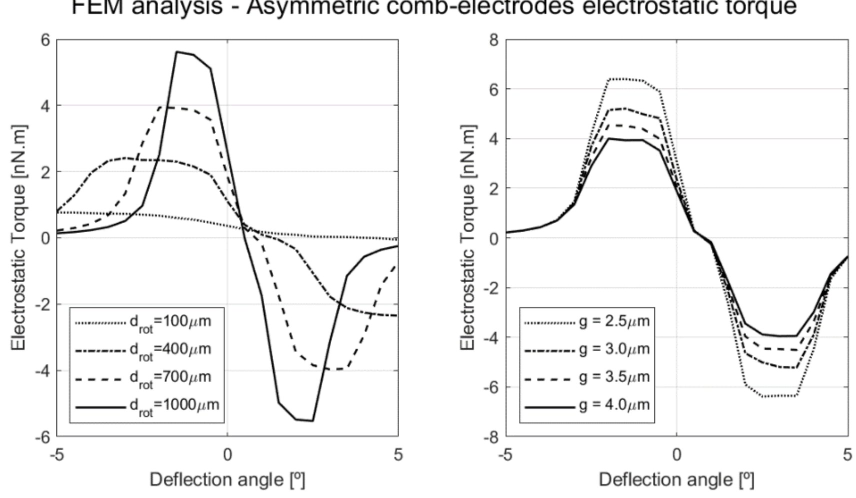

Figure 3-33 – FEM results of the asymmetric electrodes geometry for different d_{rot} (left) and electrode's gaps (right) values.

So, if it is assumed the same electrodes geometry, i.e., same electrode length, gap size, electrode-to-torsional axis distance, for symmetric and asymmetric geometries, as depicted in Figure 3-34, the peak torque achieved is approximately the same in both.

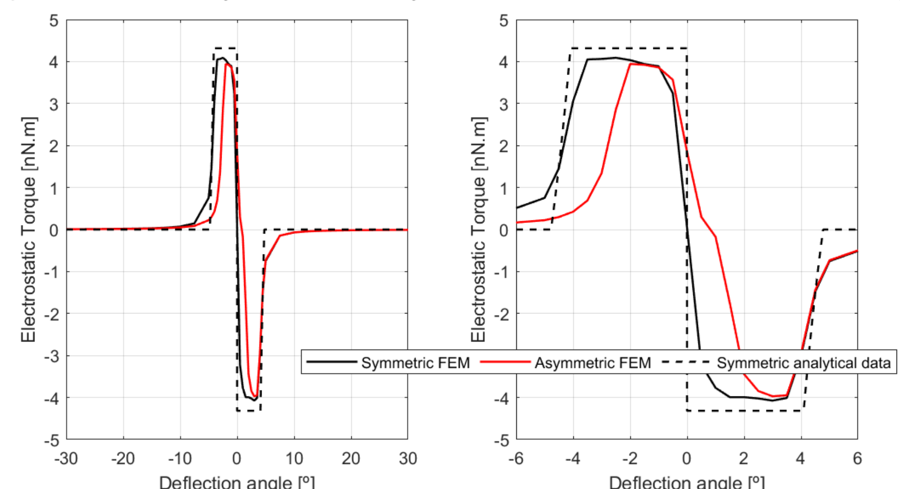

Figure 3-34 – Comparison between symmetric and asymmetric FEM results and the analytical model.

3.4.4 Out-plane natural deflection – Structural Simulation

Besides the natural frequency response and elastic coefficient, a static structural FEM model was also developed to assess the inherent deformation of the device, accounting for gravitational acceleration (9.8 m/s²). This simulation aims to evaluate the structural integrity of the fabricated device following the micromachining process and during handling procedures. Figure 3-35 illustrates the three-dimensional plot depicting the results of the structural analysis for the two-dimensional architecture. Notably, the structure exhibits a maximum deformation of merely 40 nm within the inner axis. This outcome serves as compelling evidence of the device's robustness.

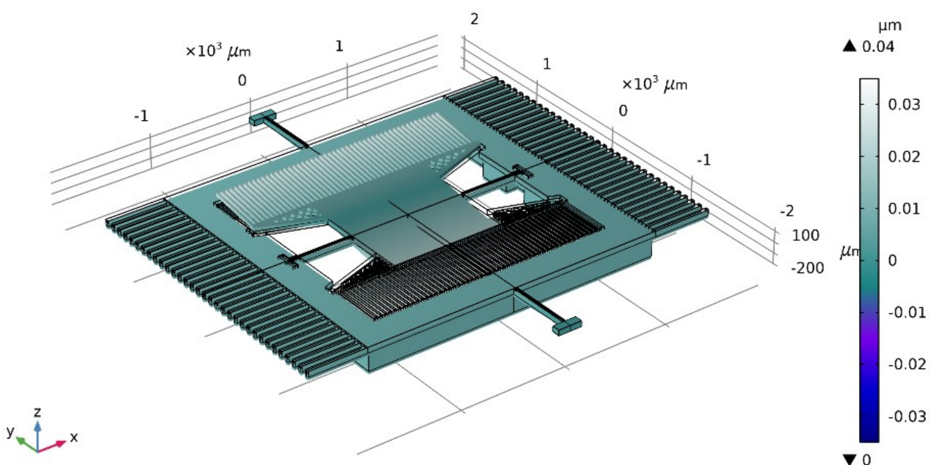

Figure 3-35 – Three-dimensional FEM results for an external gravitational acceleration in the zz direction (9.8 m/s²).

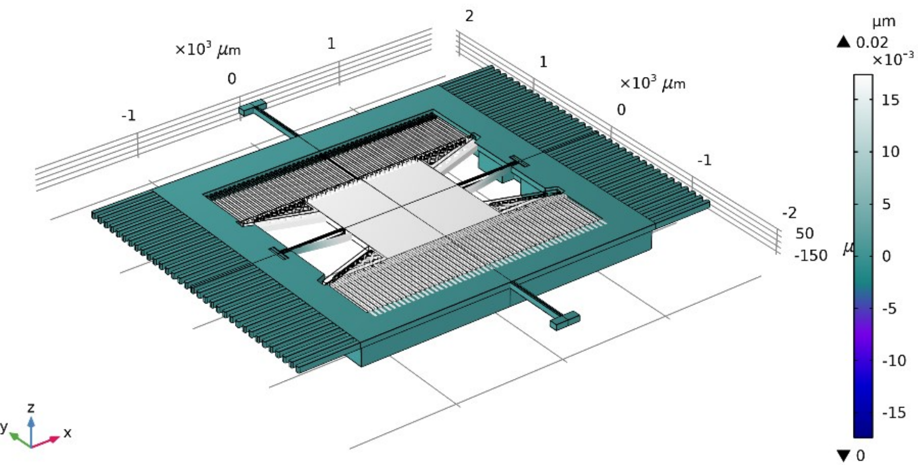

Figure 3-36 – Three-dimensional FEM results for an external gravitational acceleration in the yy direction (9.8 m/s²).

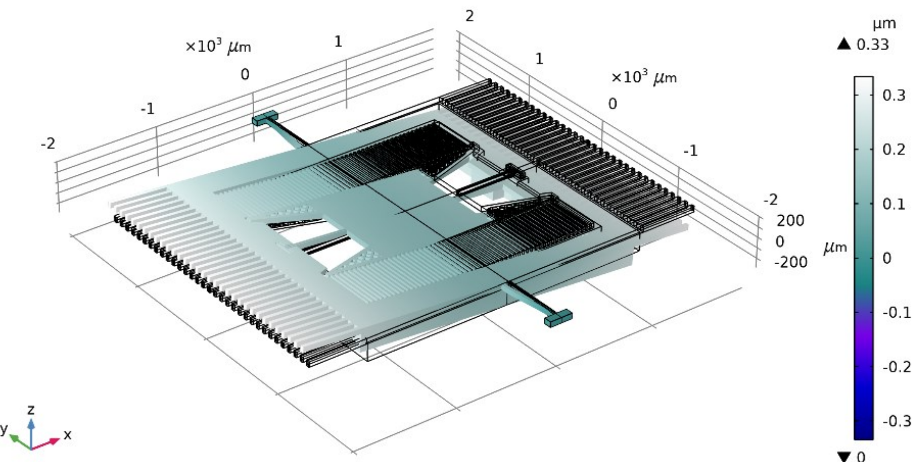

Figure 3-37 – Three-dimensional FEM results for an external gravitational acceleration in the xx direction (9.8 m/s²).

3.5 Designed MEMS Structures

In the previous section, the analytical, dynamic and FEM analysis and model of the MEMS dynamics were described. In this section, the MEMS structures designed will be presented considering the results obtained in the various evaluations carried out using the models. Two MEMS mirror devices were designed, one with two torsional axes, i.e. a 2D MEMS mirror, using a gimbal as a movement concept, and a second for validation of the inner axis dynamic design and micromachining process, with only one torsional axis. Figure 3-38 presents the 3D model developed using a CAD software.

As previously mentioned, the MEMS structures developed in this thesis were designed to be fabricated in an SOI Wafer with a thickness of the active layer of 50 µm, the buried oxide layer of 2 µm and the handle layer of 625 µm (Table 3-1). The mirror presents a reflective area with 1.1 mm per 1.1 mm in the centre

of the die, which is suspended by two sets of torsional springs, one for the inner axis (horizontal deflection) and another for the outer one (vertical deflection).

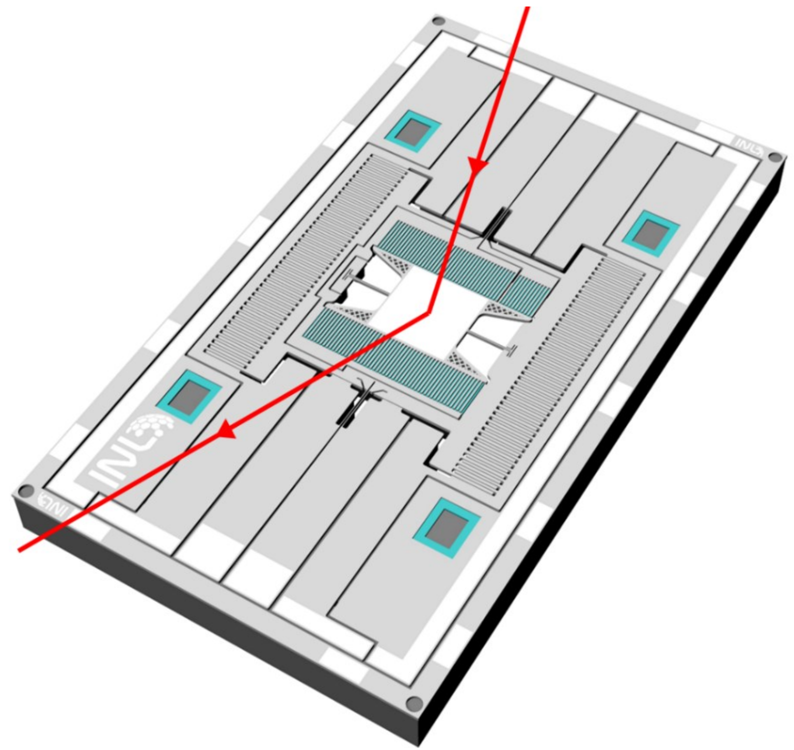

Figure 3-38 – 3D model of the MEMS mirror designed.

The top and bottom views of the two-dimensional MEMS mirror are represented in Figure 3-39. Here, the micromachining process imposes certain restrictions on the design of the MEMS mirror masks. The main limitations are the minimum possible dimension of the structures, the space between the silicon structures, which in the INL process is 2.2 μm in the active layer for symmetric electrodes structures and 30 μm in the handle layer, and the multilevel topography for the asymmetric electrodes.

The inner structure presents a set of asymmetric electrodes for actuation and another for sensing the mirror angle. The area of each capacitor (array of comb-like beams) is defined by the product of the beams' height, which corresponds to the thinner thickness achieved in the device layer of the SOI wafer and the overlapping length. Each inner axis electrode pair consist of a fixed and a movable comb actuator, and an electrostatic torque is generated when a voltage is applied across the comb electrodes, thus rotating the mirror around the inner springs' axis, as displayed in the 3D model of Figure 3-40.a. The electrode gaps depend directly on the micromachining process limitations, namely on the minimum feature size and the over-etch in the active layer, as well as on the multilevel patterning of the asymmetric electrodes. Within the Microfabrication and Exploratory Nanotechnology (MeN) group at INL, a novel fabrication process, developed in this thesis, using a single grayscale lithography for the inner electrode's

patterning was established and optimized [116], and the inner axis electrodes' gap was defined with 3 µm to increase the process yield, the robustness of the actuation electrodes, and to prevent pull-in between the movable and fixed ones.

Figure 3-39 – Schematic of the 2D MEMS mirror.

The implementation of a vertical comb-drive electrostatic actuator in the same initial silicon layer is a key feature of the inner axis actuation since it enables the natural operation of the device in resonant mode, eliminating the need for external perturbation. By integrating the actuator in this manner, the system is inherently predisposed to resonate, enhancing its efficiency and effectiveness in applications where such dynamic behaviour is advantageous.

The outer structure presents symmetric comb-electrodes for sensing and staggered electrodes for actuation. Staggered comb-drive electrodes were implemented using the handle layer as an active part of the MEMS device. In these actuators, when a DC voltage is applied between both electrodes, a constant

electrostatic torque is generated, twisting the mirror to a fixed angle around the outer springs' axis, Figure 3-40.b. The higher the DC actuation voltage, the larger the torque applied until the equilibrium between the torque produced and spring restoring elastic torque. The maximum angle attainable in static mode is geometrically defined.

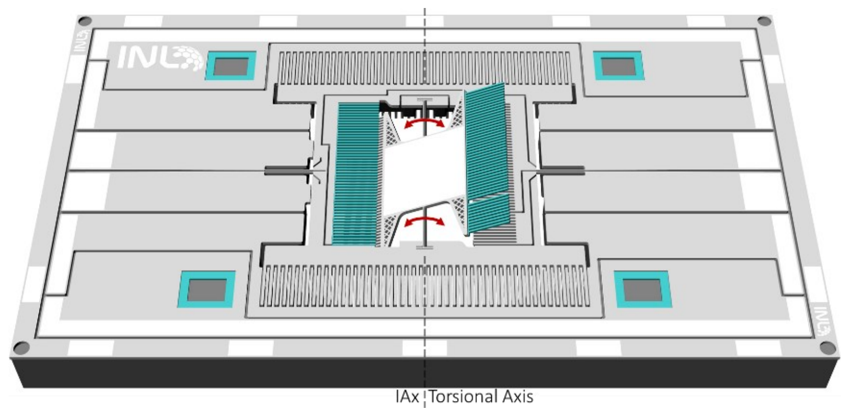

(a) Inner axis deflection

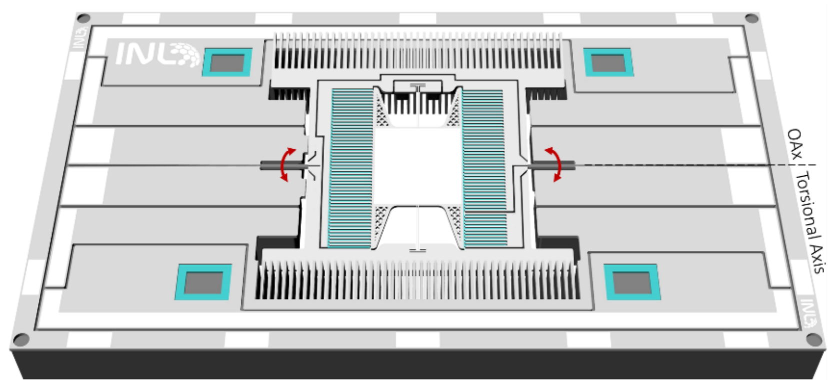

(b) Outer axis deflection

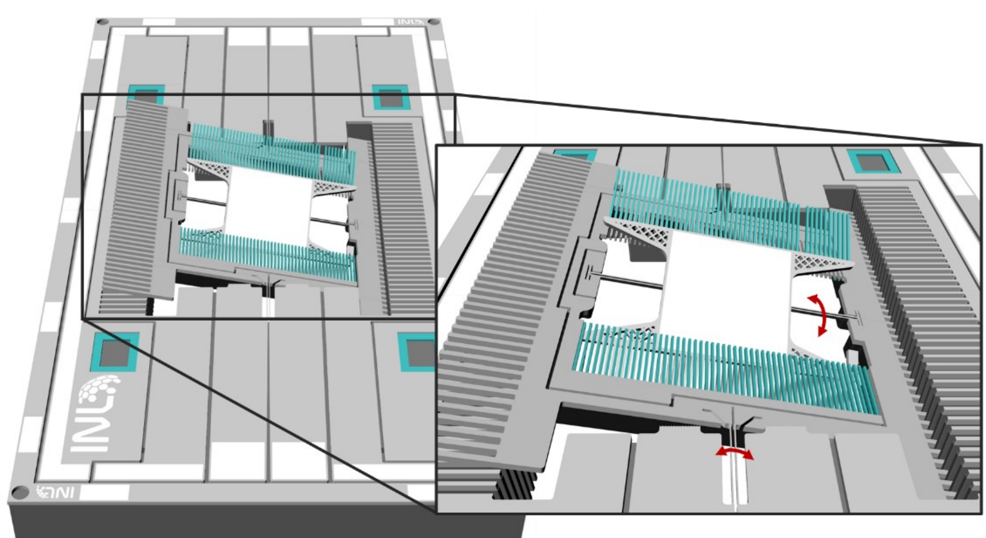

(c) Inner and outer axis simultaneous deflection.

Figure 3-40 – Fast axis and slow axis movement design.

The inner structure, such as the mirror surface and electrodes, is connected to a handle-thinned frame, achieving a mechanically coupled microstructures while remaining electrically decoupled. This frame is suspended by the outer axis springs, which were designed with a double spring layout, enabling the routing of more than one potential for the inner axis. This allows the system to have both sensing and actuation of the inner axis in a single layer of electrical routing connections. The outer axis actuation presents windows to the handle layer, enabling access to the back-side electrodes for metal deposition or direct bonding and creating the necessary electrical connection to actuate the slow axis.

3.5.1 Electrical routing

The MEMS mirror electrical routing is detailed in Figure 3-41, with the different potentials represented in different colours.

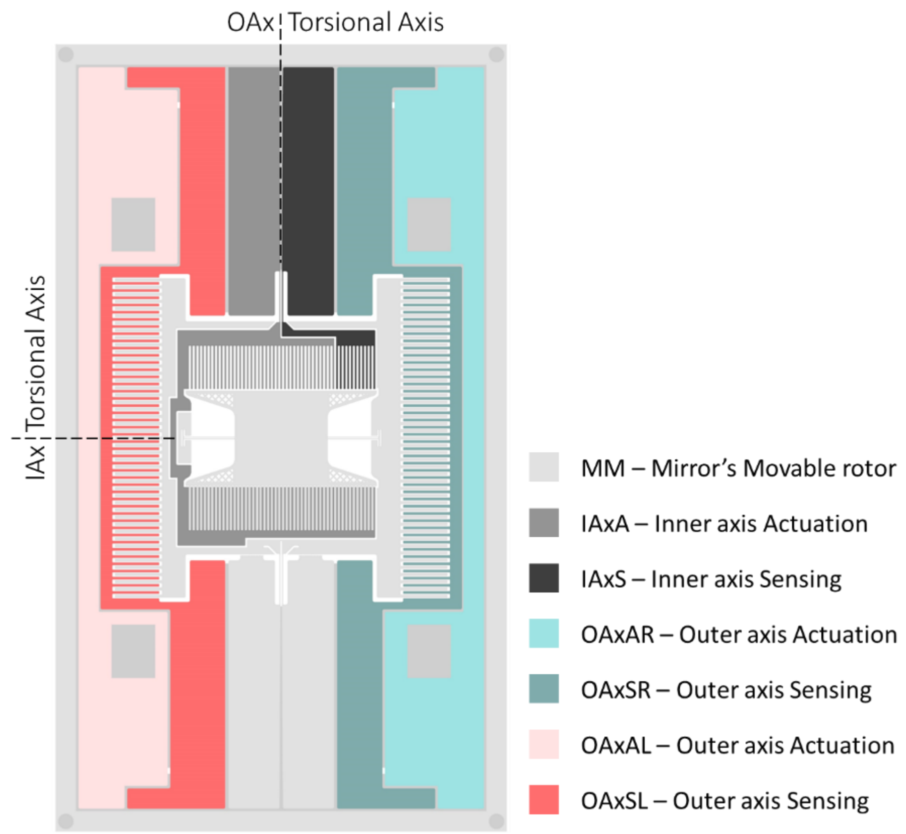

Figure 3-41 – 2D Mirror electrical routing.

The ground potential is applied at MM pads connected to the mirror's rotor in both the inner and outer axis, represented in light grey. The IAxA contact pads are connected to the actuation electrodes through one of the outer axis torsional springs (dark grey), while IaxS pads are connected to the sensing electrodes (black) through another (to sense the capacitance changes with the mirror's angle). The handle layer inner frame will mechanically support all these electric connections, ensuring their electrical separation

and giving the inner axis the necessary stiffness. The electrodes for the slow axis are divided into four sets: two for the actuation, OaxAR (light blue) and OaxAL (light red), and another two for the angular sensing, OaxSR (dark blue) and OaxSL (dark red), to each side, right and left, respectively.

This design, where the torsional springs are used not only as a mechanical anchor but also as the electrical route for different potentials to the inner movable structure, enables the possibility of having all the electrical connections using only a single SOI wafer without using a complex bonding process or TSV (Through Silicon Vias) needed in single spring standard designs.

The pads are the contact channels of the mirror with the outside. These were designed to be as large as possible without compromising the total area of the device to make the entire wire bonding process more accessible and more efficient.

3.5.2 2D MEMS Mirror variation

Different variations of the MEMS mirror layout were implemented into two designs, where the outer axis springs' geometry and the number of electrostatic electrodes were changed. Two designs with 200 electrostatic electrodes were implemented with different springs, one with a larger width of 20 μm and the other with 10 μm-width. This change results in the mirrors having different resonance frequency and maximum deflection angles.

Table 3-6 shows the parameters of the different 2D MEMS mirror layouts, such as the number of electrodes and respective features, natural resonance frequency, and spring features.

To summarize, the key features of the designed 2D MEMS mirror are the implementation of:

- Double spring to enable different electrical paths for the gimbal's inner axis actuation and mirror positioning sense;
- A thinned frame on the handle mechanically attaches all the different FS features, enabling electrical insulation between them;
- Asymmetric vertical electrodes on the inner axis to enable a resonant mode of operation for the horizontal projection;
- Fixed actuation electrodes patterned on the handle layer to enable quasi-static actuation for the vertical projection;
- Top side access to handle electrodes for metal deposition or direct bonding creating the necessary electrical connection to actuate the slow axis.

A 1D MEMS mirror was also designed as a support device in the development of the final device. This presents the same specifications as those implemented in the inner axis of the 2D mirror, enabling a broader and more comprehensive characterization of this axis without influence from the structure of the

outer axis. This device was also used to validate the micromachining process and the nanoimprint replication process.

Table 3-6 – Parameters of the layouts developed.

	Parameters		Design A	Design B
Inner Axis	Mirror area (l × w)		1100 µm × 1100 µm	
	Double Springs length (l)		600 µm	
	Double Springs width (w)		10 µm	
	Natural resonance frequency, $f_{n\,IAx}$		1443 Hz	
	Number of actuation electrodes		90	
	Number of sensing electrodes		10	
	Electrodes dimensions (l × w × h)	Fixed	500 µm × 20 µm × 50 µm	
		Movable	500 µm × 20 µm × 30 µm	
	Electrodes gaps size		3 µm	
Outer Axis	Double Springs length (l)		600 µm	
	Double Springs width (w)		10 µm	15 µm
	Natural resonance frequency, $f_{n\,OAx}$		305 Hz	538 Hz
	Number of actuation electrodes		45	45
	Electrodes dimensions (l × w × h)	Fixed	550 µm × 36 µm × 400 µm	
		Movable	550 µm × 35 µm × 50 µm	
	Actuation Electrodes gaps		7 µm	
	Number of sensing electrodes		45	45
	Sensing Electrodes dimensions (l × w × h)		550 µm × 35 µm × 50 µm	
	Sensing Electrodes gap size		10 µm	

3.6 Conclusions

In this chapter, the numerical model and evaluation were presented, as well as the FEM modelling and simulation. The modelling and analysis of the dynamics of a microdevice is an important topic when designing a MEMS device. The resonant field of view of the inner axis has been analysed from a dynamic perspective using the Simulink model. The actuation electrode geometry was extensively analysed, demonstrating that the implementation of asymmetric electrodes to induce an initial out-of-plane torque

does not compromise the mirror deflection neither its operation. To increase the angle of the mirror at resonance, the quality factor must be high (which can be achieved for example by reducing the air pressure in 50%), and/or the applied voltage as well (for example, up to 150 V).

The mirror damping was also analysed and depends mainly on the reflective area size and electrode geometry. With the fluid simulation, it was possible to conclude that with the decrease of pressure conditions, the damping coefficient could be decreased and higher mirror angles achieved.

Besides the numerical evaluation using MATLAB and Simulink model, a FEM analysis was also performed using the COMSOL tool to validate the previous results. So, to facilitate the process of simulation, a set of simplified models were developed and used in the FEM simulations. The simulations focused on the structural behaviour of the device, such as frequency of resonance, deformation of the springs and their induced stress. Besides, the damping and the electrical distribution of the actuating electrodes were also simulated. With these FEM simulations, a 3D model of the device was designed.

4. Optical Elements

Diffractive optical elements are devices based on light interference and diffraction. These phenomena have been well known since the beginning of the XIX century with the establishment of the Huygens-Fresnel theory [155]. However, the DOE only started to take off with the development of modern photolithographic techniques in the 1950s [2], [156]. Since then, fabrication techniques, such as modern high-resolution lithography and integrated circuit techniques, have become affordable and able to produce devices with higher complexity and sizes smaller than or comparable in size to the wavelength of light.

DOEs are used in a wide range of applications, such as beam shaping [157], beam splitters, interferometers [158], photonic crystal fabrication [159], [160], and lenses [161], among others. More recently, spot array DOEs have gained interest for LiDAR sensors [128], [129] since this technology is moving towards the solid state.

This chapter presents the overall analysis regarding the optical components of the MEMS device, such as the Dammann diffractive optical element and the reflective coating. Here, the light theoretical foundations, namely light propagation and diffraction, are presented, as well as the foundations of Dammann gratings and the constraints that will arise from the combination of the DOE into the MEMS mirror surface. Moreover, several analytical simulations were developed to attain the splitting performance of the DOE design, and the final device layout with the DOE entailed on the MEMS mirrors is presented.

4.1 Theoretical Foundations

Light, while it can be usually represented by rays at the macro scale, it does not merely propagate in straight lines at the micro-scale, especially when encountering obstacles or apertures. Instead, it undergoes diffraction, a phenomenon where waves spread and interfere, which is directly explained by classical geometric optics. To predict these patterns, several diffraction theories and solutions to the wave equations have been established, including the Rayleigh-Sommerfeld, Fresnel, and Fraunhofer formulations, Figure 4-1. The Rayleigh-Sommerfeld theory, derived from the scalar wave equation, views every point on a wavefront as a secondary spherical wavelet source, offering a comprehensive description of light propagation, especially for near-field diffraction. On the other hand, the Fresnel approximation is apt for scenarios where the observation point is neither extremely close nor far from the diffracting aperture, capturing the essence of near-field diffraction. In contrast, the Fraunhofer approximation, ideal for far-field diffraction, simplifies the phenomenon when the observation point is significantly distant from the diffracting aperture, often describing patterns like single-slit and double-slit diffractions observed in laboratories. Together, these formulations bring tools to understand light's behaviour across various scenarios, from intricate near-field patterns to predictable far-field diffractions.

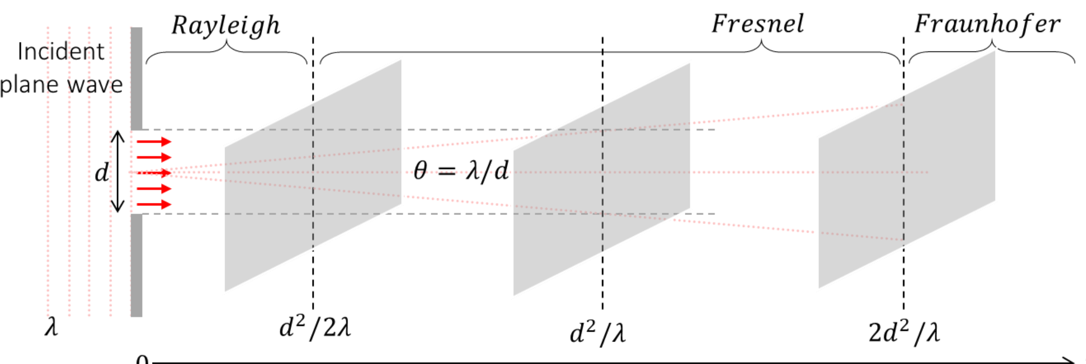

Figure 4-1 – Sketch of three different imaging regions in a lens-less imaging system as a function of the Fresnel distance [17], [162].

4.1.1 Light propagation foundations

Rayleigh-Sommerfeld propagation

The Kirchhoff theory, developed by Gustav Kirchhoff, is a mathematical approach used to describe the diffraction of waves, remarkably light and sound waves, part of the broader field of wave theory. In the context of optics, the Kirchhoff theory provides a framework for understanding how light waves interact with obstacles and apertures, leading to diffraction patterns. The theory is based on certain boundary conditions that must be imposed on both the field strength and its normal derivative. These boundary

conditions are used to solve the wave equation in the region of interest, allowing for the prediction of how waves will propagate and interfere. Mathematically, the diffraction electric field $U(P_0)$ at a point P in the observation plane is given by:

$$U(P_0) = \frac{1}{j\lambda} \iint_{\Sigma} U(P_1) \frac{\exp(jkr_{01})}{r_{01}} \cos(\theta)\, ds \tag{4-1}$$

Where $U(P_1)$ is the electric field at a point P_1 in the aperture plane, r_{01} is the distance between points P_0 and P_1, θ is the angle between P_1, k is the wave number, given by $k = 2\pi/\lambda$, and the normal to the wavefront at P_0, λ is the wavelength of the wave [17]. The Rayleigh-Sommerfeld formulation has been compared to the Kirchhoff solution and found to yield comparable results, mainly when the aperture diameter is much greater than the wavelength. It provides a more accurate mathematical description of diffraction phenomena and is widely used in practical applications.

Fresnel diffraction

The Huygens-Fresnel principle is a fundamental concept in wave optics that provides an intuitive and mathematical understanding of wave propagation, including diffraction. It is based on the idea that every point on a wavefront can be considered a secondary source of spherical wavelets spread out in all directions with a speed equal to the speed of propagation of the waves [17]. The new wavefront at a later time is the envelope of these secondary wavelets. The Huygens-Fresnel principle can be mathematically represented as,

$$U(P_0) = \frac{1}{j\lambda} \iint_{\Sigma} U(P_1) \frac{\exp(jkr_{01})}{r_{01}^2} \cos(\theta)\, ds \tag{4-2}$$

Assuming that $r_{01} \gg \lambda$, where $U(P_1)$ is the field at the source P_1, λ is the wavelength of the wave, k is the wave number, given by $k = 2\pi/\lambda$, P_0 and P_1 are the vectors from the source point to the observation point, θ is the angle between P_1 and the normal to the wavefront at P_0. The Fresnel approximation can be applied to reduce the Huggens-Fresnel principle to a more simple and usable expression for near-field diffraction. The Fresnel approximation is valid when the observation point is not too far from the source but not highly close either and can be mathematically expressed as

$$U(x,y,z) = \frac{e^{jkz}}{j\lambda z} e^{j\frac{k}{2z}(x^2+y^2)} * \iint_{-\infty}^{\infty} \left[U(\xi,\eta,0) e^{j\frac{k}{2z}(\xi^2+\eta^2)} \right] e^{-j*\frac{2\pi}{\lambda z}(x\xi+y\eta)}\, d\xi\, d\eta \tag{4-3}$$

where (x, y, z) are the coordinates of the observation point, $(\xi, \eta, 0)$ the coordinates of the source aperture. And z the distance between the source and observation planes.

Fraunhofer diffraction

The Fraunhofer approximation, also known as far-field diffraction, is a simplification of the general diffraction phenomenon that is valid when the observation screen is at a much greater distance from the source than the size of the aperture itself [17]. In the region of Fresnel diffraction, the observed field strength $U(x,y)$ can be found from the Fourier transform of the product of the aperture distribution $U(\xi,\eta)$ and a quadratic phase function $\exp[j(k/\ 2z)(\xi^2\ +\ \eta^2)]$, from equation (1-3). However, if the observation point is at large distances from the diffracting aperture, the following condition is satisfied:

$$z \gg \frac{k(\xi^2+\eta^2)\max}{2} \tag{4-4}$$

The quadratic-phase factor under the integral sign is approximately unity over the entire aperture, and the observed field strength can be found directly from a Fourier transform (FFT) of the aperture distribution itself. Thus, in the region of Fraunhofer diffraction,

$$U(x,y,z) = \frac{e^{jkz}}{j\lambda z} e^{j\frac{k}{2z}(x^2+y^2)} * \iint_{-\infty}^{\infty} U(\xi,\eta,0)\exp\left[-j*\frac{2\pi}{\lambda z}(x\xi+y\eta)\right]d\xi\, d\eta \tag{4-5}$$

4.1.2 Damman diffractive element

Dammann Diffractive Optical Elements represent a category of diffractive optical components characterized by their ability to split an incoming light beam into multiple equidistant and equally intense sub-beams arranged in a well-defined geometric pattern, i.e., Dammann DOEs are binary phase gratings that can be used to generate a 1-D or 2-D array of equal-intensity spots. These components were introduced by Fritz Dammann in the mid-20th century. Due to the convenience and simplicity of the Dammann grating (DG), it decreases the complexity of the optical system and allows beam splitting by DG at a lower cost. DGs have been applied to laser technology, laser detection, laser direct writing, 3D measurement, particle manipulation, optical fibre communication, and other fields due to their fascinating properties, such as high diffraction efficiency, small size, and lightweight.

At the heart of a Dammann DOE's functionality lies the concept of diffraction. When an incident laser beam interacts with a Dammann DOE, it undergoes diffraction, a phenomenon resulting from the interaction of light with the periodic microstructures etched or encoded onto the surface of the DOE. These microstructures effectively serve as a diffractive grating, imposing a phase shift on the incident light that leads to the formation of multiple diffraction orders or beams. The distinguishing feature of Dammann DOEs is their ability to generate a specific diffraction pattern with equally spaced, uniform-

intensity beams. This outcome is achieved through precise design and optimization of the microstructure pattern on the DOE's surface. The critical parameters involved in this design include the period, depth, and shape of the microstructures, all of which are tailored to achieve the desired beam spacing, diffraction angle, and intensity distribution.

The Dammann DOE concept was introduced in 1997 by H. Dammann, who proposed a method to produce many identical images side by side from one initial object [19]. Considered the optical setup based on Fraunhofer diffraction of Figure 4-2.

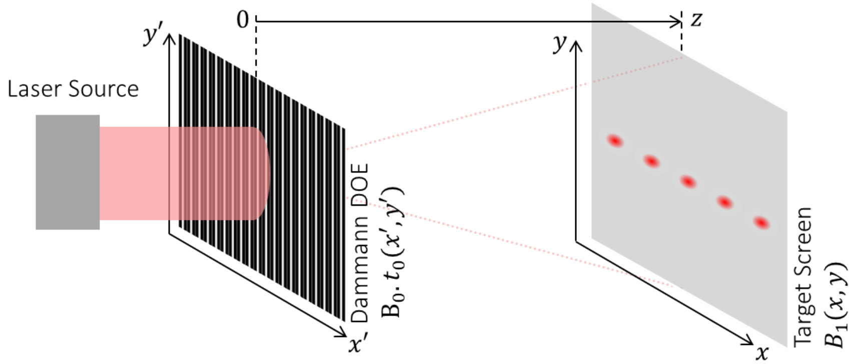

Figure 4-2 – Damman diffraction optical setup.

The desired light-intensity distribution in the image plane can be written as

$$I(x,y) = |B_1(x,y)|^2 = \sum_{n,m} |a(x - xn_0, y - my_0)|^2, \tag{4-6}$$

where $a(x,y)$ is the light-amplitude distribution within a single image structure around the optical axis of the system, and x_0 and y_0 describe the pitch of the two-dimensional image structure. So, the output of the system is given by the following convolution.

$$B_1(x,y) = B_0 t_0(-x,-y) \cdot T(x,y), \tag{4-7}$$

where $T(x,y) = \mathcal{F}\{t(\xi,\eta)\}$, so that (4-8) must hold.

$$|B_0 t_0(-x,-y) \cdot T(x,y)|\text{^}2 = \sum_{n,m} |a(x - xn_0, y - my_0)|^2, \tag{4-8}$$

A solution proposed by Dammann, assuming $a(x,y) = 0$, for $|x| \geq x_0/2$ and $|y| \geq y_0/2$

$$T(x,y) = \sum_{n=-N,m=-M}^{n=N,m=M} \exp\,(-i\varphi_{n,m})\delta(x - nx_0, y - my_0) \tag{4-9}$$

which must be valid only in the central block of the $(2N+1)(2M+1)$ diffraction orders. Optically, from Figure 4-2, a set of light spots is generated in the image plane if a transmissive diffraction grating is

added in the optical path. Illuminating a single structure yields a two-dimensional set of image structures according to $a(x - nx_0, y - my_0)$ corresponding to the diffraction orders of the grating.

The brightness distribution of the multiple images is the same as that amongst the diffraction orders, which is determined by the groove shape of the grating. This means that there is a central block of equally bright diffraction order around the optical axis and some weaker higher diffraction orders with a non-uniform brightness distribution, which are neglected.

In Figure 4-2, the grating is illuminated by a plane wave from a laser source. The amplitude of the diffraction pattern is given mathematically by the Fourier transform of the complex amplitude transmittance G(x, y) of the grating. The function $T(x, y)$ in (4-9) is the Fourier spectrum of the grating, which must be placed into the grating plane. A 2D filter transparency functions with $t_F(\xi, \eta) = t_1(\xi)t_2(\eta)$, where $t_1(\xi)$ and $t_2(\eta)$ are orthogonally symmetrical, one-dimensional, binary, phase-only transparency functions, which can be assumed as $+1$ and -1 only. The binary phase-only grating has the form depicted in Figure 4-3, where $\pm\xi_1$, $\pm\xi_2$, etc. in $t_1(\xi)$ are the transition points, and $\Delta\xi = 1$ the grating period normalized.

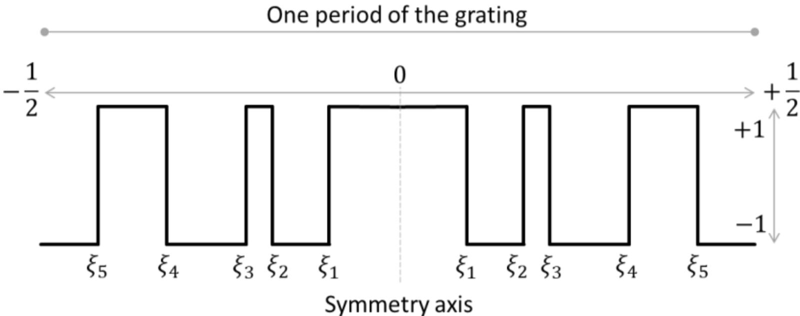

Figure 4-3 – One-dimensional, symmetrical, binary function having values +1 and -1 only from [19].

The amplitudes u_n of the diffraction orders can be computed by (4-10), where ξ_k the transition points, N is it correspondent number (between $\xi = 0$ and $\xi = 1/2$), $\xi_0 = 0$ and $\xi_{N+1} = 1/2$.

$$\begin{cases} u_0 = 2\sum_{k=0}^{N}(-1)^k(\xi_{k+1} - \xi_k) \\ u_n = \frac{1}{n\pi}\sum_{k=0}^{N}(-1)^k(\sin(2\pi n\xi_{k+1}) - \sin(2\pi n\xi_k)) \end{cases} \tag{4-10}$$

Here, the goal is to achieve the equality of (4-11), together with an efficiency η_1 as high as possible.

$$|u_0|^2 = |u_n|^2 \text{ for } n = 1,2, \dots, N \tag{4-11}$$

$$\eta_1 = |u_0|^2 + 2\sum_{n=1}^{N}|u_n|^2 \tag{4-12}$$

One-dimensional Dammann grating is a typical diffraction optical element for generating a linear array, and 2D one is a kind of grating for obtaining a 2D beam array in the far-field. The superposition of two 1D gratings in orthogonal directions (x and y) forms a 2D Dammann grating. Considering the orthogonal grating as α and β, the 2D one can be formed by logical operation and can be expressed as

$$\alpha \cdot \beta = \begin{cases} \pi, & \alpha = \beta \\ 0, & \alpha \neq \beta \end{cases}. \tag{4-13}$$

In (4-13), α and β are binary phase with two independent numbers, i.e., 0 and π [163]. The transmittance functions in the x and y directions are $T(x)$ and $T(y)$; following (4-13), the transmission function $T(x, y)$ of 2D DG can be further written as:

$$\arg[T(x, y)] = \arg[T(x)] \cdot \arg[T(y)] \tag{4-14}$$

4.1.3 Aperture angle between the diffracted beams

The diffraction angle of order m, θ_m, between the interference pattern order created by the Dammann DOE can be defined by the diffraction, which is related to the incident angle on the grating, θ_i, the grating period, d, and the diffraction order, m, which can be a positive or negative integer.

$$d(sin\theta_i + sin\theta_m) = m\lambda \tag{4-15}$$

Figure 4-4 depicts the resultant grating spacing, also denominated as pitch, for a target order aperture angle and wavelength. As can be seen, it is required to reduce the grating pitch to achieve larger aperture angles, which can be challenging in terms of microfabrication limitations.

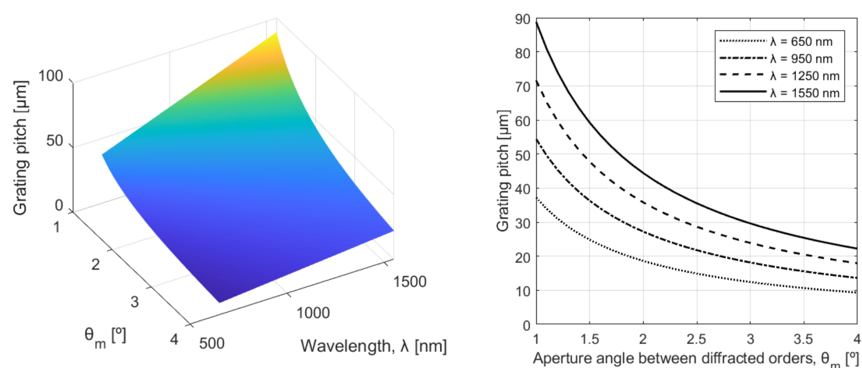

Figure 4-4 – Grating pitch relation with target aperture angle and wavelength.

4.1.4 Constraints from the merging of DOE on the MEMS surface

The optical path length refers to the equivalent distance travelled by light through an optical medium, adjusted for the refractive index of the medium as if it was travelling in vacuum. When the refractive index

is close to that of vacuum, the optical path is equivalent to the physical distance covered by the light wave, as given by

$$OP = \overline{P_1P_2}\, n_{medium} \tag{4-16}$$

As the grating is defined as a surface relief on the MEMS mirror surface, the laser incident angle on the grating will dynamically change with the mirror's two-axis actuation, resulting in a geometrical change of the beam optical path in the grating.

Consider two rays of a laser beam that come from a coherent laser source that are incident on a tilted mirror with a regular grating topography, such as a DOE, as represented in the schematic of Figure 4-5. The first ray is reflected at the bottom surface, at point B, while the second ray is reflected at the same location where the second reflected ray is aligned with the top surface, point C, with the same reflection angle and direction. However, the optical paths of these beams, denoted as OP_1 and OP_2, differ slightly as they propagate. Beam 1 travels from its origin to points A, B, and C and finally reaches the target, while beam 2 travels from its origin to points D, C and then to the target. The optical path difference (OPD) between the two beams is the difference of OP_1 and OP_2.

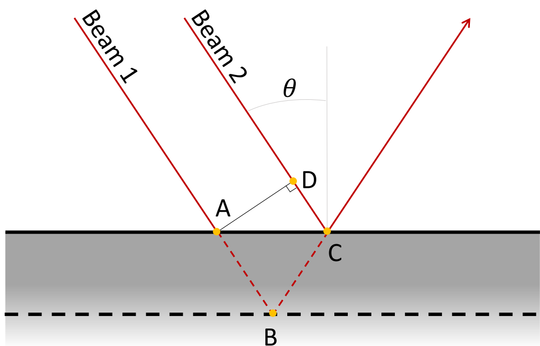

Figure 4-5 – Optical path schematic of two rays of a laser beam that comes from a coherent laser source.

Consider that the two coherent beams propagate so that they share a perpendicular wavefront formed by the plane intersecting their propagation direction and the line AD. This means that, up to that wavefront plane, beams 1 and 2 have travelled the same distance. From this point onwards, beam 1 will follow the optical path OP_1 (4-17), while beam 2 follows the optical path OP_2 (4-18).

$$OP_1 = \overline{AB} + \overline{BC} = 2\,\overline{AB} = 2\frac{d}{\cos(\theta_0)} \tag{4-17}$$

$$OP_2 = \overline{CD} = 2d\tan(\theta_0)\ sen(\theta_0) \tag{4-18}$$

The optical path difference between both beams is

$$OPD = |OP_1 - OP_2| = 2\frac{d}{\cos(\theta_0)} - 2d\tan(\theta_0)\ sen(\theta_0) = 2d\cos(\theta_0) \tag{4-19}$$

which depends on the depth, d and the angle of incidence θ_0. The phase of a wave propagating through the air (n = 1) changes periodically along the optical path. Despite both beams being coherent, they will reach the screen with a given phase shift difference $\Delta\varphi$. This difference is given by the difference in their optical paths and depends on the wavelength of the incident beam, λ, the nominal beam angle of incidence, θ_0,

$$\Delta\Phi = 2\pi\frac{OPD}{\lambda} = 2\pi\frac{2h\,cos(\theta_0)}{\lambda} \tag{4-20}$$

where h represents the etched depth of the grating structure. The binary DOE is typically designed so that its depth, h, and optical propagation paths result in a desired phase shift of π. As such, the depth is calculated as

$$h = \frac{\pi\,\lambda}{4\pi\cos\,(\theta_0)} = \frac{\lambda}{4\cos\,(\theta_0)} \tag{4-21}$$

With the merging of MEMS and diffractive optical devices into one, i.e., the Dammann DOE patterned in the mirror reflective surface, when the MEMS mirror is actuated in the inner axis, resonantly moving around the rest position, the incident angle of the laser beam is continually changing around this nominal angle at rest, since this with change accordingly to (4-22), where the angle of incidence is static, θ_0, as represented in the schematics of Figure 4-6.

$$AoI = \theta_0 + \theta_{mirror} \tag{4-22}$$

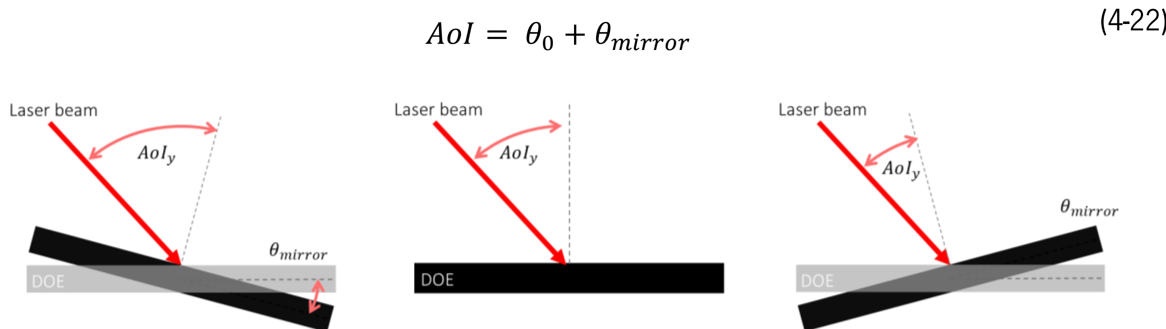

Figure 4-6 – Mirror angle influence on the laser source incidence angle.

One of the challenges when using a diffractive optical element (DOE) on a mirror surface to diffract the incident beam into several beams is the uniformity of the intensities of the multiple beams. This uniformity is dependent on the phase shift due to the reflection on the DOE, which depends on the angle of incidence. However, as the mirror tilts, θ_{Mirror}, the angle of incidence of the beam, θ_{AoI}, on the mirror also

changes, which results in a variation of the optical path and resulting phase shift. Figure 4-7 illustrates how the optical paths of two beams are altered for different mirror angles.

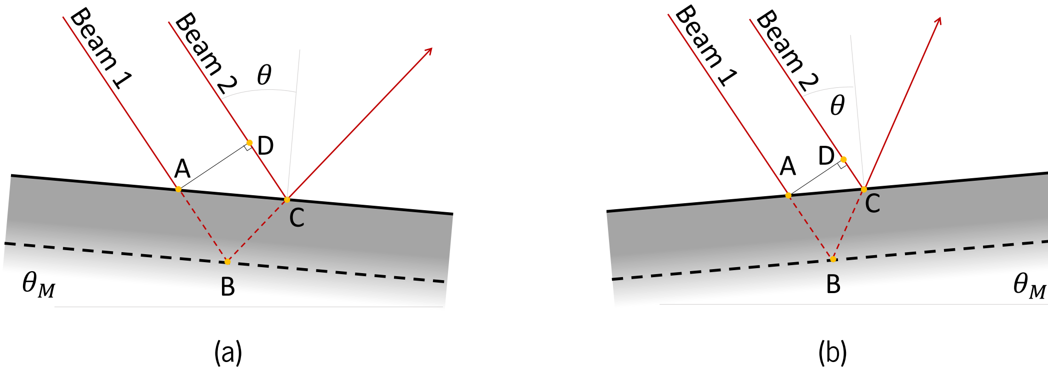

Figure 4-7 – Beams optical path schematic for an incident angle, θ (a) < 0° and (b) > 0°.

4.2 Analytic evaluation of diffractive optical element

The final device of this thesis is targeted to implement a diffractive element that splits the input beam into five, equally distributed by 2.6 degrees. This means that the Dammann grating has to be designed to have a high uniformity up to two interference diffracted orders, with a specific pitch for a laser wavelength of 1550 nm.

From the previous theoretical analysis, it is possible to define the following parameters:

1. The grating pitch, d, which assumes the desired aperture angle, θ_m, between the interference pattern orders of 2.6° and the wavelength of 1550 nm, it can be computed by (1-3), resulting in d equal to 34.2 µm.
2. Moreover, the transition points to obtain two diffraction orders. Dammann et al. [19] listed all the practical solutions up to four diffraction orders and the respective efficiency for a given minimum distance between two transition points in the grating structure. For two diffraction orders grating, two viable solutions are detailed in Table 4-1. Given the efficiency values, the highest one was chosen for the grating.

Table 4-1 – Damman solutions for N = 2.

N	η_1 [%]	ξ_1	ξ_2	$\Delta_{\min}$
2	48.2	+ 0.242	+ 0.414	0.172
	77.4	+ 0.132	- 0.480	0.040

Assuming both parameters, the grating features sizes were defined, and are detailed in Figure 4-8 and represented in the top perspective of the grating topography of Figure 4-9.

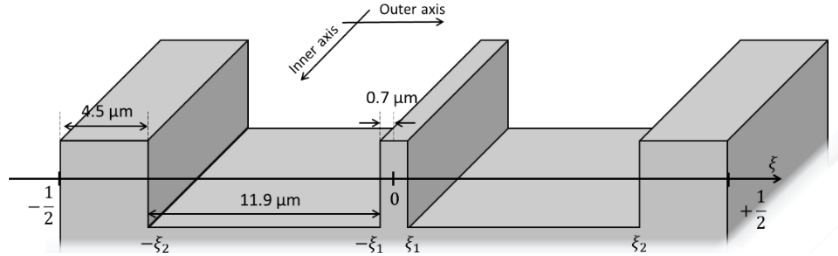

Figure 4-8 – Damman grating parameters used on optical analytical simulations – one segment perspective view.

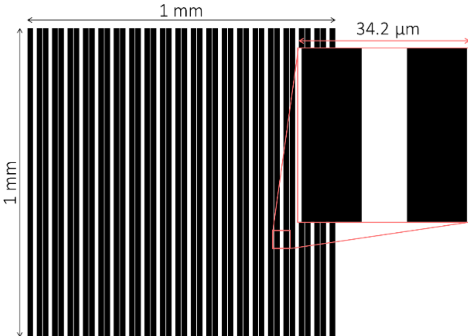

Figure 4-9 – Damman grating parameters used on optical analytical simulations – full reflective area layout top view.

In order to analyse the performance of the beam-splitting diffractive optical element, an optical analytical simulation tool was implemented using the MATLAB tool, which takes into account the geometry of the grating, such as pitch and grating depth, and the incident laser beam properties, such as angle of incidence, wavelength, diameter, among others. The simulator has several input parameters such as the grating depth and phase mask; the angle between the propagation direction of the beam and normal to DOE surface, denoted as AoI_y (regarding the MEMS structure inner axis) and AoI_x (regarding the MEMS structure outer axis), as detailed in Figure 4-10; the intensity and phase distribution of the incident beam; the incident beam wavelength; and, the position and geometry of a flat detector screen.

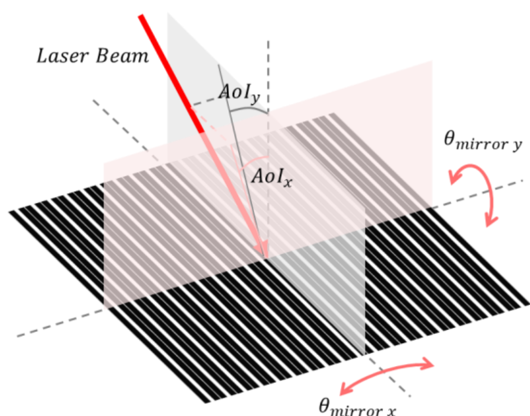

Figure 4-10 – Schematic of the influence of the mirror motion on the angle of incidence, with the inner, AoI_y and outer axes, AoI_x.

The simulator assumes that the input DOE phase mask is given for AoI in both axes of 0°. Then, it corrects both the surface relief topography as well as the phase modulation according to the input AoI for the inner and outer axis, AoIy and AoIx, respectively, and recalculates the phase shift of the grating according to the depth input. Such operations are respectively carried out in blocks *Adapt surface relief inclination* and *Adapt phase modulation*.

In the former block, the surface relief pattern is projected along a plane perpendicular to the propagation of the beam, whereas in the latter one, an additional phase shift due to the tilt of the grating with respect to the beam is computed. The two contributions are added in block *AoI correction,* and the DOE response is computed in the block *Compute field at DOE output*.

After obtaining the diffracted beam, an additional block is inserted (*Propagate Beam*) that is used to compute the propagation of the beam from the DOE to a detector whose position, orientation, and geometry are set as input parameters. Moreover, it is possible to switch between using a standard FFT or a non-uniform FFT method to compute the response. The resulting beam at the detector is computed in block *Compute resulting beam,* and the phase, amplitude or intensity can be plotted using visualization tools *Extract phase*, *Extract amplitude* and *Extract intensity*. Currently, the simulation tool is limited to flat rectangular detectors. A block diagram of the simulator is depicted in Figure 4-11.

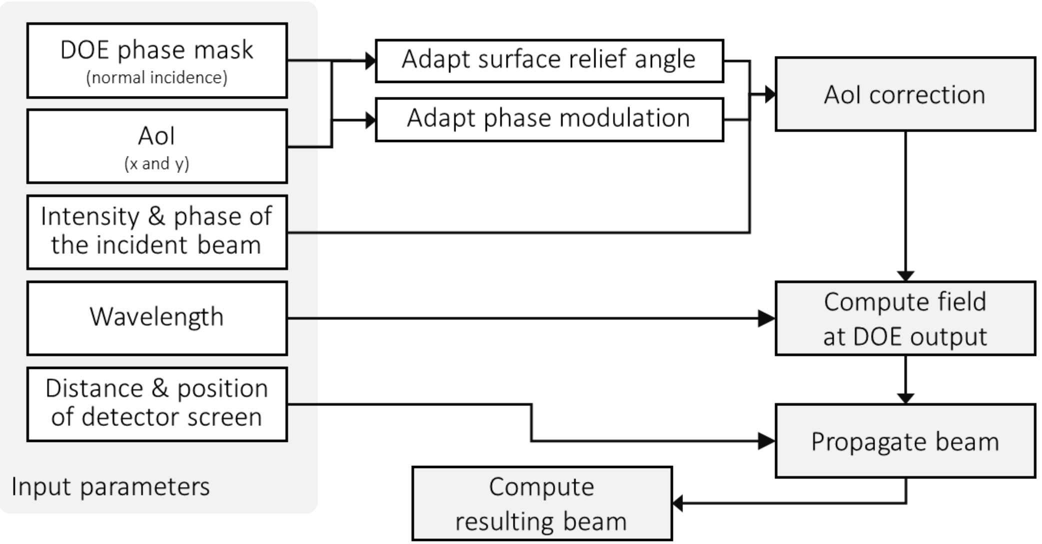

Figure 4-11 – Dammann grating diffraction simulation tool architecture.

4.2.1 Projection pattern

The incident laser beam is considered to follow a Gaussian distribution with a beamwidth ($\sigma_{x,y}$) defined by the FWHM (full-width half maximum) and described in the following equation (4-23). Figure 4-12 depicts a perspective and top view of the simulated incident laser beam.

$$U_0(x,y) = A * exp\left(-\frac{x - x_0}{2\sigma_x^2} - \frac{y - y0}{2\sigma_y^2}\right) \tag{4-23}$$

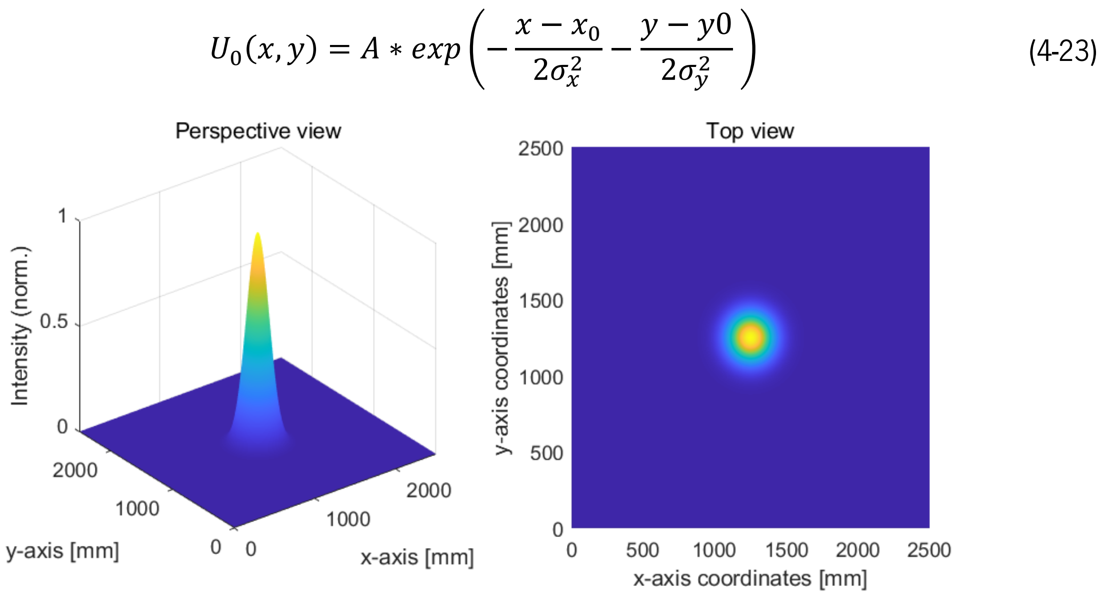

Figure 4-12 – Laser source simulated beam, perspective, and top view.

The field of the beam after the interaction with the DOE, i.e., with the phase shift interference, is calculated and the free space propagation of the diffracted beam is computed, using the Fresnel approximation for a projection screen below 10λ, and for higher values (far field) the Fraunhofer one. Figure 4-13 presents a perspective and top view of the simulated diffracted pattern using the Dammann DOE grating values of Figure 4-8, assuming the static rest position with an incident angle of 45°. It is possible to see that the 5 central spots (m = -2, -1, 0, +1, +2) present a higher intensity compared to the remaining higher orders.

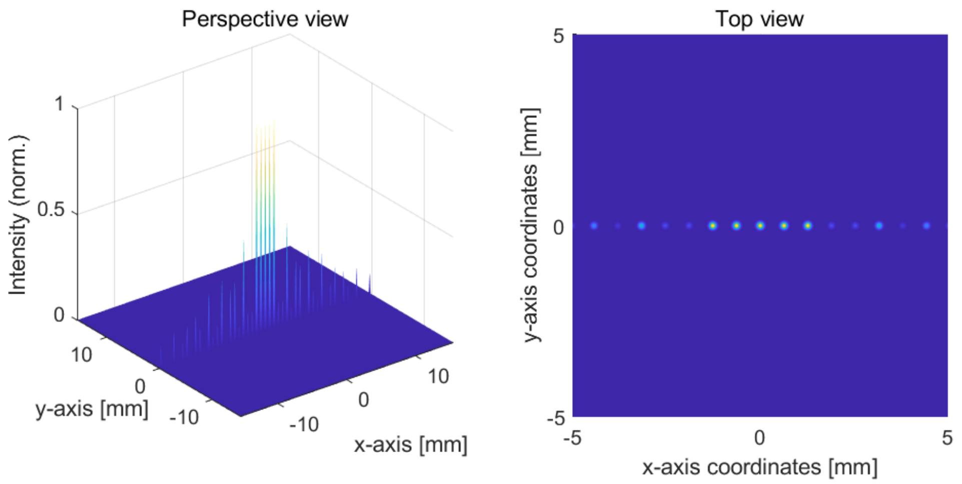

Figure 4-13 – Simulated diffracted beam, perspective, and top view.

4.2.2 Grating depth

In the proposed integration of the diffractive element into the reflective surface of the MEMS mirror, the grating depth presents a critical role in the overall optical performance of the final device. With the

developed analytical model, it was possible to simulate the optical projection and uniformity of the five central spots for different grating depths.

Figure 4-14 presents the required depth to achieve a phase shift of π, for a determined angle of incidence to the horizontal axis at the rest position, i.e., when the mirror is not actuated. As can be seen, for larger AoI, a larger grating depth is required. For example, to an AoI of 45°, the grating must have 548 nm of depth. This means that for the same angle of incidence, the same Dammann layout will present different projection profiles when micromachined with different depths. Figure 4-15 depicts the maximum vertical normalized intensity of four gratings, differing on the micromachined depth (100 to 700 nm), for an AoI of 45°.

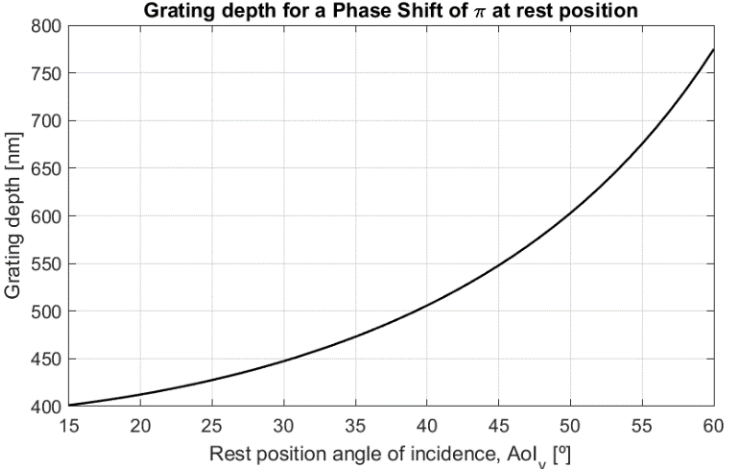

Figure 4-14 – Grating depth and angle of incidence assuming a phase shift of π.

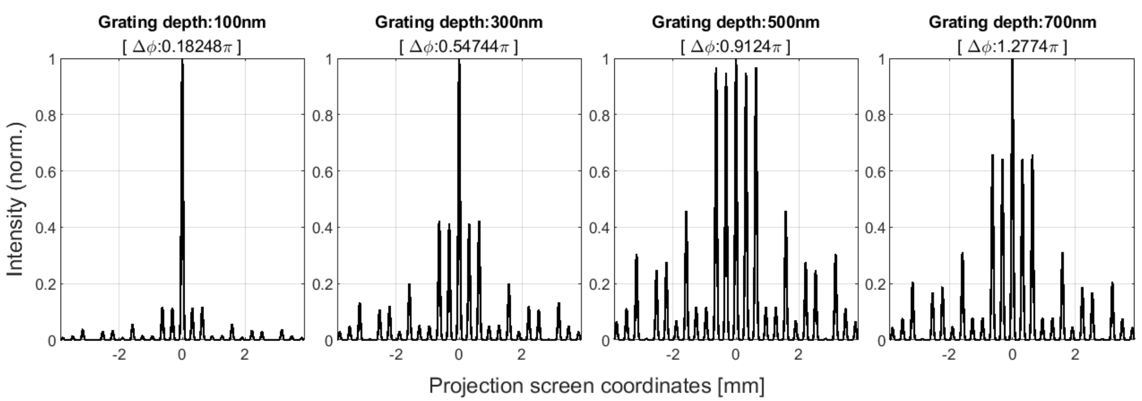

Figure 4-15 – Diffracted projection, assuming an AoI$_y$ of 45°, for different grating depths (100, 300, 500, and 700 nm).

Consider the top plots, with an AoI of 45°, in which the depth that results in a phase shift of π is 548 nm. As can be seen, the diffracted pattern presents the highest uniformity on the five central spots on the 500 nm-depth gratings and drastically decreases on the remaining topographies.

4.2.3 DOE Dynamic performance

Mechanically, the MEMS mirror needs to deflect ±15° (total of 30°) to optically steer the incident beam in ±30° (total of 60°), assuming a static position for the laser source, which results in a dynamic optical performance, and consequently in a dynamic projection uniformity, since the angle of incidence will continuously change.

MEMS inner axis influence

Consider the previous analysis, where the grating depth that resulted in the highest uniformity for a given AoI at the rest position, now it is analysed assuming the inner axis motion of ±15° around the rest position. Figure 4-16 presents the optical projection of a grating implemented to a rest position AoI of 45°, which required a depth of 548 nm, and the angular bandwidth of interest was from 30° to 60°

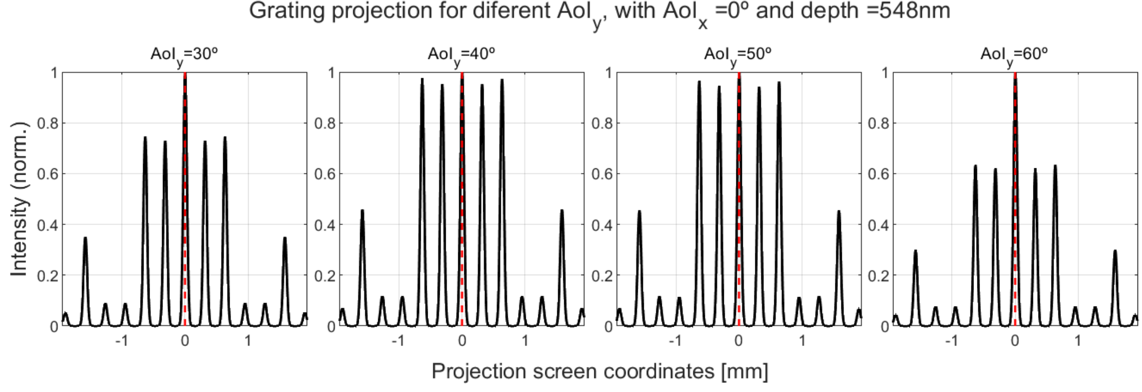

Figure 4-16 – Diffracted projection, assuming an AoI$_y$ of 30, 40, 50 and 60°, for a grating depth of 548 nm.

This analysis was conducted for a range of grating depths from 100 nm to 700 nm and for a laser beam AoI from 0° to 60° to analyse if there is a grating depth that presents a 30° range with a high uniformity. Figure 4-17 presents a gradient plot of the average intensity of the five central spots, and as can be seen, the 45° grating presents a non-uniform projection for the ±15° range around the rest position.

However, it is possible to conclude that by decreasing the laser AoI, it is possible to increase the uniformity. Since it is impossible to arrange the reflective grating and laser with an AoI of 0° (because the reflective beams would reflect directly to the laser source, a margin of 3° was established to accommodate the laser source and respective collimation without blocking the reflected beams. So, the possible arrangement between the grating and the laser that has a better response is the 18° AoI at the rest position, with 407 nm and the angular region from 3° to 33°.

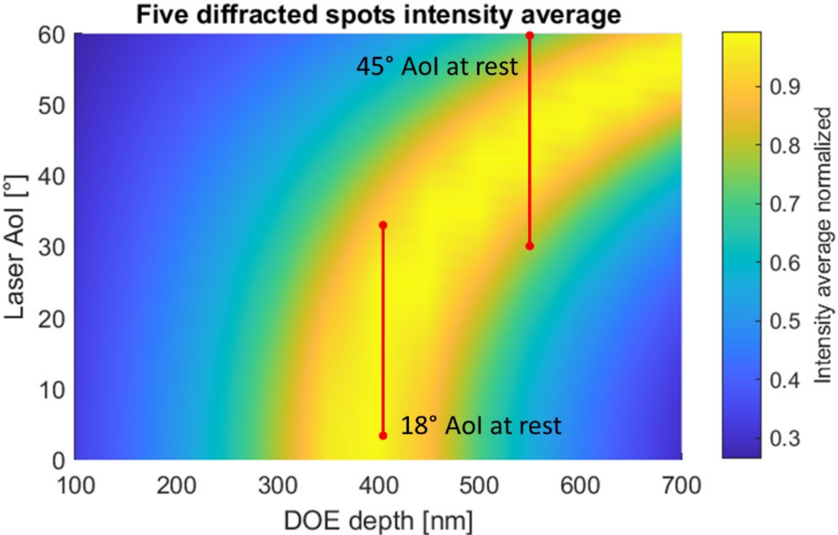

Figure 4-17 – Diffracted pattern central spots intensity average normalized, as function of the grating depth and laser angle of incidence AoI_y. Highlight the initial assumption of a system with a normal AoI_y of 45° and the optimal solution with an AoI_y of 18°.

The experiment of Figure 4-16 was redone for the 18° AoI, as represented in Figure 4-18. As expected, both gratings present a high uniformity close to the rest position AoI, namely 40° for the 45° and 20° for the 18° one. However, for the interest angles, the new one presents a higher uniformity of the five central spots within the target range compared to the first one, which decreases to half of the intensity on the non-zero orders.

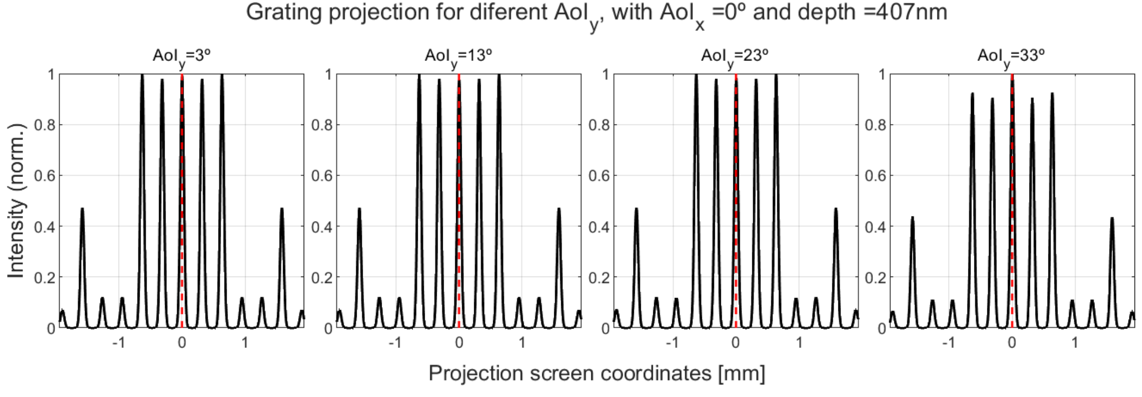

Figure 4-18 – Diffracted projection, assuming an AoI_y of 3, 13, 23 and 33°, for a grating depth of 407 nm.

MEMS outer axis influence

Consider the previous analysis, where the grating depth that resulted in the highest uniformity for a given AoI at the rest position, now it is analysed assuming the outer axis motion of ±1.3° around the rest position. Figure 4-19 presents the optical projection of a grating implemented to a rest position AoI of 18° regarding the inner axis (y-axis).

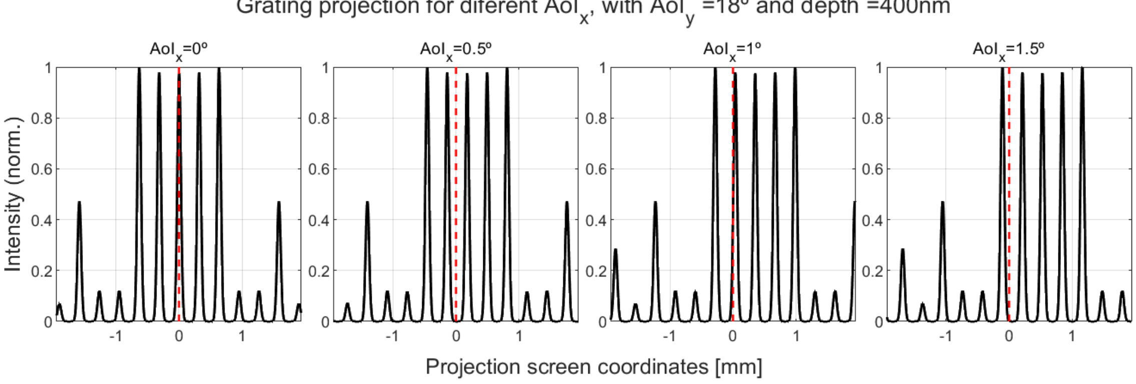

Figure 4-19 – Diffracted projection, assuming an AoI$_x$ of 0, 0.5, 1 and 1.5°, for a grating depth of 407 nm.

As can be seen, the projection, with the increase of the outer axis angle (AoIx), starts shifting regarding the actuated side, and the uniformity of the central spots remains constant for the overall motion. This analysis was again conducted for a range of grating depths from 100 nm to 700 nm and for a laser beam outer axis AoI from 0° to 1.5° to attain if there is a grating depth effect on the outer axis deflection uniformity, assuming the AoI of 18° regarding the inner axis (y-axis), Figure 4-20. These results sustain the previous conclusion, where the effect of the outer motion can be neglected in the final projection of the Damman DOE.

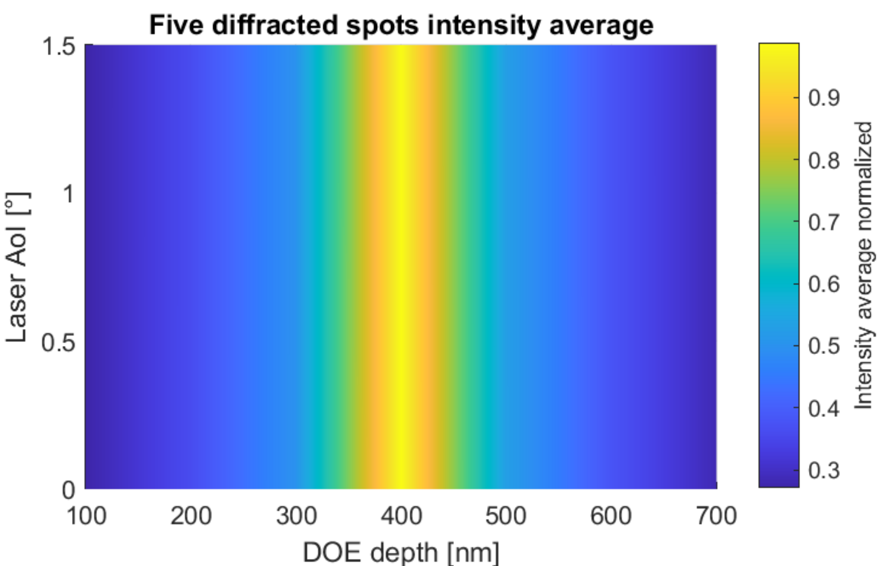

Figure 4-20 – Diffracted pattern central spots intensity average normalized, as function of the grating depth and laser angle of incidence, AoI$_x$.

4.2.4 Incident beam collimation effects

Laser beam collimation refers to the process of minimising the divergence of a laser beam, resulting in a beam that does not spread significantly as it travels through space. Collimation is essential for applications

where a concentrated beam of light is required over long distances, such as in laser pointers, surveying equipment, and various scientific apparatuses.

In a perfectly collimated laser beam, all the light waves (photons) would travel in the same direction, with their wavefronts (the surfaces of peak wave amplitude) in parallel planes. This ideal state would mean no divergence or convergence of the beam over distance, allowing the laser to project a small and intense spot of light at targets far away. However, due to the physical properties of light described by diffraction, perfect collimation is impossible. Diffraction is the bending of light waves around the edges of an aperture or obstacle, which inherently causes the light to spread out. The degree of collimation that can be achieved in practice is determined by the quality of the laser's optical design, including the shape and alignment of the laser cavity and the lenses or mirrors used to focus and direct the beam.

In laser systems, collimation is often achieved using a collimating lens, which converts the diverging light from a laser source into a parallel beam. The effectiveness of collimation can be influenced by factors such as the wavelength of the laser light, the size of the emitting aperture, and the precision with which the collimating optics are manufactured and aligned.

The impact of the incident beam spot size/collimation on the DOE projection was evaluated for different beam widths defined by FWHM. This parameter was simulated for a value of 0.9 mm (assuming sigma as 0.45, half of the beamwidth), 2 mm and 4 mm, and the corresponding grating projection for each case is presented in Figure 4-21. As can be seen, with the increase of the incident spot size, the width of each split beam increases in the same proportion, decreasing the angular resolution of the projected pattern. This effect in LiDAR systems can lead to a reduction in the system's resolution and accuracy, as a wider beam spread may result in less precise distance measurements and lower-quality data collection.

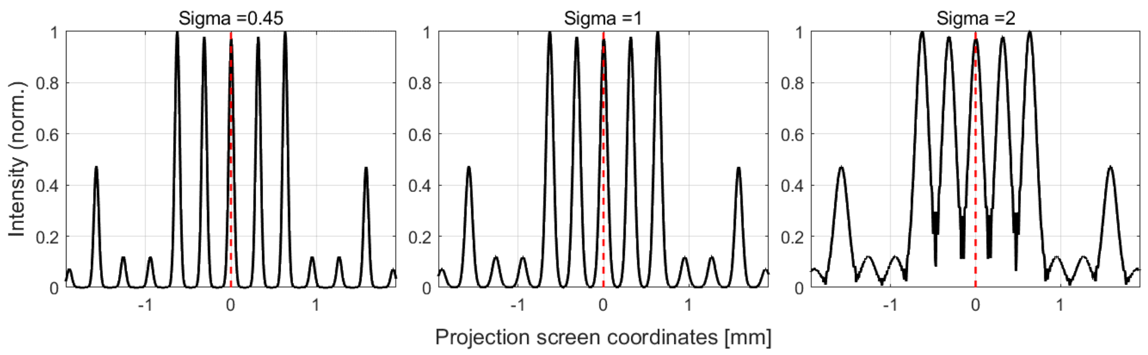

Figure 4-21 – Grating projection pattern, assuming AoI_x of 0°, AoI_y of 18° and depth of 407 nm, for different incident laser beam widths (from 0.9 mm to 4 mm).

4.2.5 Field of View simulation

The target field of view, assuming the motion projection of the MEMS mirror, was analysed using the DOE simulation tool. Initially, the simulation focused solely on the inner axis motion (horizontal projection), with an angular mirror resolution of 0.05°. The diffracted projection, simulated at 2 meters from the diffractive element for a full mirror motion cycle, is depicted in Figure 4-22. In this figure, five horizontal lines with high uniformity are observable.

Subsequently, the simulation was conducted assuming only the outer axis motion (vertical projection), and the diffracted projection at the same distance of 2 meters from the diffractive element is presented in Figure 4-23. Here, a single vertical line is depicted, which corresponds to five smaller lines of equal length. Finally, the diffracted field of view (FoV) was simulated, assuming the motion of both axes. As illustrated in Figure 4-24, five rectangular areas can be scanned. The maximum angle of the outer axis was limited to 1° to facilitate the identification of the focused sections within the total FoV.

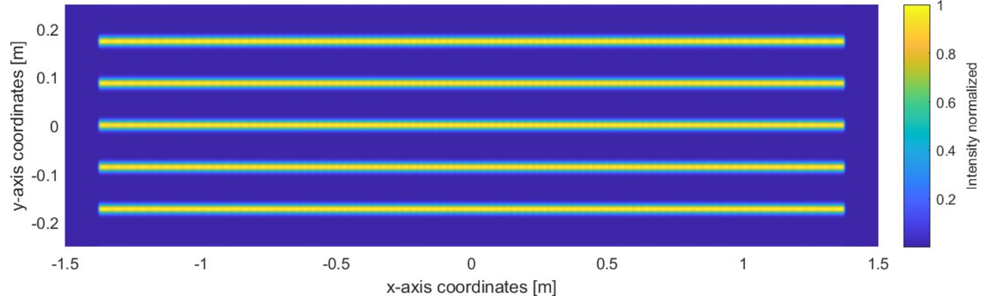

Figure 4-22 – Large diffracted FoV simulated at 2 meters from the DOE for a full motion cycle, with only inner axis motion.

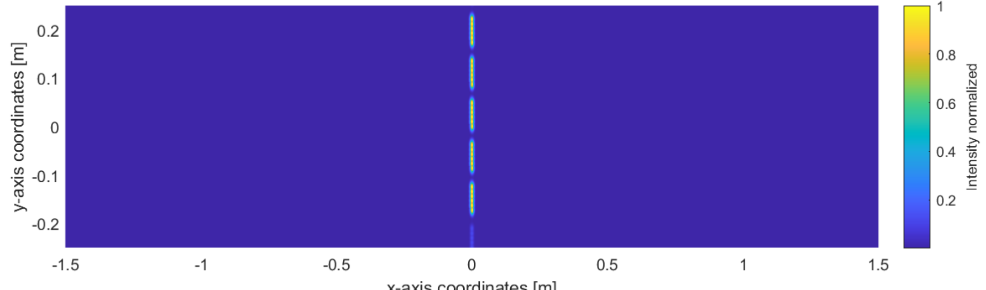

Figure 4-23 – Large diffracted FoV simulated at 2 meters from the DOE for a full motion cycle, with only outer axis motion.

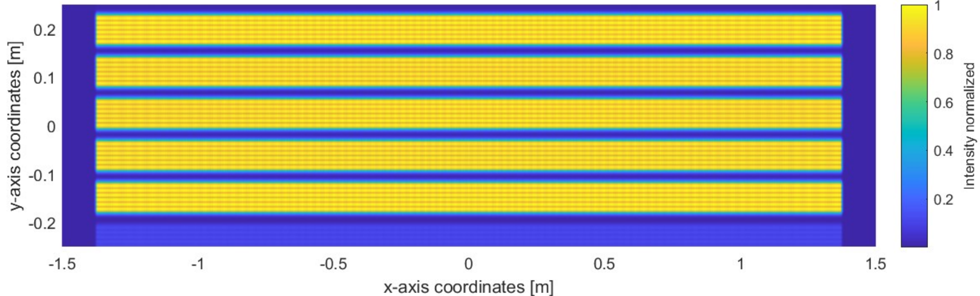

Figure 4-24 – Large diffracted FoV simulated at 2 meters from the DOE for a full mirror cycle, with inner and outer motion.

4.3 Reflective Dammann DOE micromachining techniques

The integration of Dammann gratings into MEMS reflective surfaces is facilitated by their compatibility with planar fabrication techniques, such as photolithography, due to their straightforward design. However, there are different techniques capable to entail these gratings, each with advantages and disadvantages. This section details the various micromachining techniques used for crafting both transmissive and reflective Dammann DOEs. Additionally, an examination of the reflective coating properties is conducted to guarantee that the performance of the device meets the desired specifications.

4.3.1 Microfabrication Sof surface reliefs

The Damman grating splitting outcome is achieved through precise design and optimization of the microstructure pattern on the DOE's surface, i.e., of the surface relief topography. The critical parameters involved in this design include the period, depth, and shape of the grating topography, all of which are tailored to achieve the desired beam spacing, diffraction angle, and intensity distribution. Typical surface relief DOEs, as illustrated in Figure 4-25, consist of a machined substrate with different depth structures. The substrate material can be silicon, glass, polymers, or other mediums as needed.

Figure 4-25 – Binary DOE by substrate etching.

Additionally, structures of materials of different refractive indexes may be used to create a DOE, as illustrated in Figure 4-26. Here, a flat substrate is coated with an additional material, such as SiO_2, photoresists, ORMOcomp, or other dielectric stacks, which have a given refractive index and thickness. A mask is produced on top of this layer, using lithography techniques, which is then removed to form the material pattern.

Figure 4-26 – Binary DOE by different material reliefs.

Surface relief DOEs are not limited to binary layer heights, which would correspond to two discrete values of the optical phase shift, such as 0 and π, for example, in the case of Dammann DOEs. DOEs with multilevel depths of the surface reliefs can be used to provide a stepped or continuous variation of the phase shift. These multilevel structures can improve DOE diffraction efficiency. These surface reliefs can be produced on a substrate or a coated material layer, as shown in Figure 4-27.a and b, respectively.

Figure 4-27 – Multilevel DOE by (a) different material reliefs or (b) substrate etching.

Reflective DOEs are typically fabricated by etching a rigid substrate, followed by a coating of a reflective layer, as shown in Figure 4-28.a, such as a metallic layer. A hybrid reflective DOE can also be produced, as shown in Figure 4-28.b, where a flat reflective layer is coated first on the flat substrate, and then a secondary dielectric structured medium is deposited to form the phase-shifting structure. This hybrid approach has the advantage of enabling the processing of high-performance multi-stack reflective layers, which are not deformed by the underlying topography.

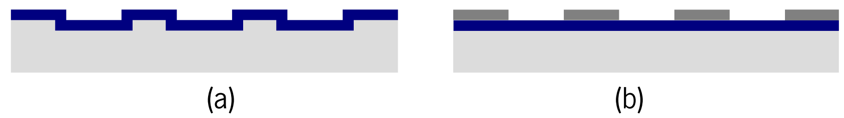

Figure 4-28 – Binary reflective DOE by (a) substrate with reflective coating followed by different material reliefs or (b) substrate etching followed by reflective coating.

4.3.2 Device reflective surface

The efficacy of LiDAR scanning devices is contingent upon the reflective properties of the surfaces within the system. Here, the reflective coating presents a critical role for such devices, with an emphasis on the implications of the incident beam's wavelength on the design considerations.

Silicon substrates are known for their low reflectivity in the near-infrared spectrum, which can lead to overheating and damage to the device. To address this issue, thin-film metal coatings are the most widely adopted method to enhance reflectivity in most MOEMS devices. The reflective layer fabrication is based on surface micromachining, where the material layers are deposited on top of the silicon substrate. In typical reflective mirrors, the reflective layer is usually some metal like silver, tin, nickel, chromium, or aluminium, as represented in Figure 4-29.

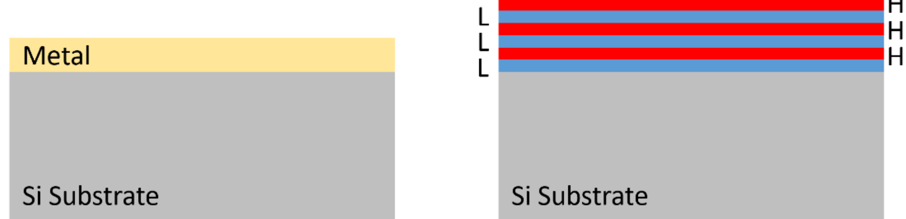

Figure 4-29 – (a) Metallic coating and (b) multilayer stacks coating (higher reflectivity and higher heat immunity).

On the other hand, a dielectric mirror, also known as a Bragg mirror, is a type of mirror composed of multiple thin layers of dielectric material, typically deposited on a substrate of glass or some other optical

material. Dielectric mirrors function based on the interference of light reflected from the different layers of the dielectric stack.

This surface reflectivity is an essential factor for the MEMS mirror with the reflective DOE performance, and this is defined as the ratio between the reflected and incident power, as expressed in equation (4-24).

$$Reflectivity\ (\%) = \frac{Preflected}{Pincident} \tag{4-24}$$

As presented in [2], materials like aluminium, gold, silver, and copper exhibit high reflectivity in the conventional band (c-band) around 1550 nm wavelength [58]. However, in choosing the appropriate coating material, factors such as coating/silicon adhesion, corrosion problems, and power threshold must be considered. However, superior performance coatings can be achieved through the stacking of multiple layers with low (L) and high (H) refractive indexes, known as dielectric or multilayer coatings (Figure 4-29, b). The deposition of both dielectric layers is made by plasma-enhanced chemical vapour deposition (PECVD). These stacks can achieve higher reflectivity values for the design wavelength.

Reflectivity is closely associated with the power threshold, which affects not only the coating but also the suspension springs of the scanning device. This threshold limits the system's power operation, as the micromirror reflectivity decreases and, after some cycles, the mirror's springs break (due to melting and mechanical fatigue) for power levels exceeding the threshold. Below the threshold, the micromirror delivers acceptable performance. Table 4-2 presents the damage threshold of different materials. as reported in [68].

Table 4-2 – Power damage threshold of different materials per unit of area [W/cm^2],

Material	Damage threshold
Aluminium	350 W/cm^2
Silver	1500 W/cm^2
Gold	750 W/cm^2
Copper	5000 W/cm^2
Silicon	200 W/cm^2
Dielectric mirrors	2000 W/cm^2

Despite the advantages of dielectric coatings in heat management, since they can absorb significant amounts of heat without being damaged, they present critical challenges. The control of the thickness of each layer is critical to satisfy the Bragg condition and to ensure a high-reflectivity reflection band. Also, the surface roughness of the reflective layers must be minimized to prevent the degradation of the coating's blocking depth and to avoid the scattering of the reflected beam.

In thin metal layer coatings, thermal damage is a real problem, and, typically, they eventually deform or even melt when absorbed the same amount of heat as the dielectric ones, which can lead to peeling effects and compromise the coating's properties.

4.3.3 Single Metal layer modelling

To identify the optimal reflective material(s) for a desired device, the optical performance of various materials was evaluated using the TFCalc tool, which facilitates the computation and design of optical thin film coatings. Figure 4-30 delineates the reflective structure as modelled within TFCalc, which simulates the reflective surface of a MEMS mirror.

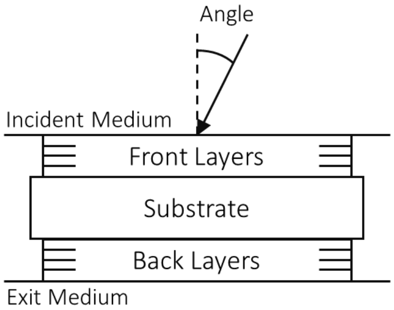

Figure 4-30 – Schematic of the standard reflective stack structure simulated on TFCalc.

The SOI-based MEMS micromachining process, typically used at INL, uses an initial 500 nm-thick metal layer of AlSiCu to create the electrical contacts of the MEMS device. Assuming the compatibility of the DOE and the MEMS mirror process and that the reflective coating of the mirror could be created in the same metal layer as the contacts, a 500 nm-thick layer of AlSiCu was assumed as the front layer of the optical model. This integration strategy simplifies the fabrication process by utilizing a single material layer for multiple functions. Figure 4-31 presents the reflectance for a wavelength band, ranging from 250 nm to 2500 nm, for an incident angle, θ_i, of 45°, of a silicon substrate (a) and a silicon substrate with a layer of aluminium (b).

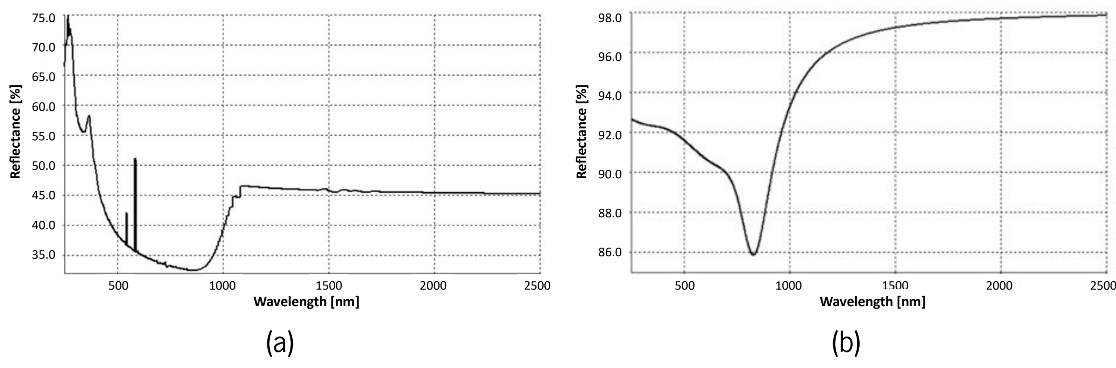

Figure 4-31 – Comparison of theoretical reflectance of the silicon substrate and a silicon substrate with a thin layer (500 nm) of aluminum. Red stars represent the reflectance for a wavelength of 1550 nm.

It is observed that in the near-infrared band, silicon demonstrates a reflectivity of less than 50% for the target wavelength of 1550 nm. This low reflectivity results in undesirable power loss through transmission and absorption. Conversely, the application of an AlSiCu coating markedly enhances reflectivity, achieving a near doubling of the percentage, surpassing the 95% threshold requisite for the device's operational efficiency.

Given the high reflectivity of the thin AlSiCu layer, coupled with its process compatibility with MEMS mirror and DOE fabrication, it was established to implement it on the MEMS device. Subsequent considerations for alternative dielectric coatings were deemed unnecessary due to their complexity in ensuring precise layer thickness control. Moreover, the micromachining process of these coatings and MEMS devices presents several incompatibilities, from the creation of the stack to the release of the MEMS device without peeling problems of the stack.

4.4 Dammann Integration with MEMS Mirror

In the previous section, the analytical analysis and design of the Damman grating were described. This section presents the DOE and the MEMS structures integration, considering the results obtained in the various evaluations. Figure 4-32 illustrates the 3D model developed using a CAD software. As can be seen, the grating reliefs were integrated into the MEMS reflective surface.

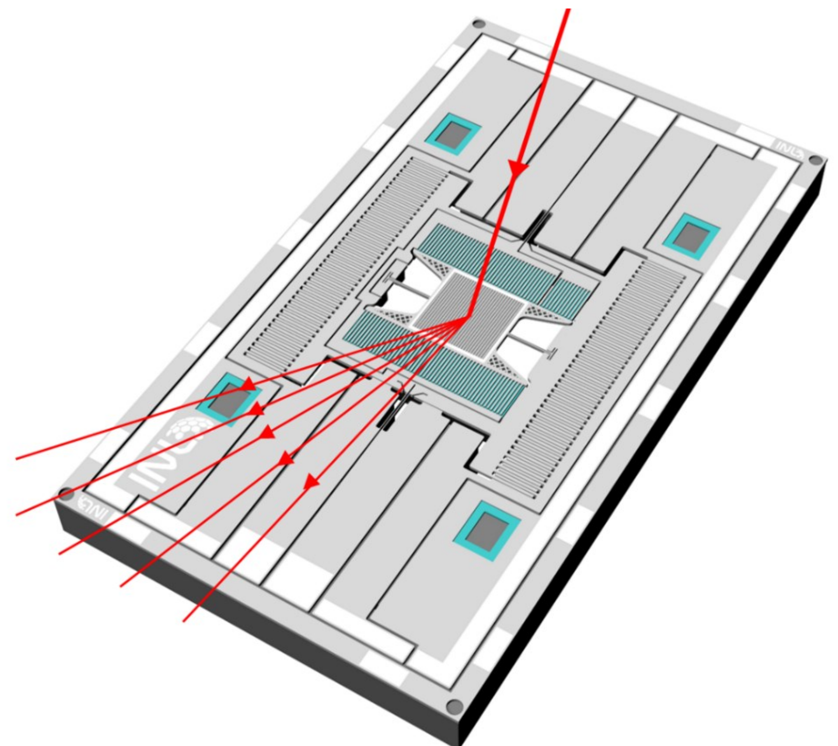

Figure 4-32 – 3D model of the MEMS mirror with DOE designed, with a schematic of the projected diffraction.

Given the compatibility of both processes, it was defined to micromachine the DOE topography prior to the typical MEMS mirror fabrication. So, initially the Dammann design is intended to be patterned directly into the SOI device layer and then, and the thin layer of AlSiCu, typically used only to the electrical contacts will be sputtered on the already patterned silicon grating, giving it the reflective property. Since the AlSiCu sputtering process is a non-conformal process, this will be only deposited into to the silicon planar surface (not deposited on the grating side walls) minimizing deformations to the critical grating features.

Figure 4-33 displays a top view model of the final device with highlight on the grating structure. Two Dammann designs are intended to be micromachined, one optimized for a AoI of 45°, which implies a grating depth of 548 nm and other for 18°, with 407 nm.

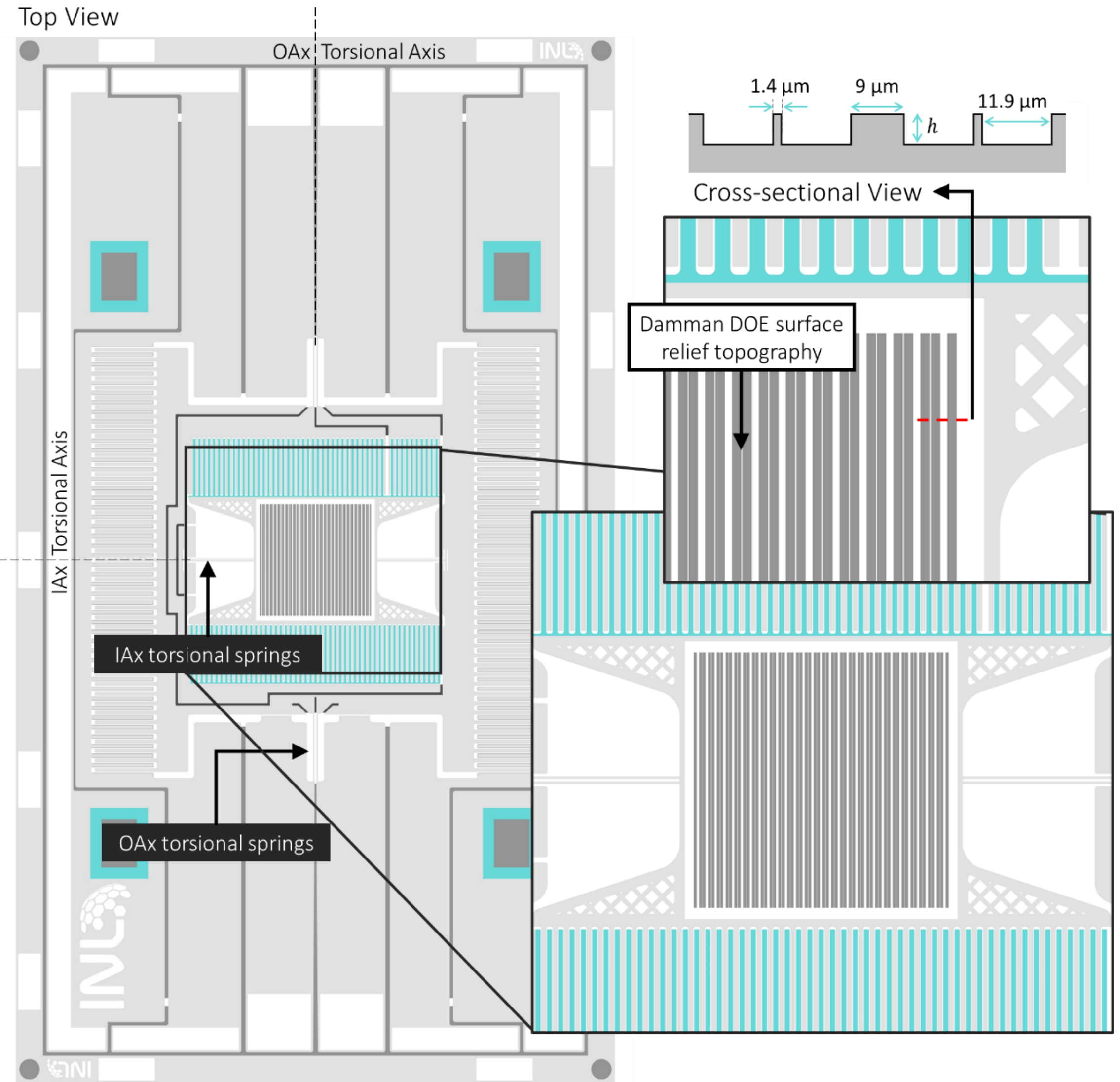

Figure 4-33 – Schematic of the 2D MEMS mirror with diffractive optical element.

4.5 Conclusions

In this chapter, the theoretical foundations of the diffractive element were presented, as well as the analytical model and evaluation. The modelling and analysis of the beam-splitting effect of a reflective DOE is a critical study towards the target device of this thesis. Here, light can not only be considered as a ray but also as a wave encountering an obstacle and consequently diffracting with a specific pattern. Several diffraction theories have been established to predict these patterns, including the Rayleigh-Sommerfeld, Fresnel, and Fraunhofer formulations.

Given the Damman simplicity and micromachining process compatibility with the MEMS mirror one, this was established to be implemented on the final device. Dammann DOEs are characterized by their ability to split an incoming light beam into multiple equidistant and equally intense sub-beams arranged in a well-defined geometric pattern, i.e., Dammann DOEs are binary phase gratings that can be used to generate a 1-D or 2-D array of equal-intensity. These span a broad spectrum of optical systems, where controlled and structured light patterns are fundamental.

The reflective splitting uniformity, aperture angle and grating depth were analysed, as well as the influence of the MEMS mirror. Given the attained results, it was concluded that a normal laser angle of incidence of 45° would not present a uniform projection for the total FoV when the mirror is actuated. So, an extensive analysis of the optical performance for different grating depths and angles of incidence was carried out, and an optimal arrangement between the mirror and the laser with 18° was found. Two designs were defined, one with the target and final system AoI of 18° and another for 45°, to facilitate the static experimental characterization of the DOE.

5. Micromachining process

This chapter delves into the micromachining developments of this thesis to produce the final mirror device, a 2D MEMS mirror merged with a diffractive optical element on its reflective surface. For this reason, several preliminary studies were conducted to evaluate the fabrication limits and constraints, such as the reflective coating analysis, minimum electrode gap, grayscale lithography patterning, among others. As previously mentioned, a 1D MEMS mirror was also fabricated to validate the process flow and the designed analytical models. Finally, nanoimprint lithography was studied and implemented to optimize the MEMS scanner process for mass production fabrication, reducing the costs, and time to fabricate and increasing yield.

The MEMS micromachining process is primarily based on planar technologies, which entail constructing MEMS components on a flat wafer substrate. The designed MEMS mirrors possess a unique attribute – the use of asymmetric electrodes for actuation. Grayscale lithography was employed to micromachine these electrodes, enabling the patterning of different masks in a single lithography step, eliminating misalignment issues, and minimizing the necessary lithography steps. In the wafer's back-side, double lithography is used in the patterning process to implement a thinned inner axis mechanical frame since the alignment here is not critical, and GS exposure takes longer.

5.1 Preliminary micromachining studies

This section details the preliminary study of the different micromachining processes. This comprises the analysis of the implementation of grayscale lithography for multilevel MEMS actuators in the same initial silicon layer, the analysis of different reflective coatings for the mirror surface and the tolerance in the patterning process of the diffractive grating. The DRIE process was analysed, focusing on the minimum gap size achievable and the creation of different electrical active parts in the SOI's handle layer. Most of the tests performed used a preliminary layout of the final 1D and 2D MEMS mirror since these micromachining processes and subsequent results are extremely dependent on the layout, such as the area exposed to etch and uniformity of the features to process, among others. These layouts do not correspond to the final MEMS devices presented in the subsequent chapters.

5.1.1 Reflective coating

The reflective coating fabrication is based on surface micromachining, where the different material layers are deposited on top of the silicon substrate. Three different reflective coating layouts were fabricated, all with a thin aluminium alloy (AlSiCu) layer on a single-side polished (SSP) wafer. The first and second samples, DC1 and DC2, presented a reflective area of 1 mm per 1 mm, while the third one was a large piece of silicon completely covered with the reflective coating. This aluminium coating was achieved by sputtering a thin film of AlSiCu (500 nm) on the FTM Timaris tool on top of the silicon surface. To measure the reflectivity of the fabricated MEMS mirror AlSiCu, an optical experimental setup (Figure 5-1) was built consisting of a collimated laser source, a rotation stage where the Device Under Test (DUT) was assembled, and a power meter. The laser is aimed at the DUT at 45°, and the power meter is placed orthogonally. The absolute power emitted was measured by shining the laser directly on the power sensor to access the reflectivity data for the reference mirrors used.

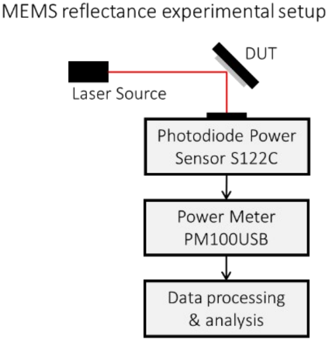

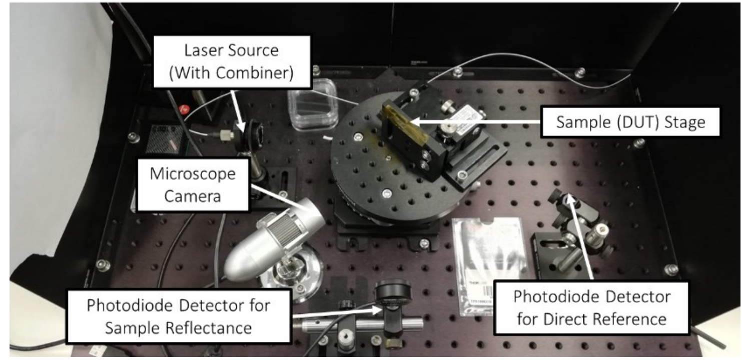

Figure 5-1 – Reflectance characterization setup

To access a reference value in this analysis, three mirrors from Thorlabs that present an extensive reflectance characterization for an incident angle of 12° and 45° for a broad wavelength band were used. The reference mirrors used are presented in Table 5-1, and the reflectance percentages of each one for a wavelength of 1550 nm are presented in Table 5-2. The laser source used was unpolarized.

Table 5-1 – Reference Mirrors Used.

PFSQ20-03-G01 - 2'' x 2''	PFSQ20-03-F01 - 2'' x 2''	PFSQ20-03-P01 - 2'' x 2''
Protected Aluminum Coating (-G01, 45° AOI)	UV-Enhanced Aluminum Coating, 45° AOI (UV to IR Wavelengths Shown)	Protected Silver Coating (-P01, 45° AOI)

Table 5-2 – Reflectance percentages of the reference Thorlabs mirrors.

Mirrors	Wavelength (°)	Incident Angle (°)	P-Pol(%)	S-Pol(%)	Unpol(%)
G01	1550	12	94.97944	94.74943	94.86443
		45	93.32634	94.91736	94.12185
F01		12	96.38026	96.66138	96.52082
		45	95.16446	96.77213	95.9683
P01		12	98.28465	98.072	98.17832
		45	98.01686	98.41218	98.21452

The experimental reflectance measurements are presented in Table 5-3, with a reference reflectance relative to the P01 Thorlabs mirror. It was observed that the fabricated samples (DC1 and DC2) that have a 1 mm per 1 mm aluminium coating presented a lower reflectance percentage (approximately 86%) relative to the bulk AlSiCu coating (approximately 94%). This difference may appear from a collimation problem since the laser beam diameter was larger than expected, i.e. larger than the mirror surface (1 mm^2).

The AlSiCu reflective coating offers advantages that elevate its applicability. Notably, it boasts a simplified micromachining process due to its singular thin-layer composition, in contrast to the more complex structure of dielectric coatings. This characteristic aligns with the DOE process, simplifying compatibility. The AlSiCu reflective coating confers the desired reflective properties to the Diffractive Optical Element. This feature assumes significance as the inherent reflective characteristics of a bare silicon wafer fall short of meeting the prerequisites for the studied infrared laser application operating at a wavelength of 1550 nm.

Table 5-3 – Experimental Reflectance measurements for a wavelength of 1550 nm.

TYPE	DUT	Reflectance	Transmittance + Absorption	Incident Angle
Thorlabs mirrors	G01	94.12185%	5.87815%	45°
	P01	98.21452%	1.78548%	45°
	F01	95.9683%	4.0317%	45°
Metal coatings	AlSiCu Coating (Big Piece)	94.34127%	5.658729%	45°
	MirrorDC1- AlSiCu	86.7349%	13.265099%	45°
	Mirror DC2 - AlSiCu	86.34244%	13.657565%	45°

5.1.2 DOE micromachining process optimization

The DOE is a surface relief topography grating etched onto the mirror surface to a phase depth and coated with a reflective coating. The complexity inherent in the micromachining of the 2D MEMS mirror process requires, thus, the compatible integration of the diffractive optical element process into the preliminary stages of the MEMS structure process is studied. For these reasons, the reflective DOE micromachining process presented in Figure 5-2 was implemented. Here, a thin layer of photoresist (PR) was coated, and the DOE pattern, using DWL lithography, was exposed into the PR, Figure 5-2.b. After this step, the desired pattern was transferred to the silicon wafer through a Reactive Ion Etching (RIE) process with the desired depth, Figure 5-2.c. Finally, the wafer passed through an organic cleaning step to remove the photoresist, Figure 5-2.d.

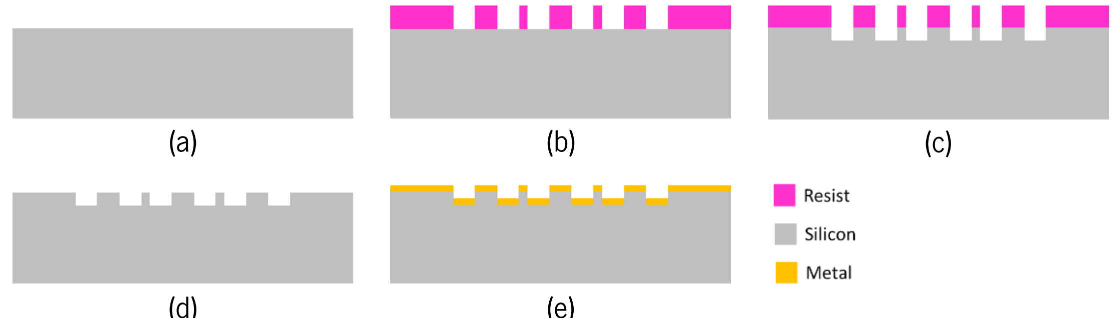

Figure 5-2 – Reflective DOE topography micromachining process.

The DOE fabrication went through an iterative process optimization to fine-tune each new batch to achieve the requirements and improve the performance. Table 5-4 summarizes the fabrication and design features as well as the optical performance of each DOE batch. Here, the main differences between the batches are the angle of incidence (AoI) for which the DOE surface relief depth is designed and the lithography technique.

Table 5-4 – Specifications of the different DOE experimental runs.

Batch	Target AoI	DOE depth	Exposure Technique
1	45°	548 nm	DWL
2	45°	548 nm	MA
3	18°	407 nm	DWL

Design grating pitch

DWL and mask aligner tools were experimentally tested for the DOE pattern's lithography. The Dammann DOE fabricated with the DWL exposure presented much more precision, 1,4%, than the DOE fabricated by using mask aligner, 29.7%, as indicated in Figure 5-3. That is shown by the variation between the target and fabricated Dammann width parameters, as detailed in Table 5-5. The absolute variation using DWL is 150 nm while using mask aligner is 750 nm.

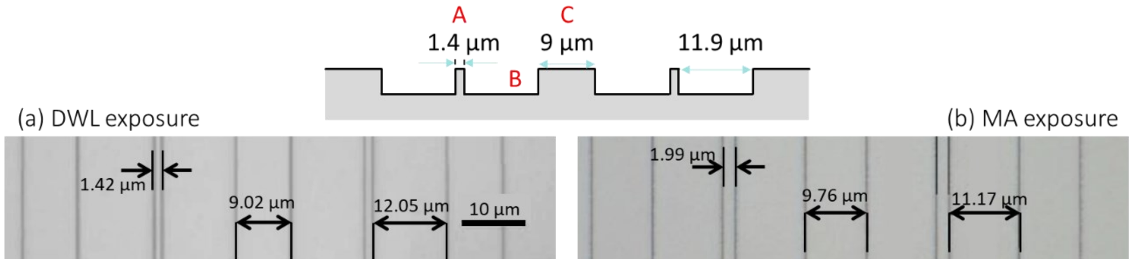

Figure 5-3 – DOE exposure results analysis, where (a) and (b) microscopic optical images from the tests using DWL and MA systems, respectively.

Table 5-5 – Fabricated DOE grove measurements and comparison using DWL or MA exposure systems.

Grove Width	A	B	C
Target [µm]	1.4	11.9	9
DWL [µm] Difference to target	1.42 +0.020	12.05 +0.15	9.02 +0.02
Mask Aligner [µm] Difference to target	1.99 +0.59	11.17 -0.73	9.76 +0.76

Grating depth

The depth of the diffractive optical elements affects the final performance of the MEMS devices since the optical path and resultant diffraction uniformity depend directly. In the initial DOE designs, the optimized AoI was 45°, which requires a DOE depth of 548 nm. However, for the AoI range of 45°±15°, the uniformity will vary from 30% to 93%, as expected theoretically. For larger nominal AoI, a certain tilt angle variation with respect to the nominal value causes a larger phase-shift, which in turn plays a key role in the uniformity. To obtain a more even uniformity over the AoI range, the next DOEs and the whole beam steering system were optimized for a nominal AoI of 18°, which required a depth of 407 nm.

To attain the precise depths for the Diffractive Optical Elements, a series of experimental micromachining tests were conducted to investigate different etching processes. Initially, experiments were performed

using Reactive Ion Etching (RIE) process on the SPTS Pegasus tool, employing a deliberately gradual Silicon etch recipe. This approach yielded suboptimal outcomes characterized by pronounced non-uniformity across the wafer. Even with a preliminary calibration of the etch rate specific to the DOE layout, it was extremely difficult to achieve the target depth with this process.

In response to these challenges and given the slower silicon selectivity exhibited by the Inductively Coupled Plasma (ICP) Titanium Tungsten (TiW) recipe, a comprehensive set of experiments were conducted using this particular recipe. Here, the exposed silicon is etched much slower (making it suitable to fine-tune the desired depth with more control) and with higher uniformity across the wafer. Table 5-6 presents the etch rate (ER) using both recipes for silicon etch.

Table 5-6 – Silicon etch rate (ER) using different etching techniques.

Tool	Silicon ER
SPTS Pegasus	816 nm/min
SPTS ICP	197 nm/min

5.1.3 Front-side (FS) multilevel process optimization

Given the vertical asymmetric comb-drive electrodes required for the MEMS actuation, a novel self-aligned, dicing-free [129] and low-cost fabrication process was implemented, combining typical SOI-based bulk micromachining and grayscale (GS) lithography to create a single mask with multilevel topography, followed by a sequence of etching and mask thinning steps. By using this fabrication process, it is possible to create vertically asymmetric structures with a small and self-aligned electrode gap. This process, when compared to previous references [130], [131], [132], [133], [134], [135], presents a simpler and cost-effective process to achieve non-resonant torsional motion using a single-layer device.

This technique facilitates the precise patterning of perfectly aligned asymmetric structures, such as self-aligned electrostatic combs, wherein each GS level corresponds to a different thickness to be patterned on the silicon substrate. One noteworthy advantage of this technique is that it eliminates the need for alignment between separate lithography steps, thereby minimizing misalignment sources that may arise from the resolution of the system camera or the quality of alignment marks, among others. The use of a multilevel hard mask enables the creation of multilevel structures self-aligned through a two-step silicon bulk micromachining etch, which typically is extremely difficult to achieve when using other fabrication methods, like several lithography steps or varied materials as masks. Grayscale lithography can be used to generate discrete photoresist levels in the same layer, which can be combined with a sequential bulk micromachining process to transfer this discrete mask onto the substrate.

Grayscale lithography calibration

A preliminary GS lithography calibration process was developed to achieve the exposure curve (exposure level vs final photoresist thickness) and to ensure the optimum laser intensity that would be needed during the process. For that, a simple layout with 128 layers was designed, each layer representing a specific exposure level (i.e., layer 1 – GS level 1, layer 2 – GS level 2, ...). For this calibration, an initial AZP4110 photoresist layer with a thickness of 2.2 μm was used. After the exposure and respective photoresist development, Figure 5-4, an inspection was performed using an optical microscope and the mechanical profilometer system regarding the thickness of each layer. The calibration curve is shown in Figure 5-5 and presents over 80 grayscale levels in the linear region defined between thickness 2.2 μm and 0 μm.

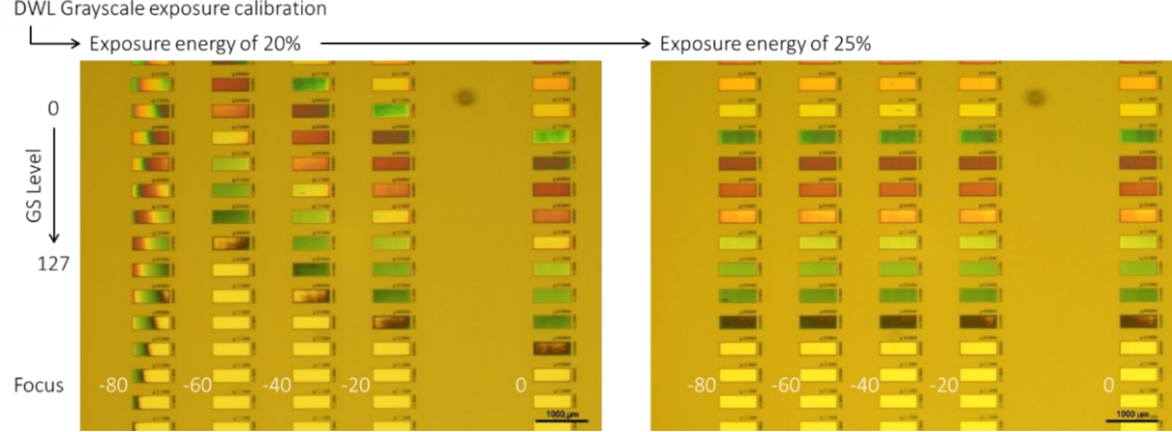

Figure 5-4 – Optical microscopic images of the grayscale calibration exposure for 20% and 25% energy.

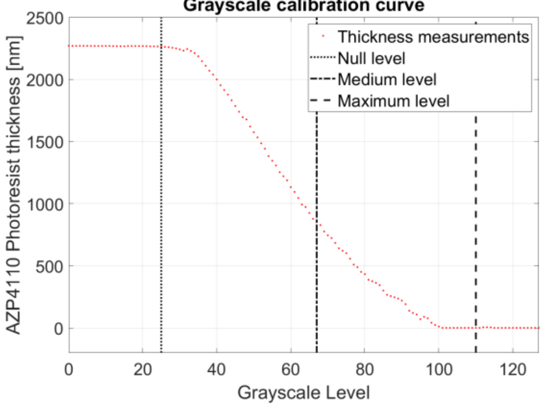

Figure 5-5 – Grayscale characterization curve, showing that at least 80 different GS levels are possible.

This technique facilitates the precise patterning of perfectly aligned multilevel structures, wherein each GS level corresponds to a different thickness to be patterned on the silicon substrate. In the MEMS mirror design, only three GS levels were used to define the asymmetric comb electrodes, which presented a final resist thickness of 0 μm (maximum level), 1.1 μm (medium level) and 2.2 μm (null level), as depicted in the topography measurement of Figure 5-6.

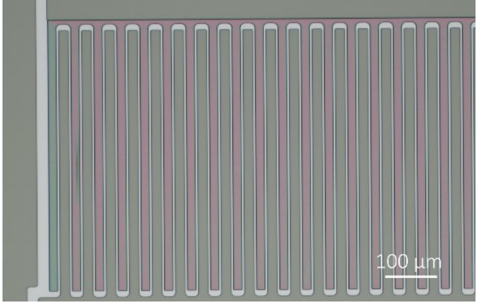

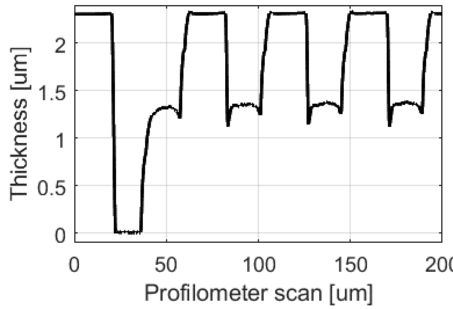

Figure 5-6 – Mechanical profilometer scan of the photoresist thickness after GS lithography on the asymmetric electrodes.

GS exposure alignment with previous process steps

To analyse the success of the implementation of grayscale lithography in MEMS asymmetric structures, experimental runs with a MEMS mirror preliminary design were conducted. Here, an initial metal layer was patterned in a single-side polished (SSP) wafer with the electrical pads and alignment marks to analyse the alignment conditions of grayscale lithography. Using the standard alignment conditions of the DWL system, a large misalignment between the GS mask and the previously patterned metal layer was obtained, as shown in Figure 5-7.

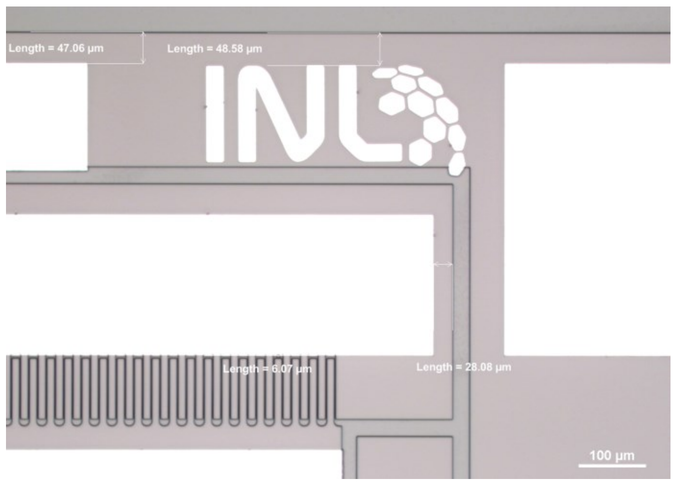

Figure 5-7 – Optical microscopic image and measurements of the alignment between the grayscale lithography with previous masks

This offset, while proving to be a systematic offset in GS lithography using the DWL 2000 from Heidelberg, was characterized for the first time at INL in these experimental tests, as it marked the initial attempt at aligned grayscale lithography. This misalignment can be effectively compensated prior to the grayscale exposure, ensuring accurate alignment in future runs.

Multilevel pattern transfer and EKC Cleaning to remove passivation layer

With the target interelectrode gap aspect ratio of the MEMS mirror of 16.7 (on FS, 50 µm-deep/3 µm-wide), the difficulty of obtaining the multilevel topography in the silicon without removing and damaging the GS photoresist mask increases, given the different etch rate of silicon and

photoresist and the resulting selectivity during the etching process. To address this issue, sacrificial hard-mask layers were employed, and the multilevel pattern was transferred by a sequential RIE on the SPTS APS system and photoresist thinning process.

The FS silicon patterning can be considered the most critical step of the micromachining process. The target topography implies several inspections since the goal is to achieve the same silicon layer features with 50 μm of thickness, others with 20 μm, and others where the silicon is completely removed, reaching the BOX layer. Taking advantage of the high substrate-to-mask selectivity of the etching process, a sequential iterative etching process is used to etch the FS silicon layer to different discrete depths in the various regions defined by the multiple GS mask levels. An initial silicon etch step, through DRIE on the SPTS Pegasus system, based on the etch time is performed, followed by a hard-mask thinning phase by RIE on the SPTS APS system. At this point, an accurate final DRIE silicon etch step is performed to thin down the exposed electrodes to a 20 μm thickness.

This means that, in the current multilevel transfer process, after the first silicon etch step, the walls of the asymmetric electrodes are covered with a passivation layer. In the second DRIE step, during the substrate thinning, these organic residues from the first step can work as a mask and jeopardize the success of the process and the performance of the final device. To address this problem, different cleaning processes were experimentally analysed, from oxygen strip and plasma ashing to EKC processes cleaning, being only the last one capable of demonstrating success in the removal of the remaining passivation layer. Figure 5-8 displays SEM images of different experimental runs of the multilevel asymmetric electrodes sequential DRIE process, with and without the organic residue cleaning process.

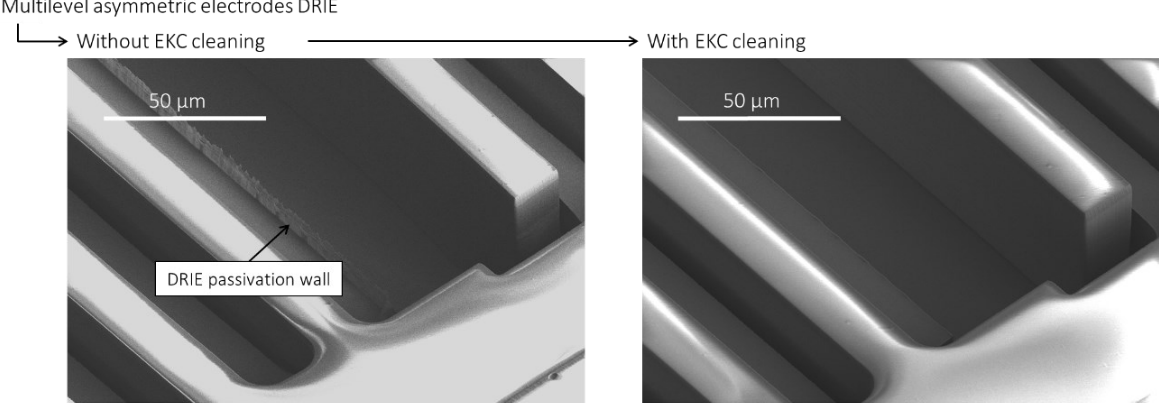

Figure 5-8 – Multilevel asymmetric electrodes SEM images after the sequential DRIE process, with and without the organic residue cleaning process.

As can be observed in the left image, the thinned electrodes present a thin DRIE passivation wall that, after some cycles of DRIE, can start to work as a mask to the following the silicon patterning. In this case,

the edge of the thinned electrode does not present the desired thickness. Moreover, these walls can even break during the etching process and form a bridge between the movable and the fixed electrodes, constraining the removal of the silicon that is in the electrodes' gap under the passivation wall, which will result in the non-release of the movable structure of the MEMS mirror. The EKC cleaning process successfully removes these residues, as shown in the right image, increasing the yield of the overall MEMS process.

5.1.4 Back-side (BS) process optimization

The handle layer patterning was also subject to several experimental processes analysis and optimization.

BS MEMS mirror cavity

The BS MEMS cavity underneath the movable mirror structure is important to ensure the desired free motion of the final device. Figure 5-9 presents optical microscopic images of the MEMS cavity process on the non-polished BS of an SSP test wafer in order to mimic the final SOI process as closely as possible. As observed, the granularity of the BS face makes it difficult to inspect this process optically; however, this does not represent a problem in the MEMS process since a double-sided polished (DSP) SOI wafer will be used.

The BS design was etched into the silicon layer by the DRIE process on the SPTS Pegasus system. This process posed several challenges. One of them was the variation in the etch environment across different parts of the layout. The larger regions, namely the cavities, exhibited a significantly higher etch rate compared to the springs and trenches areas, where the etch rate decreased notably along the silicon etch process. As a result, some areas reached the etch stopper much earlier than others, and in some regions of the wafer, where the BOX layer presented some damage, the silicon device layer was even etched from the bottom.

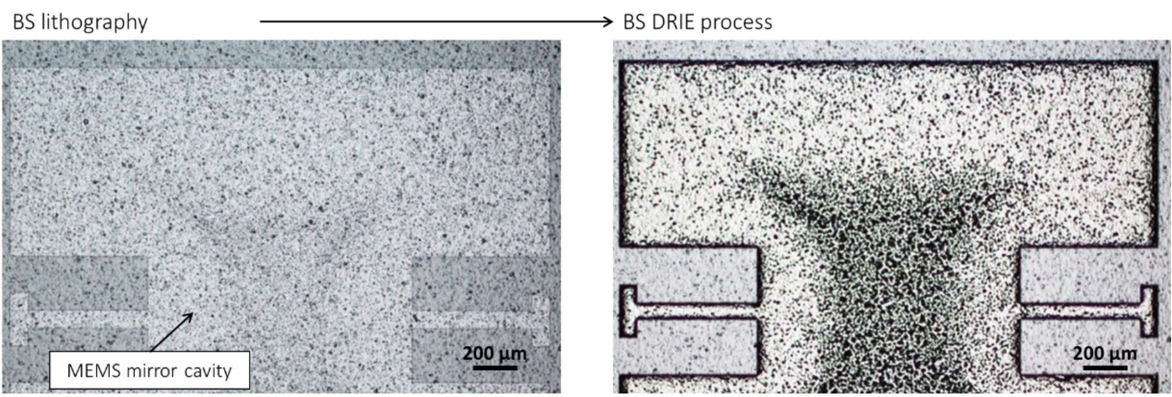

Figure 5-9 – Optical microscopic images of the BS mirror cavity process.

Furthermore, the formation of needle-like structures, also known as “grass” or black silicon, was observed in these large cavities, which is a critical issue during anisotropic etching of silicon using DRIE, as illustrated in the SEM image in Figure 5-10.a. The formation of grass is caused by various micro-masks on the silicon surface, which can appear, for example, by re-sputtering of the existing mask material. This issue can be minimized by the uniformization of the layout trenches' size, thus ensuring a more uniform etch environment across the wafer. For that, sacrificial grid-like structures can be designed in the large cavities, as depicted in Figure 5-10.b, and afterwards removed at the end of the process by the HF vapour process.

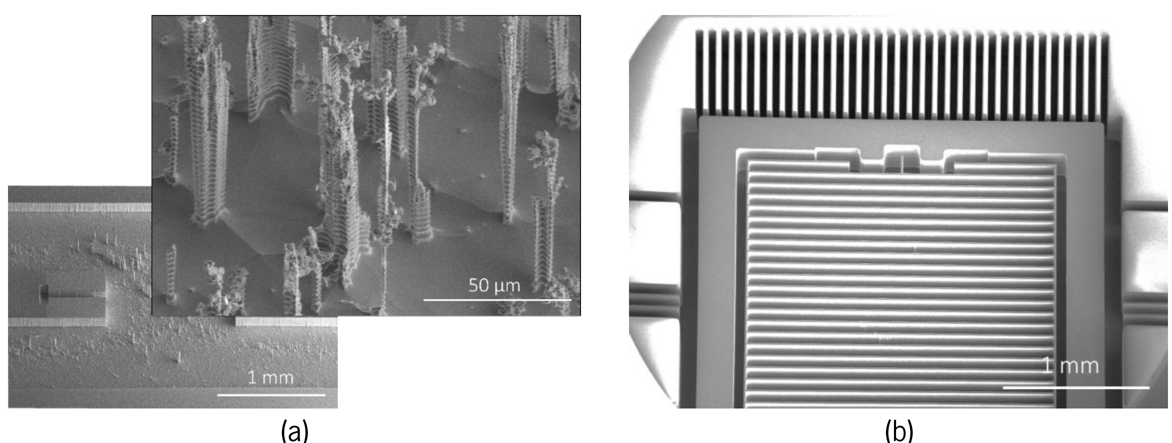

Figure 5-10 – Silicon grass SEM image of the MEMS mirror cavity (a) and on the sacrificial grid solution (b).

Handle layer gap size and fast Silicon DRIE process optimization

In the 2D MEMS mirror design, the slow axis electrodes present high aspect ratio (1:20) features, e.g. 30 μm width through the SOI 625 μm handle layer, and it is very challenging to fabricate them. A series of tests were conducted in the manufacturing process in order to find the minimum gap/trench possible on the back side, i.e., the minimum dimension where it is possible to etch the silicon entirely up to the oxide barrier in the handle layer. In this layer, thin gaps are difficult to achieve since the total thickness of this layer is large.

In a 725 μm thick silicon dummy wafer, several lines with 10 μm to 40 μm thickness were patterned. The set that was able to remove the total silicon was 25 μm-width, so this is the minimum gap on the back side established in the design of the device. However, the resulting structures may not exhibit high gap uniformity depending on the depth.

Several studies have reported on the influence of the different DRIE process parameters on the etched feature characteristics and quality of the process [164], evidencing trends in etch rate and sidewall angle variation with bias power, chamber pressures, and trench widths [165] and the appearance of sidewall

defects [166], notably relevant in deep silicon trenches. None of these studies have reported on the variation of these process trends at wafer scale.

In order to evaluate different etch conditions, the sets of trenches ranging from 10 µm to 500 µm width were repeated across the wafer, covering the whole wafer area (Figure 5-11.a), employing different DRIE process parameters [167]. The wafers were diced across the trench sets, and each trench cross section was imaged using an automatic optical inspection system setup, generating a large dataset of 143 images per process condition. A computer vision algorithm was developed in partnership with the Laboratory of Automation and Robotics from the University of Minho using the OpenCV library to process a large number of cross-section images automatically and extract relevant features. In this analysis, the images are first horizontally aligned, and the four trench corners are determined. The cavity contour points are linearly fit to extract the average straight lines corresponding to the wafer surface, left and right sidewalls, and the trench floor. The depth of the cavity is determined from the midpoint of the trench floor, and the sidewall angles are measured from the cavity top to each side as in (Figure 5-11.b). An error metric is defined as the deviation of the contour points to the linear fit, which increases in the presence of the wall defects.

Using this extracted data, a quantitative evaluation of the influence of different process parameters on trench features was performed at a wafer scale. Sidewall angles tend to increase with trench width, with improved variation across the wafer, for lower flow rates (Figure 5-12.a) but depend little on gas pressure (Figure 5-12.b). The etch rate shows a strong dependence on the etching pressure, while the correlation with the flow rate seems weak (Figure 5-12. c). Here, etch lag is observed as expected [168] but appears to reduce for trench widths above 100 µm. It was verified that wall defects are reduced for lower etch pressures, although this comes at the cost of reduced etch rate. Instead, by decreasing the gas flow, it was observed that both defects and uniformity were improved without a significant impact on the etch rate.

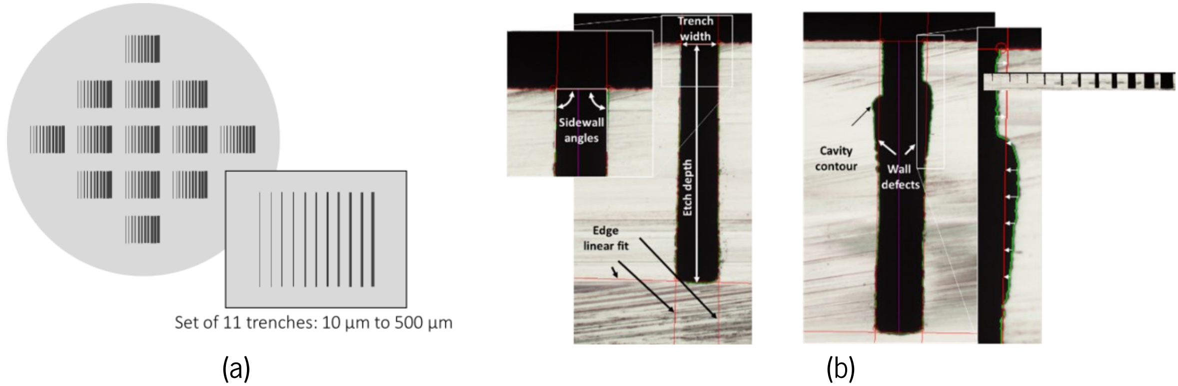

Figure 5-11 – (a) Representation of the mask used to define the trenches on the whole wafer area. (b) Acquired cross sections of an example set of etched trenches with features extracted from trench cross sections using automatic computer vision algorithm.

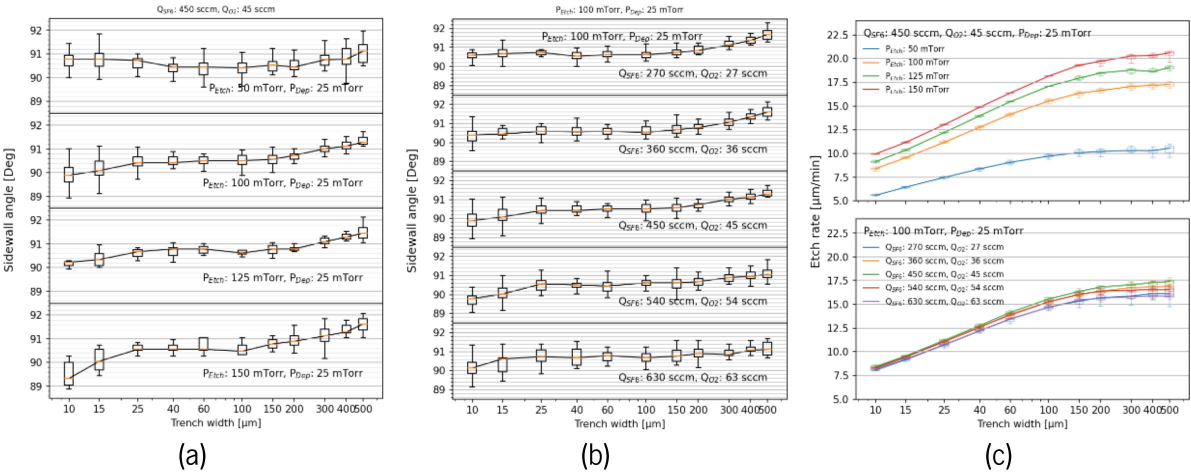

(a) (b) (c)

Figure 5-12 – Wafer scale analysis of sidewall angle for different etch gas flow rates (a) and etching chamber pressures (b). Etch rate trends for gas flow rate and etching chamber pressure variation (c).

The sidewall quality was improved, using a lower gas flow rate when etching deep electrostatic comb actuators, allowing for better feature definition, production yield and device reliability. Figure 5-13 presents examples of SEM images of different etching iterations with different DRIE process recipes for the MEMS mirror BS layout.

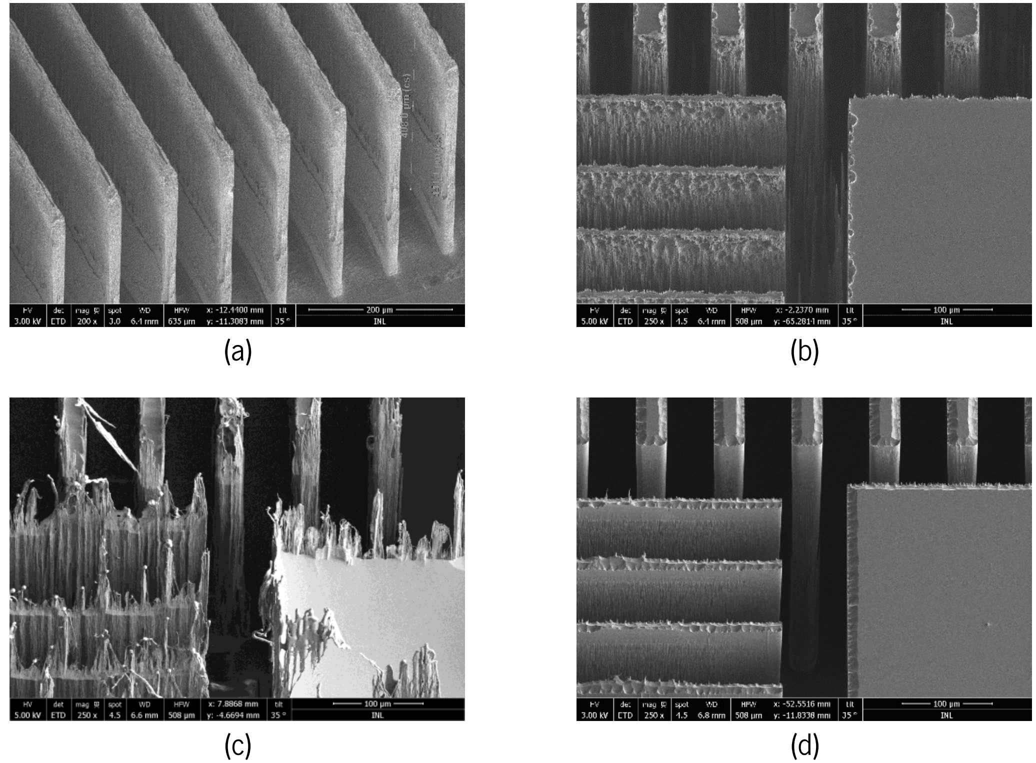

Figure 5-13 – Back side DRIE etching tests with different recipes.

Variations in the recipes, such as temperature and pressure, among others, were considered between iterations. As can be seen, the wall quality changes a lot with the small difference in the etching recipe, and it also depends highly on the layout. For example, in (a), at certain depths, wall defects started to appear, which propagated as the etching proceeded. Then, the required thinning of the back-side frame

resulted in ion bombardment defects on the walls (b) and flaking (c). In the end, a DRIE recipe optimized for the 2D MEMS mirror design with a high wall quality for the aspect ratio desired (relation between electrode gaps and electrode thickness) was reached (d). SOIs with thinner back sides (e) resulted in further minimization of wall defects and improved finger quality for electrostatic operation.

Back-side multilevel mask with double lithography process

Since the BS multilevel mask does not present such critical features that must be perfectly aligned, it was possible to implement the multilevel topography using two separate exposure steps. The second mask level was created by two sequential lithographies instead of using grayscale lithography, following the process flow presented in Figure 5-14.

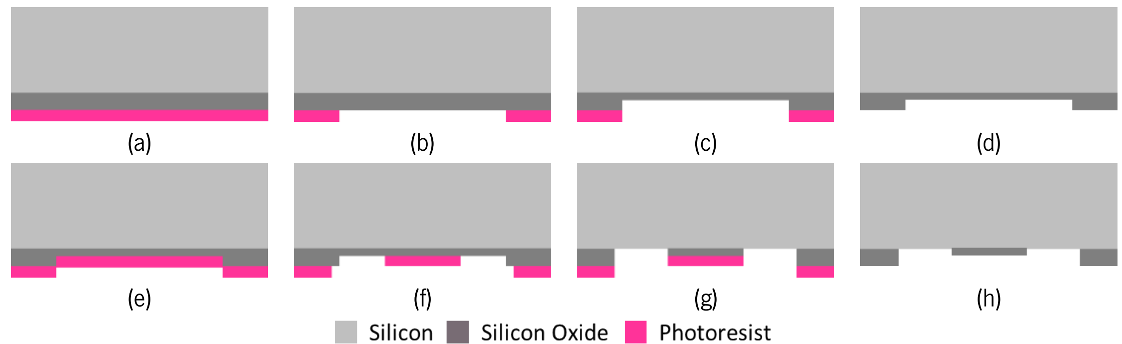

Figure 5-14 – Process flow of BS double lithography process to create multilevel mask without grayscale lithography.

The first mask (Figure 5-14.a-b) contains the areas where it is desired to remain with the full thickness of silicon. This mask is then transferred to the silicon oxide layer, but only half of the SiO_2 thickness is removed (Figure 5-14.c-d). The second mask (Figure 5-14.e-f) has the areas desired to have the entire thickness and thinned thickness (patterned in the SiO_2 thinned areas). The exposed SiO_2 layer is then again etched until the silicon surface (Figure 5-14.g-h). The optical microscopic images after the first lithography and the second are presented in Figure 5-15. As seen in image (a), the patterned layout presents the device frame and (b) the thicker device frame mask and the thinner mask with the BS electrodes and inner axis frame.

Figure 5-15 – OM images of BS double lithography process to create multilevel mask without grayscale lithography.

5.2 MEMS Mirror micromachining process on SOI wafer

The devices under consideration were micromachined on a 200 mm 50 µm-thick SOI wafer. The handle layer was thinned to a 400 µm-thickness by grinding techniques prior to the MEMS micromachining process since the desired BS electrode features were not feasible to be fabricated with an initial handle thickness of 650 µm. Here, the INL's standard MEMS micromachining process was adapted and optimized to manufacture the FS asymmetric electrodes and the BS mechanical frame. Figure 5-16 depicts the primary steps of the 2D MEMS mirror merged with a DOE micromachining process through cross-sectional diagrams.

(a) (b) (c)
(d) (e) (f)
(g) (h) (i)
(j) (k) (l)
(m) (n) (o)
(p) (q) (r)

Resist Silicon BOX Metal

Figure 5-16 – 2D MEMS mirror with DOE micromachining process steps.

The process consists of several steps, including: (a) SOI Wafer preparation; (b) DOEs lithography and FS silicon etch; (c) Organic residues cleaning process; (d) Sputtering of a thin film of aluminium; (e) Patterning of the metal layer; (f) FS SiO_2 layer deposition; (g) BS SiO_2 layer deposition; (h) BS grayscale

lithography; (i) BS grayscale hard-mask patterning; (j) FS grayscale lithography; (k) FS grayscale hard-mask patterning; (l) FS 1st DRIE; (m) FS SiO_2 hard-mask thinning; (n) FS 2nd DRIE, using the buried oxide layer (BOX) as etch stopper; (o) BS 1st DRIE; (p) BS SiO_2 hard-mask thinning; (q) BS 2nd DRIE, using the buried oxide layer (BOX) as etch stopper; (r) Structures release using Hydrogen Fluoride (HF) vapour etching. The MEMS mirror's cross-sectional diagram is presented in Figure 5-17.

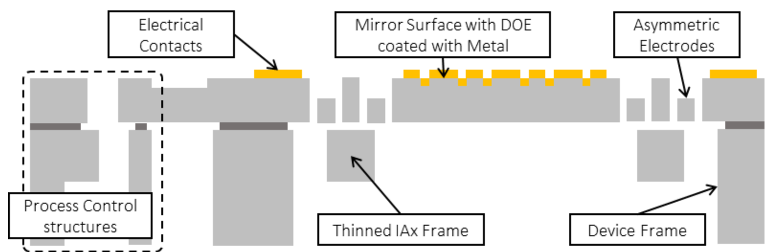

Figure 5-17 – Cross-section schematic of the 2D MEMS mirror with DOE structure.

In the wafer's device layer, the mirror reflective surface, the inner and outer axes' torsional springs, and the actuation asymmetric electrodes were micromachined. In the handle layer, the device's fixed frame with a cavity to suspend the mirror, BS electrodes, and an inner axis movable frame were patterned. This inner frame mechanically attaches the inner axis electrical routes and needs to be thinned to ensure the free motion of the outer axis.

5.2.1 Wafer preparation

Since the MEMS mirror design presents active features in the device and handle layer, it is important to process the two layers with a fine alignment between each other. Given that, initially, the alignment marks (AM) of the FS were patterned and etched through a Slow Si Deep Reactive Ion Etching (DRIE) process, and the photoresist of the lithography was removed on the Plasma Asher system. Once the marks were ready on the FS, it was necessary to undergo the same steps to add AM in the BS using the mask aligner lithography system. Then, the BS AMs were patterned in the BS oxide layer by a RIE process.

5.2.2 DOE pattern and reflective layer

The patterning of the diffractive grating topography was directly executed on the device's active layer. Initially, a thin layer of photoresist (PR) was coated and using the DWL lithography technique, the DOE pattern was exposed onto the PR. After this step, the desired pattern is transferred to the silicon wafer through a slow silicon etch recipe with the desired depth in the SPTS ICP tool. Finally, the wafer passes through an organics cleaning step to remove the photoresist. The diffractive optical element pattern is detailed in Figure 5-18, where the pitch desired for the grating presented the desired sizes. The final DOE

depth achieved using the ICP system was 390.9 nm, with a non-uniformity of 16.1% along the wafer. Then, a thin non-conformal layer (500 nm) of AlSiCu was sputtered and patterned through a wet-etch process on the wafer front-side to create the device electrical contacts, the mirror coating, and the FS alignment marks, as can be observed in Figure 5-18.

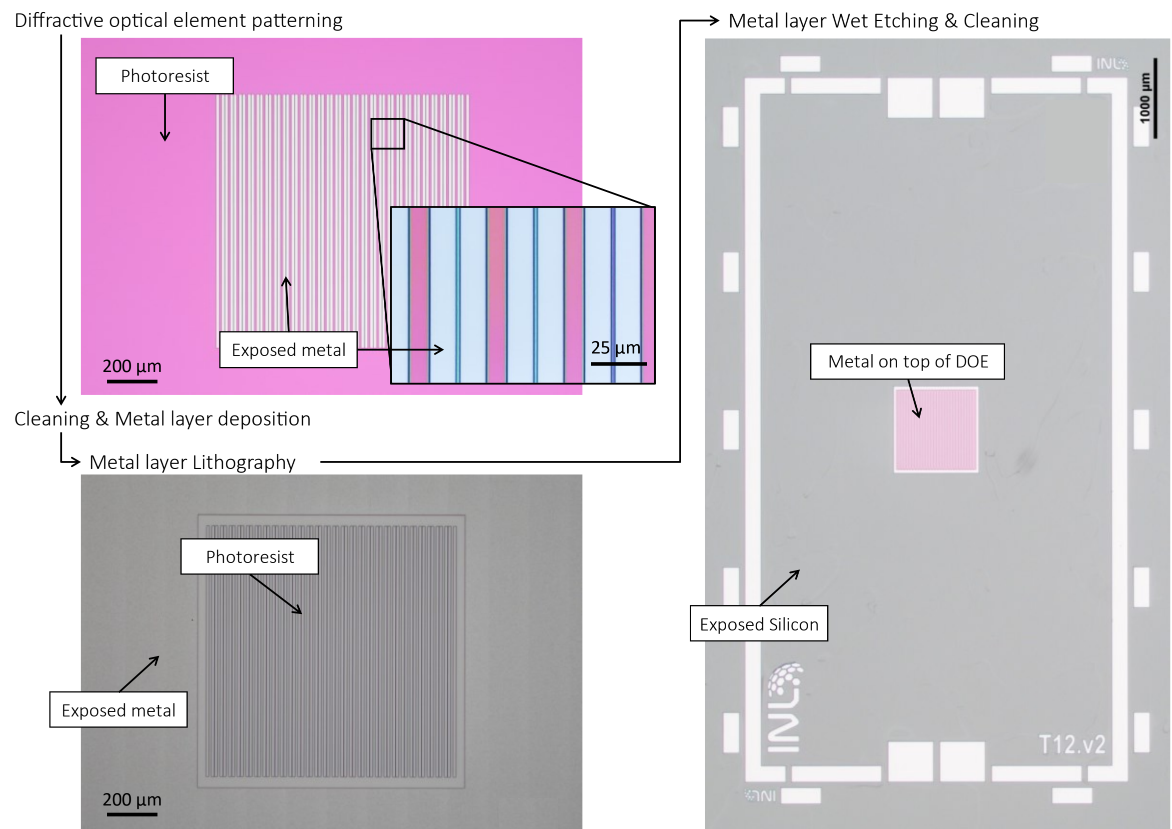

Figure 5-18 – Optical microscope images of the DOE and metal steps of the 2D MEMS mirror process.

5.2.3 Silicon oxide (SiO_2) Hard-masks

A thick layer of silicon oxide (3 µm of SiO_2) was deposited on both sides of the SOI wafer by Plasma Enhanced Chemical Vapor Deposition (PECVD) on the SPTS CVD system, Figure 5-16 (f) and (g). The SOI wafer prior to the micromachining process already presents, from the manufacturer, a 2 µm thermal SiO_2 layer on the BS; this means that with the addition of a 3 µm-thick layer, the handle hard-mask has a thickness of 5 µm. Besides serving as hard-mask, these layers also present a critical role in stress compensation to adjust the wafer bow for the subsequent processes.

For the FS mirror design (mirror structure, springs, and electrodes), a multilevel mask with three different thicknesses of photoresist was exposed as well as on the BS mirror design (inner thinned frame, outer axis electrodes). Since the critical parts of the device are entailed in the device layer, the BS mask was

the first to be patterned. In order to keep a uniform etch environment across the devices on the BS process, a sacrificial grid was designed in the mirror cavity, ensuring the same trench size in this area.

The multilevel mask of the BS is achieved by a double lithography using a DWL binary exposure system, Figure 5-19. By a sequential process consisting of mask exposure – SiO_2 RIE – PR removal, a hard-mask layer with three different levels/thicknesses (5 µm, 2.5 µm, and 0 µm) was achieved. Figure 5-20 presents optical microscopic images of the BS multilevel mask.

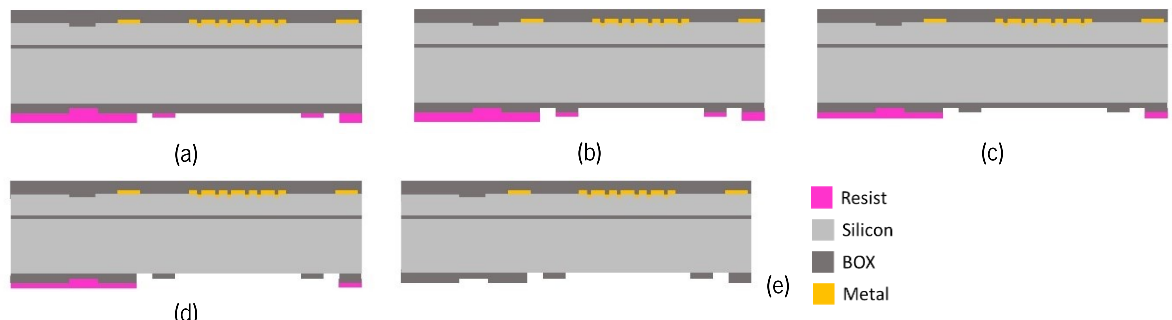

Figure 5-19 – Cross-section process flow of the BS hard-mask patterning of the 2D MEMS mirror.

Figure 5-20 – Optical microscope images of the BS hard-mask of the 2D MEMS mirror process.

The FS multilevel masks can be achieved using DWL grayscale or through NIL lithography with a previously developed master, Figure 5-21. The complex process of transferring the previously developed multilevel photoresist mask to the SiO_2 layer was executed by a sequential process of silicon oxide etching

using RIE and thinning of the photoresist mask through an O_2 plasma strip, resulting in a multilevel topography on the hard-mask layer. This topography comprised three distinct levels with varying thicknesses: 3 µm, 1.5 µm, and 0 µm. It is important to note that each mask step height was intentionally designed with an additional thickness to compensate for the mask material that would be removed during the etching of the substrate material.

The sequential process of SiO_2 RIE and resist strip requires careful inspection through the overall process in order to ensure that the oxide layer is completely removed from the electrode gaps without increasing the gap size and still presents enough thinned mask for the following steps. Figure 5-22 presents optical microscopic (OM) images of the FS multilevel masks.

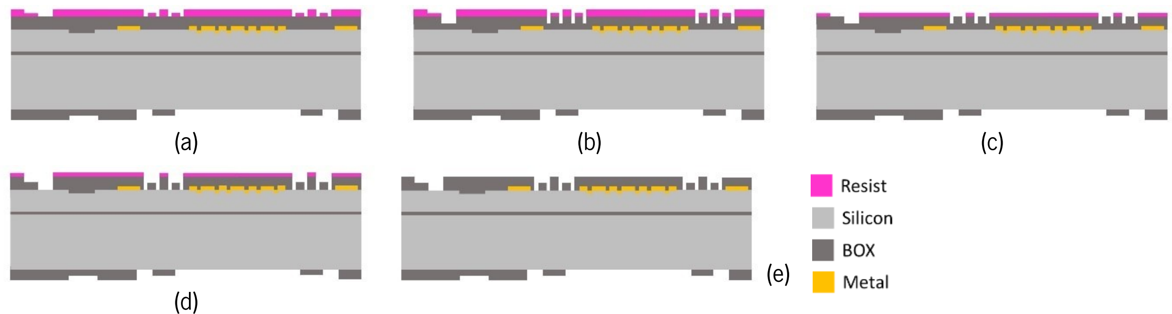

Figure 5-21 – Cross-section process flow of the FS multilevel hard-mask patterning of the 2D MEMS mirror.

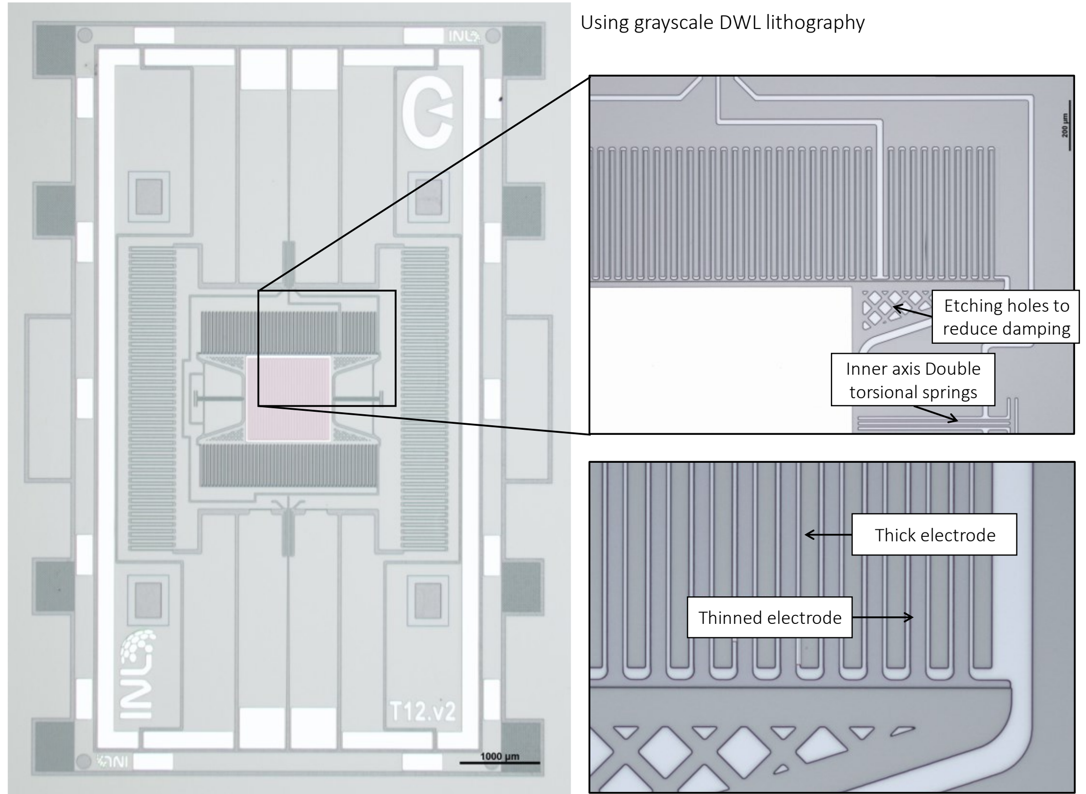

Figure 5-22 – Optical microscope images of the FS multilevel hard-mask of the 2D MEMS mirror process.

5.2.4 Structure Etching

It is essential to etch the structures on the FS first and only after those, the ones on the BS. This order is due to the etch stopper, which is the oxide layer between the active and the handle layers, and it is crucial that the oxide layer is intact for the most sensitive and small structures, like springs or electrodes. A particularity of the design of the masks was the etch environment of the process, i.e., the masks were designed to ensure uniformity in the silicon etching during fabrication. This is expected if there are no significant differences in the size of the various gaps in the device layout. Therefore, in the FS, the gaps are within the range of 2.8 μm and 50 μm and in the BS between 35 μm and 80 μm. The FS silicon target topography presents areas with 50 μm of thickness, others with 30 μm, and others where the silicon is completely removed, reaching the BOX layer, as presented in the schematic of Figure 5-23. If this final condition is not perfectly performed, the overall performance of the device is compromised since the actuation electrodes can be electrically and mechanically connected. The BS etch is important as well since the mirror's inner frame must be thinned to 200 μm of thickness, while the cavity below the mirror has to be removed for it to be free to move. The structure etching process followed these next steps:

- The etching of the FS structures using the SPTS Pegasus and APS systems;
- Thermal tape application in the FS to protect the structures already etched on this side;
- BS structures etching, also using the SPTS Pegasus and APS systems;
- 5Finally, FS thermal tape removal and cleaning of the residues left on the wafer from the etching process and thermal tape through an O_2 cleaning.

Device layer

A sequential iterative etching process was used to etch the FS silicon layer to different discrete depths in the various regions defined by the multiple GS mask levels. The exposed substrate was etched, in different steps, through DRIE on the SPTS Pegasus system, based on the etch time, Figure 5-23.b. Each substrate etching step is followed by a SiO_2 hard-mask thinning process, performed by RIE on the SPTS APS system, to expose the substrate in the next GS region (Figure 5-23.c), enabling further etching of the substrate. Then, an EKC cleaning process of the organic residues resulting from the DRIE process was performed since this, during the substrate thinning, can become a mask and pattern the silicon, as detailed in the preliminary studies sub-section.

In the first etching step, a depth of 40 μm is defined in the substrate, creating the necessary depth ratio that allows the next etch process to achieve the desired substrate topography. The SiO_2 mask on top of

the thinner electrodes is then removed, exposing the substrate in these regions. Subsequently, during the second etching process, the exposed substrate is etched, resulting in a 30 μm thickness in the electrodes, while in the previously partially etched regions, the BOX (buried oxide) is reached, decoupling the movable of the fixed asymmetric electrodes. Figure 5-24 presents the evolution from the multilevel SiO_2 hard-mask to the asymmetric silicon structures, where the two silicon levels are easily identified.

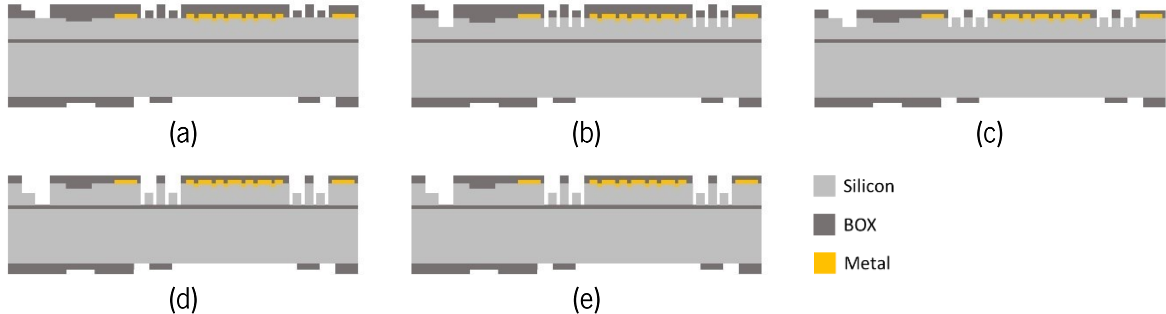

Figure 5-23 – Cross-section process flow of the FS multilevel transfer to the device layer of the 2D MEMS mirror.

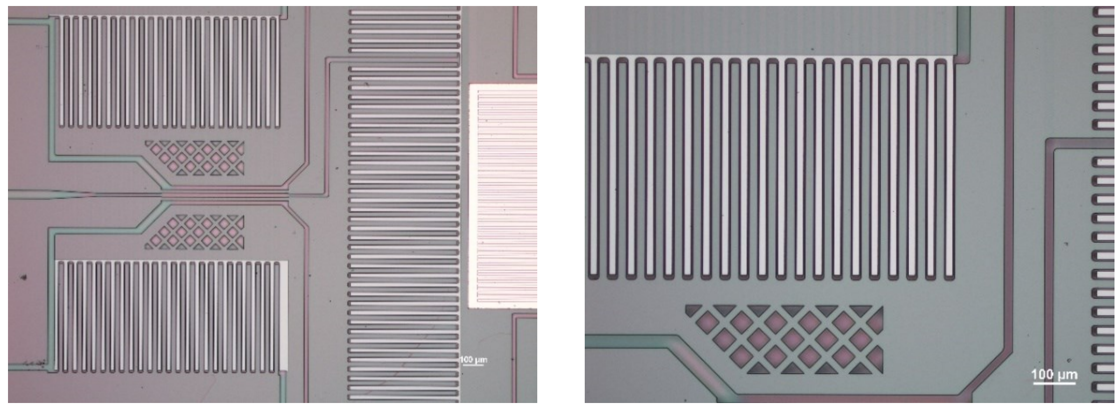

Figure 5-24 – Optical microscope images of the FS multilevel transfer of the 2D MEMS mirror process.

As can be seen in Figure 5-24.b, the gaps between electrodes are entirely aligned, i.e., the gaps are equal on both sides of the electrodes. This is a crucial feature in this type of actuator since the electrostatic forces in the plane must be in equilibrium. Figure 5-25 presents SEM images of the fabricated actuators.

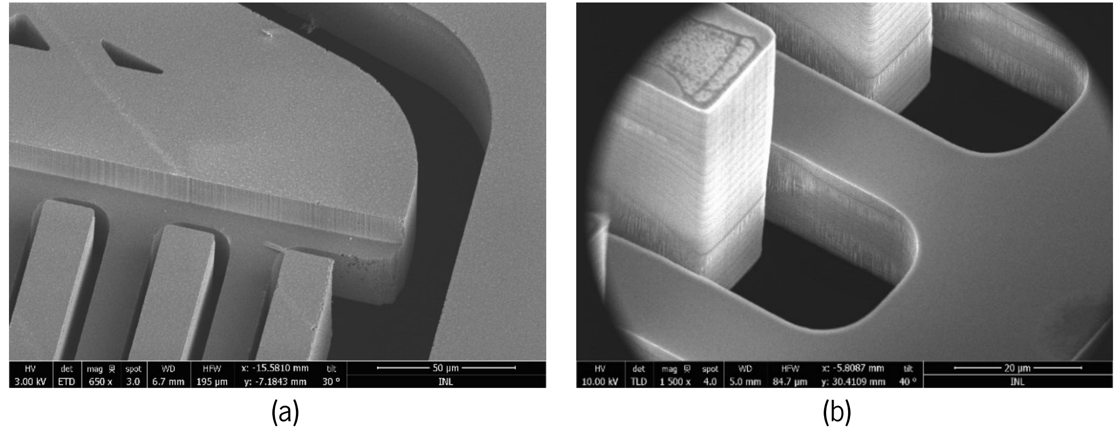

Figure 5-25 – SEM images of the asymmetric electrodes.

Handle layer

The BS was also etched with a sequential iterative etching process, using a thermal tape to protect the already patterned structures of the device layer, as detailed in Figure 5-26. As shown in Figure 5-27, in this layer, the thinned inner axis frame, the outer axis fixed electrodes, and the mirror cavities are patterned to allow the free movement of the mirror. The DRIE process used in this step was much more aggressive than the one used for the device layer in order to minimize process time and costs, and it was optimized to increase the handle walls' quality.

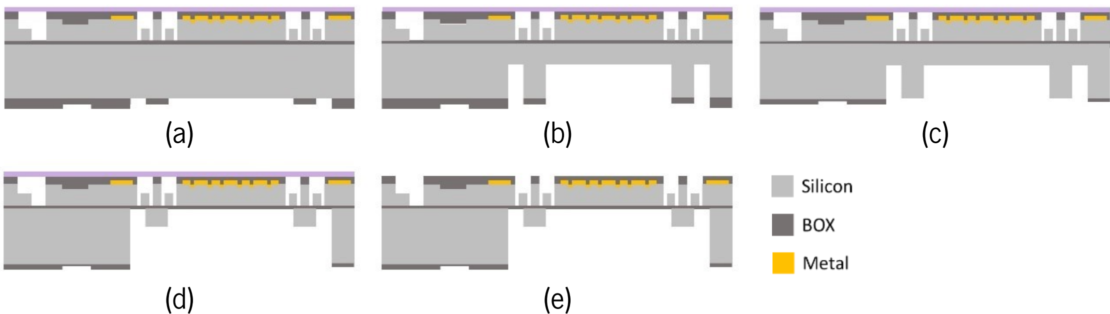

Figure 5-26 – Cross-section process flow of the BS multilevel transfer to the handle layer of the 2D MEMS mirror.

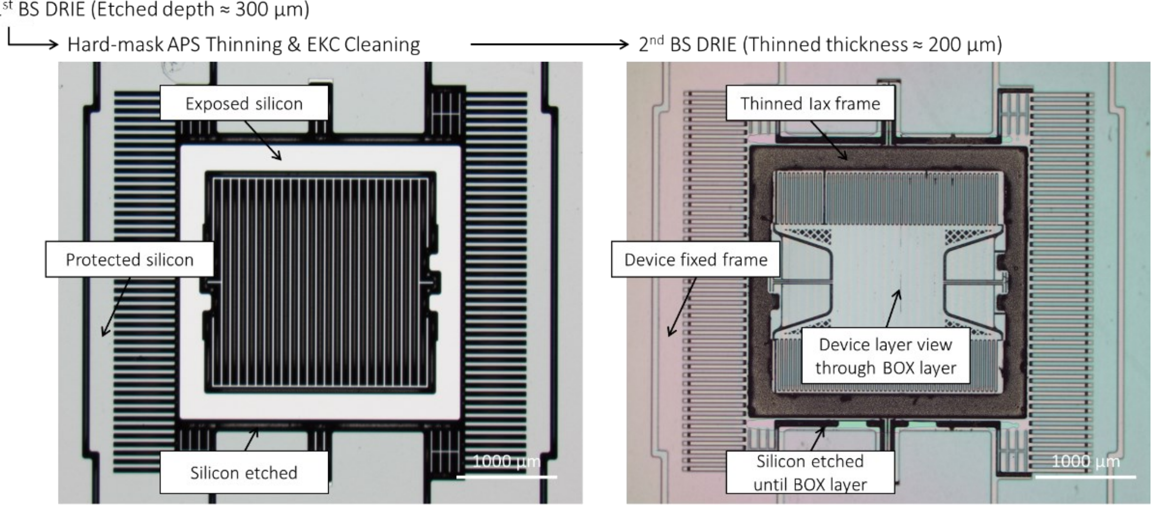

Figure 5-27 – Optical microscope images of the BS multilevel transfer of the 2D MEMS mirror process.

5.2.5 Structure release

The phase of structural release involves the deliberate removal of the exposed BOX, which is accomplished using the SPTS Primaxx – HF Vapour Etcher. This step is specifically designed to achieve isotropic etching of the sacrificial layers of silicon oxide. By employing a combination of steam Anhydrous hydrogen fluoride (HF), and alcohol vapour, the silicon oxide that has been exposed is successfully eliminated from the structure. Importantly, this dry process effectively prevents unwanted stiction of released moving parts or potential damage to delicate structures.

During the HF process, the patterned wafer is positioned over a dummy wafer, with four supports placed along the edges to ensure a reasonable distance between the two wafers. This approach guarantees that when the structures are suspended by the springs, they do not adhere to the dummy wafer. Typically, in the manufacturing process, MEMS structures are separated by dicing, which, unfortunately, results in the breaking of several delicate devices. However, these particular devices have distinct features that enable their separation.

To achieve this, a dicing-free [129] trench with a width of 50 µm was incorporated around the sensor in the BS mask. Similarly, the FS mask also had a trench with the same width overlaid on the BS, with supports on each corner measuring approximately 1 mm x 1 mm, complete with etching holes. These supports are designed to ensure that during the HF process when the oxide between the device layer (on the brackets) and the handle layer is removed, the die falls and is suspended by the four supports. Consequently, the device becomes independent of the wafer, making the dicing step unnecessary.

The trenches have been designed by outlining two rectangular shapes in both layers. As a result of the oxide removal process, the interior of these rectangles and the sacrificial grids become free and fall down, creating two holes outside the structure and revealing the mirror cavity. These two openings allow the sensor to be extracted from the wafer with the use of tweezers. Figure 5-28 displays the completed wafer, featuring the aforementioned tweezer holes.

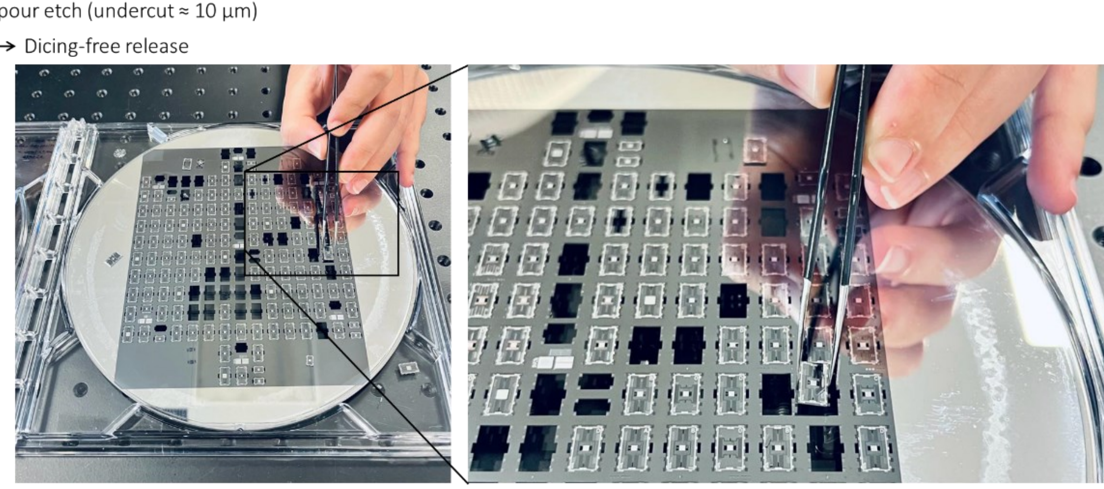

Figure 5-28 – Released devices suspended on DOI wafers frame.

5.2.6 Fabricated 2D MEMS mirrors with DOEs

Figure 5-29 shows SEM images of the fabricated devices, presented in the previous sub-sections (an overall device image, a zoom image in the mirror spring of the fast and slow axis). The mechanical

characterization of the fabricated devices was performed to ensure that all the designed features meet the fabrication specifications.

(a)

(b) (c)

Figure 5-29 – SEM images of the fabricated 2D MEMS mirror device.

The gaps between the two electrodes are perfectly aligned, i.e., the gaps are equal on both sides of the electrodes. This is a crucial feature in electrostatic actuation since when an actuation voltage is applied, the in-plane electrostatic forces must be in equilibrium, and only the out-of-plane force should induce the torsional motion of the mirror. It can also be noticed that the gap of 3 μm was over-etched, resulting in a

gap of 3.5 μm in the fabricated devices. This over-etch of the trenches with respect to the mask is correlated with the GS exposure, DRIE processes and geometry/depth-dependent and was accounted for in order to not compromise the performance of the mirror. All the other mechanical features, such as spring dimensions and mirror area, are within the design specifications, with variations below 4 % and 0.08 %, respectively. The two silicon levels are easily identified in both Figure 5-29.b.

The fabricated devices presented the desirable features, proving that this novel technique of using a multilevel bulk micromachining process is an excellent and reproducible technique. It also proves to be an effective way to create robust multilevel structures with a reduced fabrication process. The DOE pattern on top of the MEMS mirror surface is highlighted in Figure 5-30.

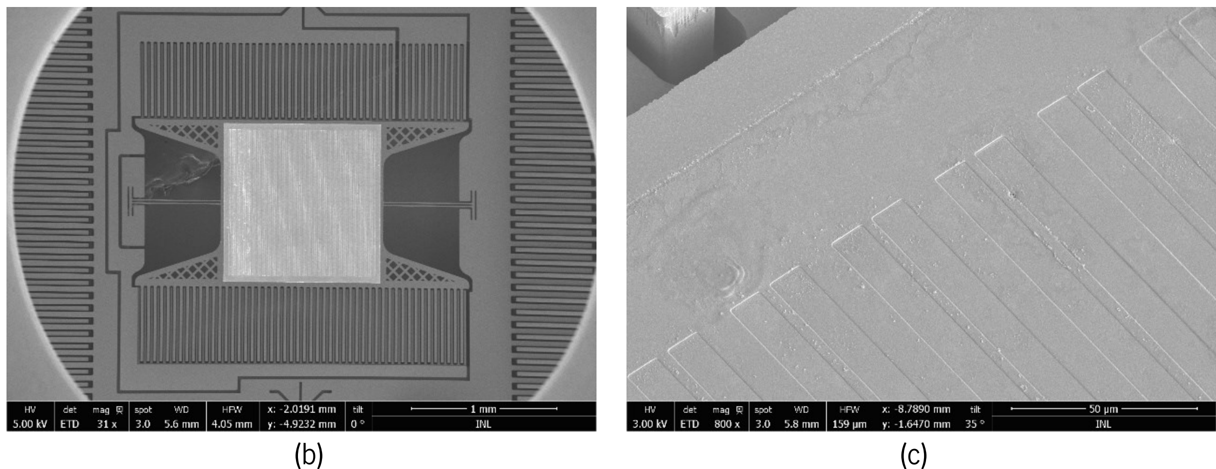

(b) (c)

Figure 5-30 – SEM images of the Dammann grating entailed in the reflective surface of the 2D MEMS mirror.

5.2.7 Process simplification for 1D MEMS mirror

A 1D MEMS mirror, with the explicit aim of experimentally validating the theoretical mechanical models, was also micromachined, serving as a preliminary step prior to the realization of a 2D MEMS mirror. For this reason, it does not present the implementation of the diffractive optical element integrated into its reflective surface. Additionally, the micromachining process was thoroughly optimized using these devices, being used as the base for the nanoimprint lithography developments, which are further explained. This sub-section provides comprehensive details of the 1D MEMS mirror micromachining process. These devices were fabricated in a 200 mm SOI wafer with a device layer 50 μm-thick. In Figure 5-31, the main steps and cross-sectional views of the MEMS mirrors' micromachining process are depicted. These consist of: (a) SOI Wafer preparation; (b) Sputtering and patterning of a thin film of aluminium; (c) FS and BS SiO_2 hard-mask layer deposition; (d) BS hard-mask patterning; (e) FS grayscale lithography; (f) FS grayscale hard-mask patterning; (g) FS 1st DRIE; (h) multilevel mask thinning; (i) FS 2nd

DRIE, using the buried oxide layer (BOX) as etch stopper; (j) BS DRIE, using the BOX as etch stopper; (k) Structures release using Hydrogen Fluoride (HF) vapour etching.

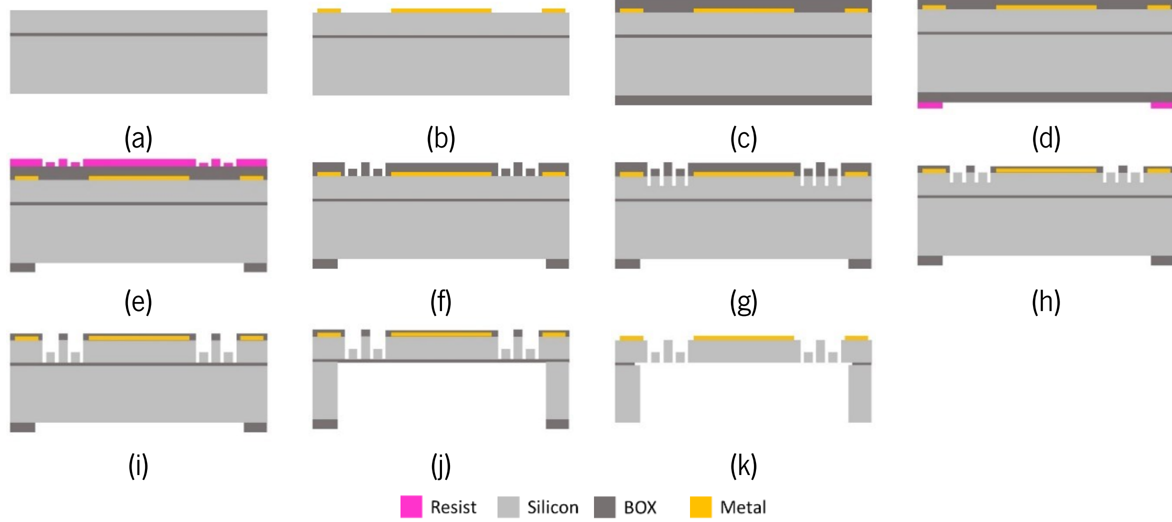

Figure 5-31 – 1D MEMS mirror micromachining process steps.

In Figure 5-32, the SEM images of the final fabricated 1D mirror design presented previously (an overall device image, a zoom image in the mirror spring, and the electrodes) are shown. The fabricated devices presented the desirable features, proving that this novel technique of using a multilevel bulk micromachining process is a reproducible technique. Besides, it also proves to be an effective way to create robust multilevel structures with a reduced fabrication process since it requires fewer lithography exposure steps [116]

5.3 Packaging

After the release from the devices' manufacturing, these were mounted in a customized package solution that can be used as a THT (Through Hole Technology) or SMT (Surface Mount Technology) component in the final product. With this package, it is possible to access the mirror BS and use that to help the optical characterization. Figure 5-33 presents a micromirror mounted and bonded micromirror on the customized packaging.

(a)

(b)

(c)

Figure 5-32 – SEM images of the 1D MEMS mirror device fabricated.

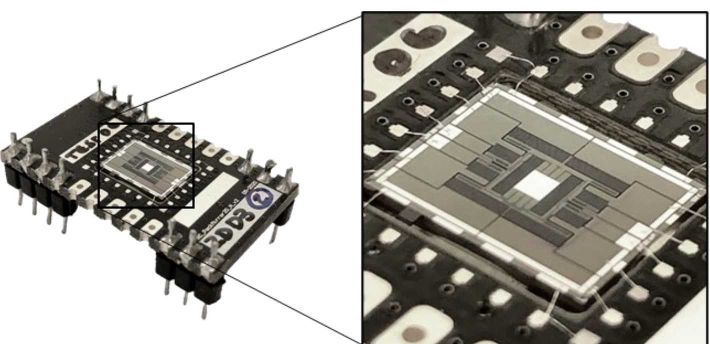

Figure 5-33 – Packaged MEMS mirror in a customized packaged solution.

5.4 Nanoimprint Lithography (NIL)

Grayscale lithography presents several advantages in MEMS processes. However, this can take several hours to expose. To expose a full 200 mm-wafer, 40 hours of the Heidelberg DWL 2000 system were necessary, translating to almost two days. In order to increase the throughput and reduce overall costs, nanoimprint lithography (NIL) was employed to replicate the multilevel mask at a 200 mm wafer scale.

5.4.1 Master

The nanoimprint silicon master contains the same multilevel pattern to be positively replicated onto the FS of the MEMS mirror. The master was micromachined by combining GS lithography and silicon RIE onto a single-side polished (SSP) wafer, as depicted in Figure 5-34. Here, a thin AZP4110 (from Microresist) photoresist layer with a thickness of 2.2 μm was uniformly coated onto the wafer surface. The photoresist layer was subsequently GS exposed with the MEMS mirror and asymmetric comb electrodes pattern, which presented a final thickness after the development of 0 μm (maximum GS level), 1.1 μm (medium GS level) and 2.2 μm (null level).

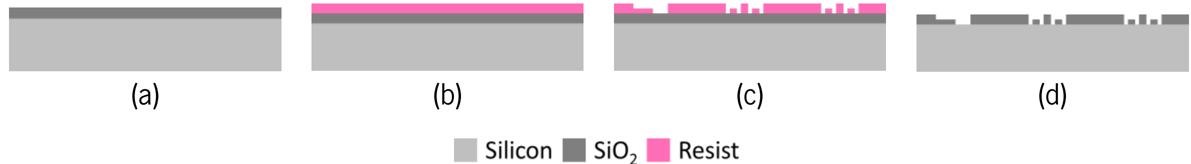

Figure 5-34 – Multilevel silicon master micromachining process main steps, where (a) SiO_2 CVD; (b) photoresist spin coating; (c) grayscale lithography; (d) pattern transpose by a sequential RIE/O_2 strip to the had-mask layer.

Following the same process used for the MEMS mirror fabrication, the multilevel photoresist mask previously developed was then transferred to the SiO_2 layer through a sequential RIE/O_2 plasma strip process.

5.4.2 Intermediate working stamp

The proposed NIL process uses an intermediate working stamp with the negative replica of the master structures. After the successful fabrication of the master, the subsequent phase involved the creation of an intermediate working stamp, which is a negative replica of the master, illustrated in Figure 5-35. For this purpose, UV curing NIL, using the Eitre® 8 system from Obducat, was employed. First, a fluorinated anti-sticking layer was deposited on the master surface (Figure 5-35.a). Then, OrmoStamp was dispensed into the centre of the silicon master (Figure 5-35.b). A 200 mm transparent glass wafer was used as the substrate for the intermediate stamp and prepared through a series of steps, including O_2 plasma

treatment, followed by the deposition of an adhesion promoter OrmoPrime08 (Micro resist Technology) (Figure 5-35.b). This glass substrate with the adhesion promotor was brought into contact with the OrmoStamp while avoiding any air bubble to remain trapped in the viscous liquid (Figure 5-35.c). The glass wafer coated with the adhesion promoter is then manually stacked on the master with the OrmoStamp. The stamp was moulded at room temperature, $T = 21$ °C, (Figure 5-35.d) following the recipe depicted in Table 5-7. The negative replica was demoulded from the master and underwent a hardbake step at 130 °C for 10 min (Figure 5-35.e).

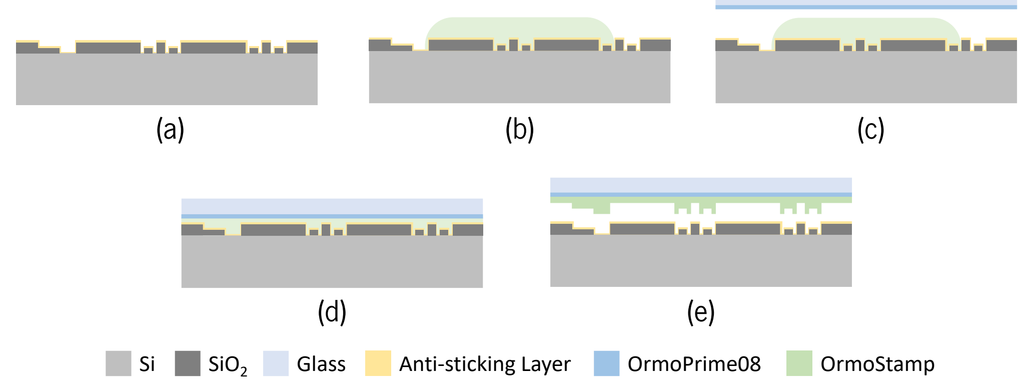

Figure 5-35 – Intermediate working stamp micromachining process main steps: (a) Master anti-sticking treatment; (b) OrmoStamp disposal onto the Si master; (c) placing the glass substrate with adhesion promotor OrmoPrime08 on top of OrmoStamp; (d) OrmoStamp moulding and curing; and (e) Demolding.

Table 5-7 – Working stamp NIL recipe.

Step	Temp (°C)	Pressure (bar)	Time (sec)	UV
Master filling	21	5	600	Off
Curing	21	5	35	On

Intermediate working stamp quality

In order to provide a closer examination of the intermediate working stamp, scanning electron microscopy (SEM) was performed, enabled by a 10 nm thickness gold layer deposited on it. The resulting images (Figure 5-36) show the negative of the expected MEMS mirror features.

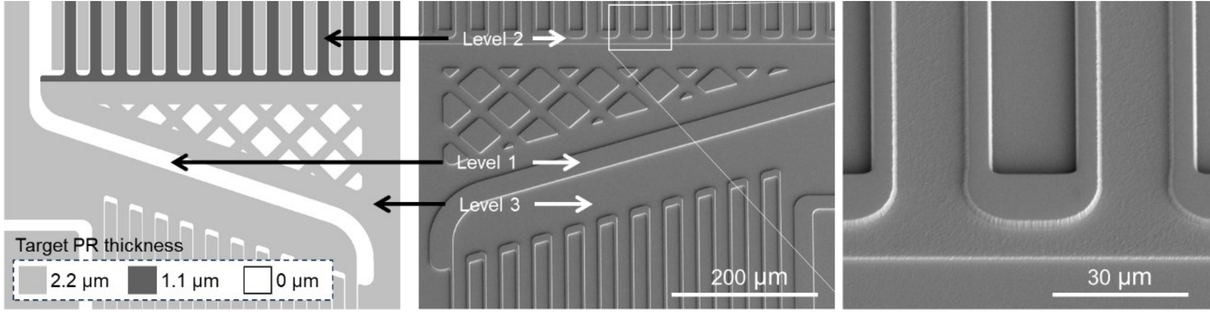

Figure 5-36 – SEM images of the intermediate working stamp (with 10 nm-Au coating).

The specific layout details, as well as the three distinct levels of the replicated microstructures on the stamp, can be observed. The features' edges present a high-quality vertical wall. Some roughness on the

etched low-levelled silicon can be observed due to the gold layer granularity, but it did not have an impact on the NIL replica and subsequent micromirror performance.

Mechanical profilometry (P-16+, KLA Tencor) measurements were performed to assess the surface topography more accurately and provide quantitative data on the height variations across the intermediate working stamp (Figure 5-37). The measurements obtained using the mechanical profilometer clearly demonstrated the presence of distinct levels and provided valuable insights into the three-dimensional characteristics of the replicated microstructures, showing a perfect match between the dimensions of the main master and the intermediate stamp.

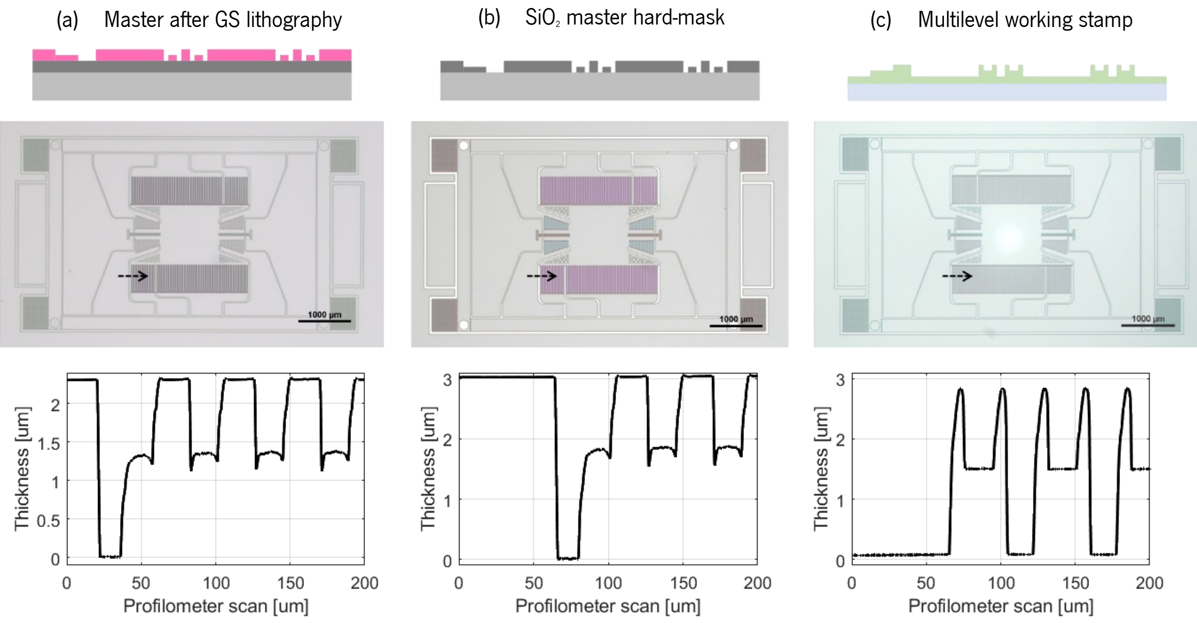

Figure 5-37 – OM images and profilometer data of the master, upon the GS lithography and the multilevel pattern and of the working stamp.

5.4.3 Replica

The final device was replicated from the intermediate working stamp to a silicon wafer with a layer of SiO_2 (hard-mask layer) coated with a thin layer of mr-NIL6003 (Micro resist Technologies) by means of a simultaneous thermal and UV-curing NIL process. The use of a simultaneous thermal and UV-curing resist allows an isothermal imprint process using both heating at moderate temperatures and UV exposure on a UV-curable thermoplastic resist, avoiding issues related to thermal expansion differences and polymer deformation that may arise at higher temperatures [169].

Prior to the NIL process, the intermediate stamp was also coated with a fluorinated anti-sticking layer. The replication process follows the process flow depicted in Figure 5-38. Once again, the stack composed

of the Si wafer with a SiO_2 layer and resist (Figure 5-38.a), and the intermediate stamp was manually prepared.

Then, the NIL process started with the stack being pre-heated, and after that, the imprinting pressure was applied. The implementation of higher temperature (around 65 degrees) and pressure values (up to 15 bar) during a certain time interval ensures that the coated resist viscosity decreases, decreasing flow resistance and filling the intermediate stamp topography prior to the curing step. After exposure to incident UV light, the resist was cured. Finally, the stamp and the replica were again separated immediately after the NIL process.

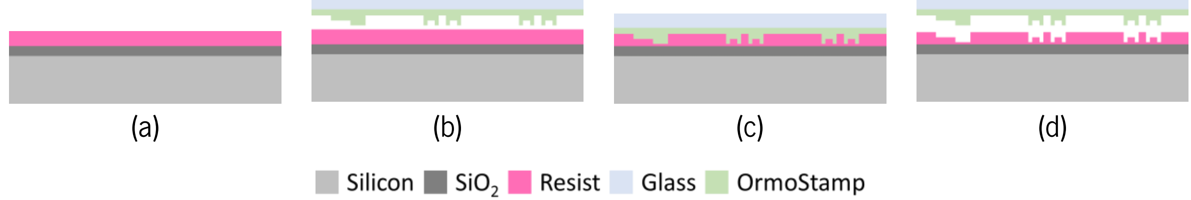

Figure 5-38 – Multilevel replica micromachining process main steps, where (a) photoresist spin coating; (b) stacking of replica wafer and stamp; (c) Stamp filling and curing (d) Separation.

For optimization of the fabrication process, three different replicas, denoted as A, B and C, were imprinted in order to access the different variables of the replication process and the resultant impact of each on the final replica. The parameters studied were the initial thickness of the resist layer (Table 5-8) and the temperature, time, and pressure (Table 5-9) of the process in the Eitre® 8 system.

Table 5-8 – Photoresist initial thickness of the replicas

Replica	Thickness	NU.
A	2594 ± 12.9 nm	1.59%
B		
C	3073 ± 16.6 nm	0.97%

Table 5-9 – NIL replication parameters of the different replicas.

Step	Replica	Temp, °C	Pressure, bar	Time, sec	UV
Filling	A	65	10	300	Off
	B	70	10	300	
	C	70	10	300	
	A	65	15	300	Off
	B	70	15	1500	
	C	70	15	1500	
Curing	A	65	15	60	On
	B	70	15	60	
	C	70	15	60	

Replica quality and Residual Layer

The replica quality depends on the NIL process parameters, such as imprinting temperature, pressure, and filling time, in order to fill the cavities of the stamp uniformly. These process steps (resist curing and demolding) required special handling so as not to deform and/or break the resulting structures. After the NIL process, it is essential to characterize the quality, which is related with the imprinting and demolding steps, and the residual layer of the replicas. The resist's residual layer was characterized because the resist will be used as a mask to etch the MEMS hard-mask. This residual layer is a common occurrence after the NIL processes and can have a significant impact on the quality and accuracy of replicated patterns, such as pattern distortion or incomplete pattern transfer. The residual layer thickness can be influenced by various factors, such as initial resist thickness or bending of the mould, that can be related to the design of the patterns, the material and the thickness of the mould [170], [171], [172].

In order to optimize the NIL process, three different initial resist layer thicknesses were studied. For replica A, an initial thickness of resist of 2594 ± 12.9 nm was used (measured with the NanoCalc-XR system), and the NIL process occurred at 65 °C and 15 bar, with resist filling the wafer topography for 10 minutes. On the other hand, Replica B used the same initial resist thickness and process conditions, except the value of NIL temperature, which was increased to 70 °C. Replica C followed the same recipe as B, but the initial resist thickness was increased to 3073 ± 16.6 nm.

Figure 5-39 presents optical images of the three microfabricated replicas after the nanoimprint process. As can be observed, replica A did not successfully replicate the stamp topography, and voids were observed in the resist coating.

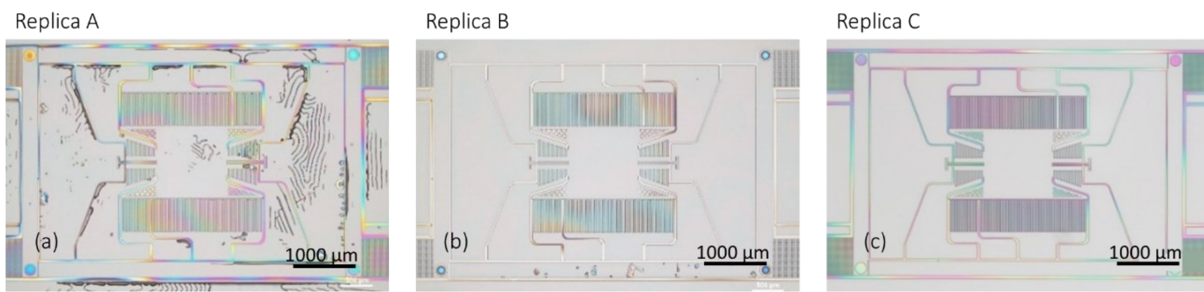

Figure 5-39 – Optical microscopic images of the NIL replicas microfabricated.

With the increase of the imprint temperature, replica B showed better results with fewer voids. However, it still did not present the desired yield, and in the critical parts of the MEMS devices, such as springs, and electrodes, some voids appeared, indicating insuficient initial resist thickness. For replica C, the initial thickness of the resist layer was increased to the value of the stamp topography (3000 nm). After the NIL process (70 °C, 15 bar for 25 min), this replica did not present any voids and the desired topography

was successfully achieved. The maximum process time required per replica was approximately 40 minutes, 60 times faster then GS process.

The residual layers of the three replicas were measured using the mechanical profilometer. For that purpose, a scratch was made in each replica with a blade to remove the resist and enable the measurement of the step in resist thickness from the silicon wafer to the residual layer. The scratch was intentionally located in the vertical asymmetric electrodes, as shown in Figure 5-40 since it is the region with the multilevel topography. Replica A presented a residual layer of 157±87 nm, B of 103±58 nm, and C of 553±25 nm (measured by mechanical profilometry). The residual layer of replica C was considerably higher. However, the multilevel topography was defined to accommodate the removal of this layer without compromising the dimensions of the final structures.

A process based on O_2 plasma was employed to remove this thin residual layer in the areas expected to have exposed substrate without compromising the multilevel topography along the wafer.

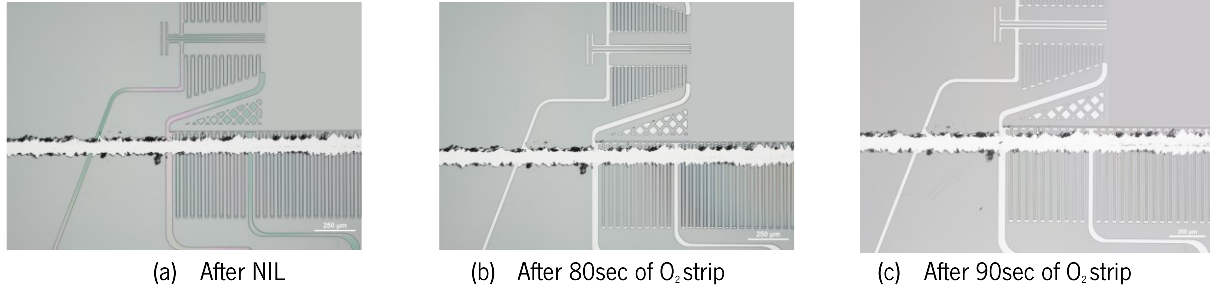

(a) After NIL (b) After 80sec of O_2 strip (c) After 90sec of O_2 strip

Figure 5-40 – Optical microscopic images of the MEMS mirror pattern during the removal of the residual Layer.

5.4.4 Replication with alignment

After the optimization of the replication process, the conditions used for Replica C were employed to perform the NIL process on MEMS mirrors. Prior to the NIL process for the multilevel patterning, the target device substrate contains a micromachined surface; at this point, the metal layer for the reflective coating and electrical contacts have been patterned, and the hard-mask layers were deposited by CVD on both sides of the SOI wafer. This means that the multilevel lithography is the second lithography to be patterned in the MEMS FS process, which means that an alignment has to be performed. The device layout was designed to accommodate a maximum misalignment between lithographies of 20 μm in x and y axis. If a misalignment higher than this value is obtained, the final structure will not work.

In order to achieve precise alignment during the stacking process of the Si wafer and the stamp, an x, y, z, and rotational stage is employed to hold the stamp. By utilizing two high-precision cameras, the alignment marks patterned on both the wafer and the stamp are carefully observed, and the stamp's

position is adjusted to ensure the proper alignment of the marks. Given the weight of the fabricated working stamp, a new stamp holder was then designed, 3D printed in SLA, and employed in the Eitre 8 system, where a goniometer and external vacuum line were implemented. The goniometer was used to adjust the tilt of the stamp (Figure 5-41). Furthermore, the vacuum line to ensure the necessary holding force. With this system, it was possible to align the stamp to the previous lithography in the replica wafer, with a misalignment of 5 µm and 10 µm in the x and y direction, respectively. Figure 5-42 presents optical microscopic images of the NIL replica aligned by the developed system.

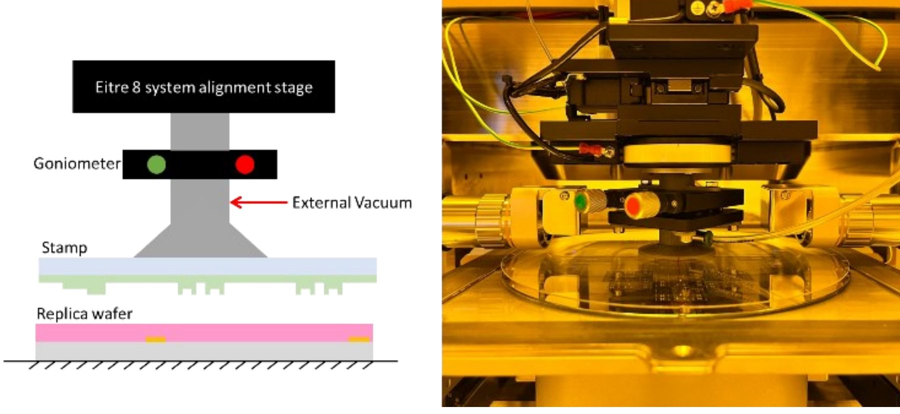

Figure 5-41 – NIL alignment stage, with dedicated 3D printed holder.

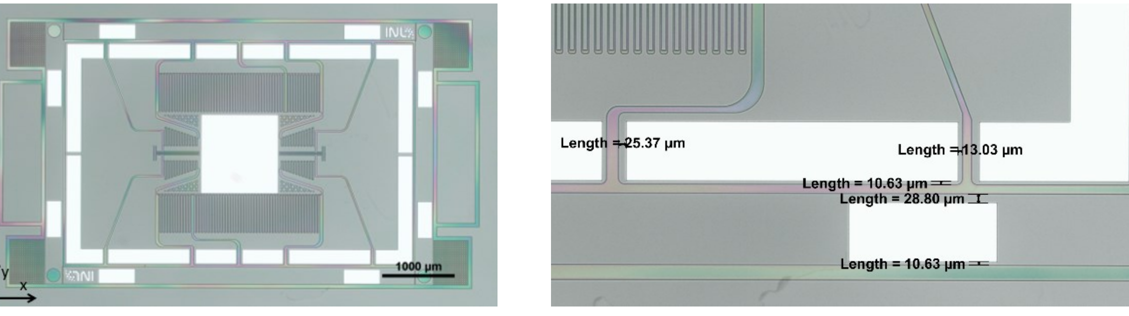

Figure 5-42 – OM of the replica with alignment with the metal layer.

Replica fidelity of the aligned device

In order to assess the match of the replicated topography with respect to the original GS pattern (Figure 5-43), an examination was conducted on the replica, including the resist thickness of the multilevel pattern and the dimensions of the critical features of the MEMS devices, such as gap sizes and springs width. Both the master and the intermediate working stamp underwent the same analysis to evaluate their consistency with the final replica in terms of the aforementioned features. This inspection was carried out at multiple points across the 200 mm wafer, aiming to validate the uniformity and yield of the multilevel NIL process.

Table 5-10 summarizes the results of this inspection, presenting the deviation of the gap dimensions of the master, stamp, and replica. As can be observed, the final replica presented an excellent agreement with the desired design with less than 200 nm feature width variation of the replica with respect to the master, demonstrating the success of the proposed process for multilevel MEMS devices. Moreover, since this variation results from the residual layer removal (isotropic etching), it is possible to predict and compensate the gap dimensions on the initial layout design. Furthermore, a comparative analysis was conducted on the thickness of the two resist levels post-GS lithography and NIL replication and residual layer removal. As presented in Table 5-10, larger final thicknesses were observed in the replica, which is advantageous as it provides an enhanced margin for the efficient transfer of the multilevel pattern onto the hard-mask layer.

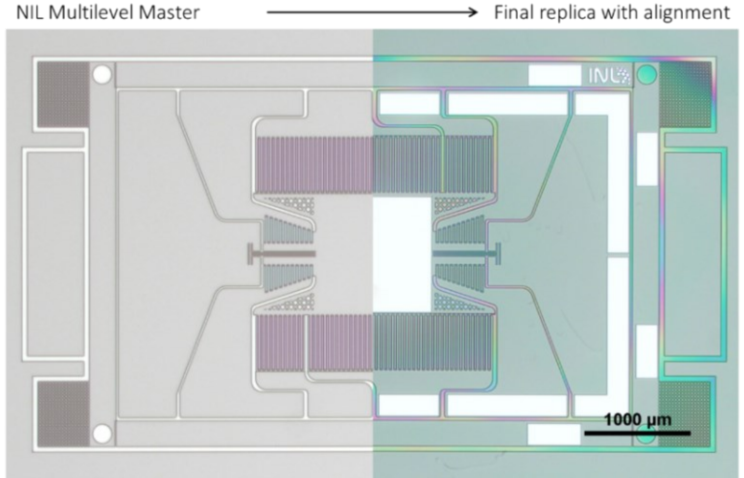

Figure 5-43 – Match between master and replica pattern.

Table 5-10 – Comparison of the electrode gap size of the master, stamp and final replica.

Feature	Master	Replica
Electrode Gap	3.52 µm n.u. = 3.69%	3.66 µm n.u. = 3.93%
Springs Width	9.73 µm n.u. = 2.62%	9.41 µm n.u. = 3.66%

Level	Multilevel mask thickness	Replica PR thickness
Thinned Level	1.38 µm	1.53 µm
Thick level	2.3 µm	2.83 µm

5.5 Conclusions

In this chapter, the required adaptations, and optimizations to the standard 3-mask SOI-based fabrication process at INL have been detailed. Preliminary tests were conducted to assess the limitations and constraints of various process steps. These tests included an experimental analysis of the reflective

coating, which was found to be effective for the intended application. The patterning of the DOE was also examined, where different lithography and etching techniques were evaluated to ensure successful transposition of the minimum grating feature of 1.4 μm onto the silicon layer. Additionally, the multilevel process was refined using grayscale lithography, enabling the creation of self-aligned asymmetric electrodes for mirror actuation.

The EKC cleaning process was incorporated into the multilevel sequential process to remove the passivation layer on the electrode gap walls deposited during the DRIE step, thus preventing these organic walls from acting as a mask in the subsequent silicon etching step. The BS multilevel topography was also optimized using a sequential lithography process, and sacrificial grids were implemented in the mirror BS cavity to prevent silicon grass or over-etching on the BS layer, ensuring a uniform etch environment.

The 2D MEMS mirrors with an integrated Dammann DOE into the reflective surface were successfully fabricated on a 50 μm -thick 200 mm DSP SOI wafer with a handle layer of 400 μm, demonstrating the success of the novel fabrication process implemented in this thesis, using grayscale lithography to create different levels in a single layer in a single lithography step. A process simplification was also tested for a 1D MEMS mirror design.

Grayscale lithography offers several advantages in MEMS processes but can take several hours for exposure. To expose a full 200 mm wafer, 40 hours were required on the Heidelberg DWL 2000 system, amounting to almost two days. Nanoimprint lithography was employed to replicate the multilevel mask at a 200 mm wafer scale to increase throughput and reduce overall costs. A multilevel master with the mirror design was fabricated, and using a glass substrate and ORMOcomp, a negative stamp was created as an imprint. With this mould, different replicas were made under varying temperature, pressure, and time conditions, and an optimal combination was achieved to successfully replicate the initial pattern.

6. Experimental Characterization

The 2D MEMS mirror developed in this thesis uses asymmetric capacitive MEMS structures that are electrostatically actuated to induce an out-of-plane torque, tilting the reflective surface to the desired angle and consequently steering the incident laser beam. Given the DOE implemented in the MEMS mirror surface, the reflective beam is diffracted into five linearly arranged and equidistance spots, dividing the target FoV into five smaller ones in the vertical angle.

In this chapter, the experimental tests performed on the fabricated mirrors are detailed. These tests aim to characterize the microstructure performance, mechanical and optical, and conclude if the innovations implemented on the device are capable of achieving the targeted performance.

6.1 Experimental setups development

For the MEMS structure experimental tests, different setups were used to validate several aspects of the device's performance. The Polytec MSA-500 system was used. This system combines three measuring techniques into one system, allowing a complete characterization of MEMS devices without moving the device under test (DUT) to another test station. In this system, it is possible to perform static characterization of the topography by scanning white-light interferometry, appropriate for rough and smooth surfaces; real-time dynamic characterization of “out-of-plane” vibrations by laser-Doppler

vibrometry at frequencies up to 24 MHz with a displacement resolution in the picometer range; and dynamic characterization of "in-plane" movements by stroboscopic video microscopy up to 1 MHz with a displacement resolution in the nanometer range. In the MEMS characterization, only the topography and the out-plane vibrations measurement systems were used.

A dedicated optical FoV experimental setup where the incident angle is approximately 0° was implemented in order to validate the optical deflection performance without any optical distortion.

6.1.1 Surface Metrology

When designing or fabricating microsystems, structured functional surfaces require precise topography verification to assure quality and deviation from theoretical design. Due to its spatial resolution in both in-plane and out-of-plane directions, the Micro System Analyzer's topography measurement unit of the Polytec MSA-500 system is ideally suited for the 3-D profile analysis of microstructures.

Principle of operation

When two monochromatic, coherent light sources are merged, their phases determine whether they produce constructive or destructive interference. To verify the superposition of light waves and the resulting interference, a Michelson interferometer is used, Figure 6-1.

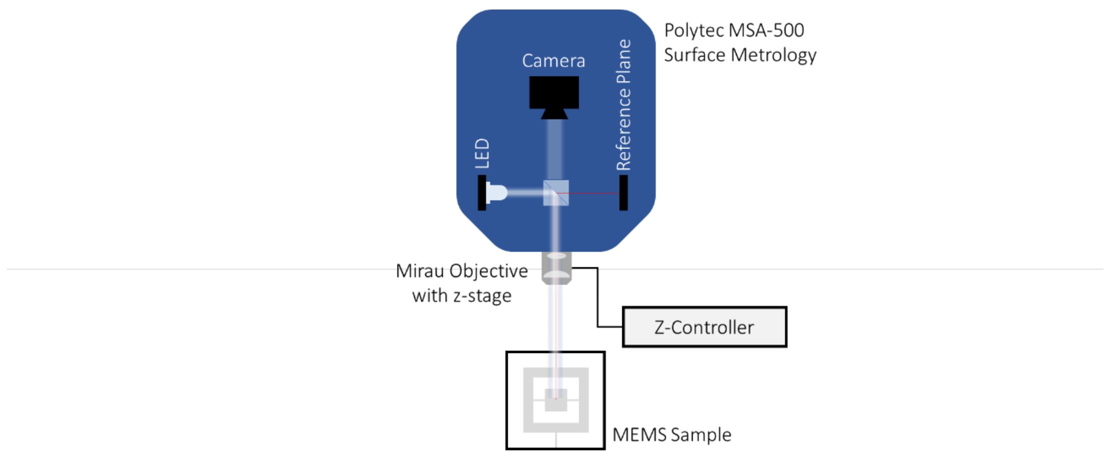

Figure 6-1 – Surface metrology setup, using Polytec MSA-500 topography measurement systems (TMS).

This device splits light into two beams using a beam splitter, directing one toward a reference surface and the other towards the surface of the studied object. Light is reflected from both surfaces, causing constructive or destructive interference depending on the path length differences, which can be detected by a camera. If the device's surface is not joined or has large steps, the order number of fringes is lost, creating ambiguity. However, using a broadband "white light" source can overcome these obstacles. Interference only occurs within a small range and has the shape of a correlogram. By analysing

correlograms after moving the reference mirror, an accurate topographical representation of the surface can be reconstructed.

In a few words, an x-y-z mapping can be generated by shifting an interference objective with nanometer precision with respect to the samples. The interference microscope images both the specimen and reference flat on the camera, thus detecting the interference pattern. Given this, a rapid, non-contact topography measurement is extracted, which can be shown in 2-D or 3-D view and where it is possible to determine key parameters, such as flatness, parallelism, curvatures, heights, and roughness, among others.

6.1.2 Scanning laser-Doppler vibrometer setup

Scanning laser-Doppler vibrometry allows non-contact measurements in real time to characterise out-of-plane vibrational behaviour and determine the vibration velocity and displacement at any sample point. The Polytec MSA-500 system's unique features include the ability to acquire data with picometer displacement resolution, capture frequency response up to 24 MHz, and analyse non-ideal or non-linear systems. In this setup, the devices can be characterized in normal atmospheric or vacuum conditions under the Polytec MSA-500 interferometer, which is able to measure vertical deformation synchronized with an actuation signal, as depicted in the schematic of Figure 6-2. An internal generator using Polytec software control provides a calibrated vibration excitation of the MEMS device. The internal generator allows excitations with an arbitrary waveform and with a wide range of different excitation patterns. This actuation signal from the Polytec system can be amplified from 0 to 200V for both fast and slow axis actuation by an external high-voltage amplifier.

Principle of operation

The laser-Doppler vibrometer is a precision optical transducer for determining the vibration velocity and displacement at a measurement position. It works by sensing the frequency shift of backscattered light from a moving surface. The object scatters or reflects light from the laser beam, and the Doppler frequency shift is used to measure the component of velocity which lies along the axis of the laser beam.

For the fast axis characterization, the approximate 600 μm x 800 μm aperture of the Polytec system allows the capture of deformation around the axis of rotation of the mirror and compares this deformation with points in the static frame, as presented in Figure 6-3.a. The mechanical deformation is calculated as the angle formed by the height difference between any two points along the same vertical line on the mirror, knowing their distance. For statistical purposes, all the points are compared with the remaining

ones for multiple actuation periods to get a mean value and standard deviation error. One crucial aspect to consider in the fast axis is that some measurement clipping occurs at large deformations. As the interferometer beam is incident on the mirror, it is reflected. For low deformations, the reflected signal is still captured by the interferometer system, although attenuated, and is able to measure the deformation. However, for large displacements (above approximately 10° mechanical deformation or 20° optical field of view), the reflected signal does not reach the interferometer, which either saturates, clips the signal, or provides an erroneous measurement.

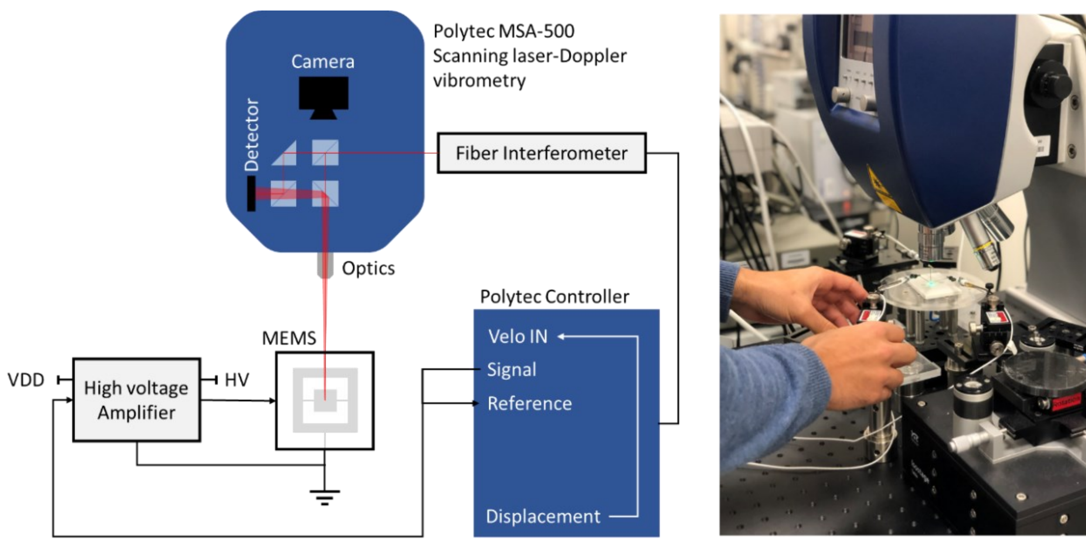

Figure 6-2 – Out-of-plane displacement setup, using Polytec MSA-500 topography measurement systems (TMS).

For the outer axis characterization, the aperture of the Polytec system limits the observable region to a small section at the edge of the inner frame, which is rotated by the slow axis actuation. However, the axis of rotation is not observed together with a static region, Figure 6-3.b. When the mirror is actuated to the right, the vertical position of the measured points decreases, and when it is actuated to the left, the vertical position increases. Again, similarly to the fast axis measurements, the mechanical deformation is calculated by the height difference formed by any two points along the same horizontal line. For statistical purposes, all points are compared with the other ones to obtain a mean value and standard deviation.

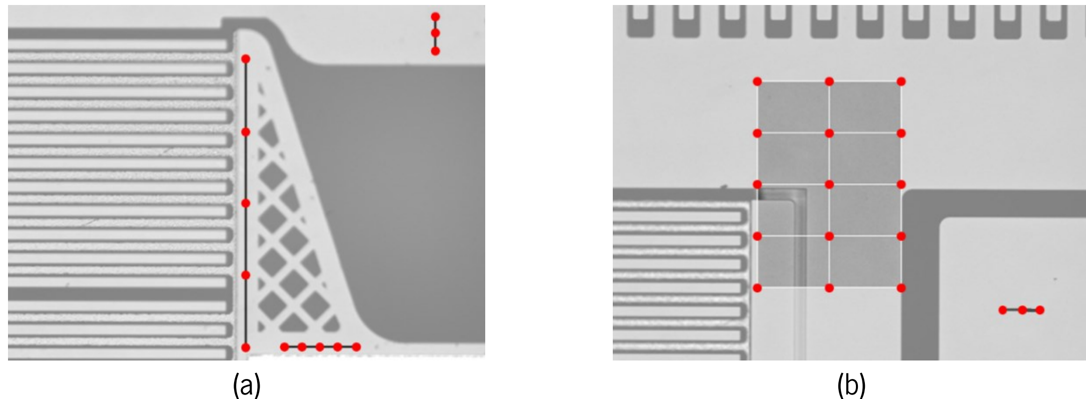

Figure 6-3 – Measurement points for the (a) fast and (b) slow axis characterization.

6.1.3 Large optical FoV setup (with $\theta_i \approx 0°$) for visible laser wavelength

For larger out-of-plane displacements, i.e., larger field of views, the Polytec laser scanner vibrometer is not capable of measuring it since the mirror deflects the measuring laser beam to a position outside of its range. For this reason, a dedicated optical field of view experimental setup was implemented based on a laser as a light source and a fixed target. With this new setup, it was possible to measure larger angles and test another type of actuation. Here, the laser source was positioned strategically to have an incident angle of approximately 0° in order to characterize the mirror deflection without any optical distortion.

As can be seen in Figure 6-4, the laser source is placed behind the angular target, and the laser beam passes through the small hole entailed in the target until it reaches the MEMS mirror reflective surface. To ensure a fine alignment between the beam and the reflective surface, the MEMS device board is attached to an XYZ linear high-precision stage from Thorlabs. When the mirror is actuated, the reflected beams are projected into the angular target. Here, the origin of the angular target must be aligned with the MEMS device.

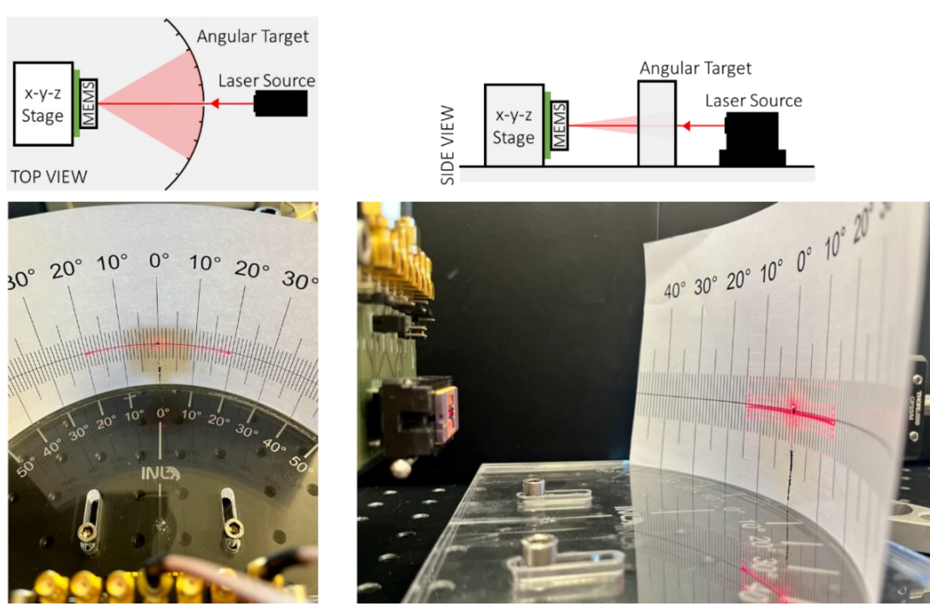

Figure 6-4 – Large Optical FoV experimental setup schematic and images.

6.1.4 NIR optical FoV setup (with configurable θ_i) for 1550 nm laser wavelength

The following setup was used to experimentally characterize the MEMS and DOE performance for the target wavelength, 1550 nm. Here, a 1 mW collimated laser beam at λ=1550 nm (Thorlabs MCLS1) was attached to a rotational structure to change the static incident angle, θ_i, and is incident on the MEMS

reflective surface. The reflected pattern is measured by a negatively biased InGaAs photodiode (Thorlabs FGA015) with a scanning diameter of ø150 µm. This photodiode is connected to an XYZ linear stage (Thorlabs DDS220) in order to scan the large area of the projected FoV. The optical signal current is amplified using a trans-impedance amplifier (FEMTO DLPCA-200), which is acquired by a data acquisition system (Measurement Computing DT9836) together with the encoded stage positions. Figure 6-5 presents a schematic and photo of the NIR FoV experimental setup.

A control software was developed that was able to define the number of points per mm of stage displacement (spatial resolution), stage speed, and trajectory along the X and Y directions. The scanning area is user-definable, and the height of the scanning head is controlled by the software using a motorized lab jack assembled under the XY stages.

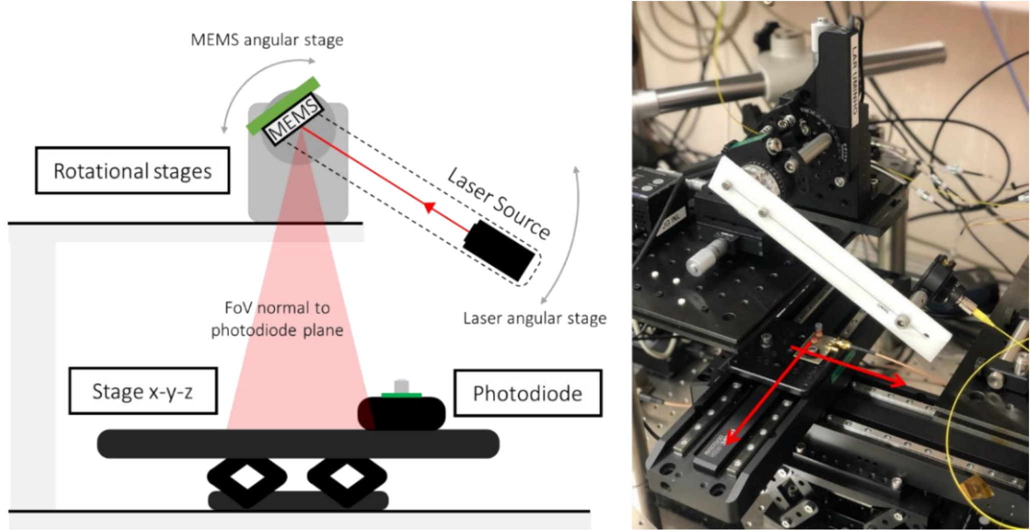

Figure 6-5 – NIR optical FoV experimental setup schematic and image.

The MEMS device plan angle is always calibrated to have a normal projection to the XYZ linear stage (photodiode plan) to minimize the influence of photodiode sensitivity on the measurements (Figure 6-6).

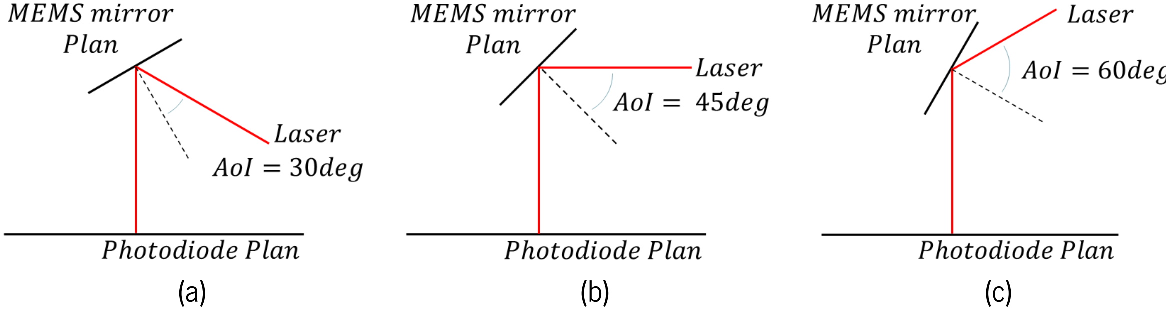

Figure 6-6 – Schematic of the calibration of the device plane and laser source AoI to guarantee a normal projection on the photodiode plan.

This setup can be used not only to characterize the DOE performance for the target wavelength but also to scan the projected field of view when the MEMS structure is operated. The projected pattern is

measured at two stage heights, and the corresponding relative spatial separations determine the dispersion angle of each beam and FoV by the following equation:

$$\theta = \tan^{-1}\left(\frac{x_2 - x_1}{h}\right) \tag{6-1}$$

where h is the difference between the two scan heights, and x_1 and x_2 the scanned spot coordinates.

6.2 2D MEMS mirror experimental characterization

6.2.1 Topography

The asymmetric electrode topography was experimentally characterized utilizing the previously described surface metrology setup. The experimental data of the inner axis electrodes of 2D MEMS mirrors is presented in Figure 6-7. As observed, the thinned electrodes exhibit a thickness of 32 µm, whereas the thicker electrodes measure 50 µm in thickness. In the top left corner of the scan, the mirror's reflective surface can be discerned, along with the associated diffractive pattern.

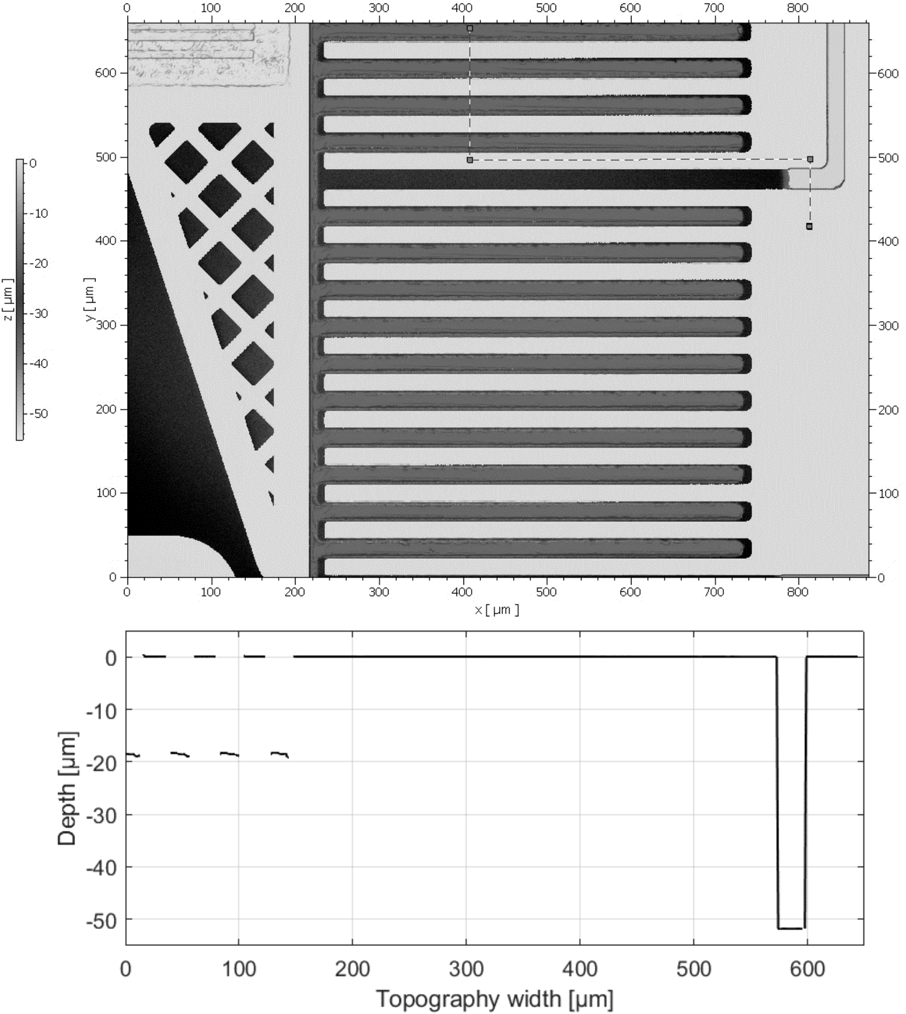

Figure 6-7 – Asymmetric electrodes topography measurement, (a) x and y view; and (b) z view.

6.2.2 Inner natural resonance frequency

The natural resonance frequency of the MEMS devices was experimentally characterized through the utilization of the Polytec MSA-500 scanning laser-doppler vibrometer. To scan the MEMS frequency response, a pseudo-random signal was independently applied to each axis. For the inner axis, a defined maximum amplitude of 15 V, along with an offset of 15 V, was established, and the Fourier Transform was calculated over the frequency range spanning from 100 Hz to 5 kHz. Conversely, for the outer axis, an amplitude of 100 V, accompanied by an offset of 100 V, was employed within the frequency interval of 10 Hz to 1 kHz. The extracted frequency response for the device A and B are depicted in Table 6-1.

Table 6-1 – Frequency response of the inner (IAx) and outer (OAx) axes of devices A and B.

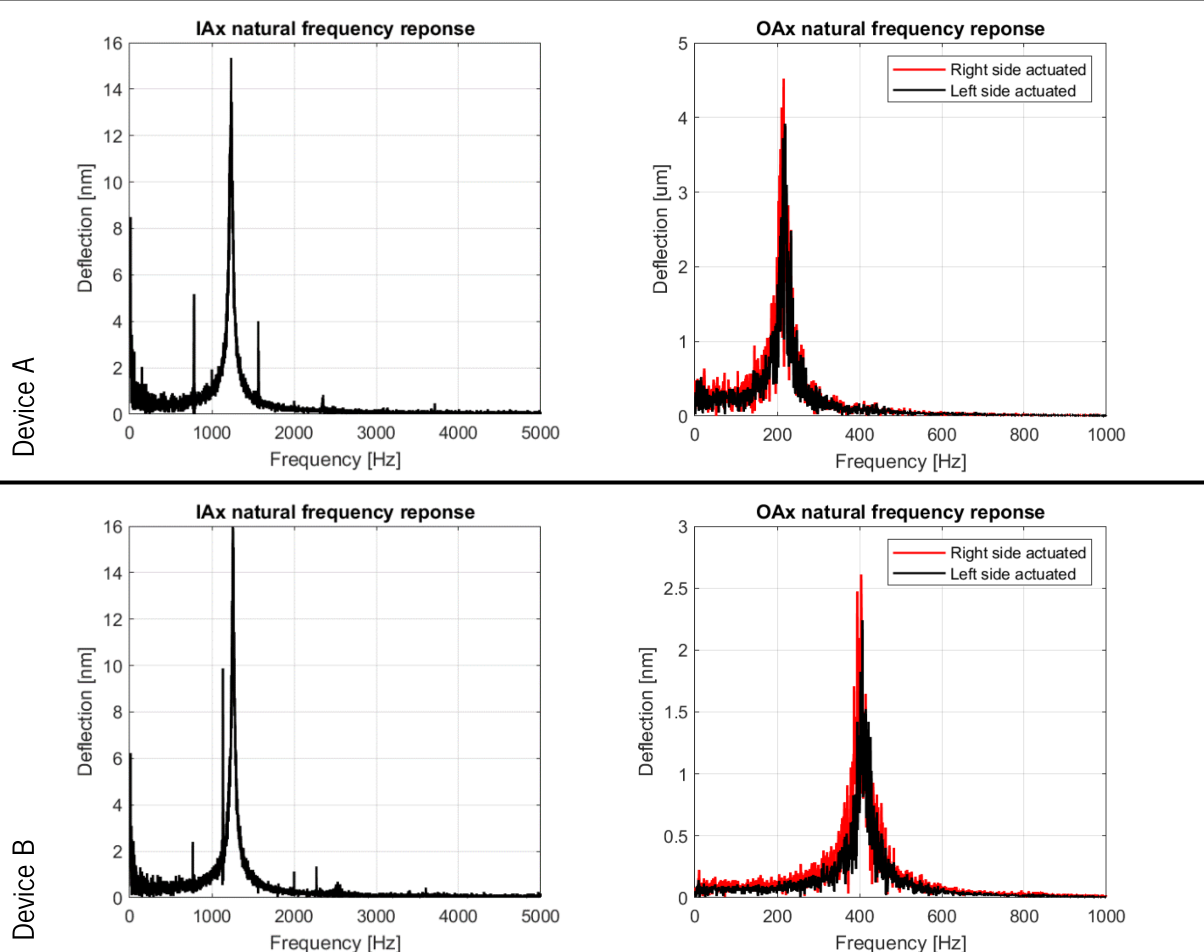

As is evident, within the harmonics of the natural resonance frequency, the mirror exhibits an out-of-plane displacement. However, as anticipated, the resulting FoV is comparatively smaller in the harmonics when compared to the natural resonance frequency. Each design was subjected to experimental testing, and the results, including the natural resonance frequency and quality factor, are summarized in Table 6-2. The distinction between both designs hinges on the width of the OAx springs. Consequently, it was

expected that design B would manifest a higher natural frequency and a lower quality factor, as proven experimentally.

Table 6-2 – Experimental natural frequency and Q-factor of devices A and B.

		Inner axis			Outer axis		
Device	OAx Spring width	Theoretical Fn	Experimental Fn	Q-factor	Theoretical Fn	Experimental Fn	Q-factor
A	10 μm	1244 Hz	1236.2 Hz	24.32	263 Hz	216.6Hz	13.38
B	15 μm	1244 Hz	1277.7 Hz	6.8	490 Hz	410.2 Hz	20.25

As can be seen, both designs present a natural frequency close to the theoretically expected one when assuming a spring over-etch of 500 nm. The larger shift measured on the OAx is due to variation in the outer structure mass, dependent on the handle layer thinning uniformity.

Frequency shift – spring hardening and softening

To further experimentally characterize the frequency response of the MEMS structure, a sine wave with a frequency sweep was separately applied to each axis within the same frequency interval as an alternative to using a pseudo-random signal. The signal amplitude was incrementally raised from 5 V to 25 V in 5 V increments for the inner axis, with an offset set at half of the maximum amplitude. For the outer axis, the amplitude was increased up to 50 V. Figure 6-8 and Figure 6-9 depict the deflection response of device A in the inner and outer axes, respectively. The observed positive shift in resonance frequency can be attributed to the spring hardening behavior, which manifests as an increase in the effective spring constant with the application of higher voltages in the system.

Spring hardening and spring softening are non-linear phenomena observed in electrostatically actuated MEMS devices. These nonlinearities arise from various MEMS specifications, including excitation voltage, mirror structure, device dimensions, and pressure conditions [36]. Spring softening involves a reduction in the effective spring constant, leading to a downward shift in resonance frequency, while spring hardening entails an increase in the effective spring constant and an upward shift in resonance frequency. In the literature, several works explored these two nonlinearities in MEMS. The work detailed in [37] demonstrates that applying a constant DC voltage while varying the AC voltage leads to a spring hardening effect, where the resonance frequency increases with increasing AC voltages. Conversely, by varying the DC voltage while maintaining a constant AC amplitude, the response is associated with spring softening behavior, where an increase in DC voltage leads to a decrease in resonance frequency.

Spring hardening results in an increase in resonance frequency as the oscillation amplitude increases, with the maximum displacement occurring at this frequency. Conversely, spring softening causes the

resonance frequency to decrease as the oscillation amplitude increases. Additional tests were conducted to validate these behaviors.

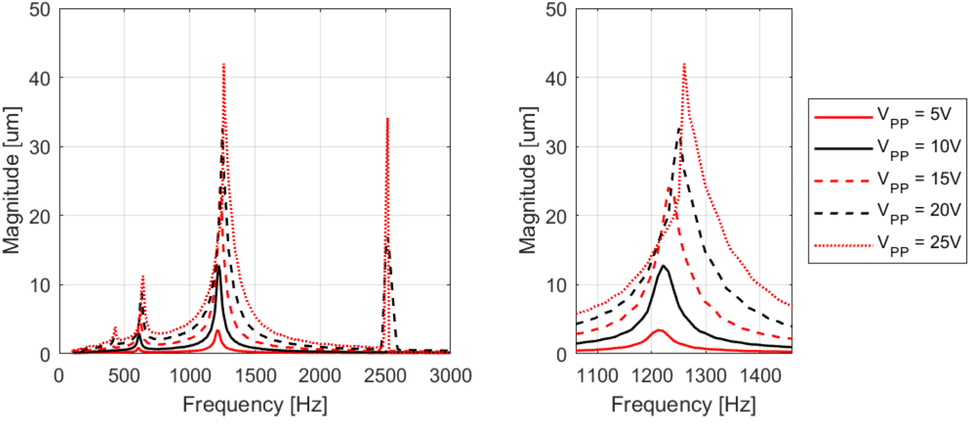

Figure 6-8 – IAx frequency response experimental data for different actuation voltages.

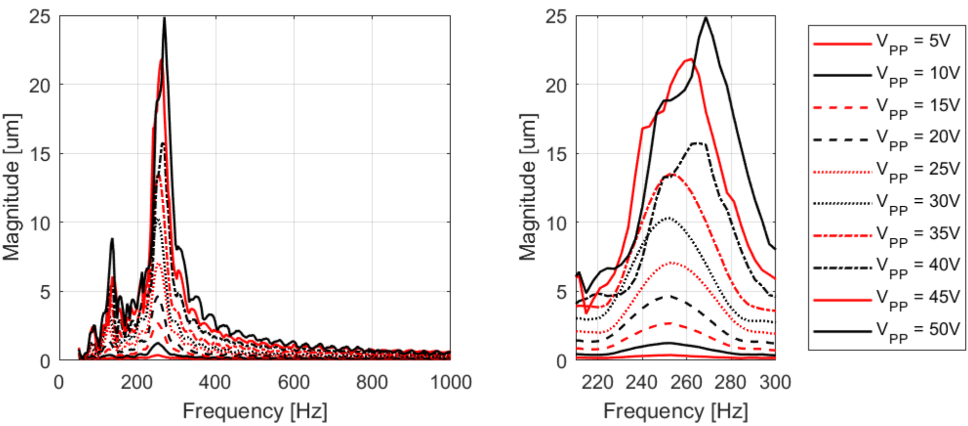

Figure 6-9 – OAx frequency response experimental data for different actuation voltages.

6.2.3 Pull-in voltage

The pull-in effect is a critical phenomenon in electrostatically actuated MEMS devices. When voltage is applied across the actuation electrodes, an electrostatic force is generated, attracting the movable plate towards the fixed plate and causing mirror deflection. In the case of staggered vertical electrodes, the motion of the movable electrode is theoretically rotational along the torsional axis, aligning between the fixed electrodes with equal inter-electrode gaps on both sides to prevent in-plane forces and imbalance. However, misalignments between different layers in the micromachining process can lead to slight differences in these gaps. As voltage increases, a point may be reached where the electrostatic in-plane forces, unbalanced due to the differing gaps, overpower the mechanical restoring torque that prevents plate collapse. This point is known as the pull-in voltage or pull-in point. Beyond this point, the system becomes unstable, potentially causing the movable plate to rapidly collapse onto the fixed plate, leading

to short circuits or other failure modes in the device. To experimentally characterize this effect in the outer axis, set a limit on the operational voltage and define a range in which the device can function safely and predictably, a ramp voltage signal was amplified between 0-200 V at a low frequency (0.5 Hz) for each side, and the mechanical deflection was measured. Figure 6-10 plots present the mechanical deflection and the applied voltage of the OAx of devices A and B.

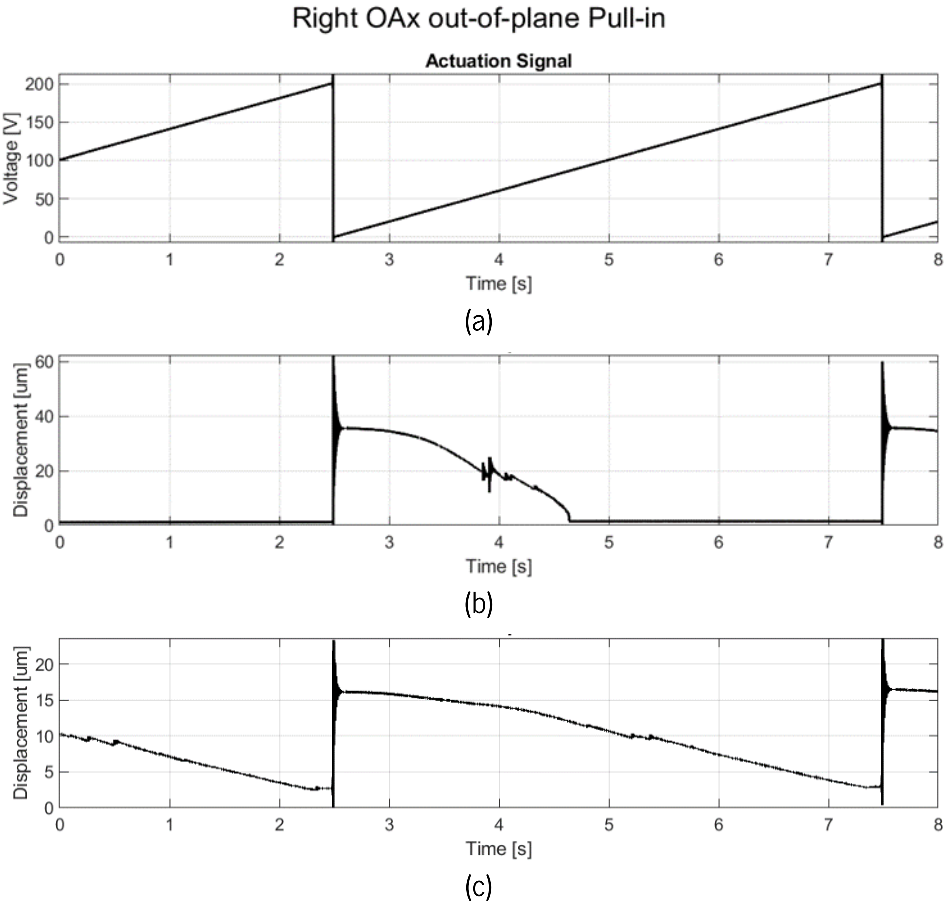

Figure 6-10 – Pull-in experimental data, where (a) is the applied voltage, (b) the pull-in on device A, and (c) of device B.

It was observed that device A collapsed, meaning it got stuck with no remaining displacement at an actuation voltage of 80 V, which is identified as its pull-in voltage. In contrast, Device B did not experience pull-in within the applied voltage range, indicating it never reached the point of getting stuck. Therefore, Device A has a lower pull-in voltage compared to Device B. This outcome was anticipated, as Device A's outer axis (OAx) possesses a lower elastic coefficient, making it more susceptible to achieving the desired Field of View (FoV) at a lower actuation voltage but also more prone to pull-in due to potential slight misalignments in the electrodes. However, it is important to note that Device A also presents a smaller margin for actuation voltage.

6.2.4 Inner and outer axis mechanical deflection

The mechanical deflection of the MEMS devices was also experimentally characterized using the Polytec MSA-500 scanning laser-doppler vibrometer. In the inner axis, given the target resonant mode of operation, a sine wave at the natural resonance frequency (previously extracted) with 30 Vpp was applied, and the deformation was measured at multiple points along the mirror, synchronized with the pulse trigger start, resulting in a mechanical deformation versus phase of the fast axis actuation (clipping occurs at over 10° mechanical deformation). The projected field of view line was computed using the out-of-plane deformation of two different points. The mechanical deflection of these two points is depicted in Figure 6-11.

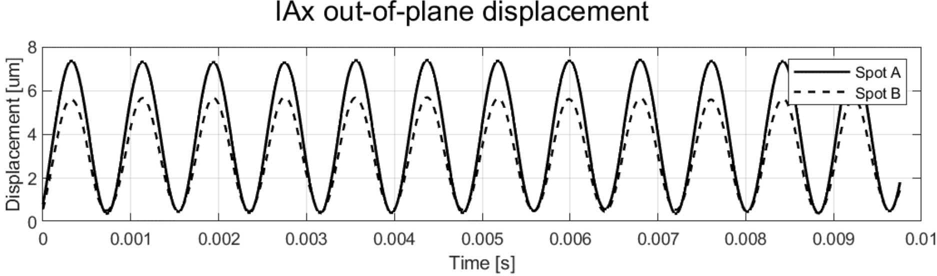

Figure 6-11 – IAx mechanical deflection.

In the outer axis, which is targeted to a static operation mode, the overlapping of the electrodes has a critical role since the initial overlapped area is zero, maximizing the attraction torque when voltage is applied. Here, a triangular voltage signal was amplified between 0-100 V at low frequency (0.5-10 Hz) for each side, and again, the mechanical deformation at multiple points was measured. Figure 6-12 presents the experimental mechanical response of device A for both sides of the outer axis.

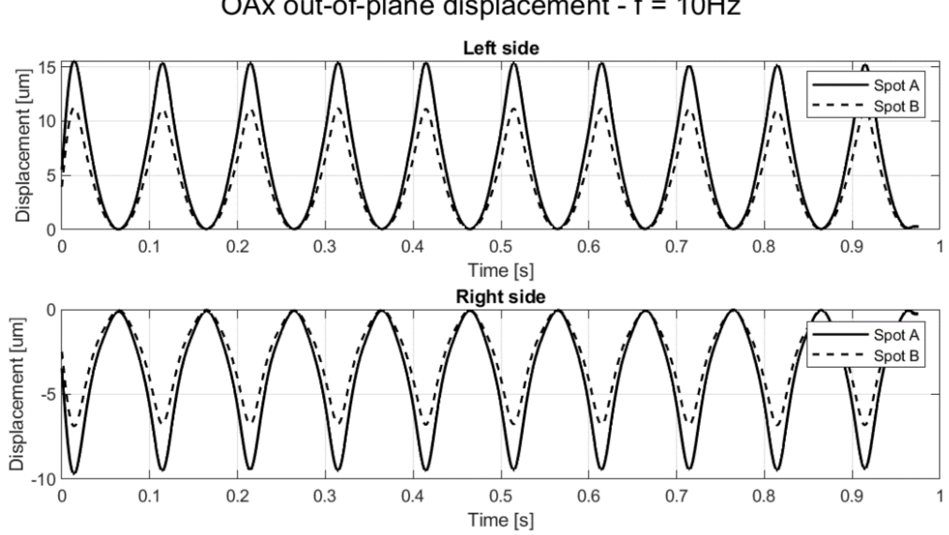

Figure 6-12 – OAx mechanical deflection and FOV.

The mechanical angles and resultant optical field of view for the inner and outer axes of device A, extracted from the mechanical deflection experiments, are shown in Figure 6-13 and Figure 6-14, respectively.

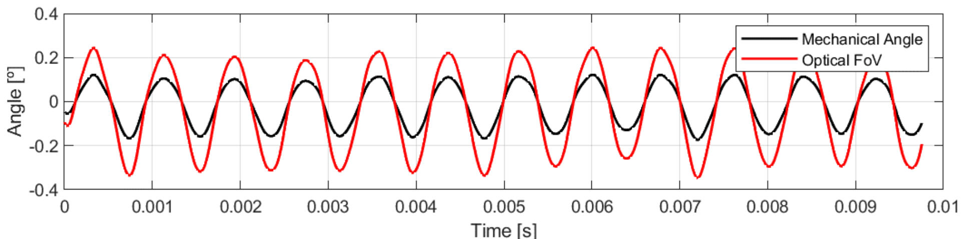

Figure 6-13 – Experimental IAx deflection angle and resultant FoV.

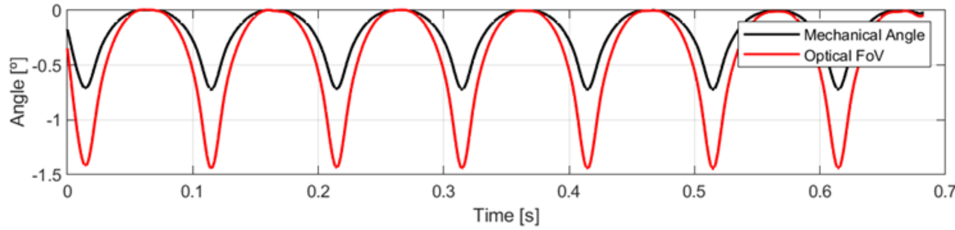

Figure 6-14 – Experimental OAx deflection angle and resultant FoV.

The relationship between the field of view (FoV) and the applied voltage for the outer axis (OAx) can be directly established through mechanical deformation measurements without the ambiguity and distortion inherent in optical targeting, as depicted in Figure 6-15. Note that the positive FoV is related to the left electrodes of the OAx actuation, while the negative FoV is related to the right electrodes. This figure provides detailed insights into the responses of both devices A and B, with device B requiring a higher applied voltage to achieve the target FoV, as anticipated. Additionally, an imbalance in the FoV of device B is observable when comparing each side. This discrepancy arises from a slight misalignment previously noted between the BS electrodes and the microstructure of the device layer, exacerbated by over-etching of the handle layer.

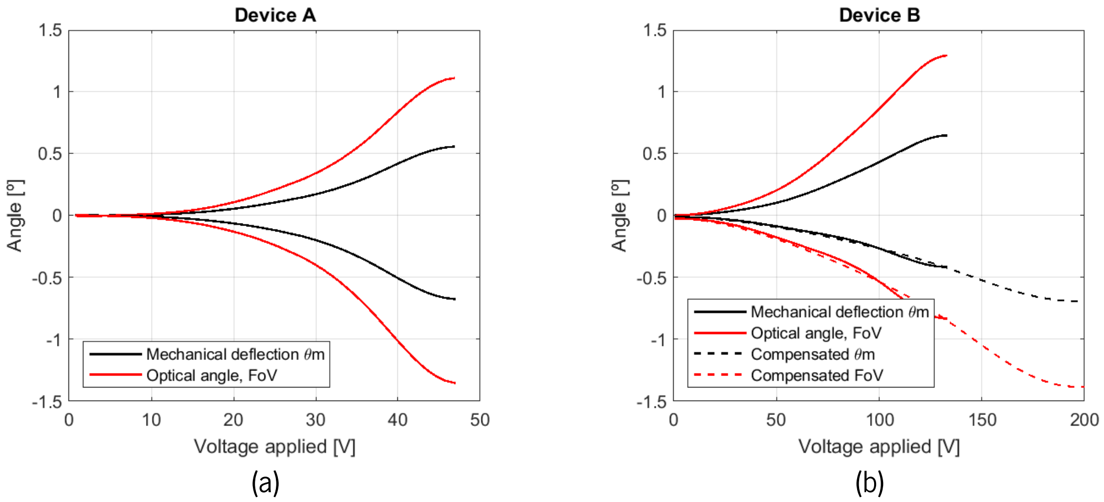

Figure 6-15 – OAx FoV as a function of the applied voltage for devices A (a) and B (b)

This imbalance can be compensated by employing a close loop system that continuously senses the mirror deflection and adjusts the actuation voltage to achieve the target angle. As shown in Figure 6-15.b, device B can achieve the target FoV by applying an actuation voltage to the right side of 200 V. Table 6-3 summarizes the FoV data and required actuation values to achieve it.

Table 6-3 – Experimental FoV and correspondent actuation values of devices A and B.

		Right side		Left side	
Device	OAx Spring width	OAxR FoV	Actuation Voltage	OAxL FoV	Actuation Voltage
A	10 μm	1.35°	46.71 V	1.11°	46.89 V
B	15 μm	1.31°	176.25 V	1.31°	133.10 V

Using the Polytec system, an extended measurement of the main surfaces of the 2D MEMS mirror was performed to analyze the overall structural deformation of the device when the inner and outer axes are independently actuated. Figure 6-16 and Figure 6-17 display the IAx and OAx deformation experimental data.

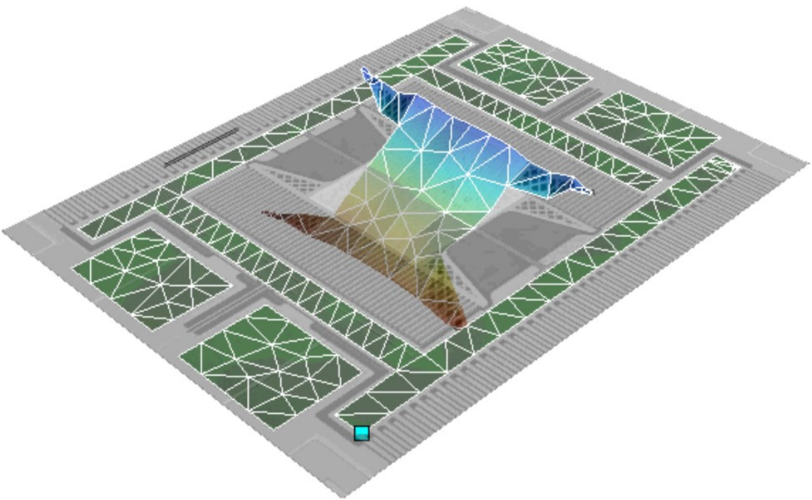

Figure 6-16 – IAx large surface deformation experimental data.

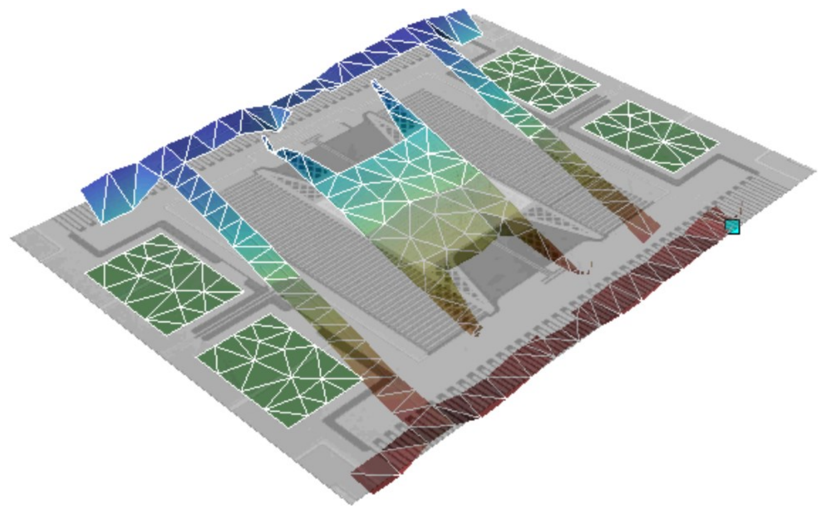

Figure 6-17 – OAx large surface deformation experimental data.

6.2.5 Inner axis large FoV

For the larger field of view, which is the case of the inner axis one, the Polytec laser scanner vibrometer is not capable of measuring it since the mirror deflects the measuring laser beam to a position outside of its range. Given this, the large optical FoV setup (with $\theta_i \approx 0°$) for visible laser wavelength was used to characterize the maximum angle of the inner axis at ambient pressure conditions.

Here, a square wave with a duty cycle of 15% initially, with a frequency above the natural one and an amplitude Vpp of 10 V, was applied. The amplitude was progressively increased to a maximum value of 200 V, and the signal frequency slowly decreased. A maximum FoV of 86° was achieved at 1241.8 Hz, as depicted in Figure 6-18.

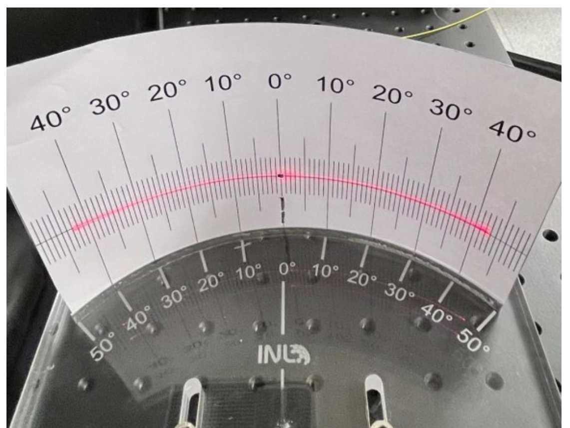

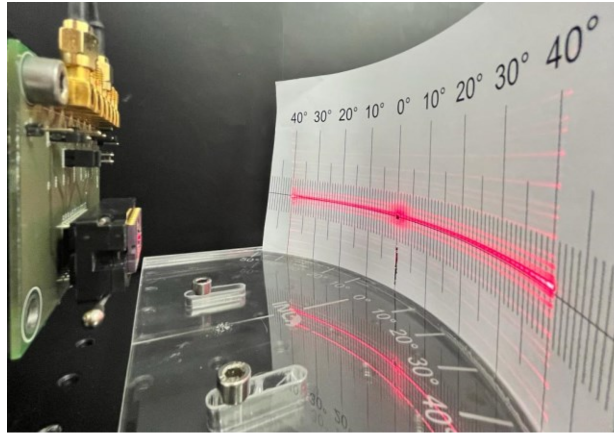

Figure 6-18 – IAx large filed of field (86°) experimentally achieved.

With this experimental optical setup, it is possible to analyse the FoV without any optical dispersion, with a wavelength within the visible range, in this case 638 nm. However, as shown in Figure 6-18, the diffraction pattern resultant from the patterned DOE on the mirror surface is highly non-uniform and presents several diffraction orders. This projected pattern cannot be analysed in this setup given that laser wavelength, but it is possible to see that it appears for all inner axis FoV.

6.3 Experimental characterization of the diffractive optical element

6.3.1 Topography

The diffractive optical element topography was also analysed using the Polytec MSA-500 surface metrology setup. Here, the depth of the patterned grating for 45° and 18° were measured, and it is summarized in Table 6-4.

Table 6-4 – DOE depth measurements with Polytec MSA-500 tool.

Samples	DOE depth [nm]	Target depth [nm]	Deviation [nm]
DOE@45°	595.04	548	47.04
DOE@18°	390.9	407	16.1

Figure 6-19 presents the experimental data of the topography of a DOE patterned on the reflective surface of a 2D MEMS mirror, with a highlight on a small profile line. The slight variation measured on the DOE depth is due to the interferometer fringes effects.

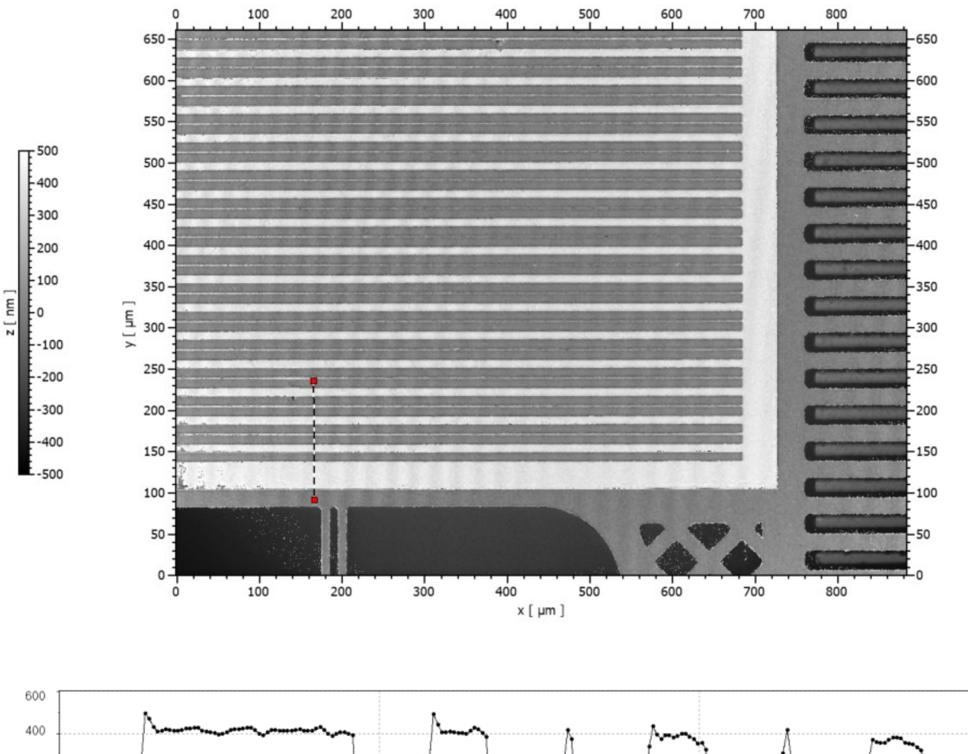

Figure 6-19 – DOE patterned on the reflective surface of the MEMS mirror topography measurement for an AoI of 18°.

6.3.2 Diffraction pattern measurements

The laser beam's incident angle changes, as explained in the previous sections, when the MEMS mirror is rotated around the fast axis, resulting in a dynamic optical path and decreasing the average intensity of the five spots, deteriorating the uniformity.

To statically characterize the diffractive optical element performance for the different incident angles that the mirror motion induces, the NIR FoV experimental setup was used. As previously detailed, using this setup, the MEMS mirror plan/DOE angle is always calibrated to have a normal projection to the

photodiode plan in order to minimize the projection distortion and photodiode sensitivity influence on the measurements, as can be seen in the schematic of Figure 6-20.

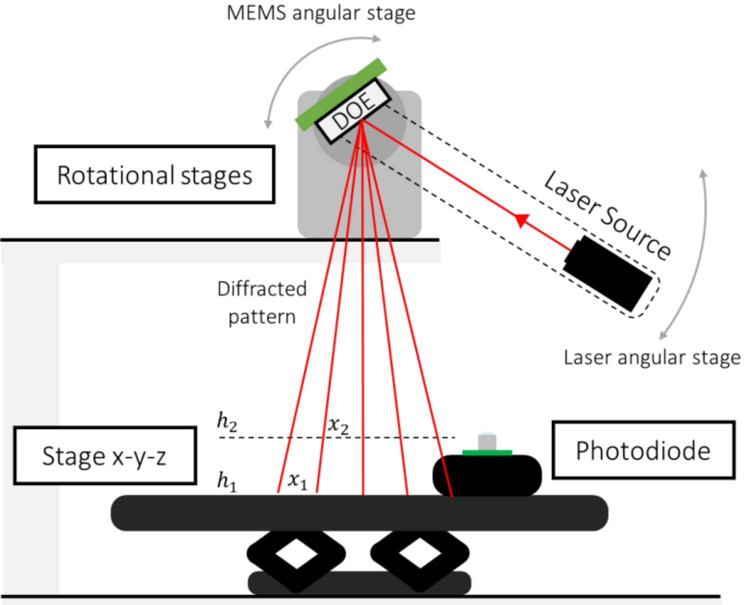

Figure 6-20 – NIR optical FoV experimental setup schematic for static diffraction projection.

DOEs were fabricated for a nominal incidence of 45° and 18°, i.e., when the mirror is at the rest position, denoted as DOE@45° and DOE@18°, respectively. This analysis was performed using a 1550 nm wavelength laser, assuming the fast axis mechanical deflection range of ±15°. This means that for the DOE@45°, it was measured from 30° to 60°, and for DOE@18°, it was measured from 3° to 33°. The diffracted pattern for each incident angle (AoI) was scanned by the photodiode with a line pitch of 150 µm (diameter of the photodetector). Figure 6-21 and Figure 6-22 display an example of the measurement output in different views, where it is possible to identify the zero, first, and second diffraction orders. To have a differential measure, so the scanning angle and diffraction aperture can be estimated without the need for absolute distance measurements and can also be independent of the DOE spatial position, for each AoI, the projection was measured twice, with a height of 0 mm and 40 mm (Figure 6-23).

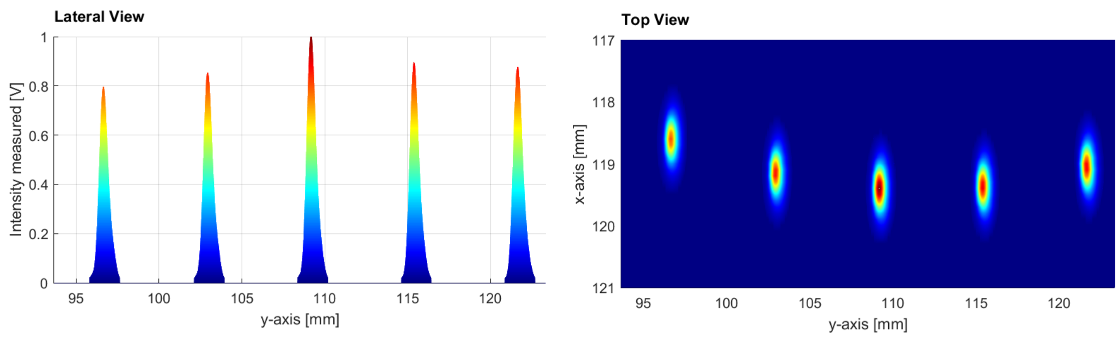

Figure 6-21 – Diffracted pattern scanned data lateral and top views.

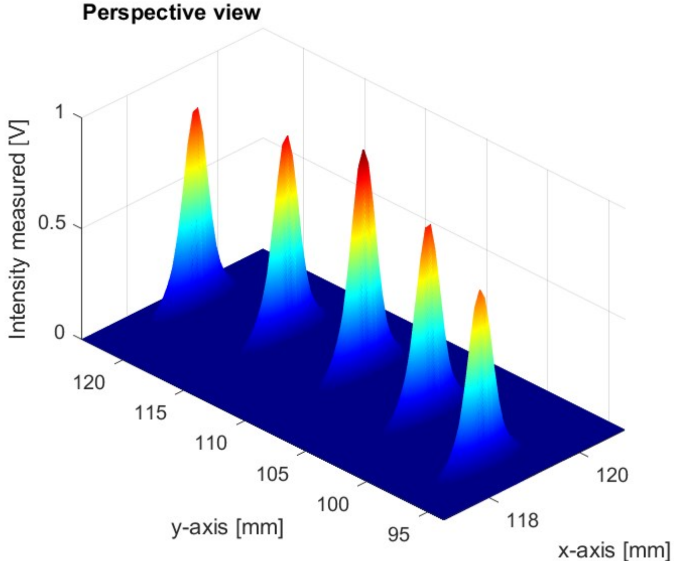

Figure 6-22 – Diffracted pattern scanned data, perspective view.

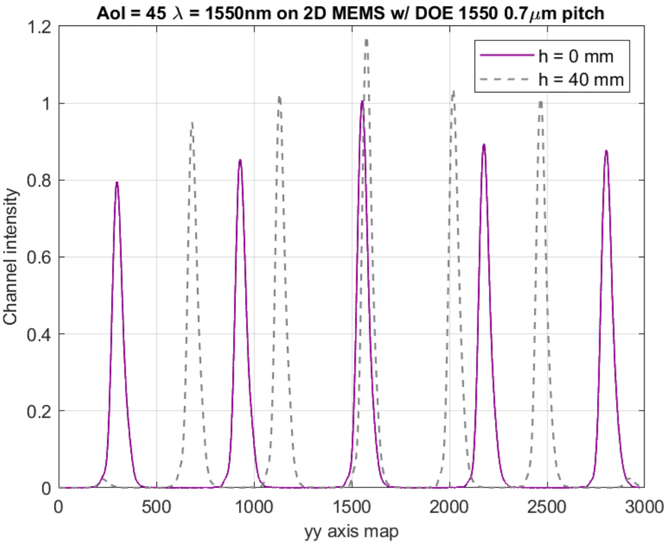

Figure 6-23 – DOE pattern scan for z=0mm and z=40mm.

6.3.3 Diffraction angular aperture

Regarding the geometry integrity, changing the AoI of the laser on the DOE surface might influence the initial geometry of the diffracted pattern. This strongly depends on the diffractive grating design. To guarantee that the diffracted pattern is geometrically uniform throughout the scanning, the required specifications are deviations from collinearity of less than $\pm 1°$ and angular separation between dots of $2.60° \pm 0.15°$. By the extraction of each diffraction peak planar position (x, y) for each stage height, the angular aperture of each peak regarding the zero-order beam was computed through a straightforward trigonometrical equation presented in (6-1). Figure 6-24 presents the average angular separation of the five spots from the different AoIs, and the respective minimum and maximum range of $\pm 0.15°$ for the (a)

DOE@45° and (b) DOE@18°. As can be seen, both Dammann gratings present an aperture extremely close to the target one of 2.6°, with a slight shift of below 0.05°

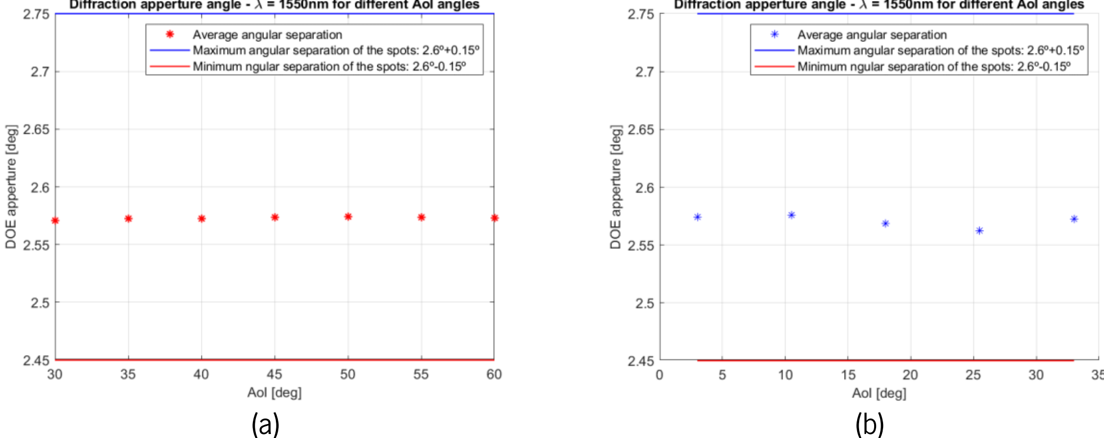

Figure 6-24 – Diffraction aperture angle, for a rest position incident angle of (a) 45° and (b) 18°.

6.3.4 Diffraction pattern uniformity

For range-related specifications, as well as for scanning consistency, the intensity of all five spots shall be uniform. The required peak uniformity for this system must guarantee a power variance of less than 15% in relation to the peak of the most significant power. The projection uniformity is calculated using the following equation.

$$nu[\%] = \left(1 - \frac{max(Ppeaks) - \min(Ppeaks)}{2 * mean(Ppeaks)}\right) * 100 \tag{6-2}$$

Figure 6-25 presents the computed uniformity of the five spots for the different AoIs, of the (a) DOE@45° and (b) DOE@18°. As can be seen, the DOE@45° presents a high non-uniformity for the MEMS AoI range, varying from close to 30% to values above 90% in the rest of the position. Comparatively, the DOE@18° presents values above 72% in all angles, resulting in a more uniform pattern.

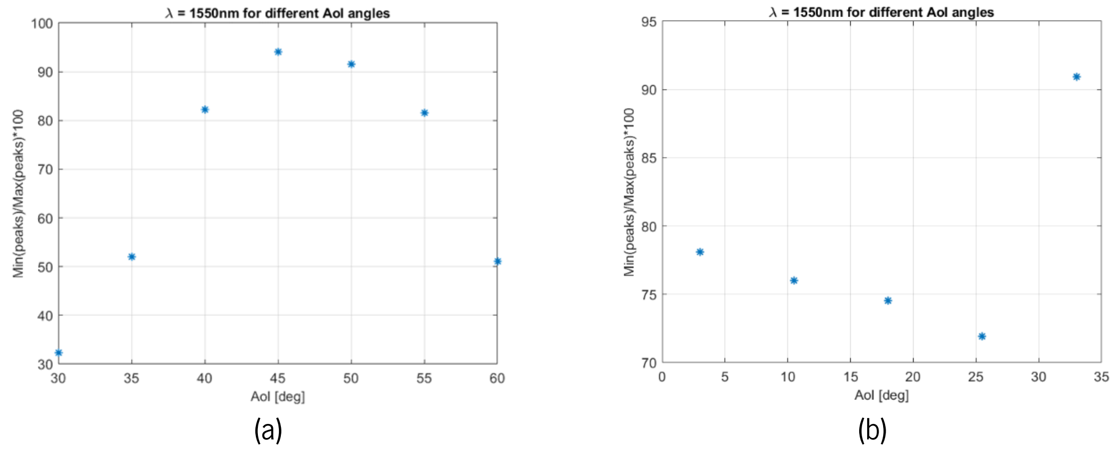

Figure 6-25 – Diffraction pattern uniformity, for a rest position incident angle of (a) 45° and (b) 18°.

6.4 Multibeam field-of-view scans

Using the large NIR FoV experimental setup, the multispot FoV was also experimentally characterized. Here, different experiments were implemented and scanned using the 2D MEMS mirror with a diffractive optical element embedded on the reflective surface, where:

1. Only the inner axis was actuated at resonance to achieve a large field of view, and the outer one remained in the rest position, as presented in the measurement output of Figure 6-26.a and Figure 6-27.a.
2. The inner axis was actuated at resonance to achieve a large horizontal field of view, and the outer axis was also actuated, but to achieve a small vertical FoV (below 2°), as presented in Figure 6-26.b and Figure 6-27.b.
3. The inner axis was actuated at resonance to achieve a large horizontal field of view, and the outer axis was also actuated to achieve a large vertical field of view (above 2°), as presented in Figure 6-26.c and Figure 6-27.c.

As can be seen, initially, when only the IAx is working, the projected FoV is composed of five lines, and when the OAx is working, these lines change to rectangles created by the diffraction pattern on top of the mirror surface. In Figure 6-27.c, the final five FoV cannot be distinguished since the MEMS structure is operated in order to scan the overall target area.

As can be seen, the measured projection presents higher intensity values on the horizontal edges. Here, this non-uniformity is not related to the diffraction pattern as it is in this region that the MEMS mirror has the lowest velocity and changes the angular direction, resulting in a higher integration time.

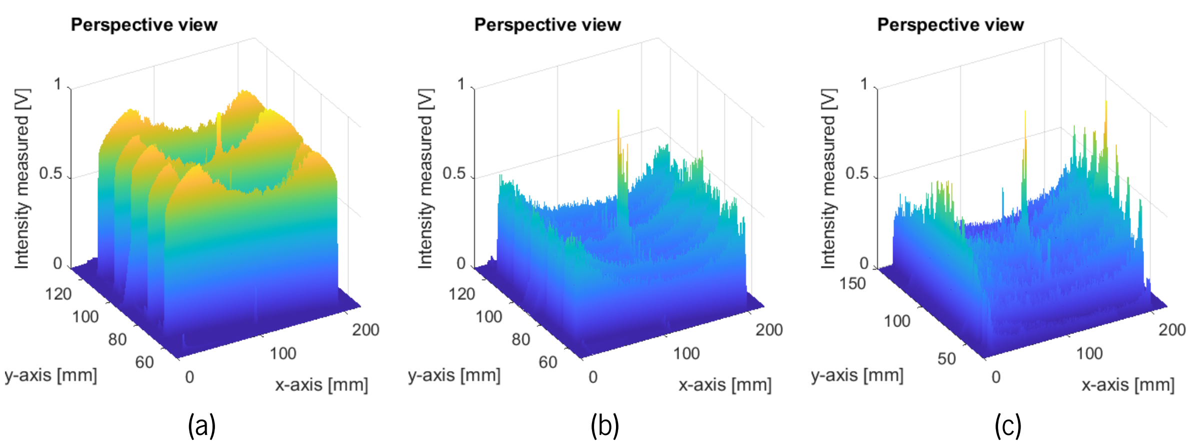

Figure 6-26 – Perspective view of the scanned FoV measured under the large scan photodiode setup, with (a) only IAx actuation, (b) IAx and low OAx actuation, and (c) IAx and high OAx actuation.

(a)

(b)

(c)

Figure 6-27 – Top view of the scanned FoV measured under the large scan photodiode setup, with (a) only IAx actuation, (b) IAx and low OAx actuation, and (c) IAx and high OAx actuation.

In this topology, using the MEMS mirror embedded with a DOE, the MEMS device's outer axis has to deflect only 20%, compared to an architecture using a typical reflective micromirror, as it uses five points to scan the entire FoV.

6.5 Conclusions

In this chapter, the 2D MEMS mirror with the diffractive optical element characterization was detailed. With the experimental results achieved, it is possible to conclude several aspects regarding the fabricated MEMS mirrors. The devices presented a quality factor and resonance frequency close to the theoretical values, validating this way the reliability of the analytical and FEM models. Moreover, a maximum horizontal FoV of 86° was achieved under ambient pressure conditions when modulating the square wave

actuation signal with an amplitude of 200 V at the resonance frequency value. Spring hardening was experimentally observed, presenting itself as a positive shift in the resonance frequency value with the increase of the actuation voltage amplitude.

The Dammann diffractive optical elements were also experimentally analysed. Dedicated experimental setups were implemented to evaluate the beam-splitting performance for the target wavelength, 1550 nm. Both grating micromachined to an AoI for 18° and 45° were characterized, and this followed the theoretical results, proving that the reduction on the normal angle of incidence for 45° to 18° was the correct decision in order to ensure a high uniformity with the for range of angles when the mirror is actuated. Furthermore, the angular aperture of the split pattern was presented, as well as the 2.6° between each diffraction order.

7. Conclusions

The research presented in this thesis focused on the development of a 2D MEMS mirror with a Dammann diffractive optical element for multibeam steering in LiDAR applications. Electrostatic actuation was selected for the MEMS mirror due to its compatibility with a simple SOI-based micromachining process and overall power efficiency. The theoretical foundations of the 2D gimbal-based MEMS mirror and the Dammann diffractive elements were thoroughly studied, both statically and dynamically, to identify key parameters essential to meet the targeted LiDAR specifications: a Field of View of 54°H x 13°V, angular resolution of 0.15°, and a frame rate of 10 Hz.

This thesis development methodology was segmented into four main phases: 1) modelling of the MEMS mirror, encompassing analytical and FEM simulation of its performance; 2) design and modelling of the DOE, focusing on the desired diffraction pattern and its compatibility with the MEMS structure; 3) optimization of the micromachining process, which involved the use of grayscale lithography to fabricate self-aligned asymmetric electrodes on a single silicon layer in a single patterning step, as well as the implementation of thinned handle masses to create structures that are electrically decoupled yet mechanically coupled on an SOI wafer; and 4) the experimental characterization of the fabricated 2D MEMS mirrors integrated with a Dammann DOE.

7.1 Thesis main achievements

Key conclusions drawn from this research's are outlined as follows:

1. **Verification of 2D MEMS Mirror with Diffractive Optical Elements**

A comparison between the initial requirements set for the device, driven by LiDAR application needs, and the achieved performance metrics are summarized in Table 7-1. All requirements were successfully met, demonstrating the potential of integrating Dammann diffractive elements into the MEMS mirror used for LiDAR applications. The figure of merit for the fabricated devices, calculated based on the criteria reported in [5], reached a value of 0.29. Although this figure may seem modest when compared to other electrostatic-based mirrors, as shown in Figure 7-1, it is important to note that the MEMS resonant frequency, which is a critical factor in this context, was adequately suited for the targeted LiDAR system. The developed system exhibited a better performance than most state-of-the-art systems regarding the Field of View area.

Table 7-1 – Initial parameters application-driven and achieved values.

Parameter	Target		Achieved	Unit
Reflective area	1.1 x 1.1		1.1 x 1.1	mm^2
Horizontal Natural resonance frequency, f_0	Without DOE	>434	1236	Hz
	With DOE	>87		
Horizontal FoV	54		86 (max)	°
Vertical scan frequency, f_0	10		10	Hz
Vertical FoV	2.6		2.6	°
Beam-diffracted aperture angle	2.6		2.57	°

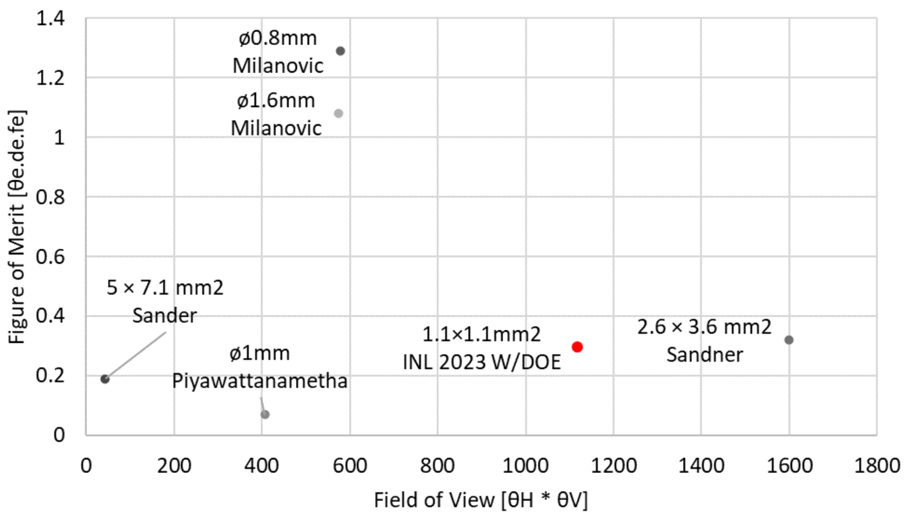

Figure 7-1 – Resonant plus non-resonant figure of merit comparison, based on [5].

The experimental performance of the multibeam system was compared with other systems in the literature, focusing on multibeam steering systems based on MEMS and DOE technology for LiDAR. Table 7-2 summarizes the different parameters of the different multibeam steering systems, such as FoV, scanning frequency, and diffraction aperture angle. Moreover, to easily identify the major differences between each work, the research schematics of each one are depicted in Figure 7-2.

Table 7-2 – Multibeam steering for LiDAR applications comparison with this work.

Parameter	(a) Niclass et al. 2012 [81]	(b) Kang et al. 2022 [82]	(c) Rodrigez, et al. 2020 [83]	(d) This work
Horizontal resonance frequency, f_0	1.3kHz	-	3.34kHz	1.24 kHz
Horizontal FoV	45°	38°	48°	86° (max)
Vertical scan frequency/Scan rate	10 Hz	1.7 Hz	-	10 Hz
Vertical FoV	11°	7°	-	13°
FoV $[\theta_H * \theta_V]$	495°x°	266°x°	-	1118°x°
Beam-diffracted aperture angle	15°	5~6°	3.4°	2.57°

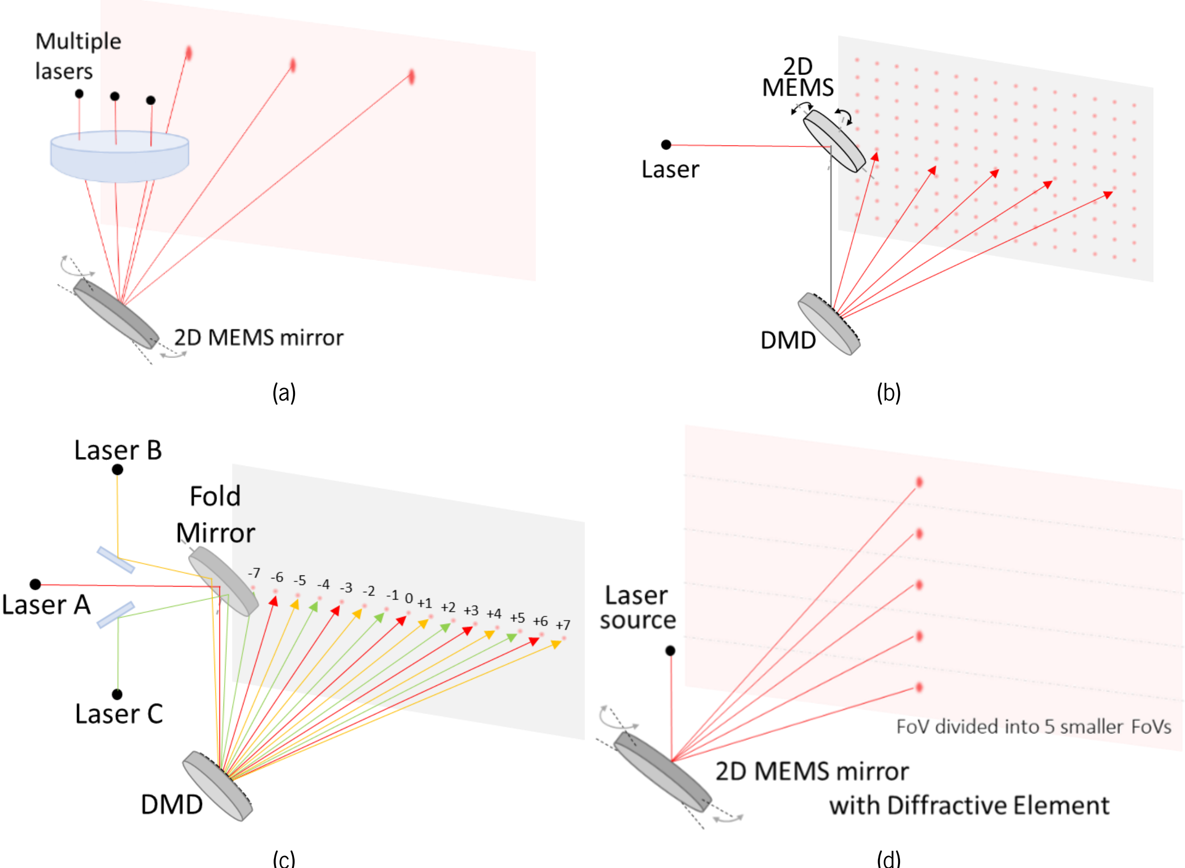

Figure 7-2 – Multibeam steering system schematic of the works compared in Table 7-2.

As can be seen, the developed multibeam steering device stands out in different aspects; first, in terms of field of view, the final scanned area of this work achieved a maximum value of 86° horizontal to 13°

vertical (FoV area of $1118^{\circ \times \circ}$), which is 2.25 times larger than the best-performing one from [81]. Moreover, the overall system implemented in this thesis does not require multiple laser sources neither multiple steering elements. This feature makes it a good solution for a miniaturized LiDAR system without the need for fine and complex alignment between multiple laser sources and optical devices.

2. Multilevel self-aligned process:

The main innovation regarding the MEMS structure relies on the self-aligned asymmetric electrodes. The micromachining process of these multilevel structures on a single silicon layer using one lithography step is one of the significant outcomes of this thesis. This process enabled the creation of self-aligned electrodes, allowing the inner axis motion without the need for wafer bonding or complex post-assemble caps to create asymmetry on the electrodes.

These improvements implemented on the standard INL SOI microfabrication process have already been used in new MEMS devices concepts. One of them is the use of the handle layer thinned masses as a movable structure to mechanically couple different structures on the device's layer, i.e., to achieve movable structures that are electrically decoupled but mechanically coupled. This has opened new possibilities for new MEMS sensors at INL, one of them a hierarchical nested 3-axis MEMS accelerometer [173]. Moreover, the sacrificial handle grids have been implemented as a standard technique to ensure a uniform etch environment on SOI-based devices with large cavities on the BS.

Moreover, the multilevel self-aligned process using grayscale lithography combined with a sequential process of bulk micromachining processes has also been explored in the development of new MEMS magnetometers.

3. Multilevel pattern replication using NIL:

A multilevel nanoimprint replication process was also optimized to produce a 1D MEMS mirrors employing vertical asymmetric comb-drive electrostatic actuation in a 200 mm wafer SOI process. Compared to direct write laser grayscale lithography, this process significantly enhances fabrication throughput. An extensive characterization of the morphology and topography of the intermediate working stamp is provided, along with an optimization study of the replica fabrication and the alignment procedure between the replica and the mirror substrate. The results obtained were in accordance with the theoretical design parameters, demonstrating that NIL can be successfully used as a fast, low-cost alternative lithography process to fabricate multilevel MEMS structures.

In an analysis focused solely on the costs associated with tool usage, it has been determined that the hourly cost of using the Heidelberg DWL 2000 system (for grayscale exposure) is approximately twice that of the Obducat Eitre® 8 system (for imprint). However, the exposure of a full 200 mm wafer using the grayscale lithography process needs approximately 40 hours. In contrast, upon the micromachining of the working stamp, the NIL process is considerably more time-efficient, taking roughly 1 hour (with alignment, stamping, and demolding processes).

This efficiency does not translate into a notable advantage in scenarios where only a single wafer is micromachined. However, the situation changes significantly in batch production or when processing more than two wafers. Under these circumstances, the multilevel pattern transfer to the SOI wafer via the imprint process is not only substantially faster—requiring only one hour (40 times faster)—but also remarkably more cost-effective, with a cost reduction of around 82 times.

7.2 Scientific contributions

The research led to three major scientific contributions: two journal publications and a patent application. The first journal publication, published in June 2020, in the Journal of Microelectromechanical Systems, is entitled "Fabrication of a MEMS Micromirror Based on Bulk Silicon Micromachining Combined With Grayscale Lithography". As the name suggests, it focuses on the micromachining process of asymmetric self-aligned electrodes of a 1D MEMS micromirror using grayscale lithography [116].

The second one, published in 2024 in the Journal of Manufacturing Process, is entitled "Nanoimprint lithography for grayscale pattern replication of MEMS mirrors in a 200 mm wafer", and it focused on the optimization of the MEMS fabrication process, not only in terms of time but also costs for batch production, using nanoimprint lithography to replicate the multilevel grayscale mask.

The worldwide patent application WO2023111667A1, entitled "Scanning system for range detection sensor", describes a system and method to scan the Field of View (FoV) of interest of a LiDAR system. The invention discloses an innovative method to scan a wide-angle FoV by combining diffractive optical elements with a beam steering mechanism designed for small to moderate scanning angles and an array of photodetectors.

Additionally, one more journal publication is under preparation, detailing the work on the 2D MEMS mirror with diffractive elements for multibeam steering. A preliminary title for this publication is "All-Silicon, Multispot 2D MEMS mirror for LiDAR Applications".

A scientific oral presentation regarding the nanoimprint techniques applied to replicate the grayscale pattern for MEMS applications was also presented at the international conference Micro and Nano Engineering (MNE) & EUROSENSORS 2022 in Leuven, Belgium.

The optimised micromachining process in the thesis has opened new opportunities for new MEMS accelerometer concepts, using the handle layer to mechanically couple and electrically decouple different parts of the device layer. This outcome was also presented in an oral presentation at the international conference Micro and Nano Engineering (MNE) & EUROSENSORS 2022 in Leuven, Belgium. It was also published in Micro and Nano Engineering journal, entitled "Microfabrication of double proof-mass SOI-based matryoshka-like structures for 3-axis MEMS accelerometers" [173], in 2023.

The developments regarding grayscale lithography have also been applied to new optical devices and moulds and were also published in the journal Micro and Nano Engineering, one entitled "Assessing tolerances in direct write laser grayscale lithography and reactive ion etching pattern transfer for fabrication of 2.5 D Si master molds" [174], in 2023, and other "Fabrication and optical characterization of large aperture diffractive lenses using greyscale lithography" [29], in 2022.

7.3 Future work

Within the MEMS micromachining process developed in this thesis, there is still room for further optimization and improvement. In the future, this novel self-aligned multilevel micromachining process can be optimized in order to fabricate devices with more than three levels, as well as to enable the patterning of different materials, such as the metal layer and the silicon structures in a single GS mask. A typical fabrication process for this specific device would require four different lithographic processes. This can potentially reduce the number of lithography steps required for processing such MEMS structures to two (one for the frontside and another for the backside of the SOI wafer). This process could also be optimized to create more levels in the SOI device layer, such as to create membranes or springs with thinner or varying heights, which are self-aligned with the rest of the MEMS structure.

A dynamic DOE can also be analysed, given the integration of a Dammann DOE into the MEMS reflective surface and the uniformity variations of the diffracted beam when the structure is actuated. This could also be achieved by MEMS technology, creating a structure where the bottom or top surface of the DOE is movable, and its height can be adjusted to present the desired grating depth for each laser incident angle. This can present several challenges since the DOE minimal features are 1.4 µm in width and 407 nm in depth; however, a highly uniform diffracted pattern could be achieved with in a larger FoV.

Moreover, the integration and, most importantly, the microfabrication process of this MEMS dynamic grating and the MEMS mirror can be highly complex.

Concerning the integration of the developed device within a comprehensive Light Detection and Ranging (LiDAR) system, or even in different applications where the developed 2D MEMS mirror could also be implemented, several works/research and experimental characterization are imperative for its successful incorporation. To achieve it, various steps are requisite:

1. Implementing a closed-loop system is critical, which requires an electronic readout system to sense the position of the mirror via the sensing electrodes already incorporated in the current design.
2. The development of a dedicated packaging solution is vital. This solution must encapsulate the MEMS mirror without obstructing the path of the incident and diffracted beams or inducing optical aberrations.
3. A comprehensive analysis and validation of the angular resolution of the steering mechanism are essential to ensure its efficacy.
4. Lastly, it is imperative to conduct experimental evaluations of the MEMS structure within the context of autonomous driving applications. These evaluations should encompass the device's performance across various temperatures and vibrations.

References

[1] S. T. S. Holmström, U. Baran, and H. Urey, "MEMS Laser Scanners: A Review," *Journal of Microelectromechanical Systems*, vol. 23, no. 2, pp. 259–275, 2014, doi: 10.1109/JMEMS.2013.2295470.

[2] G. Zhou and C. Lee, *Optical MEMS, Nanophotonics, and their Applications*. CRC Press Taylor & Francis Group, 2017.

[3] J. Da Chen, W. C. Miao, Y. H. Hong, and H. C. Kuo, "Recent Advances in Light Detection and Ranging: Optical Modulation Solutions and Novel Nanotechnologies," *Adv Quantum Technol*, vol. 2300157, pp. 1–21, 2023, doi: 10.1002/qute.202300157.

[4] Y. Qu, Y. Jiang, Y. He, Z. Qiu, S. Wang, and D. Sun, "A method of reducing stray light of 1.5 μm laser 3D vision system," *Infrared Phys Technol*, vol. 92, no. June, pp. 266–269, 2018, doi: 10.1016/j.infrared.2018.06.011.

[5] D. Wang, C. Watkins, and H. Xie, "MEMS Mirrors for LiDAR: A Review," *Micromachines (Basel)*, vol. 11, no. 5, p. 456, 2020, doi: 10.3390/mi11050456.

[6] A. Gelbart, B. C. Redman, R. S. Light, C. A. Schwartzlow, and A. J. Griffis, "Flash lidar based on multiple-slit streak tube imaging lidar," *Laser Radar Technology and Applications VII*, vol. 4723, no. July 2002, p. 9, 2002, doi: 10.1117/12.476407.

[7] D. J. Natale, R. L. Tutwiler, M. S. Baran, and J. R. Durkin, "Using full motion 3D flash LIDAR video for target detection, segmentation, and tracking," *Proceedings of the IEEE Southwest Symposium on Image Analysis and Interpretation*, pp. 21–24, 2010, doi: 10.1109/SSIAI.2010.5483929.

[8] Roman Burkard, R. Viga, J. Ruskowski, and A. Grabmaier, "Eye safety considerations and performance comparison of flash- and MEMS-based lidar systems," *Photonics and Digital Technologies for Imaging Applications VI*, vol. 11353, 2020, doi: https://doi.org/10.1117/12.2554726.

[9] S. M. Kim, E. S. Lee, K. W. Chun, J. Jin, and M. C. Oh, "Compact solid-state optical phased array beam scanners based on polymeric photonic integrated circuits," *Sci Rep*, vol. 11, no. 1, pp. 1–9, 2021, doi: 10.1038/s41598-021-90120-x.

[10] N. Li *et al.*, "A Progress Review on Solid-State LiDAR and Nanophotonics-Based LiDAR Sensors," *Laser Photon Rev*, vol. 16, no. 11, pp. 1–24, 2022, doi: 10.1002/lpor.202100511.

[11] H. W. Yoo *et al.*, "MEMS-based lidar for autonomous driving," *Elektrotechnik und Informationstechnik*, vol. 135, no. 6, pp. 408–415, 2018, doi: 10.1007/s00502-018-0635-2.

[12] R. Halterman and M. Bruch, "Velodyne HDL-64E lidar for unmanned surface vehicle obstacle detection," *Unmanned Systems Technology XII*, vol. 7692, p. 76920D, 2010, doi: 10.1117/12.850611.

[13] S. Royo and M. Ballesta-Garcia, "An overview of lidar imaging systems for autonomous vehicles," *Applied Sciences (Switzerland)*, vol. 9, no. 19, 2019, doi: 10.3390/app9194093.

[14] J. Hasselbach, F. Kastner, R. Has, S. Bogatscher, and C. Rembe, "Demonstration of a Mems-Mirror, 3D-Lidar System with Large Aperture and Scanning Angle," *2019 20th International Conference on Solid-State Sensors, Actuators and Microsystems and Eurosensors XXXIII, TRANSDUCERS 2019 and EUROSENSORS XXXIII*, no. June, pp. 1499–1502, 2019, doi: 10.1109/TRANSDUCERS.2019.8808370.

[15] J. Hasselbach, S. Bogatscher, and C. Rembe, "Laser scanner module with large sending aperture and inherent high angular position accuracy for three-dimensional light detecting and ranging," *Optical Engineering*, vol. 58, no. 08, p. 1, 2019, doi: 10.1117/1.oe.58.8.087101.

[16] F. Carpignano, G. Rigamonti, D. Riccardi, M. De Fazio, S. Merlo, and S. Member, "A Silicon Microsystem for Generation of Infrared Patterned Light," vol. 12, no. 9, pp. 907–911, 2016.

[17] J. W. Goodman, *Introduction to Fourier Optics*, 2nd ed. 1968.

[18] D. Werdehausen, S. Burger, I. Staude, T. Pertsch, and M. Decker, "General design formalism for highly efficient flat optics for broadband applications," *Opt Express*, vol. 28, no. 5, p. 6452, 2020, doi: 10.1364/oe.386573.

[19] H. Dammann and E. Klotz, "Coherent optical generation and inspection of two-dimensional periodic structures," *Opt Acta (Lond)*, 1977, doi: 10.1080/713819570.

[20] D. Werdehausen, S. Burger, I. Staude, T. Pertsch, and M. Decker, "Flat optics in high numerical aperture broadband imaging systems," *Journal of Optics (United Kingdom)*, vol. 22, no. 6, 2020, doi: 10.1088/2040-8986/ab8ea2.

[21] Q. Fang *et al.*, "Multi-channel silicon photonic receiver based on ring-resonators," *Opt Express*, vol. 18, no. 13, p. 13510, 2010, doi: 10.1364/oe.18.013510.

[22] N. Mohammad, M. Meem, X. Wan, and R. Menon, "Full-color, large area, transmissive holograms enabled by multi-level diffractive optics," *Sci Rep*, vol. 7, no. 1, pp. 1–6, 2017, doi: 10.1038/s41598-017-06229-5.

[23] H. Wang *et al.*, "Off-Axis Holography with Uniform Illumination via 3D Printed Diffractive Optical Elements," *Adv Opt Mater*, vol. 7, no. 12, 2019, doi: 10.1002/adom.201900068.

[24] R. Sawant, P. Bhumkar, A. Y. Zhu, P. Ni, F. Capasso, and P. Genevet, "Mitigating Chromatic Dispersion with Hybrid Optical Metasurfaces," *Advanced Materials*, vol. 31, no. 3, pp. 1–6, 2019, doi: 10.1002/adma.201805555.

[25] J. Liu, R. Shi, H. Zhao, and Y. Wang, "Design and fabrication of diffractive optical elements with complex profile by interference," *International Symposium on Photoelectronic Detection and Imaging 2013: Optical Storage and Display Technology*, vol. 8913, no. August, p. 89130P, 2013, doi: 10.1117/12.2033222.

[26] A. Goncharsky, A. Goncharsky, and S. Durlevich, "Diffractive optical element for creating visual 3D images," *Opt Express*, vol. 24, no. 9, p. 9140, 2016, doi: 10.1364/oe.24.009140.

[27] A. Goncharsky, A. Goncharsky, and S. Durlevich, "Diffractive optical element with asymmetric microrelief for creating visual security features," *Opt Express*, vol. 23, no. 22, p. 29184, 2015, doi: 10.1364/oe.23.029184.

[28] J. Albert *et al.*, "Maskless writing of submicrometer gratings in fused silica by focused ion beam implantation and differential wet etching," *Appl Phys Lett*, vol. 63, no. 17, pp. 2309–2311, 1993, doi: 10.1063/1.110509.

[29] D. E. Aguiam *et al.*, "Fabrication and optical characterization of large aperture diffractive lenses using greyscale lithography," *Micro and Nano Engineering*, vol. 14, no. February, pp. 0–7, 2022, doi: 10.1016/j.mne.2022.100111.

[30] Y. Dai, J. Antonello, and M. J. Booth, "Calibration of a phase-only spatial light modulator for both phase and retardance modulation," *Opt Express*, vol. 27, no. 13, p. 17912, 2019, doi: 10.1364/oe.27.017912.

[31] A. Georgiou *et al.*, "Liquid crystal over silicon device characteristics for holographic projection of high-definition television images," *Appl Opt*, vol. 47, no. 26, pp. 4793–4803, 2008, doi: https://doi.org/10.1364/AO.47.004793.

[32] Q. Hu, Y. Dai, C. He, and M. J. Booth, "Arbitrary vectorial state conversion using liquid crystal spatial light modulators," *Opt Commun*, vol. 459, no. November 2019, 2020, doi: 10.1016/j.optcom.2019.125028.

[33] L. De Sio, N. Tabiryan, R. Caputo, A. Veltri, and C. Umeton, "POLICRYPS structures as switchable optical phase modulators," *Opt Express*, vol. 16, no. 11, p. 7619, 2008, doi: 10.1364/oe.16.007619.

[34] H. B. Meng and L. R. Dalton, "Diphenyl - diacetylene liquid crystals for electro - optic application ," vol. 3017, no. March, pp. 3013–3017, 1994.

[35] J. F. Algorri, N. Bennis, J. Herman, P. Kula, V. Urruchi, and J. M. Sánchez-Pena, "Low aberration and fast switching microlenses based on a novel liquid crystal mixture," *Opt Express*, vol. 25, no. 13, p. 14795, 2017, doi: 10.1364/oe.25.014795.

[36] V. Milanović, G. A. Matus, and D. T. McCormick, "Gimbal-less monolithic silicon actuators for tip-tilt-piston micromirror applications," *IEEE Journal on Selected Topics in Quantum Electronics*, vol. 10, no. 3, pp. 462–471, 2004, doi: 10.1109/JSTQE.2004.829205.

[37] T. Izawa, T. Sasaki, and K. Hane, "Scanning micro-mirror with an electrostatic spring for compensation of hard-spring nonlinearity," *Micromachines (Basel)*, vol. 8, no. 8, 2017, doi: 10.3390/mi8080240.

[38] I. W. Jung, S. B. Mallick, and O. Solgaard, "Hgh-reflectivity Broadband Photonic Crystal Mirror MEMS With Low Dependence on Incident Angle and Polarization," *IEEE Journal of Micromechanical systems*, vol. 18, no. 4, p. 924, 2009, doi: 10.1109/JSTQE.2009.2021863.

[39] Y. Ohira, A. Checkovskiy, T. Yamanoi, T. Endo, H. Fujita, and H. Toshiyoshi, "A high-power handling MEMS optical scanner for display applications," *2008 IEEE/LEOS International Conference on Optical MEMS and Nanophotonics, OPT MEMS*, pp. 70–71, 2008, doi: 10.1109/OMEMS.2008.4607833.

[40] L. Ye, G. Zhang, and Z. You, "Large-aperture kHz operating frequency ti-alloy based optical micro scanning mirror for lidar Application," *Micromachines (Basel)*, vol. 8, no. 4, 2017, doi: 10.3390/mi8040120.

[41] D. Bayat, C. Ataman, B. Guldimann, S. Lani, W. Noell, and N. F. De Rooij, "Large electrostatically and electromagnetically actuated mirror system for space applications," *2010 International Conference on Optical MEMS and Nanophotonics, Optical MEMS and Nanophotonics 2010*, pp. 193–194, 2010, doi: 10.1109/OMEMS.2010.5672118.

[42] L. J. Hornbeck, "The DMD™ Projection Display Chip: A MEMS-Based Technology," *MRS Bull*, vol. 26, no. 4, pp. 325–327, 2001, doi: 10.1557/mrs2001.72.

[43] S. Ueda and M. Hirata, "Final-state control for a galvano scanner: Minimizing mirror vibration in an inclined direction relative to the rotation axis," *2017 IEEE 56th Annual Conference on Decision and Control, CDC 2017*, vol. 2018-Janua, no. Cdc, pp. 3289–3294, 2018, doi: 10.1109/CDC.2017.8264142.

[44] M. Yoda, K. Isamoto, C. Chong, H. Ito, A. Murata, and H. Toshiyoshi, "A MEMS 1-D Optical Scanner for Laser Projection Display using Self-assembled Vertical Combs and Scan-angle Magnifying Mechanism," in *The 13th International Conference on Solid-state Sensors, Actuators and Microsystems*, 2005, pp. 19–20.

[45] Y. Ohira, A. Checkovskiy, T. Yamanoi, T. Endo, H. Fujita, and H. Toshiyoshi, "A high-power handling MEMS optical scanner for display applications," *2008 IEEE/LEOS International Conference on Optical MEMS and Nanophotonics, OPT MEMS*, pp. 70–71, 2008, doi: 10.1109/OMEMS.2008.4607833.

[46] D. Bayat, C. Ataman, B. Guldimann, S. Lani, W. Noell, and N. F. De Rooij, "Large electrostatically and electromagnetically actuated mirror system for space applications," *2010 International Conference on Optical MEMS and Nanophotonics, Optical MEMS and Nanophotonics 2010*, pp. 193–194, 2010, doi: 10.1109/OMEMS.2010.5672118.

[47] K. H. Koh, T. Kobayashi, J. Xie, A. Yu, and C. Lee, "Novel piezoelectric actuation mechanism for a gimbal-less mirror in 2D raster scanning applications," *Journal of Micromechanics and Microengineering*, vol. 21, no. 7, 2011, doi: 10.1088/0960-1317/21/7/075001.

[48] D. T. McCormick, W. Jung, Y. Ahn, Z. Chen, and N. C. Tien, "A Three Dimensional Real-Time MEMS Based Optical Biopsy System for In-Vivo Clinical Imaging," in *TRANSDUCERS 2007 - 2007 International Solid-State Sensors, Actuators and Microsystems Conference*, IEEE, Jun. 2007, pp. 203–208. doi: 10.1109/SENSOR.2007.4300106.

[49] D. J. Bell, T. J. Lu, N. A. Fleck, and S. M. Spearing, "MEMS actuators and sensors : observations on their performance," *Journal of Micromechanics and Microengineering*, vol. 15, no. 7, 2005, doi: 10.1088/0960-1317/15/7/022.

[50] S. Moon *et al.*, "Two-Axis Electrostatic Gimbaled Mirror Scanner with Self-Aligned Tilted Stationary Combs," *IEEE Photonics Technology Letters*, vol. 28, no. 5, pp. 557–560, 2016, doi: 10.1109/LPT.2015.2513483.

[51] A. D. Yalcinkaya, H. Urey, D. Brown, T. Montague, and R. Sprague, "Two-axis electromagnetic microscanner for high resolution displays," *Journal of Microelectromechanical Systems*, vol. 15, no. 4, pp. 786–794, 2006, doi: 10.1109/JMEMS.2006.879380.

[52] U. Baran, S. Holmstrom, D. Brown, W. Davis, O. Cakmak, and H. Urey, "Resonant PZT MEMS scanners with integrated angle sensors," *International Conference on Optical MEMS and Nanophotonics*, pp. 99–100, 2014, doi: 10.1109/OMN.2014.6924612.

[53] M. Lara-Castro *et al.*, "Design and modeling of polysilicon electrothermal actuators for a MEMS mirror with low power consumption," *Micromachines (Basel)*, vol. 8, no. 7, 2017, doi: 10.3390/mi8070203.

[54] H. Xie, S. Strassle, S. Koppal, A. Stainsby, Y. Bai, and D. Wang, "A compact 3D lidar based on an electrothermal two-axis MEMS scanner for small UAV," no. May, p. 14, 2018, doi: 10.1117/12.2304529.

[55] A. D. Yalcinkaya, H. Urey, D. Brown, T. Montague, and R. Sprague, "Two-axis electromagnetic microscanner for high resolution displays," *Journal of Microelectromechanical Systems*, 2006, doi: 10.1109/JMEMS.2006.879380.

[56] M. Freeman, M. Champion, and S. Madhavan, "Scanned Laser Pico-Projectors: Seeing the Big Picture (with a Small Device)," *Opt Photonics News*, vol. 20, no. 5, pp. 28–34, 2009.

[57] F. Li, P. Zhou, T. Wang, J. He, H. Yu, and W. Shen, "A large-size MEMS scanning mirror for speckle reduction application," *Micromachines (Basel)*, vol. 8, no. 5, pp. 1–10, 2017, doi: 10.3390/mi8050140.

[58] T. Iseki, M. Okumura, and T. Sugawara, "Two-dimensionally deflecting mirror using electromagnetic actuation," *Opt Rev*, vol. 13, no. 4, pp. 189–194, 2006, doi: 10.1007/s10043-006-0189-0.

[59] Ç. Ataman, S. Lani, W. Noell, and N. De Rooij, "A dual-axis pointing mirror with moving-magnet actuation," *Journal of Micromechanics and Microengineering*, vol. 23, no. 2, 2013, doi: 10.1088/0960-1317/23/2/025002.

[60] V. Milanovic, "Linearized Gimbal-less Two-Axis MEMS Mirrors," in *Optical Fiber Communication Conference and National Fiber Optic Engineers Conference, OSA Technical Digest (CD)*, 2009.

[61] Ulrich Hofmann *et al.*, "Resonant biaxial 7-mm MEMS mirror for omnidirectional scanning," *Journal of Micro/Nanolithography, MEMS, and MOEMS*, vol. 13, no. 1, 2013, doi: https://doi.org/10.1117/1.JMM.13.1.011103.

[62] A. C. L. Hung, H. Y. H. Lai, T. W. Lin, S. G. Fu, and M. S. C. Lu, "An electrostatically driven 2D micro-scanning mirror with capacitive sensing for projection display," *Sens Actuators A Phys*, vol. 222, pp. 122–129, 2015, doi: 10.1016/j.sna.2014.10.008.

[63] L. Zhou, X. Zhang, and H. Xie, "An electrothermal Cu/W bimorph tip-tilt-piston MEMS mirror with high reliability," *Micromachines (Basel)*, vol. 10, no. 5, pp. 23–26, 2019, doi: 10.3390/mi10050323.

[64] D. Wang, X. Zhang, L. Zhou, M. Liang, D. Zhang, and H. Xie, "An ultra-fast electrothermal micromirror with bimorph actuators made of copper/tungsten," *International Conference on Optical MEMS and Nanophotonics*, pp. 17–18, 2017, doi: 10.1109/OMN.2017.8051478.

[65] S. Gu-Stoppel *et al.*, "New designs for MEMS-micromirrors and micromirror packaging with electrostatic and piezoelectric drive," *Advanced Materials - TechConnect Briefs 2016*, vol. 4, no. May, pp. 87–90, 2016.

[66] B.-W. Yoo *et al.*, "MEMS micromirror characterization in space environments," *Opt Express*, vol. 17, no. 5, p. 3370, 2009, doi: 10.1364/oe.17.003370.

[67] H. Hemmati, A. Biswas, and I. B. Djordjevic, "Deep-Space Optical Communications: Future Perspectives and Applications," *Proceedings of the IEEE*, vol. 99, no. 11, pp. 2020–2039, 2011, doi: 10.1109/JPROC.2011.2160609.

[68] P. F. McManamon *et al.*, "Optical phased array technology," in *Proceedings of the IEEE*, 1996, pp. 268–298. doi: doi: 10.1109/5.482231.

[69] D. N. Hutchison *et al.*, "High-resolution aliasing-free optical beam steering," *Optica*, vol. 3, no. 8, p. 887, 2016, doi: 10.1364/optica.3.000887.

[70] Y. Wang and M. C. Wu, "Micromirror based optical phased array for wide-angle beamsteering," *Proceedings of the IEEE International Conference on Micro Electro Mechanical Systems (MEMS)*, pp. 897–900, 2017, doi: 10.1109/MEMSYS.2017.7863553.

[71] S. Hamann, A. Ceballos, J. Landry, and O. Solgaard, "High-speed random access optical scanning using a linear MEMS phased array," *Opt Lett*, 2018, doi: 10.1364/ol.43.005455.

[72] P. A. Blanche, L. LaComb, Y. Wang, and M. C. Wu, "Diffraction-based optical switching with MEMS," *Applied Sciences (Switzerland)*, 2017, doi: 10.3390/app7040411.

[73] S. Rudra, D. Van Thourhout, A. Witvrouw, J. De Coster, and R. Van Hoof, "Static and dynamic characterization of poly-SiGe grating light valves," *International Conference on Optical MEMS and Nanophotonics*, pp. 203–204, 2011, doi: 10.1109/OMEMS.2011.6031031.

[74] P.-A. Blanche, D. Carothers, J. Wissinger, and N. Peyghambarian, "Digital micromirror device as a diffractive reconfigurable optical switch for telecommunication," *Journal of Micro/Nanolithography, MEMS, and MOEMS*, vol. 13, no. 1, p. 011104, 2013, doi: 10.1117/1.jmm.13.1.011104.

[75] M. C. Wu *et al.*, "Optical phased array using high contrast gratings for two dimensional beamforming and beamsteering," *Opt Express*, vol. 21, no. 10, p. 12238, 2013, doi: 10.1364/oe.21.012238.

[76] T. Sun *et al.*, "High-speed 32×32 MEMS optical phased array," *MOEMS and Miniaturized Systems XIII*, vol. 8977, p. 89770H, 2014, doi: 10.1117/12.2044197.

[77] "LUMOTIVE." [Online]. Available: https://www.lumotive.com/

[78] F. Xu, D. Qiao, X. Song, W. Zheng, Y. He, and Q. Fan, "A Semi-coaxial MEMS-based LiDAR," *IECON Proceedings (Industrial Electronics Conference)*, vol. 2019-Octob, pp. 6726–6731, 2019, doi: 10.1109/IECON.2019.8927392.

[79] X. Zhang, S. J. Koppal, R. Zhang, L. Zhou, E. Butler, and H. Xie, "Wide-angle structured light with a scanning MEMS mirror in liquid," *Opt Express*, 2016, doi: 10.1364/oe.24.003479.

[80] I. Maksymova, P. Greiner, L. C. Niedermueller, and N. Druml, "Detection and Compensation of Periodic Jitters of Oscillating MEMS Mirrors used in Automotive Driving Assistance Systems," in *SAS 2019 - 2019 IEEE Sensors Applications Symposium, Conference Proceedings*, 2019. doi: 10.1109/SAS.2019.8706008.

[81] C. Niclass *et al.*, "Design and characterization of a 256x64-pixel single-photon imager in CMOS for a MEMS-based laser scanning time-of-flight sensor," *Opt Express*, 2012, doi: 10.1364/oe.20.011863.

[82] E. Kang *et al.*, "All-MEMS Lidar Using Hybrid Optical Architecture with Digital Micromirror Devices and a 2D-MEMS Mirror," *Micromachines (Basel)*, vol. 13, no. 9, 2022, doi: 10.3390/mi13091444.

[83] J. Rodriguez, B. Smith, B. Hellman, and Y. Takashima, "Fast laser beam steering into multiple diffraction orders with a single digital micromirror device for time-of-flight lidar," *Appl Opt*, vol. 59, no. 22, p. G239, 2020, doi: 10.1364/ao.393075.

[84] T. Uchida, F. Yu, M. Nihei, and J. Taniguchi, "Fabrication of antireflection structures on the surface of optical lenses by using a liquid transfer imprint technique," *Microelectron Eng*, vol. 153, pp. 43–47, 2016, doi: 10.1016/j.mee.2016.01.019.

[85] N. Yu *et al.*, "Multi-beam multi-wavelength semiconductor lasers," *Appl Phys Lett*, vol. 95, no. 16, 2009, doi: 10.1063/1.3253713.

[86] R. A. Hyde, "Eyeglass. 1. Very large aperture diffractive telescopes," *Appl. Opt.*, no. 38, 1999.

[87] H. Cai *et al.*, "Ultrathin transmissive metasurfaces for multi-wavelength optics in the visible," *Appl Phys Lett*, vol. 114, no. 7, 2019, doi: 10.1063/1.5082557.

[88] Y. Zhou, Q. Wen, Z. Wen, J. Huang, and F. Chang, "An electromagnetic scanning mirror integrated with blazed grating and angle sensor for a near infrared micro spectrometer," *Journal of Micromechanics and Microengineering*, vol. 27, no. 125009, 2017.

[89] H. Yu, G. Zhou, S. K. Sinha, and F. S. Chau, "Scanning grating based in-plane movement sensing," *Journal of Micromechanics and Microengineering*, vol. 20, no. 8, 2010, doi: 10.1088/0960-1317/20/8/085007.

[90] Y. Zhou, Q. Wen, Z. Wen, and T. Yang, "Modeling of MOEMS electromagnetic scanning grating mirror for NIR micro-spectrometer," *AIP Adv*, vol. 6, no. 025025, p. 9, 2016, doi: 10.1063/1.4942973.

[91] Q. Nie, Z. Wen, and J. Huang, "Design and fabrication of a MEMS high-efficiency NIR-scanning grating based on tilted (1 1 1) silicon wafer," *Eur. Phys. J. Appl. Phys.*, vol. 72, no. 1, pp. 1–8, 2015, doi: 10.1051/epjap/2015150285.

[92] M. Kraft, A. Kenda, A. Frank, and W. Scherf, “Single-detector micro-electro-mechanical scanning grating spectrometer,” *Anal Bioanal Chem*, vol. 386, pp. 1259–1266, 2006, doi: 10.1007/s00216-006-0726-5.

[93] Y. Du, G. Zhou, K. L. Cheo, Q. Zhang, H. Feng, and F. S. Chau, “A 2-DOF circular-resonator-driven in-plane vibratory grating laser scanner,” *Journal of Microelectromechanical Systems*, vol. 18, no. 4, pp. 892–904, 2009, doi: 10.1109/JMEMS.2009.2023844.

[94] Y. Wang *et al.*, “2D broadband beamsteering with large-scale MEMS optical phased array,” *Optica*, 2019, doi: 10.1364/optica.6.000557.

[95] B. Bhushan, *Springer Handbook of Nanotechnology*. Berlin, Heidelberg: Springer Berlin Heidelberg, 2004. doi: 10.1007/3-540-29838-X.

[96] C. Liu, “Foundations of MEMS,” 2005.

[97] W. D. Westwood, “Physical Vapor Deposition,” in *Microelectronic Materials and Processes*, Dordrecht: Springer Netherlands, 1989, pp. 133–201. doi: 10.1007/978-94-009-0917-5_4.

[98] G. Gupta, R. K. Tyagi, S. K. Rajput, P. Saxena, A. Vashisth, and S. Mehndiratta, “PVD based thin film deposition methods and characterization / property of different compositional coatings - A critical analysis,” *Mater Today Proc*, vol. 38, pp. 259–264, 2021, doi: 10.1016/j.matpr.2020.07.132.

[99] S. T. AG., “TIMARIS Cluster Tool Modules - PVD Production Platform Semiconductor Industry.” Accessed: Nov. 16, 2023. [Online]. Available: https://www.singulus.com/products/timaris-modules/

[100] © KENOSISTEC Srl, “KENOSISTEC,” 2020.

[101] S. Vepřek, “Plasma-induced and plasma-assisted chemical vapour deposition,” *Thin Solid Films*, vol. 130, no. 1–2, pp. 135–154, Aug. 1985, doi: 10.1016/0040-6090(85)90303-7.

[102] FirstNano®, “EASYTUBE® 3000.” Accessed: Nov. 16, 2023. [Online]. Available: https://www.firstnano.com/systems/process-equipment/easytube-3000/

[103] S. T. Ltd., “SPTS: a KLA Company.” Accessed: Nov. 19, 2023. [Online]. Available: https://www.spts.com/

[104] W. Ruythooren *et al.*, "Electrodeposition for the synthesis of microsystems," *Journal of Micromechanics and Microengineering*, vol. 10, no. 2, pp. 101–107, Jun. 2000, doi: 10.1088/0960-1317/10/2/301.

[105] A. A. Ojo and I. M. Dharmadasa, "Electroplating of Semiconductor Materials for Applications in Large Area Electronics: A Review," *Coatings*, vol. 8, no. 8, p. 262, Jul. 2018, doi: 10.3390/coatings8080262.

[106] A. GmbH, "uGalv Electroplating." Accessed: Nov. 19, 2023. [Online]. Available: https://ammt.com/products/electroplating/mu-galv/

[107] M. Knez, K. Nielsch, and L. Niinistö, "Synthesis and Surface Engineering of Complex Nanostructures by Atomic Layer Deposition," *Advanced Materials*, vol. 19, no. 21, pp. 3425–3438, Nov. 2007, doi: 10.1002/adma.200700079.

[108] J. S. Ponraj, G. Attolini, and M. Bosi, "Review on Atomic Layer Deposition and Applications of Oxide Thin Films," *Critical Reviews in Solid State and Materials Sciences*, vol. 38, no. 3, pp. 203–233, Jan. 2013, doi: 10.1080/10408436.2012.736886.

[109] B. Tfs, "BENEQ TFS 200 Specifications Beneq Research Equipment ".

[110] B. Bräuer, D. R. T. Zahn, T. Rüffer, and G. Salvan, "Deposition of thin films of a transition metal complex by spin coating," *Chem Phys Lett*, vol. 432, no. 1–3, pp. 226–229, Dec. 2006, doi: 10.1016/j.cplett.2006.10.070.

[111] H. A. M. Mustafa and D. A. Jameel, "Modeling and the main stages of spin coating process: A review," *Journal of Applied Science and Technology Trends*, vol. 2, no. 03, pp. 91–95, Aug. 2021, doi: 10.38094/jastt203109.

[112] S. M. SE, "Mask Aligner." Accessed: Nov. 19, 2023. [Online]. Available: https://www.suss.com/en/products-solutions/mask-aligner

[113] C. McKenna, K. Walsh, M. Crain, and J. Lake, "Maskless Direct Write Grayscale Lithography for MEMS Applications," in *2010 18th Biennial University/Government/Industry Micro/Nano Symposium*, IEEE, Jun. 2010, pp. 1–4. doi: 10.1109/UGIM.2010.5508906.

[114] H. Instruments, "DWL 2000." Accessed: Nov. 19, 2023. [Online]. Available: https://heidelberg-instruments.com/product/dwl-2000-4000-laser-lithography-systems/

[115] A. Grushina, "Direct-write grayscale lithography," *Advanced Optical Technologies*, vol. 8, no. 3–4, pp. 163–169, 2019, doi: 10.1515/aot-2019-0024.

[116] I. S. Garcia *et al.*, "Fabrication of a MEMS Micromirror Based on Bulk Silicon Micromachining Combined With Grayscale Lithography," *IEEE J. Microelectromechanical Syst.*, pp. 1–7, 2020.

[117] D. E. Aguiam *et al.*, "Fabrication and optical characterization of large aperture diffractive lenses using greyscale lithography," *Micro and Nano Engineering*, vol. 14, no. February, pp. 0–7, 2022, doi: 10.1016/j.mne.2022.100111.

[118] A. A. Tseng, Kuan Chen, C. D. Chen, and K. J. Ma, "Electron beam lithography in nanoscale fabrication: recent development," *IEEE Transactions on Electronics Packaging Manufacturing*, vol. 26, no. 2, pp. 141–149, Apr. 2003, doi: 10.1109/TEPM.2003.817714.

[119] Y. Chen, "Nanofabrication by electron beam lithography and its applications: A review," *Microelectron Eng*, vol. 135, pp. 57–72, Mar. 2015, doi: 10.1016/j.mee.2015.02.042.

[120] S. Chou, "Nanoimprint lithography," *Technol. Rev*, vol. 106, no. 1, p. 42, 2003, doi: doi: 10.1116/1.588605.

[121] H. Schift and A. Kristensen, *Nanoimprint Lithography*. New York: Springer, 2007.

[122] M. J. Madou, *Fundamentals of Microfabrication*, 2nd ed. Florida: CRC Press, 2002. doi: 10.1201/9781482274004.

[123] H. Jansen, H. Gardeniers, M. de Boer, M. Elwenspoek, and J. Fluitman, "A survey on the reactive ion etching of silicon in microtechnology," *Journal of Micromechanics and Microengineering*, vol. 6, no. 1, pp. 14–28, Mar. 1996, doi: 10.1088/0960-1317/6/1/002.

[124] I. Adesida, C. Youtsey, A. T. Ping, F. Khan, L. T. Romano, and G. Bulman, "Dry and Wet Etching for Group III – Nitrides," *MRS Proceedings*, vol. 537, p. G1.4, Feb. 1998, doi: 10.1557/PROC-537-G1.4.

[125] J. Hopwood, "Review of inductively coupled plasmas for plasma processing," *Plasma Sources Sci Technol*, vol. 1, no. 2, pp. 109–116, May 1992, doi: 10.1088/0963-0252/1/2/006.

[126] M. Huff, "Recent Advances in Reactive Ion Etching and Applications of High-Aspect-Ratio Microfabrication," *Micromachines (Basel)*, vol. 12, no. 8, p. 991, Aug. 2021, doi: 10.3390/mi12080991.

[127] P. J. Revell and G. F. Goldspink, "A review of reactive ion beam etching for production," *Vacuum*, vol. 34, no. 3–4, pp. 455–462, Mar. 1984, doi: 10.1016/0042-207X(84)90083-6.

[128] N. T. S. Ltd, "Nordiko 7500 – Broad Ion Beam Milling system." Accessed: Nov. 16, 2023. [Online]. Available: https://nordiko-tech.co.uk/nordiko-7500-broad-ion-beam-milling-system

[129] I. S. Garcia, E. E. Moreira, R. A. Dias, J. Gaspar, F. S. Alves, and L. A. Rocha, "Sub-Micron Mems Accelerometer with Handle-Layer Patterning for Damping Enhancement Using Time Transduction," in *2019 20th International Conference on Solid-State Sensors, Actuators and Microsystems and Eurosensors XXXIII, TRANSDUCERS 2019 and EUROSENSORS XXXIII*, Berlin, Germany, 2019, pp. 2045–2048. doi: 10.1109/TRANSDUCERS.2019.8808247.

[130] J. Cheng *et al.*, "AN AUTO-ALIGNED VERTICAL COMB DRIVE FOR LOW-COST VARIABLE OPTICAL ATTENUATORS School of Optoelectronic Engineering , Xi ' an Technological University , Shaanxi , CHINA Wuxi WiO Technology Co ., Ltd , Jiangsu , CHINA Department of Electrical and Computer E," vol. 1, no. c, pp. 622–625, 2017.

[131] Z. Hailu, S. He, and R. Ben Mrad, "A novel vertical comb-drive electrostatic actuator using a one layer process," *Journal of Micromechanics and Microengineering*, vol. 24, no. 11, 2014, doi: 10.1088/0960-1317/24/11/115016.

[132] H. Hamaguchi, K. Sugano, T. Tsuchiya, and O. Tabata, "A Differential Capacitive Three-Axis SOI Accelerometer using Vertical Comb Electrodes," in *TRANSDUCERS and EUROSENSORS '07 - 4th International Conference on Solid-State Sensors, Actuators and Microsystems*, 2007. doi: 10.1109/SENSOR.2007.4300425.

[133] T. Tsuchiya and H. Funabashi, "A z-axis differential capacitive SOI accelerometer with vertical comb electrodes," *Sens Actuators A Phys*, 2004, doi: 10.1016/j.sna.2004.05.008.

[134] M. Zickar, M. Mita, M. Ataka, and H. Fujita, "Low cross talk design and simple fabrication process of electrostatic vertical comb-drive actuators for positioning application," *IEEJ Transactions on Electrical and Electronic Engineering*, vol. 2, no. 3, pp. 289–294, 2007, doi: 10.1002/tee.20144.

[135] J. Xie, R. Agarwal, Y. Liu, and J. M. Tsai, "A three-axis SOI accelerometer sensing with both in-plane and vertical comb electrodes," *Microsystem Technologies*, vol. 18, no. 3, pp. 325–332, 2012, doi: 10.1007/s00542-011-1393-9.

[136] H.-T. Su, G.-L. Luo, J. Hsieh, Y.-C. Fu, and W. Fang, "Process platform for high aspect-ratio self-aligned vertical comb actuators," in *Proc. 18th Int. Conf. Solid-State Sens., Actuators Microsyst. (TRANSDUCERS)*, Anchorage, Alaska, 2015, pp. 1342–1345.

[137] Y. Fan, C. Cui, H. Yu, W. Shen, Z. Wang, and J. Li, "An electrostatic vertical comb-drive micromirror with self-Aligned assembly," *2017 IEEE 12th International Conference on Nano/Micro Engineered and Molecular Systems, NEMS 2017*, no. 1, pp. 268–272, 2017, doi: 10.1109/NEMS.2017.8017022.

[138] Q. Deng, Y. Yang, H. Gao, Y. Zhou, Y. He, and S. Hu, "Fabrication of micro-optics elements with arbitrary surface profiles based on one-step maskless grayscale lithography," *Micromachines (Basel)*, vol. 8, no. 10, 2017, doi: 10.3390/mi8100314.

[139] S. D. Senturia, *Microsystem Design*. 2000.

[140] M. R. Horne, *Formulas for stress and strain*, vol. 3, no. 1. 1954. doi: 10.1016/0022-5096(54)90042-3.

[141] R. Farrugia *et al.*, "Air damping of high performance resonating micro-mirrors with angular vertical comb-drive actuators," *Microsystem Technologies*, vol. 28, no. 6, pp. 1451–1465, 2022, doi: 10.1007/s00542-019-04416-0.

[142] R. A. Dias, R. F. Wolffenbuttel, E. Cretu, and L. A. Rocha, "Squeeze-film damper design with air channels: Experimental verification," in *Procedia Engineering*, 2011, pp. 47–50. doi: 10.1016/j.proeng.2011.12.012.

[143] R. A. Dias, *Micro-g MEMS Accelerometer based on Time Measurement*. 2013.

[144] R. Farrugia, I. Grech, D. Camilleri, O. Casha, E. Gatt, and J. Micallef, "Theoretical and finite element analysis of dynamic deformation in resonating micromirrors," *Microsystem Technologies*, vol. 24, no. 1, pp. 445–455, 2018, doi: 10.1007/s00542-017-3335-7.

[145] F. C. Meral and I. Basdogan, "Design methodology for microelectromechanical systems. Case study: Torsional scanner mirror," *Journal of Mechanical Design*, vol. 129, no. 10, pp. 1023–1030, 2007, doi: 10.1115/1.2756087.

[146] H. Urey, C. Kan, and W. O. Davis, "Vibration mode frequency formulae for micromechanical scanners," *Journal of Micromechanics and Microengineering*, vol. 15, no. 9, pp. 1713–1721, 2005, doi: 10.1088/0960-1317/15/9/013.

[147] J. G. Korvink and O. Paul, *MEMS : A Practical Guide to Design , Analysis , and Edited by*. 2006. doi: 10.1007/978-3-540-33655-6.

[148] T. Izawa, T. Sasaki, and K. Hane, "Scanning micro-mirror with an electrostatic spring for compensation of hard-spring nonlinearity," *Micromachines (Basel)*, vol. 8, no. 8, 2017, doi: 10.3390/mi8080240.

[149] C. H. Manh and K. Hane, "Vacuum operation of comb-drive micro display mirrors," *Journal of Micromechanics and Microengineering*, vol. 19, no. 10, 2009, doi: 10.1088/0960-1317/19/10/105018.

[150] C. Xia, D. Qiao, Q. Zeng, and W. Yuan, "The squeeze-film air damping of circular and elliptical micro-torsion mirrors," *Microfluid Nanofluidics*, vol. 19, no. 3, pp. 585–593, 2015, doi: 10.1007/s10404-015-1585-1.

[151] J. D. Sherwood, "Stokes drag on a disc with a Navier slip condition near a plane wall," *Fluid Dyn Res*, vol. 45, no. 5, 2013, doi: 10.1088/0169-5983/45/5/055505.

[152] M. U. Kim, K. W. Kim, J. H. Kim, and B. M. Kwak, "Hydrodynamic force on a plate near the plane wall," *2000 International Conference on Modeling and Simulation of Microsystems - MSM 2000*, vol. 29, pp. 583–585, 2000.

[153] W. ZHANG and H. A. STONE, "Oscillatory motions of circular disks and nearly spherical particles in viscous flows," *J Fluid Mech*, vol. 367, pp. 329–358, Jul. 1998, doi: 10.1017/S0022112098001670.

[154] W. N. Sharpe, K. M. Jackson, K. J. Hemker, and Z. Xie, "Effect of specimen size on young's modulus and fracture strength of polysilicon," *Journal of Microelectromechanical Systems*, 2001, doi: 10.1109/84.946774.

[155] J. Z. Buchwald, *The rise of the wave theory of light: Optical theory and experiment in the early nineteenth century*. Chicago and London: The Unversity of Chicago Press, 1989.

[156] L. Hazra, "Diffractive optical elements: past, present, and future," *Selected Papers from International Conference on Optics and Optoelectronics '98*, vol. 3729, no. April 1999, pp. 198–211, 2003, doi: 10.1117/12.346782.

[157] J. Suszek *et al.*, "3-D-printed flat optics for THz linear scanners," *IEEE Trans Terahertz Sci Technol*, vol. 5, no. 2, pp. 314–316, 2015, doi: 10.1109/TTHZ.2015.2398313.

[158] R. Schnabel, A. Bunkowski, O. Burmeister, and K. Danzmann, "Three-port beam splitters–combiners for interferometer applications," *Opt Lett*, vol. 31, no. 5, pp. 658–660, 2006, doi: 10.1364/OL.31.000658.

[159] Y. Lin, D. Rivera, and K. P. Chen, "Woodpile-type photonic crystals with orthorhombic or tetragonal symmetry formed through phase mask techniques," *Opt Express*, vol. 14, no. 2, pp. 887–892, 2006, doi: 10.1364/OPEX.14.000887.

[160] Y. J. Liu and X. W. Sun, "Electrically tunable two-dimensional holographic photonic crystal fabricated by a single diffractive element," *Appl Phys Lett*, vol. 89, no. 171101, 2006, doi: 10.1063/1.2364471.

[161] W. Furlan, V. Ferrando, J. Monsoriu, P. Zagrajek, E. Czerwińska, and M. Szustakowski, "3D printed THz diffractive lenses can be used in focusing and imaging systems, offering features like extended depth of focus or bifocalization," *Opt Lett.*, vol. 41, no. 8, pp. 1748–1751, 2016, doi: 10.1364/OL.41.001748.

[162] M. Ahmad, N. Kabalan, and S. Omran, "An Analytical Study of the Diffraction of Light by a Circular Aperture Using Spherical Harmonics for n≤1," *Int J Opt*, vol. 2020, 2020, doi: 10.1155/2020/3057674.

[163] X. Zheng, J. Yang, R. Wang, and T. Lan, "Visible light waveband Dammann grating based on all-dielectric metasurface," *Appl Opt*, vol. 61, no. 9, p. 2184, 2022, doi: 10.1364/ao.448192.

[164] M. Huff, "Recent Advances in Reactive Ion Etching and Applications of High-Aspect-Ratio Microfabrication," *Micromachines (Basel)*, vol. 12, no. 8, p. 991, Aug. 2021, doi: 10.3390/mi12080991.

[165] T. Xu, Z. Tao, H. Li, X. Tan, and H. Li, "Effects of deep reactive ion etching parameters on etching rate and surface morphology in extremely deep silicon etch process with high aspect ratio," *Advances in Mechanical Engineering*, vol. 9, no. 12, pp. 1–19, 2017, doi: 10.1177/1687814017738152.

[166] L. Meng and J. Yan, "Effect of process parameters on sidewall damage in deep silicon etch," *Journal of Micromechanics and Microengineering*, vol. 25, no. 3, 2015, doi: 10.1088/0960-1317/25/3/035024.

[167] P. González-Losada *et al.*, "Computer vision assisted full wafer scale evaluation of process parameters and trends in deep silicon etch," in *MNE EUROSENSORS 2022 (Oral presentation)*, Leuven, Belgium: MNE EUROSENSORS 2022 - Micro and Nano Engineering Confereence, 2022.

[168] R. Ghodssi and P. Lin, *MEMS Materials and Processes Handbook*, vol. 1. in MEMS Reference Shelf, vol. 1. Boston, MA: Springer US, 2011. doi: 10.1007/978-0-387-47318-5.

[169] N. Kooy, K. Mohamed, L. T. Pin, and O. S. Guan, "A review of roll-to-roll nanoimprint lithography," *Nanoscale Res Lett*, vol. 9, no. 1, pp. 1–13, 2014, doi: 10.1186/1556-276X-9-320.

[170] H. J. Lee, H. W. Ro, C. L. Soles, R. L. Jones, E. K. Lin, and W. I. Wu, "Effect of initial resist thickness on residual layer thickness of nanoimprinted structures," *J. Vac. Sci. Technol. B*, no. 23, pp. 3023–3027, 2005.

[171] M. Yin, H. Sun, and H. Wang, "Effect of stamp design on residual layer thickness and contact pressure in UV nanoimprint lithography," *Micro Nano Lett*, vol. 13, pp. 887–891, 2018.

[172] C. Thanner and M. Eibelhuber, "UV nanoimprint lithography: Geometrical impact on filling properties of nanoscale patterns," *Nanomaterials*, vol. 11, p. 822, 2021.

[173] I. S. Garcia *et al.*, "Microfabrication of double proof-mass SOI-based matryoshka-like structures for 3-axis MEMS accelerometers," *Micro and Nano Engineering*, vol. 19, no. January, 2023, doi: 10.1016/j.mne.2023.100204.

[174] J. Cunha *et al.*, "Assessing tolerances in direct write laser grayscale lithography and reactive ion etching pattern transfer for fabrication of 2.5D Si master molds," *Micro and Nano Engineering*, vol. 19, no. April, pp. 1–8, 2023, doi: 10.1016/j.mne.2023.100182.